10.51975/24390201.som
Journal of the Nigerian Society of Chemical Engineers, 39(2), 2024

DESIGN OF A HYDROTHERMAL LIQUEFACTION REACTOR WITH COOLING SYSTEM FOR CONVERTING 1000g MICROALGAE BIOMASS TO BIOCRUDE

Ikhazuangbe, P.M.O[1,2]., Eboibi, B.E[2,3], Amabogha, B.[3], Ikalumhe, W.O.[4], Orugba, H.[2] and Agarri, S.E.[2,3,5]

[1]Chemical Engineering Department, Edo State University Uzairue, Nigeria
[2]Chemical Engineering Department, Delta State University Oleh Campus, Nigeria.
[3]Chemical Engineering Department, Federal University Otueke, Nigeria.
[4]Mechanical Engineering Department, Edo State University Uzairue, Nigeria
[5]Chemical Engineering Department, Ladoke Akintola University, Ogbomosho, Nigeria.
Corresponding author: ikhazuangbe.prosper@edouniversity.edu.ng

ABSTRACT

Biomass from microalgae used for the production of biocrude by hydrothermal liquefaction operation is a viable source of renewable energy and is gaining more attention globally. This work dwells on the design of a batch reactor for the conversion of 1000g microalgae biomass to biocrude by hydrothermal liquefaction. The material and energy balances carried out on the reactor were based on 5wt% gas, 50wt% biocrude, 30wt% liquid phase and 15wt% solid residue, which are the products of hydrothermal liquefaction (HTL), on a ratio of 4:1 for the solvent and microalgae biomass as raw material. The specific heat capacity of Tristearin (triglyceride) was used in the design and the maximum amount of energy required in the unit was obtained as 2222 W. The reactor volume, the reactor height, its wall thickness, thickness of the top flat end, the thickness of the insulation material and the flowrate of the cooling system were designed as 0.0188 m^3, 0.31 m, 0.003 m, 0.0067 m, 0.023 m and 0.0023 m^3/min respectively. The cost analysis of the reactor, based on market reality show that the cost of materials, design, fabrication and personnel is estimated at eight hundred and twenty eight thousand, seven hundred naira only (N828,700). Consequently, this research work presents designed reactor for converting microalgae biomass into biocrude and the design data can be used as a standard in reactor design for the production of biocrude.

Keywords: Biocrude, hydrothermal liquefaction, microalgae biomass, reactor design, renewable energy,

1. INTRODUCTION

Energy consumption globally is on the increase, and about 88% of this energy is obtained from fossil fuels (Guo *et al*, 2015). Rapid industrialization and urban development in the past decades resulting to increased consumption of fossil fuels, have led to the degradation of water quality and increased global warming (Ikhazuangbe *et al*., 2023a), hence the need for other sources of energy that are renewable (Tareket *et al*., 2022). Microalgae are photosynthetic eukaryotic or prokaryotic microorganisms that have the ability to grow rapidly in different environment (Jahn *et al*., 2014; Hameed, 2016). Due to its faster growth rate, economic importance, high oil content, high biomass productivity and its renewability, Microalgae are been considered widely as promising feedstock for the production of biocrude (Jahn *et al*., 2014; Eboibi, 2019).

Hydrothermal liquefaction is one of the new technologies in the production of biocrude at high process temperature of about 200 to 380^{o}C (Tian *et al*, 2014), high pressure of about 2 to 25 bar (Eboibi, 2019) and residence time of about 5 to 120 minute (Barreiro *et al*, 2014), in the presence of water. Hydrothermal liquefaction operation can be used to convert dry or wet biomass to biocrude, thereby overcoming the major problem of energy consumption that accompany dewatering, usually encountered in the use of other methods such as pyrolysis (Le *et al*, 2019; SundarRajan *et al*, 2021), transesterification (Eboibi *et al*, 2015) and gasification (Xu *et al*, 2019). Consequently, hydrothermal liquefaction operation does not require extra energy to dry the biomass and it is not highly corrosive to the reactor (SundarRajan *et al*, 2021). Previous reports on hydrothermal liquefaction operation investigated the effects of catalyst, temperature, residence time, solid concentration, strain of microalgae and solvent mix, on the quality and yield of biocrude (Eboibi *et al,* 2015). This hydrothermal liquefaction operation can be carried out with or without the use of catalyst (Xu *et al*, 2019), and the products of this operation after cooling and separation are the aqueous

phase, biocrude, gaseous phase and solid residue (Kumar *et al*, 2018).

Several researchers who worked on the production of biocrude from microalgae biomass, by hydrothermal liquefaction, did not exhaustively report details of the reactor design configuration and the cooling system in particular. However, Chemical engineering design typically encompasses conceptualization, feasibility analysis, process synthesis, equipment selection and sizing, cost estimation, safety considerations and environmental impact assessment. Jazrawi *et al*, (2015) used a 20 mL capacity stainless steel 316 batch reactor of about 120mm length, 0.75 inch outer diameter and wall thickness of about 1.65 mm. The mode of cooling the reactor after the hydrothermal liquefaction operation was not stated, although they did not report in their work that they designed and fabricated the batch reactor. Kandasamy *et al,* (2021) reported in their work that they used stainless steel 316, 50 mL capacity batch reactor for the hydrothermal liquefaction, but the cooling effect of the reactor after the hydrothermal liquefaction operation, and the design configuration of the reactor were not reported. Neveux *et al*, (2014) used a 20 ml stainless steel reactor to produce biocrude using 1 g dry algae and 14 ml water. The researchers effected the cooling of the reactor after the hydrothermal liquefaction in an iced water bath for about 1 min, but the reactor design configuration was not reported. Wang *et al*, (2021) used a stainless steel 316 batch reactor of about 50 mL internal volume, fitted with electric furnace and a rotary evaporator. It was reported that the reactor could withstand a maximum temperature of about 400 ^{o}C and a pressure of about 60 bar, but the mode of cooling the reactor after the hydrothermal liquefaction operation, and the reactor configuration were not reported. Wang *et al*, (2018) reported in their work that 1800 ml stainless steel reactor was used for the conversion of 120 g of *Nanochloropsis* sp. and 480 g of water to biocrude. It was also reported that the reactor was operated for about 30min at 6 – 8 MPa pressure, but the operating temperature, mode of cooling the reactor after the hydrothermal liquefaction and the design configuration were not reported. Barreiro *et al*, (2015) used 10ml stainless steel 14571 reactor, filled to about 70% with a mixture of algae and water at a ratio of 1:10. It was reported that the reactor was operated at about 300 – 375 ^{o}C for about 15 min in each operation, and the reactor submerged in an ice-water bath for fast cooling. Costanzo *et al*, (2015) carried out their reaction in a 75ml reaction vessel fitted with band heater in an aluminum block of about 250 W. 7 g of algae and 32 ml deionized water at different temperature, with 225 ^{o}C as maximum, and for a maximum of 21 min were charged into the reactor. It was also reported that the vessel was removed from the aluminum block and the bottom section submerged in a water bath to cool to ambient temperature. The reactor material and the design configuration were not reported. Ikhazuangbe *et al*, (2023b) designed a 4.2 liter batch reactor for the conversion of 500 g microalgae to biocrude. It was reported that stainless steel 316 was used, with 2.2 mm thickness, 150 mm internal diameter, height of 240 mm, 4.8 mm flat end thickness and 2 mm insulation thickness. The reactor was designed to operate at a maximum of 400 ^{o}C and 40 bar. Nevertheless, the reactor was designed to cool at room temperature without been induced.

2. HYDROTHERMAL LIQUEFACTION REACTOR

Microalgae are a unicellular or simple multicellular ubiquitous group of fast-growing microphototrophs which has major ecological and economic importance (Jahn *et al.,* 2014; El Sheekh *et al.*, 2020). Microalgae are preferred to traditional feedstock such as Rape seed, soybean, sugar cane, palm oil, sunflower etc., for the production of biocrude because they have strong capacity of carbon fixation, high growth rate and short cell cycle, and do not compete for arable land (Tan *et al.*, 2015; Xue & Jiang, 2017), They consist mainly of carbohydrates, proteins and lipids. The main component of microalgae biomass or any other biomass that transform into biocrude is lipid. The composition of lipids varies in different microalgae: *Spirulina* specie 38.6 % (Song *et al*, 2015), *Chlorella* specie 39.4 % (Tian *et al*., 2022), *Dunaliella* specie 44.63 % (Song *et al*., 2015) and *Nanochloropsis* specie 42.67 % (Song *et al.*, 2015). During hydrothermal liquefaction operations, lipids are easily hydrolyzed to glycerol and higher fatty acids. They do not transform at all into the solid phase but exist in the form of triglyceride with low dielectric constant that easily undergoes noncatalytic hydrolysis under hydrothermal liquefaction conditions to generate higher fatty acids and glycerol (Hu *et al*, 2019; Hao *et al*, 2021). The triglycerides easily decompose to form free fatty acids and glycerol at subcritical condition under which biocrude is produced (Hu *et al.*, 2019), because they contain glycerol backbone connected to three free fatty acids. Lipids forms the main source of light components in biocrude and do not get converted during hydrothermal liquefaction into the solid phase. The

contribution of lipids to heavy components of biocrude depend on the operating temperature. At low hydrothermal liquefaction operating temperature, lipids contribute more to biocrude phase, but at higher temperature, they contribute just like proteins (Hao *et al*., 2021).

Specific heat capacities of triacylglycerols forms thermo-physical property essential in carrying out its energy balance in process design. The specific heat capacities of some forms of triacylglycerols according to Zhu *et al*., (2018) are listed in Table 1. The model to develop the volume of the hydrothermal liquefaction batch reactor using these parameters, is represented as equation (1).

Table 1. Specific heat Capacities of some Triacylglycerols

Triacylglycerols	Specific heat capacities (kJ/kg)
Trilinolenin	1.765
Trilinolein	1.813
Triolein	1.886
Tristearin	1.938

Volume of the reactor, $V = \frac{N_{AO}}{t.KC_A} X_A$ (1)

Where N_{AO} = initial moles of the lipids on the microalgae, k = maximal hydrolysis rate of lipid from beef fat 0.0095 min^{-1} (Chen *et al*., 2018), C_A = concentration of the lipids in the microalgae mixture, t = time taken for the HTL operation, and X_A = the average percentage conversion of biocrude from biomass

2.1 Wall thickness of Reactor

The thickness of the reactor is very important and must be designed to resist internal pressure buildup, having safety, mechanical and corrosion allowances for pressure gauge, safety valve and pipe threads. Process batch reactors are normally considered as thin cylinders; but high-pressure pipes or reactors such as hydrothermal liquefaction reactor of biocrude, are classified as thick cylindrical reactors and must be given special consideration (Aprilla *et al,* 2023). A vessel or reactor must be designed to withstand the maximum working pressure with a maximum allowable safety pressure of about 10% set in practice (Towler & Sinnott, 2008). The thickness of the batch reactor can be evaluated with the following formula as obtained from ASME B31.3 code:

$t_m = t_p + C$ (2)

$t_p = \frac{P\,d}{2\,(S\,E - P\,\gamma)}$ (3)

Therefore,

$t_m = \frac{P\,d}{2\,(S\,E - P\,\gamma)} + C$ (4)

Where C is the sum of corrosion and mechanical allowances; t_m is the minimum required thickness of the reactor; t_p represent the design pressure thickness; P = internal design gauge pressure in lb⁄in^2 or N⁄mm^2 ; d = reactor inner diameter; S = the basic allowable stress for the reactor material in lb⁄in^2 (N⁄mm^2) presented in Table 2; E = casting quality factor; γ = coefficient of temperature (0.6) (Sinnott, 2005).

Table 2. Stresses of typical plate design

Material	Tensile strength N/mm^2	Design stresses (N/mm^2) at different temperatures ^oC									
		0-50	100	150	200	250	300	350	400	450	500
Carbon steel	360	135	125	115	105	95	85	80	70		
Carbon-manganese	460	180	170	150	140	130	115	105	100		
Carbon-molybdenum	450	180	170	145	140	130	120	110	110		
Low alloy steel (Ni, Cr, Mo, V)	550	240	240	240	240	240	235	230	220	190	170
Stainless steel 18Cr/8Ni (304)	510	165	145	130	115	110	105	100	100	95	90
Stainless steel 18Cr/8Ni (321)	540	165	150	140	135	130	130	125	125	120	115
Stainless steel 18Cr/8Ni (316)	520	175	150	135	120	115	110	105	105	100	95

2.2 Thickness of the flat end

The cost of fabrication of flat end type of a reactor is low, but structurally, they are not efficient because very thick plates would be required for high pressures or

large diameters. The design equations used usually to determine the thickness of flat ends of a pressure reactor, are based on the stress analysis in the flat plates. The thickness of the flat end will depend on the degree of constraint at the plate periphery.
The minimum thickness that is required for a flat end is given as equation (5).

$$t_m = C_p D_e \sqrt{\frac{P_i}{f}} \quad (5)$$

Where C_p = design constant, dependent on the edge, D_e = nominal plate diameter, f = design stress.
Values for the design constant C_p and the nominal plate diameter D_e are given in the design codes and standards for various arrangements of flat end closures (Towler & Sinnott, 2008). The values of the design constant and nominal diameter for the typical designs are given below:
(a) For flanged-only end which has diameters less than 0.6m and corner radii at least equal to 0.25e, C can be taken as 0.45; D_e is equal to D_i (internal diameter).

(b) For plates welded to the end of the shell with circumferential welds in the main shell connecting a formed head take, C is taken 0.33 and $D_e = D_i$.

(c) For bolted cover with a full-face gasket, C = 0.25 and D_e equal to the bolt circle diameter.

(d) While for bolted end cover with a narrow-face gasket, C = 0.3 and D_e equal to the mean diameter of the gasket

2.3 Cooling system of the reactor
Energy balance is a fundamental concept in thermodynamics and energy analysis that accounts for the input and output of energy within a system. It ensures that the total energy entering a process (heating) equals the total energy leaving the process (cooling), plus any accumulation or depletion of energy within the system (Sinnott, 2005). Energy balance is made to determine the heating energy, cooling energy and power required of a system. The energy balance equation is represented in equation (6).

The calculation of the time required to cool the content of a reactor is dependent upon factors such as: whether it is jacketed or uses coil type of cooling, the heat transfer medium, the type of reactor, the reactor's geometrical dimensions, the content of the reactor and the physical properties (Heggs & Hills, 1995). A reactor that uses conventional jacket has the advantage of covering the full wall and base surface of the reactor, and very simple to construct. The internal coil of full helical coils is the more usual design, which allow the maximum surface to be installed, it is the cheapest form of heat transfer surface for installation in a vessel, but requires additional vessel to cover the coils with relatively expensive main flange (Towler and Sinnott, 2008).

The choice of either a jacket or coil is based on a number of considerations. If the reactor contains highly corrosive or highly reactive materials, and when there is no extra metal surface in contact with the process, a jacket is advantageous. However, the heat transfer performance of a jacket is lower than that of a coil, because there will be a lower process side coefficient and the area/volume ratio of a jacketed vessel decreases with increasing scale. A coil type of cooling provides large surface area, which makes it advantageous than jacket type. However, the coil should not be packed so tightly as to form a false wall. For a well-designed coil, the overall coefficient is in the range of 400 to 600 Wm^2K^{-1} and the minimum target velocity should be 1.5 ms^{-1} (Carpenter, 2011).

Energy balance is made to determine the energy requirements of the process: the heating, cooling and power required. The energy balance equation is:

Energy in (Q_{in}) = Energy out (Q_{out}) + consumption + accumulation (6)

When there is no leakage or accumulation of energy in the system, equation (6) reduces to equation (7.)

$$Q_{in} = Q_{out} \quad (7)$$

Where $Q = mC_p\,(T_1 - T_2)$ (8)
Q = amount of heat produced or given out by the reactor, C_p = specific heat capacity of the hot or cold fluid, m = mass of the reactor material or water, T_2 = temperature of the reactor, T_1 = initial temperature of the water.
For simple case of the time to cool the batch of mass M, the rate of heat removal can be evaluated. At time t = 0, cooling has not started, therefore, equation (6) will be expressed as follows:

Heat input = $U_{reator}\,A_{reactor}(T_{reactor} - T)$
Heat output = 0
Accumulation in the reactor = $\frac{mC\,dT}{dt}$
$U_{reactor}A_{reactor}\,(T_{reactor} - T) = 0 + \frac{MC\,dT}{dt}$ (9)

$\frac{dT}{dt} = \frac{U_{reactor}A_{reactor}\,(T_{reactor}-T)}{MC}$

$\int \frac{dT}{(T_{reactor}-T)} = \frac{U_{reactor}A_{reactor}}{MC} \int dt$ (10)

$- \ln (T_{reactor} - T) = \frac{U_{reactor}A_{reactor}}{MC} t + B \quad 1$ (11)

At t = 0, T = T_o = inlet temperature of cooling water

$- \ln (T_{reactor} - T_o) = \frac{U_{reactor}A_{reactor}\,(0)}{MC} + B$ (12)

$B = - \ln (T_{reactor} - T_o)$ (13)

Substituting for B in equation 1

$- \ln (T_{reactor} - T) = \frac{U_{reactor}A_{reactor}}{MC} t - \ln (T_{reactor} - T_o)$ (14)

$\ln (T_{reactor} - T_o) - \ln (T_{reactor} - T) = \frac{U_{reactor}A_{reactor}}{MC} t$ (15)

Therefore, the time to cool or heat a batch of mass M:

$\ln \left(\frac{T_{reactor}-T_o}{T_{reactor}-T}\right) = \frac{U_{reactor}A_{reactor}}{MC} t$ (16)

2.3 Insulation of the reactor

Insulators are materials used for covering other materials to reduce heat, sound or electricity loss or entrance when in contact with an object or in a radiative range of influence (Rehan, 2020). A wide range of these materials used for insulation exist, however, the most common types used for loose-fill include: fiberglass, cellulose and wool. Selection of material to be used for insulation is based on their initial cost, their effectiveness, durability, adaptability of its form to the material that will be insulated. Economically, it may be better to choose an insulation material with a lower thermal conductivity than increasing the thickness of the insulation of a material of higher thermal conductivity in the hold walls (Etuk *et al*., 2020).

Fiberglass insulation will be used in this research work because of its high resistance to microbiological attack, high resistance to fire attack, good resistance to most chemicals, high heat resistance, low thermal conductivity and its availability in a variety of presentations. Table 3 shows the thermal conductivity of different types of fiberglass (Zaid, 2020).

The reactor has a cylindrical pipe shape, consequently, the heat conduction in this system is in the radial direction and the area normal to flow varies with distance (Iyagba, 2008). Therefore, applying Fourier's law for a cylindrical system:

$Q = \frac{-2\pi L k\,(\Delta T)}{ln\frac{r_o}{r_i}}$ (17a)

Where Q is the rate of heat loss, L is the length or height of the cylinder, ΔT is the temperature difference, while r_o and r_i are the outer and inner radius respectively. For a cylindrical system with insulation, equation (17a) will become:

$Q = \frac{-2\pi L\,(\Delta T)}{\frac{1}{k_1} ln\frac{r_2}{r_1} + \frac{1}{k_2} \ln\frac{r_3}{r_2}}$ (17b)

Where r_1 and r_2 are the inner and outer radius of the cylinder, r_3 is the outer radius of the insulator, k_1 is the heat transfer coefficient of thermal conductivity of the cylinder, k_2 is the thermal conductivity of insulator.

Table 3. Different Thermal Conductivity and Density values at 0°C of Fiberglass

Type	Density kg/m^3	Thermal conductivity (W/m°C)
Type I	10 – 18	0.044
Type II	19 – 30	0.037
Type III	31 – 45	0.034
Type IV	46 – 65	0.033
Type V	66 – 90	0.033
Type VI	91	0.036
Glass fiber, resin bonded	64 – 144	0.036

3. PROCESS DESIGN

The process design entails material and energy balances, to properly account for the materials and energy entering and leaving the reactor.

3.1 Material balance

The overall material balance on the reactor, represented with the block diagram in Fig. 1, was carried out at steady state condition and no chemical reaction is taking place. Therefore,

Basis: 1000g of microalgae biomass

Overall material balance is given as equation (18)

Biomass input + rate of generation = Biomass output + rate of disappearance (18)

At steady state, since there is no chemical reaction and accumulation is zero,

Biomass input = Biomass output (19)

But the products of biomass conversion by hydrothermal liquefaction are gas phase, solid residue, biocrude and aqueous phase. Therefore, equation (19) becomes,

(Biomass + water) F_1 = gas phase (F_2) + solid residue (F_3) + biocrude (F_4) + aqueous phase (F_5) (20)

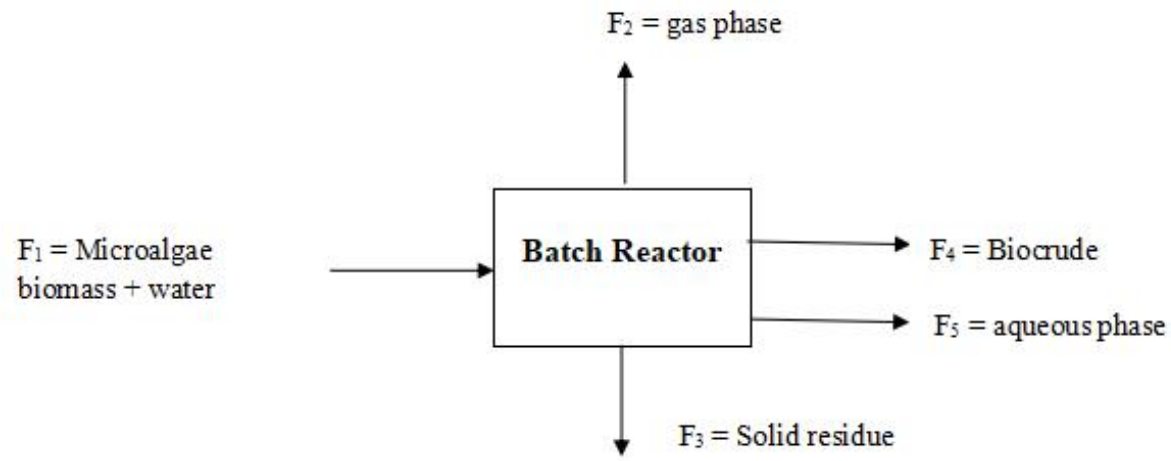

Fig 1. Block diagram of the batch reactor

According to Adrien *et al.,* (2019), the ratio of the solvent to the microalgae biomass in the reactor is 4:1. Consequently, the mass of water can be obtained as follows from the mass of the microalgae biomass which is 1000 g.

Mass of water = ratio of the mixture × mass of the microalgae biomass (21)
$= \frac{4}{1} \times 1000$ g
= 4000 g

But the density of water is 0.997 g/cm^3
Therefore,
Volume of water = $\frac{\text{Mass of water}}{\text{Density of water}}$ (22)
Volume of water = $\frac{4000g}{0.997\text{g}/cm^3}$
Volume of water ≈ 4000 cm^3

The total mass of the mixture = mass of water + mass of the microalgae biomass
= 4000g + 1000 g
= 5000 g
Therefore, the mass in stream F_1 = 5000 g

Balance on the feed and products into and from the reactor are on percentage composition basis, of gas 20wt%, biocrude 54wt%, the liquid phase 12wt% and solid residue 14wt%, under isothermal condition of 350 ℃ by hydrothermal liquefaction of microalgae biomass (Eboibi, 2019).

Therefore, in stream F_2,
The amount of biogas present is 20% of stream F_1
= 0.2 × 5000 g
= 1000 g

In stream F_3,
The amount of Biocrude present is 54% of stream F_1
= 0.54 × 5000 g
= 2700 g

In stream F_4,
The amount of aqueous phase present is 12% of stream F_1
= 0.12 × 5000 g
= 600 g

In stream F_5,
The amount of solid residue present is 14% of stream F_1
= 0.14 × 5000 g
= 700 g

3.2 Energy balance on the reactor

Using equation (8) where c_p is taken as the specific heat capacity of the Tristearin, a form of pure triacylglycerols, a saturated lipid (Zhu *et al.,* 2018).

Q = energy input = energy output
$Q = mc_p\theta$ (23)
= 5000g x $1.938\frac{KJ}{kg℃}\ x\ (400 - 25)℃$
= 5kg $1.938\frac{KJ}{kg℃}\ x\ 375℃$
= 3634 kJ

The amount of operational heat required for the hydrothermal liquefaction is 3634 kJ. But the design heat required for the hydrothermal liquefaction is 10% of the operational heat (Towler & Sinnott, 2008). Therefore,

Q = 3634 + 363
≈ 4000 kJ
Operating the reactor for 30 minutes at 400 ℃ , the maximum amount of design energy required will be:
$Q = \frac{4000kJ}{30\ min}\ x\ \frac{1\ min}{60\ sec}\ x\ \frac{1000\ J}{1\ kJ}$
≈ 2222 W

4. REACTOR EQUIPMENT DESIGN

The feed stream to the batch reactor will be taken to be operating at an optimal temperature condition (Amiri & Arabian, 2016). Therefore, average percentage conversion x_A of biocrude yield from microalgae will be, 0.4133. Using equation (1),

Volume of the reactor to be designed, $V = \frac{N_{AO}}{t.KC_A}\ x_A$

Where N_{AO} = initial moles of the lipids on the microalgae, k = maximal hydrolysis rate of lipid from beef fat 0.0095 min^{-1} (Chen *et al*., 2018), C_A = concentration of the lipids in the microalgae mixture, t = time taken for the HTL operation, and x_A = the average mass fraction of biocrude from biomass.

Chen *et al*., (2018) who worked on *Chlorella* species, obtained 20 – 50% of lipids in the microalgae biomass with molecular weight of 280.45g/mole. Consequently, lipid is the major component present in microalgae biomass that converts to biocrude. Therefore, N_{AO} can be calculated as:

$$N_{AO} = \frac{\text{1000g of the microalgae biomass} \times \text{mole fraction of the lipids in the microalgae}}{molecular\ weight\ of\ the\ lipid}$$

Therefore $N_{AO} = \frac{1000\text{g} \times 0.5}{280.45\ g/mole}$
$N_{AO} = \frac{1000\ \text{mole}}{280.45}$
=3.5657 mole

Also, mass concentration of lipid in the microalgae mixture $C_A = \frac{1000\text{g} \times 0.5}{5000cm^3}$
= 0.1 g/cm^3

Therefore, molar concentration of lipid in the microalgae mixture $C_A = \frac{0.1g}{cm^3} \times \frac{1mole}{280.45g}$
= 0.00036 mole/cm^3
k = 0.0095 min^{-1}
t = 30 min
x_A = 0.45

Therefore, where $V = \frac{N_{AO}}{t.k.C_A}\ x_A$

$V = \frac{3.5657\ mole \times 0.45}{30\ min \times 0.0095\ min^{-1} \times 0.00036 mole/cm^3}$
$V = \frac{1.6046\ cm^3}{1.026\ x\ 10^{-4}} = 15639.4cm^3$

Safety factor of the reactor = 20% of the calculated volume (Towler & Sinnott, 2008)
Safety factor = 0.2 ×15639.4
$= 3127.9\ cm^3$

Therefore, the design volume of the reactor $V = 15639.4cm^3 + 3127.9cm^3$
$= 18767.3\ cm^3$

Volume of the reactor ≈ 18.8 litter or 0.0188m
Since the reactor is similar in shape to the shape of a cylinder (without the curved surfaces), the height of the reactor can be calculated using equation (24), where volume of a cylinder V, is given as,
$V = \pi r^2 h$ (24)
Where r = radius of the reactor and h = height of the reactor

Assuming internal diameter of 28cm, (radius 14cm)
Therefore,
18.8L = π$14^2$$cm^2$h
$h = \frac{18767.3cm^3}{\pi\ x\ 196cm^2}$
≈ 0.31m

4.1 Design of the reactor thickness

The thickness of the stainless steel material to be used for the fabrication is designed using equation (4)
$t_m = \frac{P\ d}{2\ (S\ E - P\ \gamma)} + C$
Where γ = coefficient of temperature (0.6) (Sinnott, 2005). For a stainless steel 18Cr/8Ni 316, the design stress from Table 2 at 400ºC is 105.
Therefore,
P = 20 + (20 x 0.1)
= 22 bar or 2.2N/mm^2
$t_m = \frac{2.2\ x\ 280}{2(105\ x\ 1 - 2.2\ x\ 0.6)}$
$= \frac{616}{2(105 - 1.32)}$
≈ 3.0 mm or 0.003 m

4.2 Design of the thickness of the reactor flat end

For the properties of stainless steel 18Cr/8Ni 316 in Table 2, and using equation (5), the thickness of the top flat end of the reactor is given as:
$t = C.D_e\sqrt{\frac{P_i}{f}}$
Where C = design constant. For a flat end welded to the shell with a 45º fillet weld, C = 0.33, dependent on the

edge, D_e = nominal plate diameter, f = design stress. For a system with the plates welded to the shell end, D_e = $1/2$ D_i (internal diameter of the shell (Towler & Sinnott, 2008).

Therefore, the minimum thickness of the flat end required is given by:

t_m = 0.33 x 140mm x $\sqrt{\frac{2.2}{105}}$

= 46.2mm x 0.1447

= 6.7 mm or 0.0067 m

4.3 Thickness of the reactor insulation material

Equation (17b) is used for the determination of the thickness of insulation material, that is, Type I fiberglass, (see Table 3) that is required for the reactor,

$Q = \frac{-2\pi L\ (\Delta T)}{\frac{1}{k_1} ln\frac{r_2}{r_1} + \frac{1}{k_2} \ln\frac{r_3}{r_2}}$

Where r_1 and r_2 are the inner and outer radius of the cylinder, r_3 is the outer radius of the insulator, k_1 is the thermal conductivity of the cylinder, k_2 is the thermal conductivity of insulator and Q is the design energy of the reactor.

$2222 = \frac{-2\pi x\ 0.31m\ x\ (30-400)}{\frac{1}{16.3} ln\frac{0.163}{0.14} + \frac{1}{0.044} \ln\frac{r_3}{0.163}}$

$\frac{1}{16.3}\ ln\frac{0.163}{0.14} + \frac{1}{0.044}\ \ln\frac{r_3}{0.163} = \frac{720.68}{2222}$

$\frac{1}{0.044}\ \ln\frac{r_3}{0.163} = 0.3243 - 0.00933$

$\ln\frac{r_3}{0.163} = 0.315 \text{ x } 0.044$

$\frac{r_3}{0.163} = e^{0.01386}$

r_3= 1.014 x 0.163

r_3= 0.1653 m

Thickness of the insulation material = r_3 - r_2 = 0.1653 – 0.163

= 0.023 m

4.4 Design of the reactor cooling system

4.4.1 Volume of water required for the cooling

The volume of water that is required for cooling the reactor after the hydrothermal liquefaction operation per minute is determined from the mass of the water, which can be obtained using equation (8),

$Q = m\ C_p\ (T_2 - T_1)$

The quantity of heat produced by the reactor = the quantity of heat to be removed with water

3640.3 kJ = m x 4.2kJ/kg ^oC (400 – 25) ^oC

m = $\frac{3640.3}{1575}$kg

= 2.31 kg

Volume of the water to be used = $\frac{mass\ of\ water}{density\ of\ water}$

= $\frac{2.31kg}{1000kg/m^3}$

= 0.00231 m^3

For one minute of cooling

Volume of the water used = 2.3 liter/min or 0.0023m^3/min

4.4.2 Length of the coil required for cooling

Since the coil is similar in shape to that of a cylinder (without the curved surfaces), the length of the coil can be calculated using equation (24) for the volume of a cylinder, V = $\pi r^2 h$.

For a coil with radius of 0.75 cm

Length of the coil h = $\frac{2311cm^3}{\pi\ x\ 0.75^2 cm^2}$

= 1308 cm

≈ 13.1 m

5. COST ANALYSIS OF THE DESIGN

The cost analysis of the design is based on the current market prices of the various materials, transportation, cost of labor and consultancy. These entire costs are presented as the Bill of Engineering Measurement and Evaluation (BEME) in Table 4.

Table 4. Bill of Engineering Measurement and Evaluation

Item	Quantity	Price (N)
Pressure gauge	1	40,000
Pressure valve	2	17,000
Electrical heating element	2 pack	80,000
Control panel with Temperature sensor	1	150,000
Stainless steel (1mm thickness)	2	121,000
Flat plate hanger	1	10,000
Fiberglass material	1 bag, 4 wards	22,000
Stainless steel electrode	1 pack	18,000
Production cost (mechanical & electrical)	-	30,000
Miscellaneous		165,000
Stainless steel screw	12	1,200
Pressure gauge cup	1	3,000
Design and consultancy	-	150,000
Standing pipes (stainless steel)	2	25,000

Item	Quantity	Price (N)
Electrical cables	3 yards	5,500
Total		828,700*

**Eight Hundred and Twenty Eight Thousand, Seven Hundred Naira Only*

6. SAFETY OF THE REACTOR

In the operation of hydrothermal liquefaction, high temperature and pressure conditions are involved, so care was taken in this design to ensure that they are properly controlled and do not pose safety risks on the equipment and operators. Therefore, operators are advised to adhere strictly to the operating conditions to maintain the integrity of the equipment and prevent accidents. Also, the catalysts and solvents used in the operation should be properly handled to minimize risks to operators and the surrounding environment.

7. RESULTS AND DISCUSSION

Design of a reactor involves majorly process design, material selection and sizing. The material and energy balances carried out on the batch reactor, show that a total 4000 g of water will be required to process 1000 g of microalgae for the production of biocrude phase, gas phase, liquid phase and solid residue according to the composition reported by Eboibi, (2019). The energy balance on the reactor showed that a total amount of 2222 W will be required to convert the microalgae to biocrude at the operating temperature of 400 ^{o}C for 30 min.

The volume, diameter and height of the reactor were designed, based on data obtained from the material balance, operating condition of the reactor, chemical properties of the microalgae and the properties of the stainless-steel material selected for the construction. The reactor volume was design as 18.8 liter (0.0188 m^3), which on the basis of the ratio of biomass to reactor volume, agrees with the reports of Hoang *et al.*, (2021) and Kandasamy *et al.*, (2021), but did not agree with the volumes used by Costanzo *et al.,* (2015) and Wang *et al.,* (2018) under the same conditions.

The design of the height of the reactor was obtained as 0.31 m (310 mm), which is not in agreement with the 120 mm height, for a 20ml reactor used by Jazrawi *et al.,* (2015), though it was reported in their work that they used approximately 3 g biomass of the microalgae.

The design of the wall thickness of the reactor was obtained as 0.003 m (3.0 mm) which agrees with Jazrawi *et al.*, (2015) who reported reactor wall thickness of 1.65 mm, but at variance with Aprilla *et al.,* (2023), who reported wall thickness of 1mm in their design of a reactor for the production of Fe_3O_4 Nanoparticles. This variation may be as a result of the fact that, wall thickness is a function of the reactor volume.

The thickness required for the top flat end was designed separately and was obtained as 0.0067 m (6.7 mm), to be able to withstand the reactor pressure and prevent possible leakages. The fiberglass thickness used as insulation material of the reactor was designed as 0.023 m (23 mm), but none of the researchers mentioned in this article, reported the details of the top flat end of the reactor they used nor the thickness of the insulation material they used for their reactor.

The cooling of the reactor is expected to be carried out when the heating operation is shut down, before the pressure relief valve is opened to vent out the gas phase. 0.0023 m^3 (2.3 lit) volume of water is required every minute to cool the reactor volume of 0.0188 m^3, emitting 2222 W of energy and the length of the stainless steel cooling coil is designed to be 13.1m. These configuration data are presented in Table 5 below and the flow diagram is presented in Fig. 2.

Table 5. Configuration of the batch reactor design

Factor	Description
Reactor type	Batch
Material of the reactor	Stainless steel
Height of the reactor	0.31 m
Diameter of the reactor	0.28 m
Reactor capacity	18.8 liter
Maximum design temperature	400 ^{o}C
Maximum pressure	25 bar
Thickness of the reactor wall	0.003 m
Thickness of the flat end	0.0067 m
Thickness of the insulation material	
Flowrate of cooling water	0.023 m
Length of cooling water coil	0.0023m^3/min
Diameter of cooling water coil	13.1 m
	0.015 m

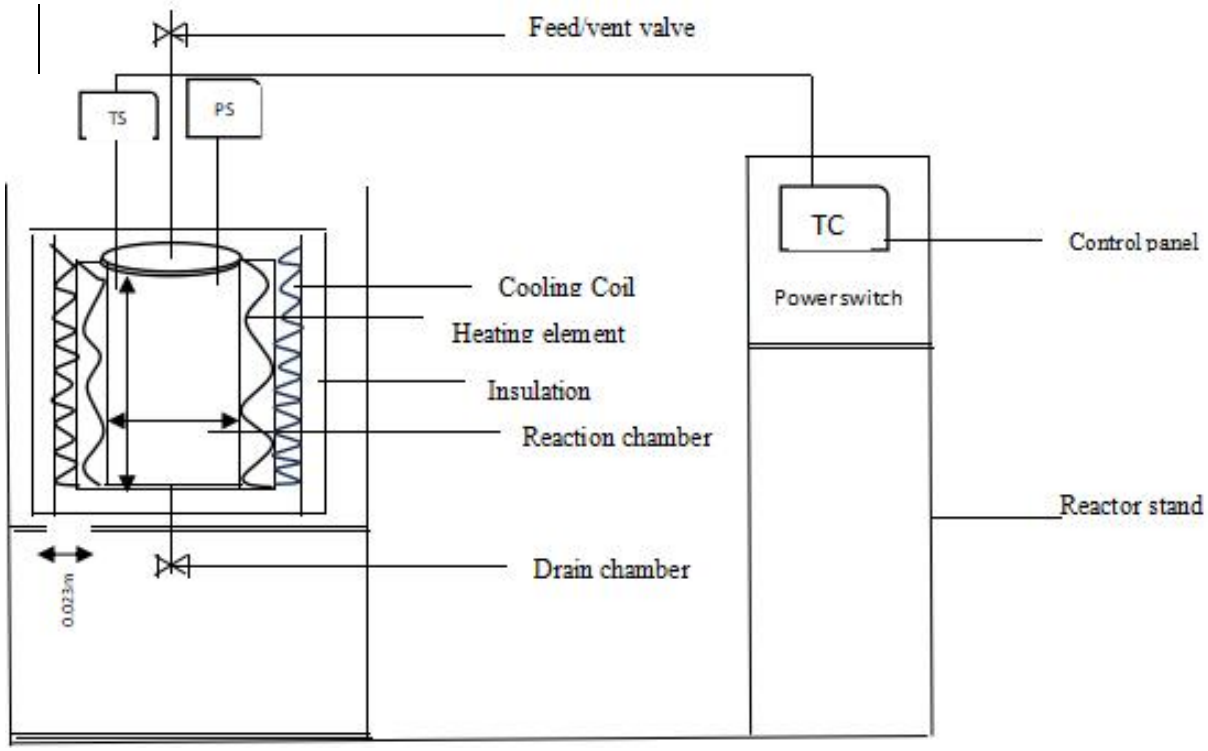

Fig. 2 The reactor setup

8. CONCLUSION

Production of biocrude from microalgae biomass is an attractive alternative source of renewable energy, and the design of this small-scale reactor for its production by hydrothermal liquefaction, is of immerse importance. The 0.003 m thick batch reactor is designed to operate with a maximum heat of about 2222 W from electrical heating coils, insulated with fiberglass with thickness of about 0.023 m. The temperature inside the reactor is designed not to exceed 400 ^{o}C and the top flat end of the reactor is designed to have a thickness of 0.0067 m to be able to withstand the internal pressure of the reactor. The flat end of the reactor is where the pressure gauge of maximum pressure of 25 bar and the temperature sensor are designed to be mounted. After completion of the hydrothermal liquefaction process, the cooling system is designed to carry 0.0023 m^3 of water per minute in a coil of 13.1 m length, fitted round the reactor. The cooling of the reactor enables the temperature to be cooled to about 30 ^{o}C before the gas phase is vented out through the vent valve. The material left in the reactor will then be evacuated and mixed with dichloromethane in a separating funnel. The solid residue will be removed followed by the biocrude, then the aqueous phase will be recovered from the separating funnel. The entire design estimated to cost about Eight Hundred and Twenty Eight Thousand, Seven Hundred Naira Only (N828,700), will be fabricated using stainless steel 316 material, and mounted on a stand which will also carry the control panel for safe operation.

REFERENCE

Adrien W., Paul B., Julien L, Le A.P.P., (2019). Finding optimal algal/bacterial inoculation ratio to improve algal biomass growth with waste water as nutrient source. *African Journals Online*, 45, 4. https://doi:10.17159/wsa/2019.v45.14.7543

Amiri, P. and Arabian, D. (2016). The Effect of Reactor Configuration and Performance on Biodiesel Production from Vegetable Oil. *Journal of Applied Biotechnology Reports*, 3 (2): pp. 403-411

Aprilia, M.P., Nandiyanto, A.B.D. and Ragadhita, R. (2023). Design of reactor for the production of Fe_3O_4 nanoparticles. *Green and Applied Chemistry*, 16, pp. 01- 07.

Barreiro, D.L., Samori, C., Terranella, G., Horiung, U., Kruse, A. and Prins, W. (2014). Assessing microalgae biofuels via hydrothermal liquefaction. Bioresources Technology, 174, pp. 256– 265. http://dx.doi.org/10.1016/j.biortech.2014.10.031

Carpenter, K.J. (2011). Agitated Vessel Heat Transfer Thermopedia, 10.1615/AtoZ.a.agitated_vessel_heat_transfer

Chen Z.; Wang L.; Qiu S. and Ge, S. (2018). Determination of Microalgal Lipid Content and Fatty Acid for Biofuel Production. *Biomedical Research International,* 1503126.

Costanzo, W., Jena, U., Hilten, R., Das, K. and Kastour, J.R. (2015). Low temperature hydrothermal pretreatment of algae to reduce nitrogen heteroatoms and generate nutrient recycle streams. *Algae resources*, 12, pp, 377–387.

Eboibi, B.E. (2019). Impact of time on yield and properties of biocrude during downstream processing of product mixture derived from hydrothermal liquefaction of microalga. *Biomass Conversion Biorefinery,* 9, pp. 379 – 387.

Eboibi, B.E., Lewis, D.M., Ashmana, P.J. and Chinnasamy, S. (2015). Influence of process conditions on pretreatment of microalgae for protein extraction and production of biocrude during hydrothermal liquefaction of pretreated *Tetraselmis* sp. *Royal Society of Chemistry advances,* 5, pp. 20193–20207

El-Sheekh, M., Abu-Faddan, M., Abo-Shady, A., Nassar, M. Z. A. and Labib, W. (2020). Molecular identification, biomass, and biochemical composition of the marine chlorophyte *Chlorella sp*. MF1 isolated from Suez Bay. *Journal of Genetic Engineering and Biotechnology, 18* (27), pp. 1 – 10. https://doi.org/10.1186/s43141-020-00044-8

Etuk, S.E.; Robert, U.W. and Agbasi, O.E. (2020). Design and performance evaluation of a device for determination of specific heat capacity of thermal insulators. Beni-Suef University *Journal of Basic and Applied Sciences*, 934: pp. 1 – 7.

Guo, Y., Yeh, T., Song, S., Xu, D. & Wang, S. (2015). A review of bio-oil production from hydrothermal liquefaction of algae. *Renewable and Sustainable Energy Reviews, 48*, pp. 776–790.

Hamed, I. (2016). The evolution and versatility of microalgal biotechnology: A Review. *Compressive review in food science and food safety*, pp. 1 – 20.

Hao, B., Xu, D., Jiang, G., Ahmed, T., Jing, S.Z. & Guo, Y. (2021). Chemical reactions in the hydrothermal liquefaction of biomass and in the catalytic hydrogenation upgrading of biocrude. *The Royal Society of Chemistry,* 23*,* pp. 1562–1583.

Heggs, P. J. and Hills, P. D. (1995). The design of heat exchangers for batch reactors. Chpt. 18 in *Heal Exchange Engineering*. 4, pp. 297-313.

Hoang, A.T., Ong, H.C., Fattah, I.M.R., Chong, C.T., Cheng, C.K., Sakthivel, R. and Ok, Y.S. (2021). Progress on the Lignocelluloses Biomass Pyrolysis for Biofuel Production towards Environmental Sustainability. *Fuel Process Technology*, 223: pp. 1 – 27.

Hu, Y., Gong, M., Feng, S., Xu, C.C. & Bassi, A. (2019). A review of recent developments of pre-treatment technologies and hydrothermal liquefaction of microalgae for bio-crude oil production. *Renewable and Sustainable Energy Reviews*, 101, pp. 476–492.

Ikhazuangbe, P. M. O., Eboibi, B.E., Amabogha, B., Orugba, O. H. & Agarri, S. E. (2023a). A Mini Review of the Potentials of *Chlorella* Species Microalge for the Production of Biocrude by Hydrothermal Liquefaction (HTL) Operation. *Journal of Engineering Research, Innovation and Scientific Development*, vol 1 (2), pp. 21 – 35. https://doi.org/10.61448/jerisd12234

Ikhazuangbe, P. M. O., Eboibi, B.E., Amabogha, B., Orugba, O. H, Ikalumhe, W.O. & Agarri, S. E. (2023b). Design of a Batch Reactor for the Conversion of 500g Microalgae Biomass to Biocrude by Hydrothermal Liquefaction. *International Journal of Engineering and Modern Technology*, 9. (3), pp. 1 – 14. https://doi:10.56201/ijemt.v9.no3.2023.pg1.14

Iyagba, E.T. (2008). Fundamentals of transport phenomena. Jita Enterprises, Port Harcourt, Nigeria, pp. 31 – 36.

Jahn, M.T., Schmidt, K. & Mock, T. (2014). A novel cost effective and high-throughput isolation and identification method for marine microalgae. *Plant methods*, *10*(26), pp. 1 – 10.

Jazrawi, C., Biller, P., He, Y., Montoya, A., Ross, A.B. and Maschmeyer, T. (2015). Two-stage hydrothermal liquefaction of a high-protein microalgae. *Algae resources*, 8, pp. 15 – 22.

Kandasamy, S.; Devarayan, K.; Bhuvanendran, N.; Zhang, B.; He, Z.; Narayanan, M.; Mathimani, T.; Ravichandran, S. and Pugazhendhi, A. (2021). Accelerating the production of bio-oil from hydrothermal liquefaction of microalgae via recycled biochar-supported catalysts. *Journal of Environmental Chemical Engineering*, 9, pp. 1 – 15.

Kumar, A., Guria, C. and Pathak, A.K. (2018). Optimal cultivation towards enhanced algae biomass and lipid production using *Dunaliella tertiolecta* for biofuel application and potential CO_2 biofixation: Effect of nitrogen deficient

fertilizer, light intensity, salinity and carbon supply strategy. *Energy*, 153: pp. 1 – 51.

Le, A.P.P., Julien, L., Paul, B. and Adrien, W. (2019). Finding optimal algal/bacterial inoculation ratio to improve algal biomass growth with waste water as nutrient source. *African Journals Online, 45* (4), pp. 1–8.

Neveux, N., Yuen, A.K.L., Jazrawi, C., Magnusson, M., Haynes, B.S., Masters, A.F., Montoya, A., Paul, N.A., Maschmeyer, T. & de Nys, R. (2014). Biocrude yield and productivity from the hydrothermal liquefaction of marine and freshwater green macroalgae. *Bioresource Technology*, *155*, pp. 334 – 341.

Rehan, A.K. (2020), Pipe thickness calculation as per ASME B31.3, Pipe thickness calculator, piping design basics, piping stress analysis, piping stress basics.

Sinnott, R. K. (2005). Chemical Engineering Design. Butterworth-Heinemann, London, pp. 811 – 820.

Song, W., Wang, S. and Guo, Y. (2015). A Review of the Biofuel Yield in Hydrothermal Liquefaction of Different Microalgae. International Conference on Advances in Energy and Environmental Science, pp. 1504 – 1509.

SundarRajan, P., Gopinath, K.P., Arun, J., GracePavithra, K., Joseph, A. and Manasa, S. (2021). Insights into valuing the aqueous phase derived from hydrothermal liquefaction. *Renewable and Sustainable Energy Reviews*, 144: pp. 1–15.

Tan, C.H., Show, P.L., Chang, J.S., Ling, T.C. and Lan, J.C.W. (2015). Novel Approaches of Producing Bioenergies from Microalgae: A Recent Review. *Biotechnology Advances*, pp. 1-30.

Tarek, D., Ahmed, M.M., Hussein, H.S., Zeyad, A.M., Al-Enizi, A.M., Yousef, A. & Ragab, A. (2022). Building envelope optimization using geopolymer bricks to improve the energy efficiency of residential buildings in hot arid regions, *Case Studies in Construction Materials,* 17, 01657.

Tian, C.; Li, B.; Liu, Z.; Zhang, Y. and Lu, H. (2014). Hydrothermal liquefaction for algal biorefinery: A critical review. *Renewable and Sustainable Energy Reviews*, 38, pp. 933–950.

Tian, S.L., Khan, A., Zheng, W.N., Song, L., Liu, J.H., Wang, X.Q. & Li, L. (2022). Efects of *Chlorella* extracts on growth of Capsicum annuum L. seedlings. *Scientific report*, 12 (15455).

Towler, G. & Sinnott, R. (2008). Chemical Engineering Design: Principles, Practice and Economics of Plant and Process Design. Butterworth-Heinemann, London, pp. 263 – 264.

Wang, S., Zhao, S., Cheng, X., Qian, L., Barati, B., Gong, X., Cao, B. & Yuan, C. (2021). Study on two-step hydrothermal liquefaction of macroalgae for improving bio-oil. *Bioresource Technology*, 319, pp. 1 – 9.

Wang, W., Xu, Y., Wang, X., Zhang, B., Tian, W. and Zhang, J. (2018). Hydrothermal liquefaction of microalgae over transition metal supported TiO2 catalyst. *Bioresource Technology*, 250, pp. 474–480.

Xu, Y., Hu, Y., Peng, Y., Yao, L., Dong, Y., Yang, B. and Song, R. (2019). Catalytic pyrolysis and liquefaction behavior of microalgae for bio-oil production. *Bioresource Technology*, pp. 1 – 37.

Xue, L.L. and Jiang, J.G. (2017). Cultivation of *Dunaliella tertiolecta* intervened by triethylamine enhances the lipid content. *Algal Research,* 25, pp. 136–141.

Zaid, R. (2020). Pipe insulation

Zhu, X., Phinney, D.M., Paluri, S. & Heldman, D.R. (2018). Prediction of Liquid Specific Heat Capacity of Food Lipids. *Journal of food sciences*, 0 (0): pp. 1 – 6.

10.51975/24390202.som
Journal of the Nigerian Society of Chemical Engineers, 39(2), 2024

DESIGN OF PHOTOVOLTAIC HYBRID GRID- TIED SOLAR POWER PLANT FOR STEADY ENERGY SUPPLY IN NIGERIA

Idongesit Effiong Sampson
Department of Chemical Engineering,
Rivers State University, Port-Harcourt, Nigeria.
Email: idongesit.sampson@ust.edu.ng
Phone: +234(0)7082658042

ABSTRACT

Steady energy supply has been a major challenge to the Nigerian Government and other stake holders in the Nigerian energy sector. Epileptic energy supply has hindered industrial, technological and economic advancement of Nigeria. This problem could be solved if the Nigerian energy deficit could be made up for by producing an extra 30,000 Megawatts of electric power. A study reveals that 7,500,000 hybrid grid-tied solar power plants of 4,000 Watts capacity evenly distributed in Nigeria can provide the additional 30,000 Megawatts required. This hybrid and grid-tied energy will enhance the steady energy supply. Also, being sourced from renewable energy source (the sun) would enhance the realization of the Nigerian quest for zero carbon emissions by the year 2060. A net cash flow of ₦54,058,598, 090-0,000.00, a Rate of Return on Investment of 72.30 % and a Pay-back Period of 1 year, four and a half months, shows that photovoltaic hybrid grid-tied solar power plants, if well managed, could be economically viable in Nigeria. Nigerians and the Nigerian Government are therefore encouraged to invest in the photovoltaic hybrid grid-tied solar power plant project as it could advance the Nigerian economy and lift hundreds of millions of Nigerians out of poverty.

Keywords*: Renewable Energy; Photovoltaic; Rate of Return on Investment; Net Cash Flow; Pay-back Period.*

1.0. INTRODUCTION

In 1972, the Nigerian Government established the National Electric Power Authority (NEPA), a merger from the Electric Corporation of Nigeria (ECN) and the Niger Dams Authority (NDA). This enhanced the linkage of more cities to the national grid and the extension of electric power to all regions of Nigeria. The Nigerian Government has since undergone power sector reforms as the power supply by NEPA was not satisfactory.

In 2005, the Nigerian Government established the Power Holding Company of Nigeria (PHCN), with all assets and liabilities of NEPA, transferred to the PHCN. Later, in November 2005, the Nigerian Electricity Regulatory Commission (NERC) was inaugurated and saddled with the responsibility of tariff regulation and monitoring to ensure that quality service is delivered by PHCN. Despite this, Nigerians never expect steady power supply, as electric power supply in Nigeria has never been constant. Ahiakwo (2019) stated that electric power in Nigeria has been fluctuating between 3,500 to 4,000 Megawatts. This is grossly inadequate for a nation of over 224 million people.

Izuora (2022) stated in leadership newspaper that the Association of Nigerian Electricity Distributors (ANED), the umbrella body of Electricity Distribution Companies (DisCos), has estimated that Nigeria requires 30,000 Megawatts of electricity generation to meet the current demand of electricity by consumers. Hart (2018) stated that despite the high potential of utilization of solar energy for electric generation in Nigerian, the Nigeria grid is not designed to be integrated with load generators that have low load factors, such as solar electricity generating stations. In Nigeria, there is a small solar electricity generating station in Kano, but that station is not grid-tied.

Ahiakwo (2019) stated that solar power, a renewable energy source, is a readily available clean source of energy with zero carbon emission, having no noise, air or water pollution to the environment. Sampson (2014) stated that zero gas flaring is important as flared gasses deplete the ozone layer hence increasing greenhouse effect. With solar electricity, zero gas flaring can be achieved.

International Trade Administration (I.T.A.) (2020) stated that in 2006, the Nigerian Government initiated the Renewable Energy Master Plan (REMP) aimed at

increasing the supply of renewable electricity from 13 % of total installed electric generation capacity in 2015 to 23 % in 2025 and 36 % in 2030, solar being a renewable energy source besides wind and biomass. Premium Times (2022) stated that on the 24th of August, 2022 the Nigerian Government launched the Energy Transition Plan (ETP). On the occasion, the Vice President, Professor Yemi Osinbajo, stated that Nigeria is currently implementing power sector initiatives and reforms focused on expanding the national grid, increasing generation capacity and deploying renewable energy to rural populations. The Nigerian Energy Transition Plan seeks to tackle the dual crisis of energy poverty and climate change. The Nigerian Energy Transition seeks to achieve net zero carbon emissions by the year 2060. To achieve this, Nigeria will have to move rapidly, from conventional fossil fuels to alternative renewable energy sources such as wind, solar and biomass. Hybridization of the various energy sources could help store energy for future use.

Waley (2018) stated that in advanced countries, solar energy has found application in pipeline surveillance and crude oil production. The attainment of global decarbonization standards has been a major challenge to the Nigerian petroleum industry. Voltage obtained from solar power plants can be stepped up to that required for operations in the Nigerian petroleum industry with the help of step-up transformers.

The use of solar energy in place of fossil fuels could help eliminate greenhouse emissions, which deplete the ozone layer causing greenhouse effect. The use of solar power could help lower the cost of production in industries as the sun is readily available, and the energy could be stored in batteries for use at night. The solar power plant comprises light equipment that requires less labour and maintenance.

Nigeria experiences sunshine all year and sunshine is available in every part of the country in various degrees ranging from 3.70 kW per m^3/day in the southern region that has an abundance of rainfall to 7.00 kW/m^3/day in the northern part that has sunshine all the year round. Studies have shown that even in the rain zone areas of Nigeria like Port Harcourt, the average solar radiation insulation is 5080 Twh/day. This can translate to 508 Gwh electricity for 1 % surface area of 1 % efficiency of a unit photovoltaic.

Agilet (2011) stated that hybrid solar power plants are more efficient and cost effective than stand -alone solar power plants as they require fewer solar panels, hence lowering the cost. Some power is also stored in power banks or batteries in the day time for use in the night when there is no sunshine. If hybrid and grid-tied, the electric generator could be supplying power to the grid even when the solar plant fails. This will result in consistent electric power supply, hence solving the problem of epileptic power supply in Nigeria.

This technical paper explains, among others, the principles of design of a photovoltaic hybrid grid-tied solar power plant of 4,000 Watts capacity to enhance make-up for the 30,000 Megawatts of electric power generation required in Nigeria, such as to achieve steady electric power supply in Nigeria. Some of the principles governing the installation and operation of the photovoltaic hybrid grid-tied solar power plant are also highlighted in the paper. Costing and economic evaluation of the process is key to the determination of the economic viability of the process.

2.0. MATERIALS AND METHODS

2.1. Materials

The following materials were used for the research: Solar Photovoltaic panels (4000 watts), modules, 140 amp charge controller, Sixteen, 350 amp hour Deep cycled batteries in battery rack; 4000 W inverter (to convert DC to AC); 4000 amp Circuit breaker (for over current protection) Battery capacity meter; lightning arrester; DC disconnect, 1200 V distribution fuse board; Voltage stabilizer (2.5 times the size of the inverter and placed before the inverter); change over 200 amp, 415V; Bypass; Combiner box; Stantion or Panel Rack

2.2. Methods

2.2.1. Plant Set-Up

The direction of the solar panel array was checked to ensure that it is facing south (the direction of the sun) so that when the sun rises, sets, or is at its peak, all sun rays fall on the solar panel. A compass placed on top of the stantion or panel rack placed on the ground in a place without shades indicated south. Twenty solar panels were placed on the ground, and a stantion or panel rack was placed on top. The solar panels and the panel rack were tightened with nuts and bolts with negative and positive connected two by two and the others paralleled. This was connected to a circuit board which comprised of a charge controller (CC), Change Over (CO), Distribution Fuse Board (DFB), and Battery Capacity Meter (BCM); other auxiliary equipment were connected to the circuit board. These were voltage stabilizer, inverter, Circuit Breaker (CB) and batteries in a battery rack. The system was hybridized with a

standby electric generator and could be connected to the national grid.

2.2.2. Earthing

A cable from the array frame was connected to an earth rod, and a bonding cable from the battery was connected to the earth at the main circuit box. The battery temperature sensor was put directly, on the negative terminal of the battery.

2.2.3. Design Equations

Agilet (2011) gave the following equations for the design of solar power plant

$$\text{Load} = \text{Number of Appliance} \times \text{Power} \quad (1)$$

$$\text{Consumption} = \text{Load} \times \text{Hours of Usage} \quad (2)$$

$$\text{Size of Inverter} = \frac{[\sum \text{Load} \times 1.25] \times 1.2}{1000} \quad (3)$$

Number of Batteries:

$$[\text{Consumption} \times 1.25] / [\text{Voltage of Inverter}] = \text{Amphou} \quad (4)$$

Then: At Zero Percent Depth of Discharge

$$\left[\frac{\text{Amphours}}{\text{Size of Battery}}\right] \times \left[\frac{\text{Input Voltage of Inverter}}{\text{Battery Voltage}}\right] \quad (5)$$

Given the Depth of Discharge (DOD) > 0

$$\left[\frac{\frac{100}{\text{DOD}} \times \text{Amphours}}{\text{Size of Battery}}\right] \times \left[\frac{\text{Input Voltage of Inverter}}{\text{Battery Voltage}}\right] \quad (6)$$

Number of Panels to be used:

$$\left[\frac{\left[\frac{\frac{100}{\text{DOD}} \times \text{Amphours}}{\text{No.of Sunshine hours}}\right]}{\text{Amps of Panel to be Used}}\right] \quad (7)$$

Number of Panels to be Used Given the Percent of Hybrid Solar:

$$\left[\frac{100}{\%\ \text{Hybrid Solar}}\right] \times [\text{No. of Panels}] \quad (8)$$

Purchased Equipment Cost (PEC)

$$PEC = Market\ Price + Procurement\ cost \quad (9)$$

Coulson & Richardson (2009) gave the following equations for costing.

Physical Plant Cost (PPC)

$$PPC = PEC\ (1 + f_1 + \ldots + f_9) \quad (10)$$

Fixed Capital (FC)

$$FC = PPC\ (1 + f_{10} + \ldots + f_{12}) \quad (11)$$

Where f_1 to f_{12} are cost factors

Working Capital (WC)

$$10\ \%\ of\ Fixed\ Capital \quad (12)$$

Total Investment (TI)

$$Fixed\ Capital + Cost\ of\ Equity + Working\ Capital \quad (13)$$

Cost of Equity

Dividends paid to the investors (co-owners) who contributed the money for building the plant.

Number of Solar Plants

$$\frac{Amount\ of\ Power\ Required}{Amount\ of\ Power\ Produced} \quad (14)$$

Sales of Electric Power

$$kilowatthours\ (kwh) Produced \times Cost\ of\ 1\ kwh \times Number\ of\ People\ that\ Paid \quad (15)$$

Nigerian Electric Regulatory Commission (NERC) (2023) stated that 59.64 Naira is the cost of one Kilowatthour.

Number of People using one Solar Plant

$$\frac{Nunber\ of\ Nigerians}{Number\ of\ Solar\ Plants} \quad \textbf{(16)}$$

United Nations (2023) gave 224, 239,005 as population of people in Nigeria but not all the people can use the solar power plant.

Net Cash Flow (NCF)

$$Sales\ of\ Electric\ Power - Total\ Cost\ of\ the\ Solar\ Plant \quad (17)$$

Green & Perry (2007) gave formulars for economic analysis as follows:

Net Present Value (NPV)

$$NPV = \frac{NCF \times N}{(1+r)^N} \quad (18)$$

Where N is the project life and r, the increase in productivity per year

Rate of Return on Investment (ROI)

$$\frac{\text{Net Cash Flow}}{\text{Total Investment}} \times \frac{100}{1} \quad (19)$$

Pay-Back Period (PBP)

$$\frac{\text{Total Investment}}{\text{Net Cash Flow}} \quad (20)$$

2.2.4. Tying the Photovoltaic Hybrid Solar Power Plant to the Nigerian National Grid

A new dual pole circuit breaker was added to the solar electric panel at a position farthest from the main circuit breaker with the help of an adequately sized photovoltaic service disconnect box.

Wires from the photovoltaic solar system were then connected to the new circuit breaker. Voltages from the solar system were stepped-up by a step up transformer linked to the National grid as shown in Figure 1 below.

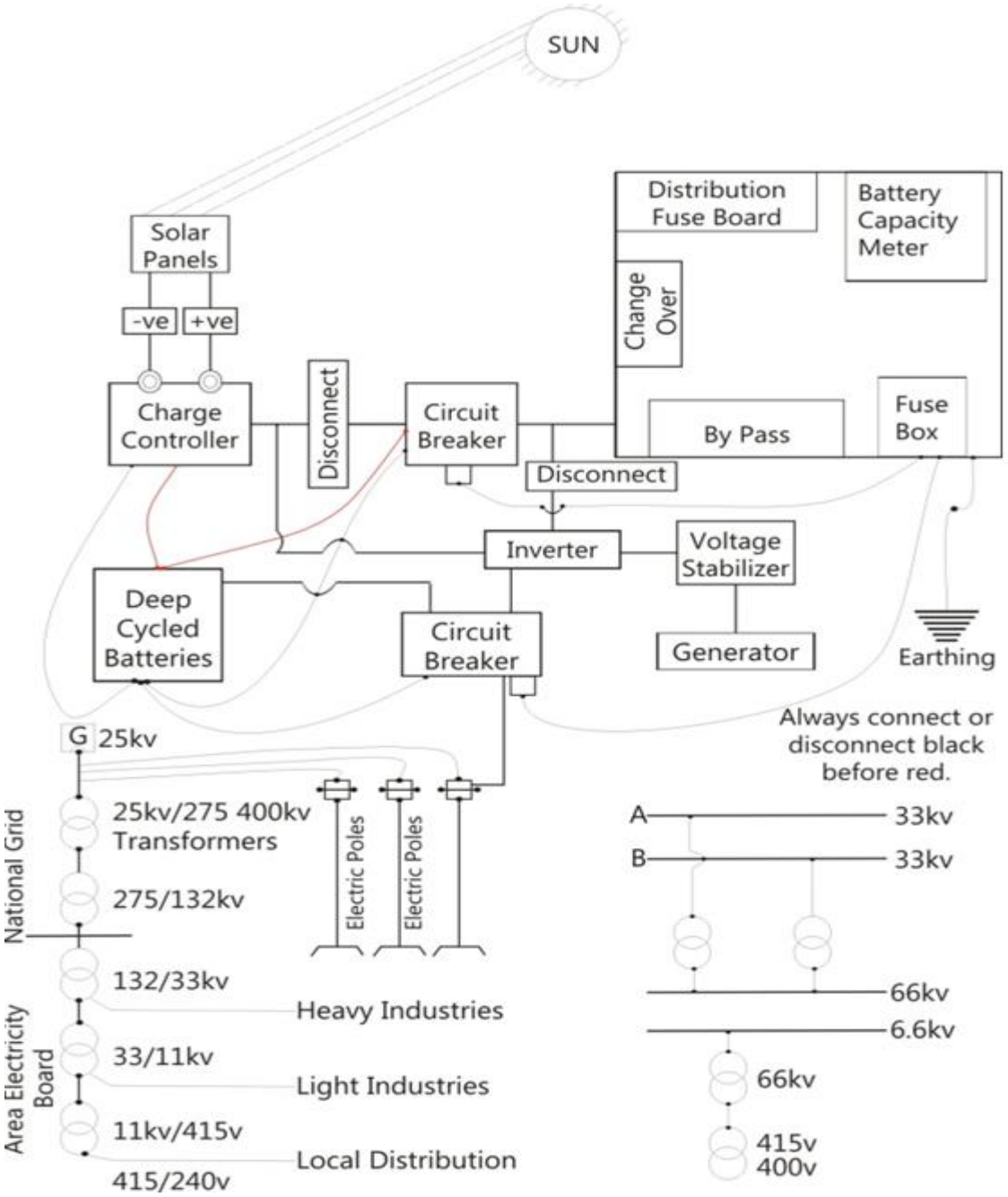

Fig. 1: Tying a Hybrid Solar Power Plant to the National Grid

2.2.5. Harnessing of Solar Power in the Oil and Gas Industry

Voltages produced from the photovoltaic Hybrid and grid- tied Solar power plant were stepped-up to that required by any oil and gas facility that is to be operated. This was done with the help of step-up transformers. The voltages were transmitted at various voltage levels from an electric substation to any process equipment requiring any particular voltage.

3.0. RESULTS AND DISCUSSION

3.1. Data Obtained

Data obtained from analysis of the photovoltaic hybrid grid - tied solar power plant is shown in Table 1 below

Table 1: Photovoltaic Hybrid Grid-Tied Solar Power Plant Data

Parameter	Value
Plant capacity	4,000 Watts
Type of solar plant	Photovoltaic
Specification	Hybrid Grid-Tied
Nigeria's Energy Requirement	30,000 Megawatts
Number of Nigerians that can use the Hybrid Grid-tied Solar Power Plant (Excluding extremely mad, very poor infants and extremely primitive men)	180,000,000 out of the 224,339,005 Nigerians
Number of Hybrid Grid-tied Solar Power Plants required	7,500,000 (can be reduced by scaling- up the design)
Number of people using one Hybrid Grid-tied solar power plant	24 (Except in locations where industries, organizations, religious bodies schools, are co-users)

According to Izuora (2022) Association of Nigerian Electricity Distribution (ANED), the umbrella body of Electricity Distribution Companies (DisCos) estimated that Nigeria requires 30,000 Megawatts of electricity generation to meet the current demand for electricity by consumers. This target can be met using 7,500,000 solar power plants of 4,000 watts' capacity evenly distributed across Nigeria as the energy required divided by the energy produced gave 7,500,000. This number of plants (7,500,000) can be reduced by scaling – up the design, but small plants are easier to maintain than big ones. The number of Nigerians divided by the number of solar plants shows that 24 people can use one Hybrid grid-tied solar power plant. However, this number of people could be more in locations where industries, organizations, religious bodies and schools are co-users.

3.2. Total Cost of the Photovoltaic Hybrid Grid-tied Solar Power Plant for Steady Electric Power Supply in Nigeria

Results obtained from cost analysis of the photovoltaic hybrid grid tied solar power plant is shown on Table 2 below.

Table 2: Total Cost of the Photovoltaic Hybrid Grid-tied Solar Power Plant

Parameter	Value (Nigerian Naira (₦))
Purchased Equipment Cost	2,528,254.498
Physical Plant Cost	2,598,254.00

Fixed Capital	2,698,254.00
Cost of Equity	7,000,427.522
Working Capital	269,825.40
Total Investment	9,968,506.922
Operating Cost	Negligible
Total Cost	9,968,506.922

The photovoltaic hybrid grid-tied solar power plant is of small size and does not occupy large land mass. The owners operate the plant, so no operators are paid. No laboratory is needed. No taxes are paid as the government is a co-owner. There are no capital charges as Nigerians are to invest money for building the plant. The community leaders are to agree in a memorandum of understanding that they are eager for steady energy supply in Nigeria, and therefore no royalties will be paid. Land acquisition is one of the cost factors inside fixed capital. The plant does not require a license so no license fees will be paid. The raw material (the sun) is a natural gift from God; it is not to be bought. Fuel for the electric generator has been captured under working capital. Therefore, the operating cost of the power plant (if any) is negligible. With negligible operating cost, the total investment of the photovoltaic hybrid grid-tied solar power plant is the total cost of the plant.

3.3. Economic Analysis

Results obtained from economic analysis of the photovoltaic hybrid grid –tied solar power plant is shown on Table 3 below.

Table 3: Economic Evaluation

Parameter	Value
Sales of Electric Power for one Hybrid Grid-tied Solar Power Plant	₦ 17,716,320.00
Sales of Electric Power for the 7,500,000 Hybrid Grid-tied Solar Power Plants	₦ 128,822,400,000,000.00
Net Cash Flow for One Hybrid Grid-tied Solar Power Plant	₦ 7,207,813.078
Net Cash Flow for all the 7,500,000 Hybrid Grid-tied Solar Power Plants	₦54,058,598,090,000.00
Net Present Value	₦ 79,815,826.83
Total Investment	₦ 9,968,506.922
Net Present Value LessTotal Investment	₦ 69,847,320.81
Rate of Return on Investment	72.30 %
Pay-back Period	1 year, 4 months, 2 weeks

A high profitability rate is expected as the sales of electric power are far higher than the total cost of the plant. The plant is economically viable as the Net Present Value less the total investment is higher than zero. A Rate of Return on investment of 72.30 % is quite

high and a pay-back period of 1 year, 4 months and 2 weeks is low enough. This show the investors who contributed money for building the plant could be repaid in a short period of a year, four and half months. This shows that a Photovoltaic Hybrid Grid-tied solar power plant, if well managed could be economically viable in Nigeria. 7,500,000 photovoltaic Hybrid Grid-tied solar

power plants evenly located across Nigeria could enhance the steady electric power supply in Nigeria and enhance Nigeria's quest to meet her energy requirement.

4.0. CONCLUSION

A photovoltaic hybrid grid-tied solar power plant of 4,000 Watts capacity has been designed. 7,500,000 photovoltaic hybrid grid-tied solar power plants evenly distributed in Nigeria could help Nigeria satisfy her 30,000 Megawatts energy requirement and end epileptic energy supply in Nigeria. The photovoltaic hybrid grid-tied solar power plants can enhance the realization of the Nigerian quest for zero carbon emissions by the year 2060, being from a renewable energy source (the sun). A net cash flow of ₦ 54,058,598,090.00, a Rate of Return on Investment of 72.30 % and a pay-back period of 1 year, four and a half months shows that the photovoltaic hybrid grid-tied solar power plants, if well managed, could be economically viable in Nigeria. Nigerians and the Nigerian government are therefore encouraged to invest in the set-up of the 7,500,000 hybrid grid-tied solar power plants as this could yield much profit and dividends to lift Hundreds of Millions of Nigerians out of poverty. The number of plants could be reduced by scaling up the design, but smaller plants are easier to maintain than big ones. The plants should be evenly distributed across Nigeria.

5.0. RECOMMENDATIONS TO THE NIGERIAN GOVERNMENT

It is recommended that:

i. The Nigerian Government initiate plans for the set-up of hybrid grid-tied solar power plants in Nigeria as this could help realize Nigeria's quest for steady energy supply for industrial, economic and technological development. This could also enable Nigeria to achieve the Nigerian Vision 2020 and – a new 2060 of zero gas flaring.

ii. To eliminate interest rates and capital charges in the operating cost of the hybrid grid-tied solar power plants, the Nigerian Government should initiate an Initial Public Offering (IPO) to enhance Equity Financing (EF) for the set-up of the hybrid grid-tied solar power plants with Nigerians as core investors. This could yield many dividends capable of lifting hundreds of millions of Nigerians out of poverty.

iii. To eliminate royalties and taxes in the operating cost of the hybrid grid-tied solar power plant, the Nigerian Government should capture in a memorandum of understanding the eagerness of all tiers of government and the community leaders in Nigeria for an end to epileptic energy supply in Nigeria with the resultant opportunity cost of royalties and taxes.

iv. To eliminate labour costs from the operating cost of the hybrid grid-tied solar power plants, the Nigerian Government should train all Nigerians on the operation and maintenance of the plant with the help of the Government's mass media. This will enable the owners of the plants to operate the plants themselves.

v. The Nigerian Government should expand the scope of work of the works department of the Nigerian Electric Regulatory Commission (NERC) which is already on the government payroll, to include maintenance of the hybrid grid-tied solar power plants. This could help eliminate maintenance costs from the operating costs of the hybrid grid-tied solar power plants, which, if efficiently operated, do not develop faults.

REFERENCES

Agilet Energy Limited (2011). *Design, Sizing and Installation of Photovoltaic Systems*. Nigeria: Akwa Ibom State Technical Education Board

Ahiakwo, C.O. (2019). *Electric Power Supply: Sources and Utility- the Nigeria Experience*. 62nd Inaugural Lecture, Port Harcourt, Nigeria: Rivers State University.

Coulson, J.M., Richardson J.F., Sinnot, R.K & Tower G. (2015). *Chemical Engineering Design*, Vol. 6, 5th Edition, Newyork: Pergamon Press.

Hart, H.I. (2018). *Sustainable Electricity Generation in Nigeria: of Enthalpy, Entropy, Exergy and all that, Not Politics*. 53rd Inaugural Lecture, Port Harcourt, Nigeria: Rivers State University.

International Trade Administration (I.T.A.) (2020). *Nigeria – Country Commercial Guide. Electricity and Power Systems*. U.S.A: (I.T.A.)

Izuora, C. (2022, August 13). Nigeria Requires 30,000 Megawatts Electricity Generation to Meet Current Demand. *Leadership Newspaper*. Retrieved from: www.google.com.ng Accessed: [3rd August, 2023]

Nigerian Electricity Regulatory Commission (NERC) (2023). New Electricity Tariff in Nigeria. Available: www.nerc.gov.ng

Perry, R.H. & Green, D.W. (2007). *Chemical Engineers'Handbook*. (English Edition), Singapore: MC Graw Hill Book Company.

Premium Times (2022, August 25). Energy Transition Plan in Nigeria. Retrieved from: www.premiumtimesng.com

Sampson, Idongesit E. (2014). Catalytic Polymerization of light gasses majorly Olefins to produce polymer Gasoline. In: *Proceedings of 44th Annual Conference of Nigerian Society of Chemical Engineers' (NSChE)* held 20th – 22nd November, 2014 at Imo Concord Hotels, Owerri, Imo State, Nigeria. Available: www.researchgate.net

United Nations (2023). Population of People in Nigeria. Available: www.google.com.ng

Waley, J. (2018). Using solar energy in oil and gas industry. *Industry Issues*, Oman: Petroleum Development Oman (PDO)

10.51975/24390203.som
Journal of the Nigerian Society of Chemical Engineers, 39(2), 2024

CARBON CAPTURE, UTILIZATION, AND STORAGE (CCUS): A KEY STRATEGY FOR NIGERIA'S ENERGY TRANSITION

***ONOH Favour Chiemela, IGBOKE Hannah Chinaza, UZOR Peculiar Chidimma, IDIKA Onyekachi Uduma and NJOKU Chigoziri**

Federal University of Technology Owerri

**Corresponding: favouronoh447@gmail.com; Phone number- 08102518490*

ABSTRACT

This study focuses on the potential application of Carbon Capture, Utilization, and Storage (CCUS) in Nigeria's oil and gas sector for an effective energy transition. The global shift towards clean energy sources and decarbonization strategies to mitigate carbon emissions and address environmental concerns has led to increased interest in CCUS technologies. This study looks into the potential and barriers of adopting CCUS in Nigeria's energy landscape, starting with an overview of its fossil fuel-heavy energy mix and the resulting economic and environmental consequences. It stresses the urgency of transitioning to cleaner energy sources. The study explores CCUS prospects in the country's oil and gas sector, covering carbon capture, transportation, storage, and utilization, drawing insights from successful global projects to highlight feasibility and benefits. The study recognizes the intricate effects of CCUS and emphasizes meticulous planning, effective policies, and community engagement for positive outcomes and lessening drawbacks. It stresses aligning CCUS with Nigeria's energy transition goals. In conclusion, the research underscores CCUS as vital for cutting carbon emissions and attaining sustainable energy in Nigeria's oil and gas. It highlights the necessity of legal, financial, and infrastructural support, alongside community engagement, for successful implementation.

Keywords: Carbon, Capture, Energy, Sustainable, Industry

1. INTRODUCTION

The energy trend is gradually drifting to clean energy due to zero carbon emissions and its environmental gains. We can reduce the amount of carbon dioxide (CO_2) in the air by using cleaner energy sources and by decarbonizing our economy (Guobadia & Belo-Osagie,2023). Nigeria is also a part of this transition. According to the energy technology perspectives (ETP), Nigeria's oil and gas assets, which include wells, flowlines, refineries, and production facilities, contribute 11% of the in-scope carbon emissions globally. These emissions are a result of gas flaring and energy usage. Similarly, Nigeria, being the giant of Africa, leads in the emission of CO_2 in sub–Saharan Africa and third in Africa in 2017 (Abubakar &Abdullahi, 2022; Olajumoke et al., 2023).

One of the major techniques for the decarbonization and net-zero emissions goal is Carbon Capture, Utilization, and Storage (CCUS). CCUS has to do with the capture of CO_2 from stationary sources, treatment, permanent storage, or utilization (Galadima &Garba, 2010; Pelissari et al. et al., 2023). This novel technology can help Nigeria reduce carbon emissions in oil and gas assets as well as aid the eminent energy transition.

CCUS has been endorsed by the United Nations Framework Convention on Climate Change as a viable method of sustaining the

use of fossil fuels and cushioning climate change (United Nations,1992).

Though the campaign for the application of Carbon Capture Utilization and Storage is ongoing, there is no Carbon Capture project in any oil and gas asset in Nigeria (Dike & Amani,2020). Though some industries have employed technologies for deploying carbon from associated gas for better oil recovery, none have domesticated Carbon capture. Nigeria currently lacks a comprehensive legal framework governing the application of Carbon Capture, Utilization, and Storage (CCUS) technology. However, the Petroleum Industry Act 2021 foresees decarbonization, thereby providing a legal framework for CCUS (Aminu et al.,2021).

While Nigeria has yet to implement the Carbon Capture Utilization and Storage technique in her oil and gas assets, some countries have started experimenting with it.

For instance, the United States of America has started implementing CCUS in their oil and gas assets in Texas (C. Jones &J. Lawson, 2022). While three of China's new projects were launched in 2023, Indonesia finalized the legal framework for their CCUS project in March 2023 (IEA, 2023).

Implementing carbon capture technologies involves capturing the carbon from stationary sources, transportation through pipelines, storage in rocks and abandoned oil and gas wells, as well as usage (Pelissari et al.,2023). This project comes with huge financial demands, which might be a challenge to the Nigerian oil and gas society. This is because there is no legal basis for its operation, little or no financial incentives to leverage, and the absence of an organized pipeline transport system. However, the International Finance Corporation and World Bank in February 2022 started to partner with the Nigerian Government to build a market for CCUS for industrial emissions (IFC, 2022).

Considering these limitations and the huge bureaucratic bottleneck in policy-making in Nigeria, what is the hope for the domestication of CCSU? Will privatization be the best option? Are there local substitutes for the technologies used for Carbon Capture? These and more are underlining questions facing the domestication of Carbon Capture in Nigeria.

Thus, this article presents a systematic and detailed literature review that evaluates the possibilities, barriers, and effectiveness of domesticating Carbon Capture in Nigeria's oil and gas assets for an effective energy transition. It also performs data evaluations on the success of such projects.

2. NIGERIA'S ENERGY LANDSCAPE

This section provides an overview of Nigeria's current energy mix, highlighting its heavy reliance on fossil fuels, particularly oil and gas. It discusses the economic and environmental implications of this dependence, laying the groundwork for the necessity of energy transition.

By terrain, Nigerian crude oil production is categorized into onshore, shallow water, deep water, and ultra-deepwater (GlobalData UK Ltd., 2021). Onshore is the largest terrain type in both crude oil and condensate and natural gas production in Nigeria in 2020. Nigeria is the largest oil and gas producer in Sub-Saharan Africa and the 13th largest in the world in 2021 (GlobalData UK Ltd., 2021). Amongst the oil and gas assets in Nigeria are:

1. Oil Fields: Nigeria has numerous oil fields located both onshore and offshore, including;
    a. Niger Delta Oil Fields: The Niger Delta region is home to several major oil fields, such as the Bonny, Bonga, Forcados, and Agbami fields.
    b. Escravos Oil Fields: These offshore fields include the Escravos, Opuama, and Okan oil fields.
    c. Qua Iboe Oil Terminal: The Qua Iboe Terminal is a key export terminal for Nigeria's crude oil.
2. Natural Gas Reserves: Nigeria possesses significant natural gas reserves. The country has explored the potential of exporting liquefied natural gas (LNG) and has several LNG production facilities, including the Bonny LNG Plant.
    a. Oil Refineries: Some of the refineries include the Port Harcourt Refinery, Warri Refinery, Kaduna Refinery, Dangote oil refinery, etc.

The Nigerian energy sector is heavily reliant on the use of fossil fuels and petroleum. Currently, according to the International Renewable Energy Agency (IRENA), 18.2% of Nigeria's electricity production comes from renewable sources, compared to 33% globally (*Nigeria Renewable Electricity Percent in Total Electricity Output*, 2014). As fossil fuel supplies dwindle, we are increasingly turning to renewable energy sources to meet our energy needs. Renewable energy sources, such as solar and wind power, are clean, sustainable, and abundant. They can help us to mitigate climate change and create new jobs.

Nigeria now produces most of its electricity using fossil fuels, and the nation's energy sector is heavily reliant on petroleum to power its population. According to Eweka et al. (2022), the three main energy sources used are coal, oil, and natural gas. Coal emits the most greenhouse gases, followed by oil and natural gas. Fossil fuels also pollute the environment in other ways, such as: methane gas release during extraction, oil spills and black carbon emissions.

The national grid has a total installed capacity of over 11,000 MW but an available capacity of only over 7000 MW. In fact, in 2012, Nigeria generated approximately 4000–5000 megawatts of power for a population of 150 million people (Ndege, 2023). By using the rule of thumb on power identified in a paper by Vincent and Yusuf (2014), there should be 1000 MW per 1,000,00 people. Currently, the Nigerian population is

approximately 202 million, which means power generation should be around 202,000 MW; as a result, Nigeria has a power deficit of over 190,000 MW (Worldometer, 2023). The poor energy situation and power deficit can be attributed to a range of problems associated with the national grid network: physical deterioration of transmission lines, lack of maintenance of facilities, illegal connections/theft, and outdated technology used by consumers (*Strategic Developments in Renewable Energy in Nigeria Energy Demand and Supply Projections for Nigeria View Project Abubakar Sambo Energy Commission of Nigeria*, 2009).

3. SUSTAINABLE ENERGY TRANSITION

The sustainable energy transition is not just a shift to a new and high-efficiency energy system but also a challenge in terms of making sure the environmental and social costs, risks, and benefits of that shift are well managed in a way that can be considered sustainable (Sareen & Haarstad, 2018).

There are a number of interrelated elements that may encourage a shift away from a primary energy source. The local or regional supply could first run out, which would then cause a scarcity. This is true for both non-renewable fossil fuels and renewable resources like forests and different types of biomasses. The price of one energy source, like petroleum, may rise while the price of another, like coal, may fall, even before the impacts of depletion are visible. Secondly, the negative health impacts associated with energy use, such as those caused by coal, may become so severe that an alternative energy source becomes more alluring. The Nigerian community must switch to a sustainable energy system and improve the management of energy demand and supply in order to aid the combat of global climate change, the increasing scarcity of petroleum, and its rising cost.

International accords like the Kyoto Protocol from 1997 mandate that a price be put on carbon dioxide (CO_2) and other greenhouse gases, placing a premium on low- and non-greenhouse gas-based energy sources (Goulder & Nadreau, 2001).

This will require some mix of energy efficiency, renewable energy use (wind, solar, biomass, hydroelectric, etc.), carbon capture and sequestration to go along with coal use, and maybe nuclear power.

4. OPTIMIZATION OF OIL AND GAS ASSETS

Optimizing Nigeria's oil production processes remains a critical factor in the nation's economic recovery drive and getting the full benefits of the country's resources.Aside from production optimization, the following strategies could be implemented to maximize the expected net value of economically recoverable oil and gas assets from Nigeria's acreages.

i. Reserves maturation: Reserves maturation is a strategy to maximize the expected net value of economically recoverable oil and gas assets from an acreage by accelerating the development and production of those reserves (Babadagli, 2007). This can be done through a variety of methods, such as exploration and appraisal, infill drilling (drilling new wells in existing fields to increase production and recovery rates), improved oil recovery or enhanced oil recovery (using waterflooding, gas injection, and chemical flooding to improve the recovery of oil from existing reservoirs), and lastly, infrastructure development (building and maintaining the pipelines, processing facilities, and other infrastructure needed to transport and process oil and gas)(Babadagli, 2007).
ii. Proper asset stewardship: This involves managing oil and gas assets in a safe, environmentally responsible, efficient, and sustainable manner.
iii. Performance evaluation and rewards, as well as risk management, involves incentivizing employees to achieve their goals and minimizing the impact of unexpected events. This would help protect investments, business continuity and sustainability, improved collaboration, and cost reduction in the oil and gas sector.

5. CARBON CAPTURE AND DOMESTICATION

The phrase "carbon capture and storage" is also referred to as "carbon dioxide capture and storage", CCS as recommended by ISO (International Organization for Standardization) in ISO 27917. This change in terminology is more precise: the goal is to capture carbon dioxide, not carbon itself.

CCS involves extracting CO_2 from industrial processes and storing it in geological formations underground or under the seabed (National Grid, 2023). This involves the use of adsorption method in a stripper column or DEA contactor (see Figure 1 below) to absorb the CO_2 and CO gases in the product stream. The process is

carried out by using a liquid absorber, usually Amines, mostly the secondary amines like Methyl Diethyl Amine. The amines are sent into the stripper, and they are used to absorb the CO_2 and CO gases, and then leave the column as Rich Amine (Rich DEA). This rich amine can be sent into a distillation column to purify amine and obtain a pure amine called Lean Amine which can be recycled back into the process, to be reused.

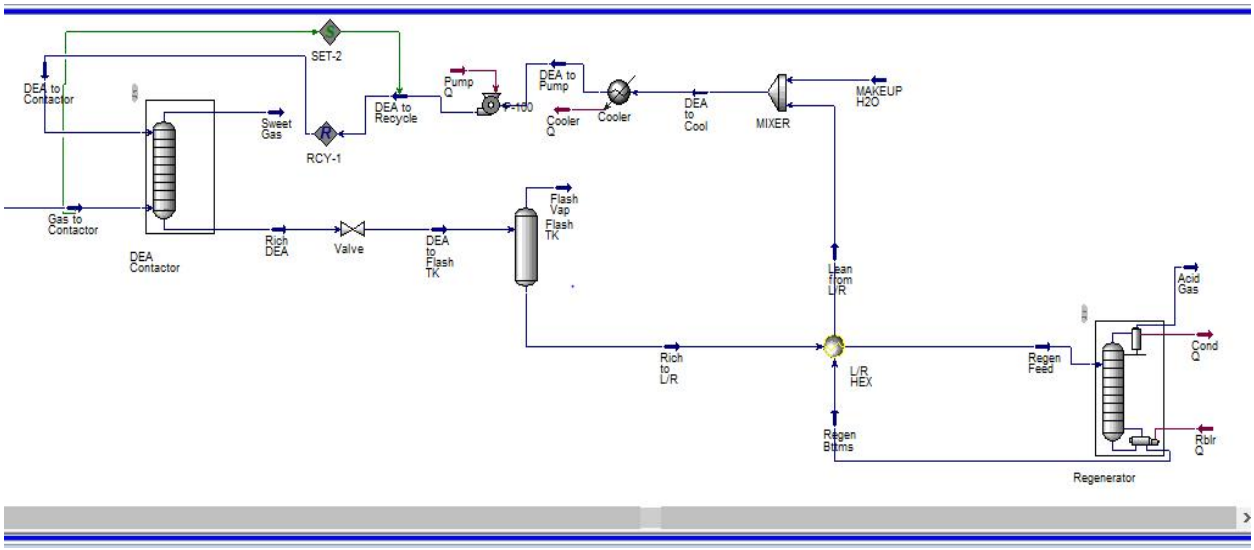

Figure 1: A Simulation of Purification of the Product Gas using a Stripper Column

These geological formations, whether onshore or offshore, include depleted oil/gas reservoirs, deep saline formations, and un-mineable coal seams. On the other hand, Carbon Capture, Utilization, and Storage (CCUS) also extract CO_2, but with a key difference: the captured CO_2 might be used for other processes instead of solely underground storage. The collected CO_2, if not used on-site, is compressed and transported via pipelines, ships, rail, or trucks for various purposes like fuel production, construction materials, enhanced oil recovery, or injection into geological formations for permanent storage(*Carbon Capture and Storage in Nigeria - Renewables - Nigeria*, 2022).Various options exist for storing CO_2, including saline aquifers, oil and gas reservoirs, coal seams, basalt formations, subsurface hydrate storage, and CO_2-based enhanced geothermal systems (Aminu et al., 2017). However, the most feasible choices are CO_2 storage in saline aquifers and oil/gas reservoirs due to their ample storage capacity and limited alternate uses for many saline aquifers (Aminu et al., 2017, 2018). Nonetheless, saline aquifer storage is less favored economically due to the absence of necessary infrastructure like injection wells and surface equipment, leading to additional expenses (Aminu et al., 2018, 2017; Aminu &Manovic, 2020). Hence, storing CO_2 in oil and gas reservoirs emerges as a highly effective choice due to several advantages. These include:

i. Extensive exploration and production history of depleted oil and gas reservoirs provides ample subsurface information, including storage capacity.
ii. The existing underground and surface infrastructure can be repurposed for storage with minor adjustments.
iii. Leveraging CO_2 injection as an enhanced oil recovery (EOR) technique offers transferable industry knowledge.

Moreover, oil and gas reservoirs serve as valuable natural analogs, demonstrating caprock efficiency. This is evident from the successful containment of fluids over geological timescales (Aminu et al., 2017). Carbon dioxide (CO2) storage in oil and gas reservoirs and saline aquifers exhibits similar characteristics, including shared rock lithologies and brine content (Li et al., 2006).

For effective CO_2 storage, assessing site feasibility against various standards is crucial. These standards ensure technology reliability, safety, environmental responsibility, and economic viability (Aminu et al., 2017; Bachu, 2000). Key criteria encompass geological, geothermal, geohazards, hydrodynamic, hydrocarbon potential, basin maturity, and economic, societal, and environmental factors (Aminu et al., 2017; Bachu, 2002, 2000; Birkholzer& Tsang, 2008; Grataloup et al., 2009; Kim et al., 2014; Meyer et al., 2008; Wei et al., 2013). These criteria not only establish technical feasibility but also illuminate risks, costs, and investment choices.

Sedimentary basins, particularly those with suitable porosity and permeability, stand out as optimal CO_2 storage sites. Parameters for evaluating feasibility within these basins include reservoir size, formation temperature/pressure, sweep efficiency due to heterogeneity, caprock permeability, injection depth pressures, mineral reactivity, and fault reactivation potential. Nigeria houses six such basins: Benue Trough, Bornu, Sokoto, Mid-Niger (Bida), Niger Delta, and Dahomey. A comprehensive analysis suggests that the Niger Delta basin holds the greatest potential for geological CO_2 storage (Umar et al., 2020).

6. POLICY AND REGULATORY FRAMEWORK

The typical policy tools used to affect energy policy are information disclosure, direct command-and-control regulation or mandates, R&D funding, taxation, and government subsidies or other incentives (Neij & Astrand, 2006). Depending on the political economy of a nation, these tools have varying degrees of strength and efficacy. For example, a more centralized economy like China has a higher capacity to regulate energy supply and consumption patterns, enabling faster transitions between major energy sources. Although making a stronger governmental commitment to this transition is critical, it is also important for policymakers to recognize that existing carbon capture efficiency technologies can be implemented much more rapidly as long as institutional barriers are recognized, addressed, and overcome (Brown & Chandler, 2008).

Carbon capture storage and sequestration technology has been identified as a significant innovation with the potential to mitigate greenhouse gas emissions, enhance energy efficiency, and optimize the utilization of fossil fuels. Previous research, exemplified by C.F. Amaechi and Ekene (2016), has predominantly focused on carbon capture, storage, and utilization (CCSU) for domestic Enhanced Oil Recovery purposes, neglecting the broader climate change mitigation and sustainable energy implications. This approach is particularly pertinent in the context of Nigeria, where fossil fuels hold substantial sway over the energy landscape. As a consequence, dedicated carbon capture initiatives aimed at commercial use have been lacking in Nigeria until recently. The Federal Government's unveiling of the Gas Flare Commercialization Policy, as discussed by S.C. Dike and N.K. Akani (2020) marks a notable development. However, the extent to which this policy can effectively facilitate large-scale carbon capture for commercial ends remains uncertain.

In developing a legal and regulatory framework for Carbon capture and storage (CCS), the following issues should be addressed (*Carbon Capture and Storage in Nigeria - Renewables - Nigeria*, 2023):

i. Review current laws to identify and address any existing legal obstacles to CCS.
ii. Create an incentive structure that makes launching a CCS project financially attractive, by correlating the amount of CO2 captured with the profits accruing to the project developer.
iii. Explicitly define the qualifications required for a CCS project developer, and other key provisions that financiers typically want in place to ensure certainty.
iv. Develop regulations for the placement of CO2 storage facilities, minimum environmental criteria, and required safety precautions.
v. Require all potential CCS projects to be based on an integrated risk assessment for CO2 leakage.

7. CASE STUDIES

i. **Sleipner Project (Norway):** The Sleipner project is one of the earliest and most well-known carbon capture and storage (CCS) projects in the world.The natural gas extracted at Sleipner contains around 9% CO_2, which is separated using amine scrubbers and injected into an Ultra saline formation 800m below the seabed. Approximately 2,800 tonnes of CO_2 are separated and injected daily. It involves capturing carbon dioxide (CO_2) emissions from the Sleipner gas platform in the North Sea and injecting them into a deep geological formation beneath the seabed. The project began in 1996 and has been successful in reducing CO_2 emissions from the natural gas production process (*Sleipner Details*, 2023).
ii. **Boundary Dam Carbon Capture Project (Canada)**: Located in Saskatchewan, Canada, the Boundary Dam project is a large-scale coal-fired power plant with integrated carbon capture technology. It became operational in 2014 and is capable of capturing approximately 90% of the CO_2 emissions from one of its units. The captured CO_2 is then used for enhanced oil recovery (EOR) operations in nearby oil fields (*Boundary Dam Carbon Capture Project*, 2023).

iii. **Petra Nova Project (USA)**: Petra Nova is a CCS project associated with the W.A. Parish Generating Station, a coal-fired power plant in Texas. The Petra Nova CCS project is designed to capture approximately 90 percent of the carbon dioxide (CO_2) from a 240 MW slipstream of flue gas and use or sequester approximately 1.4 million metric tons of this greenhouse gas annually. The captured CO2 will be compressed and transported through an 80-mile pipeline to an operating oil field where it will be utilized for enhanced oil recovery (EOR) and ultimately sequestered. It's one of the largest post-combustion carbon capture projects in the world (*Petra Nova - W.A. Parish Project*, 2023).

iv. **Gorgon Project (Australia)**: The Gorgon project is a liquefied natural gas (LNG) development in Australia that includes a large-scale CCS component. It captures CO_2 emissions from the gas processing plant and injects them into a deep saline aquifer for storage. While the project faced some technical challenges during its early stages, it eventually became operational in March, 2016 and is a notable example of CCS in the LNG industry (*Gorgon Liquefied Natural Gas (LNG) Project, Western Australia*, 2023).

v. **Air Products and Chemicals Green Hydrogen Project (Saudi Arabia)**: In this project, carbon capture is used as part of a broader effort to produce green hydrogen. Air Products and Chemicals, a global industrial gases company, is working on a project in Saudi Arabia that aims to capture CO_2 emissions from a refinery and use them in the production of hydrogen. The captured CO_2 is utilized in the process, reducing its environmental impact (*Parnell*, 2020).

vi. **Net Power Natural Gas Power Plant (USA)**: The Net Power project is a natural gas power plant that incorporates a novel combustion technology known as the "Allam Cycle." This technology enables the capture of nearly pure CO_2 emissions during the combustion process. The captured CO_2 is then used for industrial applications or stored underground (*Technology - NET Power - Making Clean Cheaper than Dirty*, 2020).

vii. **South Africa - Sasol Carbon Capture and Storage Project:** Sasol, a major energy and chemical company in South Africa, has been involved in researching and piloting carbon capture and storage (CCS) projects. They have been exploring the feasibility of capturing CO2 emissions from their industrial processes and storing it underground in geological formations. The Sasol Secunda plant has been a focal point for these efforts (CGS, 2021).

These case studies showcase a range of carbon capture approaches and applications across different industries, demonstrating the diverse efforts to mitigate carbon emissions and enhance sustainable energy transitions.

8. SOCIO-ECONOMIC IMPACTS

CCS technology can help Nigeria mitigate climate change by capturing CO2 emissions and storing them underground. However, it can also have both positive and negative socioeconomic impacts.

Positive Socioeconomic Impacts:

i. Job Creation: The implementation of CCS projects would require a skilled workforce for designing, constructing, and operating the capture and storage facilities. This could lead to the creation of new job opportunities, contributing to reduced unemployment rates and economic growth (Turan et al., 2021).

ii. Attracting Investment: As the global community becomes more focused on carbon reduction, countries that adopt innovative technologies like CCS can attract foreign investment. Nigeria could position itself as a leader in sustainable energy practices, encouraging foreign direct investment in its energy sector (Turan et al., 2021).

iii. Diversification of Economy: Nigeria's economy is heavily reliant on oil and gas exports. Investing in CCS could diversify the economy by encouraging the development of a low-carbon energy sector, reducing the country's vulnerability to fluctuations in global oil prices(IEA, 2022).

iv. Climate Commitments: By implementing CCS technology, Nigeria could demonstrate its commitment to international climate agreements and reduce its overall carbon footprint. This could enhance its reputation on the global stage and improve relationships with environmentally conscious trading partners (IPCC, 2022).

Negative Socioeconomic Impacts:

i. Initial Costs: The establishment of CCS infrastructure requires significant capital investment, including research and development costs,

construction expenses, and ongoing maintenance. These costs might strain the country's budget, diverting funds from other essential sectors(Turan et al., 2021).

ii. Resource Allocation: Nigeria's government would need to balance investments between CCS and other pressing issues, such as healthcare, education, and poverty alleviation. Competition for limited resources could impact social welfare programs (IEA, 2022).

iii. Dependency on Fossil Fuels: While CCS can help reduce emissions from fossil fuels, it might also prolong Nigeria's dependence on oil and gas. This could hinder the transition to more sustainable and renewable energy sources in the long term(IPCC, 2022).

iv. Environmental Concerns: The storage of captured CO2 underground raises potential environmental risks, such as leaks or accidental releases. Addressing these concerns and ensuring the safety of communities near storage sites is crucial(Turan et al., 2021).

v. Disruption of Local Communities: The construction of CCS facilities and related infrastructure could lead to the displacement of local communities or disruptions to their traditional livelihoods. Ensuring proper consultation and compensation for affected communities is essential(IEA, 2022).

9. CONCLUSION

Carbon capture and storage (CCS) is a technology that can help Nigeria reduce its carbon emissions and achieve its energy transition goals. It can also have both positive and negative socioeconomic impacts, so it is important to carefully consider these impacts and implement appropriate mitigation measures to maximize the benefits and minimize the drawbacks.

REFERENCES

Babadagli, T. (2007). Development of mature oil fields — A review. *Journal of Petroleum Science and Engineering*, *57*(3-4), 221–246. https://doi.org/10.1016/j.petrol.2006.10.006

Boundary Dam Carbon Capture Project. (2022). Www.saskpower.com. https://www.saskpower.com/Our-Power-Future/Infrastructure-Projects/Carbon-Capture-and-Storage/Boundary-Dam-Carbon-Capture-Project

C. Jones , A., & J. Lawson, A. (2022). *Carbon Capture and Sequestration (CCS) in the United States*.

Carbon Capture And Storage In Nigeria - Renewables - Nigeria. (2022). Www.mondaq.com. https://www.mondaq.com/nigeria/renewables/1317622/carbon-capture-and-storage-in-nigeria

Eweka, E. E., Lopez-Arroyo, E., Medupin, C. O., Oladipo, A., & Campos, L. C. (2022). Energy Landscape and Renewable Energy Resources in Nigeria: A Review. *Energies*, *15*(15), 5514. https://doi.org/10.3390/en15155514

Gorgon liquefied natural gas (LNG) project, Western Australia. (2022). Www.hydrocarbons-Technology.com. https://www.hydrocarbons-technology.com/projects/gorgon-lng-project/

Goulder, L., & Nadreau, B. (2001). *International Approaches to Reducing Greenhouse Gas Emissions*.

IEA. (2022, October). *World Energy Outlook 2022 – Analysis - IEA*. IEA. https://www.iea.org/reports/world-energy-outlook-2022

IPCC. (2022). *Climate Change 2022: Mitigation of Climate Change*. Www.ipcc.ch. https://www.ipcc.ch/report/ar6/wg3/

National Grid. (2023). *What is Carbon Capture and Storage? | National Grid Group*. Www.nationalgrid.com. https://www.nationalgrid.com/stories/energy-explained/what-is-ccs-how-does-it-work#:~:text=CCS%20involves%20the%20capture%20of

Ndege, Y. (2023). *Explaining Nigeria's energy crisis*. Www.aljazeera.com. https://www.aljazeera.com/features/2012/06/14/explaining-nigerias-energy-crisis/

Nigeria Renewable Electricity Percent In Total Electricity Output. (2014). Tradingeconomics.com. https://tradingeconomics.com/nigeria/renewable-electricity-percent-in-total-electricity-output-wb-data.html

Petra Nova - W.A. Parish Project. (2023). Energy.gov. https://www.energy.gov/fecm/petra-nova-wa-parish-project

Sleipner Details. (2023). Www.geos.ed.ac.uk. https://www.geos.ed.ac.uk/sccs/project-info/2#:~:text=Project%20Description

South Africa's Carbon Capture Utilisation and Storage Project A proud entity of the Department of Mineral Resources and Energy. (2023).

Strategic Developments In Renewable Energy In Nigeria Energy Demand and Supply Projections for Nigeria View project Abubakar Sambo Energy Commission of Nigeria. (2023).

Technology - NET Power - Making Clean Cheaper Than Dirty. (2020, November 9). NET Power - Making Clean Cheaper than Dirty. https://netpower.com/technology/

Turan, G., Zapantis, A., Kearns, D., Tamme, E., Staib, C., Zhang, T., Burrows, J., Gillespie, A., Havercroft, I., Rassool, D., Consoli, C., Liu, H., Support, Bright, M., Erikson, J., Loria, P., Nambo, H., Wu, Y., Judge, C., & Gebremedhin, R. (2021). *The team of authors included.* https://www.globalccsinstitute.com/wp-content/uploads/2021/10/2021-Global-Status-of-CCS-Report_Global_CCS_Institute.pdf

Vincent, E. N., & Yusuf, S. D. (2014). Integrating Renewable Energy and Smart Grid Technology into the Nigerian Electricity Grid System. *Smart Grid and Renewable Energy*, *05*(09), 220–238. https://doi.org/10.4236/sgre.2014.59021

10.51975/24390203.som
Journal of the Nigerian Society of Chemical Engineers, 39(2), 2024

SYNTHESIS AND CHARACTERIZATION OF SBA-15 CATALYST FOR CO-PYROLYSIS OF OIL PALM FIBRE AND PLASTIC WASTE FOR BIO-OIL PRODUCTION

***Gin, W. A. [1] and Salami, L.[2]**

[1] Department of Chemical Engineering, Federal University Wukari, Wukari 670101, Taraba State, Nigeria
[2] Environmental Engineering Research Unit, Department of Chemical Engineering, Lagos State University, Epe, Lagos State, Nigeria
* Corresponding author: ginwilliams@fuwukari.edu.ng

ABSTRACT

SBA-15 catalyst was synthesized using the sol-gel method and utilized in the co-pyrolysis of oil palm fiber and plastic mixtures within a fixed-bed reactor. The catalyst showcased a distinctive hexagonal mesoporous structure with a pore width of 8.57 ± 1.053 nm, as revealed by transmission electron microscopy (TEM) and confirmed by low-angle X-ray diffraction (XRD) analysis. This unique mesoporous architecture enhances the catalyst's effectiveness by facilitating the efficient transport and reaction of intermediate pyrolysis products. Optimal conditions were achieved with a catalyst-to-feedstock ratio of 1:8, resulting in a maximum bio-oil yield of 53.8 wt%. In terms of oil composition, a catalyst-to-feedstock ratio of 1:6 yielded the highest proportions of total desirable hydrocarbons and alcohols in the oil. The hexagonal mesoporous structure and the optimized catalyst-to-feedstock ratios significantly contributed to the efficiency of bio-oil production, demonstrating the potential of SBA-15 as a valuable catalyst for converting biomass and plastic mixtures into high-value-added chemicals and oils.

Keywords: SBA-15, co-pyrolysis, oil palm fibre, plastic mixture

1.INTRODUCTION

The contemporary challenge of depleting fossil fuel reserves coupled with escalating greenhouse gas emissions persists as a global concern (Cupertino et al. 2024; Tcvetkov 2022). Despite the recognized potential of transitioning to renewable energy sources to mitigate these emissions, such a shift remains hindered by insufficient research data. In Nigeria, oil palm fiber (OPF) emerges as a readily available agricultural residue, which studies (Abogunrin-Olafisoye et al. 2024; Kabir et al. 2018) suggest can serve as a feedstock for bio-oil production. Although traditionally employed as fuel in mill boilers, various chemical processes such as extraction (Syafiqah et al. 2022), hydrothermal carbonization (Nai et al. 2022), and acetosolv (Pereira Marques et al. 2021) have been explored for the production of bio-oil and value-added products from dried OPF.

Among these processes, co-pyrolysis stands out as a promising method due to its adaptability to both simple and complex biomass feedstocks. Previous research has predominantly focused on pyrolysis and catalytic pyrolysis techniques for oil palm fibre (OPF) valorisation (Kabir et al. 2018). For instance, Gin et al., (2022) reported an impressive oil yield of up to 40 percent via pyrolysis of OPF. However, while co-pyrolysis presents advantages, such as enhanced bio-oil production, challenges persist, notably in the limited applicability of the resulting liquid product due to its low hydrocarbon and alcohol content and hence low heating value (Qiu et al. 2022).

To address these limitations, catalytic co-pyrolysis (CCP) emerges as a promising avenue. Catalysts play a crucial role in accelerating specific reactions, such as cracking, thereby facilitating the breakdown of large feedstock intermediates and enhancing their transformation (Zheng et al. 2022). Hexagonally structured SBA-15 silica, characterized by large pores and a high specific surface area, represents a particularly attractive catalyst candidate (Romero et al. 2022). While previous studies have focused on SBA-15 functionalization and its application in various pyrolysis/co-pyrolysis processes, including tires/sawdust (Cao et al., 2009), lignin (Shafaghat et al. 2019; Wang et al. 2021), and cellulose

(Hong et al. 2017; Kim et al. 2017), synthesis methods have predominantly relied on the conventional hydrothermal technique.

This work aims to address this gap by synthesizing SBA-15 via the sol-gel route, a less energy-intensive method, and evaluating its efficacy as a catalyst for the co-pyrolysis of OPF and plastic mixtures. Additionally, we seek to analyse the composition of the liquid product obtained from this co-pyrolysis process. By leveraging the advantages of SBA-15 and exploring novel synthesis approaches, this research endeavours to advance the field of biomass valorisation and contribute to sustainable energy production.

2. MATERIALS

2.1 Feedstock for Co-pyrolysis

The biomass sample used for the co-pyrolysis was oil palm fibre while the two representative plastic polymers were High Density Polyethylene (HDPE) and Polypropylene (PP).

2.2 METHODS

2.2.1 Synthesis of Catalyst

SBA-15 was synthesized via the sol-gel method following the procedure outlined in the work of Koh et al. (2017). In a 1000 ml beaker, 11.9 g of non-ionic tri-block copolymer, Pluronic P123 ($EO_{20}PO_{70}EO_{20}$), was dissolved in 420 g of 2.0 M HCl acid and 89.9 ml of distilled water at 40°C and 100 rpm using a magnetic stirrer until a colourless solution formed. Subsequently, 29.1 g of Tetraethyl orthosilicate (TEOS) was added drop-wise and stirred vigorously for 2 hrs to form a gel solution. The mixture was aged for 48 hrs prior to crystallization. The resulting sol-gel was separated by vacuum filtration, air-dried overnight, and then heated at 550°C for 4 h in an electric furnace (ThermoLab 3000) at a rate of 5°C/min.

2.2.2 Characterization of Catalyst

The catalyst properties were examined through BET surface area analysis, Nitrogen adsorption-desorption analysis and X-ray diffraction patterns (XRD, following procedures outlined in the work of Adibah et al. (2018).

2.2.3 Thermal and Catalytic Co-pyrolysis of Feedstock

The procedure described herein is that of the authors. A cylindrical stainless-steel reactor was used for the co-pyrolysis of the feedstock mixture. Nitrogen gas was used to maintain an inert atmosphere within the reactor, flowing at a rate of 250 cm^3/min for 15 min before each experiment. For the thermal co-pyrolysis of OPF and waste mixed plastics, fixed parameters included a reaction temperature of 600 ° C, reaction time of 45 min, and a pressure of 2 bar. The plastic mixture (PM) comprised High density polyethylene (HDPE) and polypropylene (PP) in a 1:1 ratio. Equal masses of OPF (0.8 g) and plastic mixture (0.8 g) were blended to yield a total mass of 1.6 g. In catalytic pyrolysis, with a fixed feedstock mass of 1.6 g, catalyst-to-feedstock ratios of 1:9, 1:8, 1:7, and 1:6 corresponded to catalyst weights of 0.17 g, 0.20 g, 0.22 g, and 0.27 g, respectively.

2.2.4 GC-MS Analysis of the Oil

Bio-oil produced underwent gas chromatography/mass spectrometry (GC/MS) analysis (Perkin Elmer Clarus 600/600T), as described by Adibah et al. (2018). Compounds on the gas chromatogram were categorized into major classes such as hydrocarbons, acids, esters, carbonyls, aromatics, and alcohols.

3. RESULT

3.1 Characterization of feedstock

A previous report extensively discussed the elemental analysis, proximate analysis, chemical composition, higher heating value (HHV), thermochemical properties of the individual feedstocks (oil palm fibre, plastic mixture) and their blend (Gin et al. 2022).

3.2 Characterization of catalysts

Table 1 summarizes the physical characteristics of the catalyst employed in this investigation.

Table 1: Physical properties of catalyst.

Property	Unit	Value
Rod size	µm	1.71
Si/O atomic ratio	-	0.40
P/P_0	-	0.45
Carbon content	%	12.44
Micropore volume	cm^3/g	0.082
BET surface area	m^2/g	614.7

Figure 1 present the EDX spectra of the catalyst. It shows the respective weight percentage contributed by each element in SBA-15 sample. The EDX spectra of the SBA-15 catalyst revealed that the principal elements in the sample were silicon (Si) and oxygen (O) which is typical of siliceous materials.

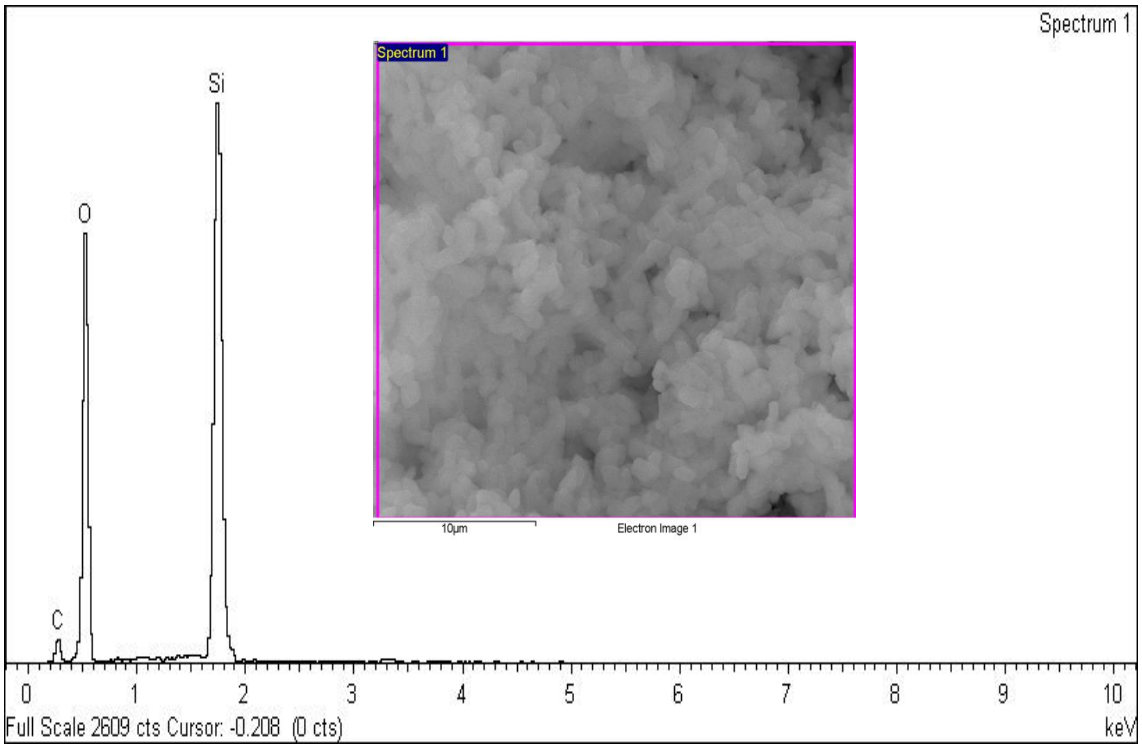

Figure 1 : EDX Spectra of SBA-15 catalyst

The SBA-15 sample, based on EDX analysis, consisted of 25.4 wt.% silicon (Si) and 62.17 wt.% oxygen (O), yielding a calculated Si/O atomic ratio of 0.40 (Table 1). The percentage carbon (12.44%) found on the catalyst structure of SBA-15 in this study was higher than 4.2% obtained in the catalyst structure of SBA-15 prepared by Tamoradi et al., (2019). The significantly higher carbon content (12.44%) in the SBA-15 catalyst structure from this study highlights a marked difference in carbon functionalization, which could influence the catalyst's activity, stability, and overall performance. The N_2 adsorption-desorption isotherms of SBA-15 at 77 K exhibited a distinct inflection at P/P0 = 0.45, indicating capillary condensation and evaporation within its uniform mesopore channels (Tseng et al. 2017). The observed hysteresis loop in the P/Po range of 0.45-0.74 confirmed the presence of mesopores, contrasting with findings by Xue et al., (2022), where a narrower range was observed (0.7–0.85). The micropore volume, determined via t-Plot, was 0.082 cm^3/g, while the total pore volume for pores less than 1227.2 Å was 0.66 cm^3/g (Table 1). This result is higher than with the SBA-15 catalyst synthesised through one-pot method in which a surface area of 573.6 m^2/g and pore volume up to 0.64 cm^3/g was obtained (Liu and Tian 2017). The disparity may be attributed to the sol-gel method employed in the synthesis of the catalyst.

The meso-porosity of the SBA-15 synthesized in this work in addition to the relative higher surface area and pore volume would aid the transport of a wide range of intermediate pyrolysis products formed from the reaction of the plastic mixture and biomass during the primary pyrolysis to form more hydrocarbon and alcohols assisted by the active site of the catalyst (Kim et al., 2017; Socci et al., 2022).

Figure 2 presents the low-angle XRD ($2\theta < 3^\circ$) regions of SBA-15. The Bragg reflection at 2θ of 0.58° with two shoulder peaks at 2θ of 1.5 ° and 1.84° are detected and corresponds to reflections of (100), (110), and (200) planes of a hexagonal mesoporous organization. These reflections are identified as (100), (110), and (200) based on their angular positions relative to the hexagonal unit cell parameters, as outlined in the structural model of SBA-15.

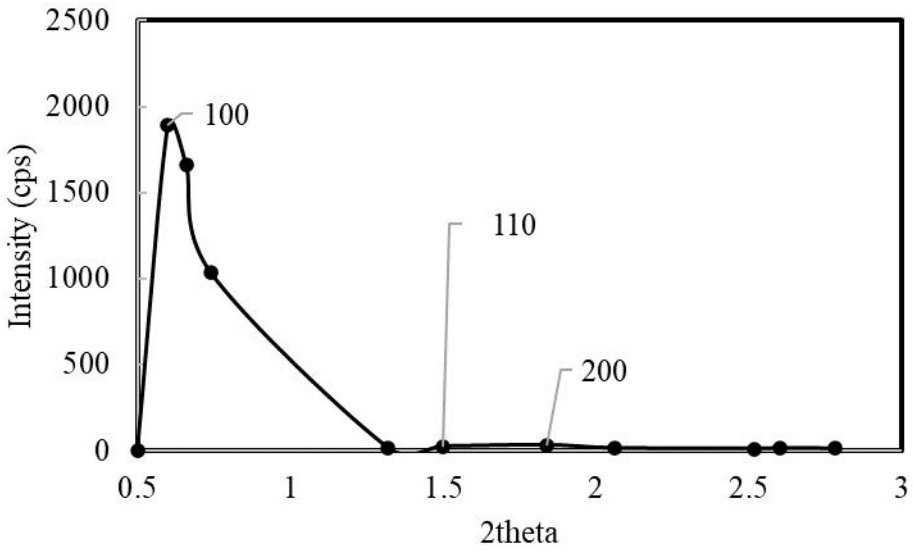

Figure 2: XRD Spectra of SBA-15 catalyst

The Bragg reflections of (100) appeared to be more intense. In the work of Tabaja et al. (2021), the Bragg reflections of (110) and (210) was between 1.5° and 2.2° in 2θ angle. The mesoporous organization of the SBA-15 is expected to increase the access of the large volatile pyrolysis intermediate products of the plastic mixture into the active sites of the catalyst and increase the internal catalytic conversion to oil.

Figure 3 presents the transmission electron microscopy (TEM) micrograph of SBA-15. The micrograph reveals a well-defined hexagonal pore structure, typical of SBA-15 materials.

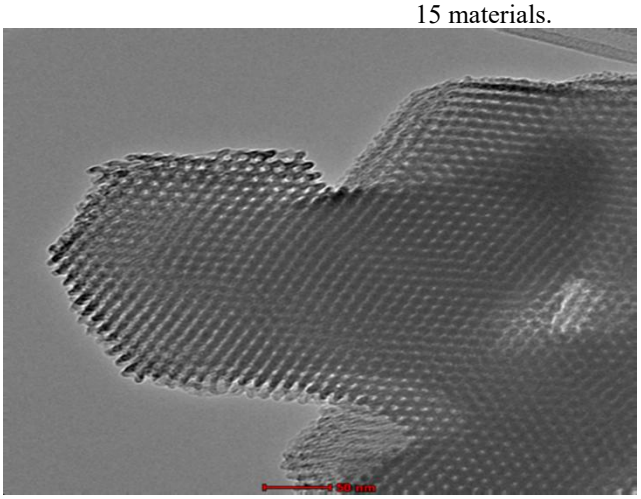

Figure 3: TEM image of SBA-15 catalyst

ImageJ analysis indicated a pore width of 8.57 ± 1.053 nm, which is expected to provide sufficient access for large pyrolysate molecules. The pore width of SBA-15 produced in this study was higher than the mesoporous silica SBA-15 synthesized by Zhu et al., (2007) which had pore width of 3.8 nm. In the work of Vargas-Osorio et al., (2022), the average pore width of the SBA-15 particles was estimated to be 10.1 ± 0.9 nm. The pore size obtained in this study will be beneficial for the diffusion of pyrolysis intermediate molecules of the feedstocks to the active sites of the catalyst.

3.2 Product yields of co-pyrolysis

The primary pyrolytic products include oil, gas, and char. Figure 4 presents the product yields of catalytic co-pyrolysis of oil palm fronds (OPF) and plastic mixture over SBA-15 at various SBA-15-feedstock ratios (1:9, 1:8, 1:7, and 1:6). The oil yield ranged from 48.1% to 53.8% as the C/F ratio changed from 1:9 to 1:6, with maximum oil yields obtained at 1:8. Most of published studies did not carry out the parameter studies on SBA-

15 catalysed co-pyrolysis of the feedstocks in terms of the influence of the catalyst to feedstock ratio on oil yield and therefore this result could not be compared.

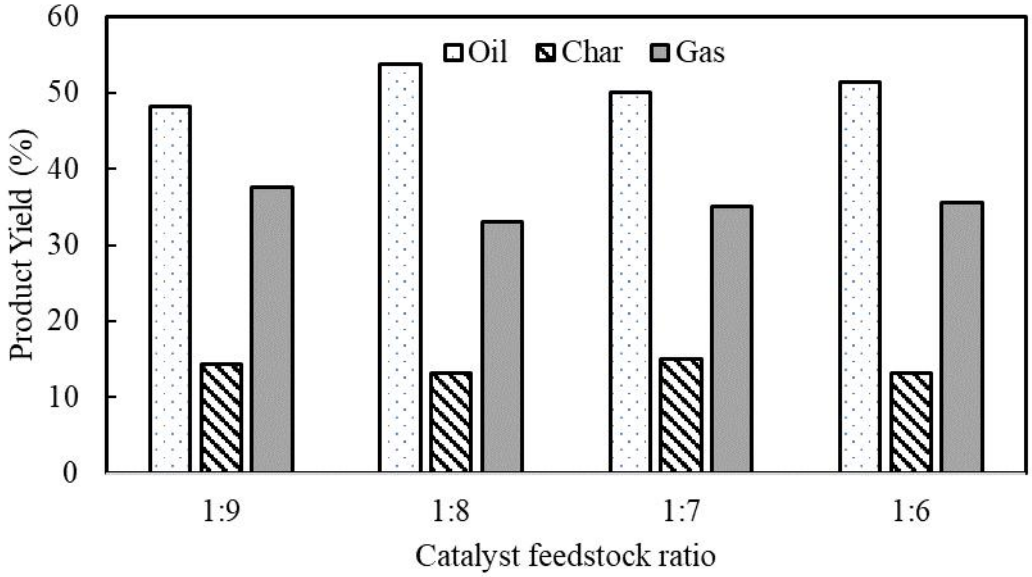

Figure 4: Product yields at different catalyst feedstock ratios

Under the same range of changing C/F ratio, the char yield in this study ranged between 13.1% and 15.0%, with the maximum char yield obtained at a catalyst-feedstock ratio of 1:7. A clear trend was observed in the co-pyrolysis of Kraft Lignin and LLDPE (1:1) over mesoZSM-5 (at 500 °C) and Al-SBA-15 (at 600 °C), where the solid residue changed from 11.71% and 11.47% at a catalyst-to-feed mass ratio of 1:1 to 16.01% and 19.55% at a ratio of 5:1, respectively (Shafaghat et al. 2019). Generally, an increase in the C/F ratio is expected to prolong the dwelling time of pyrolytic vapours in the mesopore structure of SBA-15, leading to increased char yield and decreased liquid yield (Fan et al. 2017).

In terms of gas production, the yield ranged from 33.1% to 37.5%, with the minimum and maximum obtained at 1:8 and 1:9, respectively. The mixed trend in product yield with changes in the catalyst-feedstock ratio is due to synergistic effects between the plastic mixture and OPF. However, the addition of more SBA-15 (from 1:8 to 1:6) increased the gas yield from 33.1% to 35.6%, possibly due to thermal cracking of the oil produced or secondary decomposition of chars to gas (Ozbay, 2019; Xue et al. 2019). The highest catalyst-feedstock ratio of 1:9 gave the maximum gas yield due to increased removal of oxygenated compounds in the pyrolytic vapor via increased decarbonylation and decarboxylation reactions, which could have been responsible for the low oil yield obtained at this catalyst-feedstock ratio.

Among these three products, oil is the primary one, obtained through the condensation of the vapor mixture of organic chemicals with water. Oil produced via co-pyrolysis of plastic-biomass-based feedstock constitutes a wide range of compounds categorized into hydrocarbons, esters, carbonyls, acids, and alcohols (Dyer et al. 2021).

3.3. Gas Chromatography-Mass Spectroscopy (GC-MS) of oil

Figure 5 presents the composition of the oil obtained from the catalytic co-pyrolysis of plastic mixture and OPF at different SBA-15- feedstock ratio (1:9, 1:8, 1:7 and 1:6). Figure 5 presents the composition of the oil obtained from the catalytic co-pyrolysis of the plastic mixture and OPF at various SBA-15-feedstock ratios (1:9, 1:8, 1:7, and 1:6). The primary organic compounds present in the oil were hydrocarbons and esters, with relatively lower amounts of alcohol and acids.

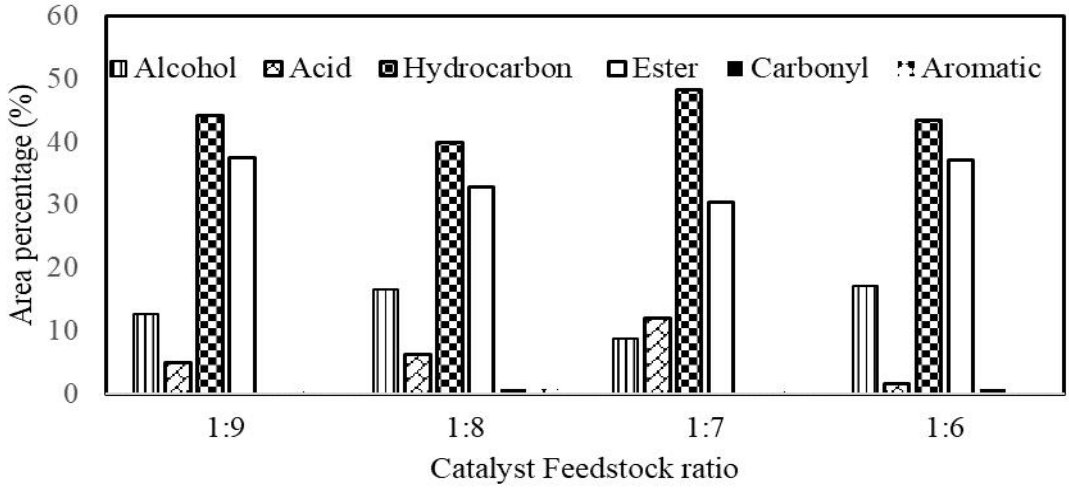

Figure 5: Oil Composition at Different Catalyst Feedstock Ratio

The hydrocarbon composition in the oil ranged between 39.96% and 48.27% as the C/F ratio increased from 1:9 to 1:6, with the minimum and maximum yields obtained at 1:8 and 1:7, respectively. This suggests that a catalyst feedstock ratio of 1:7 favoured hydrogenation reactions which improved the H/C ratio in the oil.

Within the same range of C/F ratio, the alcohol composition of the oil ranged between 8.69% and 17.11%, with the minimum and maximum yields obtained at 1:7 and 1:6, respectively. This indicates that the C/F ratio of 1:6 improved dehydrogenation and deoxygenation reactions on the surface of SBA-15, as it was effective for producing the highest amount of alcohol. Additionally, the total ester compounds in the oil ranged between 30.4% and 37.62%, with the minimum and maximum yields obtained at 1:7 and 1:9, respectively. At the C/F ratio of 1:7, SBA-15 slightly suppressed the rate of esterification reaction between the acids and aromatic compounds, forming aromatic esters or chain esters in the oil. Finally, the total acid compound in the oil ranged between 1.67% and 12.1%, with the minimum and maximum yields obtained at 1:6 and 1:7, respectively. The best catalyst-to-feedstock ratio based on the combined yield of alcohols and hydrocarbons is 1:6, which produced a bio-oil with 17.11% alcohols and 43.43 % hydrocarbons, resulting in a total of 60.54%. This ratio outperformed the others, such as 1:8 with 56.62% and 1:7 with 56.96%, by delivering the highest combined percentage of desirable components. While 1:9 also provided a high yield, its lower proportion of alcohols (12.66%) compared to 1:6 made 1:6 the optimal choice.

3.4 Comparison of Thermal and catalytic co-pyrolysis

Figure 6 presents the results which compares the product yields and composition of the SBA-15 catalytic co-pyrolysis with the thermal co-pyrolysis.

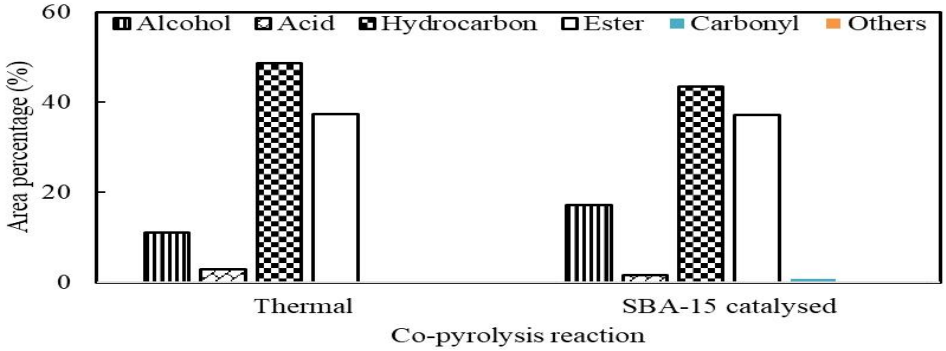

Figure 6: Comparison of (a) product yields and (b) composition of Thermal and catalytic co-pyrolysis

Catalytic co-pyrolysis generally improved the quality of the bio-oil compared to thermal pyrolysis, which produced a bio-oil with 59.74% of alcohols and hydrocarbons. The best catalytic ratio of 1:6 yielded a higher combined total of 60.54%, indicating that the catalytic process enhanced the overall quality of the bio-oil. Apart from this, the SBA-15 catalysed co-pyrolysis at this C/F ratio favoured the production of gas than oil. This might be attributed to the mild acidity of the spatial configuration attributed with SBA-15 catalyst (Pizzolitto et al. 2021).

4. CONCLUSION

The SBA-15 catalyst, synthesized via the sol-gel method, demonstrated a distinctive hexagonal mesoporous structure with high surface area and well-defined pore channels, as confirmed by XRD and TEM analyses. This unique mesoporosity enhances catalytic efficiency by facilitating optimal interaction between the catalyst and feedstock. Manipulating the catalyst-to-feedstock ratio revealed that a 1:6 ratio significantly improved the yield of desirable hydrocarbons and alcohols in the bio-oil. These findings underscore the pivotal role of SBA-15's mesoporous characteristics and precise catalyst optimization in maximizing the efficiency and quality of bio-oil production from the co-pyrolysis of oil palm fiber and plastics.

5. ACKNOWLEDGEMENTS

Special appreciation to the School of Chemical Engineering, University Sains Malaysia for providing us with materials and facilities for this research.

REFERENCES

Abogunrin-Olafisoye, O. B., Adeyi, O., Adeyi, A. J., & Oke, E. O. (2024). Sustainable utilization of oil palm residues and waste in nigeria: practices, prospects, and environmental considerations. *Waste Management Bulletin*, *2*(1), 214–228. https://doi.org/10.1016/j.wmb.2024.01.011

Adibah, W., Mahari, W., Tung, C., Kui, C., Leing, C., Hendrata, K., et al. (2018). Production of value-added liquid fuel via microwave co-pyrolysis of used frying oil and plastic waste. *Energy*, *162*, 309–317. https://doi.org/10.1016/j.energy.2018.08.002

Cao, Q., Jin, L., Bao, W., & Lv, Y. (2009). Investigations into the characteristics of oils produced from co-pyrolysis of biomass and tire. *Fuel Processing Technology*, *90*(3), 337–342. https://doi.org/10.1016/j.fuproc.2008.10.005

Cupertino, G. F. M., Silva, Á. M. da, Pereira, A. K. S., Delatorre, F. M., Ucella-Filho, J. G. M., Souza, E. C. de, et al. (2024). Co-pyrolysis of biomass and polyethylene terephthalate (PET) as an alternative for energy production from waste valorization. *Fuel*, *362*. https://doi.org/10.1016/j.fuel.2023.130761

Dyer, A. C., Nahil, M. A., & Williams, P. T. (2021). Catalytic co-pyrolysis of biomass and waste plastics as a route to upgraded bio-oil. *Journal of the Energy Institute*, *97*, 27–36. https://doi.org/10.1016/j.joei.2021.03.022

Fan, L., Chen, P., Zhang, Y., Liu, S., Liu, Y., Wang, Y., et al. (2017). Fast microwave-assisted catalytic co-pyrolysis of lignin and low-density polyethylene with HZSM-5 and MgO for improved bio-oil yield and quality. *Bioresource Technology*, *225*, 199–205. https://doi.org/10.1016/j.biortech.2016.11.072

Gin, A. W., Hassan, H., Ahmad, M. A., Hameed, B. H., & Din, A. T. M. (2022). Co-pyrolysis of polyolefin mixtures and oil palm fibre for the production of liquid fuel: kinetics and thermodynamic study. *Biomass Conversion and Biorefinery*. https://doi.org/10.1007/s13399-022-02822-5

Hong, Y., Lee, Y., Rezaei, P. S., Kim, B. S., Jeon, J. K., Jae, J., et al. (2017). In-situ catalytic copyrolysis of cellulose and polypropylene over desilicated ZSM-5. *Catalysis Today*, *293–294*, 151–158. https://doi.org/10.1016/j.cattod.2016.11.045

Kabir, G., Mohd Din, A. T., & Hameed, B. H. (2018). Pyrolysis of oil palm mesocarp fiber catalyzed with steel slag-derived zeolite for bio-oil production. *Bioresource Technology*, *249*(September 2017), 42–48. https://doi.org/10.1016/j.biortech.2017.09.190

Kim, Y., Won, H., Jae, J., Bin, K., Jung, S., Watanabe, A., & Park, Y. (2017). Catalytic co-pyrolysis of biomass carbohydrates with LLDPE over Al-SBA-15 and mesoporous ZSM-5. *Catalysis Today*, *298*(May), 46–52. https://doi.org/10.1016/j.cattod.2017.06.006

Koh, M. H., Haji Azaman, S. A., Hameed, B. H., & Mohd Din, A. T. (2017). Surface morphology and physicochemical properties of ordered mesoporous silica SBA-15 synthesized at low temperature. *IOP Conference Series: Materials Science and Engineering*, *206*(1). https://doi.org/10.1088/1757-899X/206/1/012056

Liu, Q., & Tian, Y. (2017). One-pot synthesis of NiO / SBA-15 monolith catalyst with a three-dimensional framework for CO 2 methanation. *International Journal of Hydrogen Energy*, *42*(17), 12295–12300. https://doi.org/10.1016/j.ijhydene.2017.02.070

Nai, P., Yek, Y., Keey, R., Adibah, W., Mahari, W., Peng, W., & Sonne, C. (2022). Production of value-added hydrochar from single-mode microwave hydrothermal carbonization of oil palm waste for de-chlorination of domestic water. *Science of the Total Environment*, *833*(March), 154968. https://doi.org/10.1016/j.scitotenv.2022.154968

Ozbay, N., Seyda, A., Zerrin, R., Sahin, Y., & Yaman, E. (2019). Valorization of banana peel waste via in-situ catalytic pyrolysis using Al-Modi fi ed SBA-15. *Renewable Energy*, *140*, 633–646. https://doi.org/10.1016/j.renene.2019.03.071

Pereira Marques, F., Lima Soares, A. K., Lomonaco, D., Alexandre e Silva, L. M., Tédde Santaella, S., de Freitas Rosa, M., & Carrhá Leitão, R. (2021). Steam explosion pretreatment improves acetic acid organosolv delignification of oil palm mesocarp fibers and sugarcane bagasse. *International Journal of Biological Macromolecules*, *175*, 304–312. https://doi.org/10.1016/j.ijbiomac.2021.01.174

Pizzolitto, C., Ghedini, E., Taghavi, S., Menegazzo, F., Cruciani, G., Peurla, M., et al. (2021). Acid sites modulation of siliceous-based mesoporous material by post synthesis methods. *Microporous and Mesoporous Materials*, *328*(April). https://doi.org/10.1016/j.micromeso.2021.111459

Pourhassan, F., Khalifeh, R., & Eshghi, H. (2021). Well dispersed gold nanoparticles into the multi amine functionalized SBA-15 for green chemical fixation of carbon dioxide to cyclic carbonates under solvent free conditions. *Fuel*, *287*(November 2020), 119567. https://doi.org/10.1016/j.fuel.2020.119567

Qiu, B., Tao, X., Wang, J., Liu, Y., Li, S., & Chu, H. (2022). Research progress in the preparation of high-quality liquid fuels and chemicals by catalytic pyrolysis of biomass : A review. *Energy Conversion and Management*, *261*(April), 115647. https://doi.org/10.1016/j.enconman.2022.115647

Romero, D. E., Rigutto, M., & Hensen, E. J. M. (2022). Influence of the size , order and topology of mesopores in bifunctional Pd-containing acidic SBA-15 and M41S catalysts for n-hexadecane hydrocracking. *Fuel Processing Technology*, *232*(April), 107259. https://doi.org/10.1016/j.fuproc.2022.107259

Shafaghat, H., Won, H., Yang, L., Oh, D., Jung, S., Hoon, G., et al. (2019). Catalytic co-conversion of Kraft lignin and linear low-density polyethylene over mesoZSM-5 and Al-SBA-15 catalysts. *Catalysis Today*, (November 2018), 0–1. https://doi.org/10.1016/j.cattod.2019.04.052

Socci, J., Saraeian, A., Stefanidis, S. D., Banks, S. W., Shanks, B. H., & Bridgwater, T. (2022). The role of catalyst acidity and shape selectivity on products from the catalytic fast pyrolysis of beech wood. *Journal of Analytical and Applied Pyrolysis*, *162*(May 2019), 104710. https://doi.org/10.1016/j.jaap.2019.104710

Syafiqah, N., Azlan, M., Lin, C., Gan, S., Basyaruddin, M., & Rahman, A. (2022). Materials Today : Proceedings Effectiveness of various solvents in the microwave-assisted extraction of cellulose from oil palm mesocarp fiber. *Materials Today: Proceedings*, *59*(xxxx), 583–590. https://doi.org/10.1016/j.matpr.2021.12.086

Tabaja, N., Kassas, A., Hamieh, S., Haidar, R., Foddis, M., Toufaily, J., et al. (2021). High Quality Bio-Oil Obtained from Catalyzed Pyrolysis of Olive Mill Solid Wastes in a Bi-Functional Reactor. *Materials Sciences and Application*, *12*, 52–77. https://doi.org/10.4236/msa.2021.121004

Tamoradi, T., Ghorbani-Choghamarani, A., & Ghadermazi, M. (2019). Immobilization of Pd(0) complex on the surface of SBA-15: A reusable catalyst for the synthesis of 5-substituted tetrazoles, sulfides and sulfoxides. *Polyhedron*, *157*, 374–380. https://doi.org/10.1016/j.poly.2018.10.013

Tcvetkov, P. (2022). Engagement of resource-based economies in the fight against rising carbon emissions. *Energy Reports*, *8*, 874–883. https://doi.org/10.1016/j.egyr.2022.05.259

Tseng, H., Chuang, H., & Zhuang, G. (2017). Structure-controlled mesoporous SBA-15-derived mixed matrix membranes for H 2 purification and CO2 capture. *International Journal of Hydrogen Energy*, *42*(16), 11379–11391. https://doi.org/10.1016/j.ijhydene.2017.03.026

Vargas-Osorio, Z., Klotschan, A., Arango-Ospina, M., Piñeiro, Y., Liverani, L., Rivas, J., et al. (2022). Effect of glycerol and H3PO4 on the bioactivity and degradability of rod-like SBA-15 particles with active surface for bone tissue engineering applications. *Microporous and Mesoporous Materials*, *329*.

https://doi.org/10.1016/j.micromeso.2021.111543

Wang, S., Li, Z., Yi, W., Fu, P., Zhang, A., & Bai, X. (2021). Renewable aromatic hydrocarbons production from catalytic pyrolysis of lignin with Al-SBA-15 and HZSM-5: Synergistic effect and coke behaviour. *Renewable Energy*, *163*, 1673–1681. https://doi.org/10.1016/j.renene.2020.10.108

Xue, X., Liu, Y., Wu, L., Pan, X., Liang, J., & Sun, Y. (2019). Catalytic fast pyrolysis of maize straw with a core–shell ZSM-5@SBA-15 catalyst for producing phenols and hydrocarbons. *Bioresource Technology*, *289*(April), 121691. https://doi.org/10.1016/j.biortech.2019.121691

Zhang, C., Xia, D., Wang, Y., Liang, J., & Sun, Y. (2022). Dual-catalyst catalytic pyrolysis of poplar sawdust : A systematic study on first-layered catalysts. *Chemical Engineering Journal*, *431*(P3), 134251. https://doi.org/10.1016/j.cej.2021.134251

Zheng, Y., Li, D., Pei, T., Wang, J., Liu, C., & Lu, Y. (2022). Mechanism of synergistic effects and kinetic analysis in bamboo-LDPE waste ex-situ catalytic co-pyrolysis for enhanced aromatic hydrocarbon production via CeZrAl and HZSM-5 dual catalyst. *Journal of Environmental Chemical Engineering*, *10*(December 2021), 0–2. https://doi.org/10.1016/j.jece.2022.107479

10.51975/24390205.som
Journal of the Nigerian Society of Chemical Engineers, 39(2), 2024

SIMULATION AND PERFORMANCE EVALUATION OF A SHELL AND TUBE HEAT EXCHANGER FOR METHANOL SOLUTION

***Fadayini, O.[1], Akintola J.T.[2], Bello, V.E.[3], Amodu, O. S.[1], Akinmoladun, O. M.[4], Dickson, P.O.[5], Ogbodhu, C. U, K.[6], Ajayi, A. O.[7], Kareem, G. N.[8], Salisu, S. A.[9], Kinsley, N. A.[10],**

[1]Department of Chemical Engineering, Lagos State University of Science and Technology Ikorodu, Lagos, Nigeria.
[2]Research and Development Department, Vitapur Nigeria Limited, Mushin, Lagos, Nigeria.
[3]Department of Chemical and Petroleum Engineering, University of Lagos, Akoka, Lagos, Nigeria.
[4]Department of Mathematics, Lagos State University of Science and Technology, Ikorodu, Lagos State, Nigeria
[5]Department of Agricultural and Bio-environmental Engineering, Yaba College of Technology, Lagos, Nigeria.
[6]Department of Chemical Engineering, Delta State University of Science and Technology, Ozoro, Delta, Nigeria
[7]Department of Computer Engineering, Lagos State University of Science and Technology Ikorodu, Lagos, Nigeria
[8]Department of Electrical & Electronic Engineering, Lagos State University of Science and Technology Ikorodu, Lagos, Nigeria
[9]Nigerian National Petroleum Company (NNPC), Abuja, Nigeria
[10]Louisiana State University, USA
*Corresponding author: fadayini.o@lasustech.edu.ng, olufeday@gmail.com

ABSTRACT

This paper presents a comprehensive study on the simulation, modeling, and multiphase flow analysis of a shell and tube heat exchanger used for cooling methanol with water. The process simulation was conducted using Aspen HYSYS 8.8, while statistical analysis and modeling were performed with Minitab 17.0, and multiphase flow analysis was carried out using COMSOL 5.3. The simulation results showed that the process closely resembles real-time heat exchange, indicating potential for scaling up in the industry. Statistical analysis using ANOVA demonstrated the model's accuracy, with a perfect correlation coefficient (R^2) of 100% for both heat transfer coefficients. The velocity profile of water within the exchanger revealed the optimal length for maximum flow, while pressure profiles indicated uniformity at a certain point, with a maximum pressure of 17.8 Pa. The shear stress analysis for the water-methanol system reveals a sharp increase from 0 - 0.12 Pa, then a constant shear rate at this point, before a further decrease to 0.265 s^{-1} and then increased to 0.27 s^{-1}. However, a haphazard decrease in the shear rate of the water-methanol system is observed, with a decrease from 3.9 – 0.3 s^{-1}. These findings highlight the effectiveness of the simulated model in predicting the performance of the heat exchanger, making it suitable for industrial applications aimed at cooling and energy conservation.

Keywords: *methanol, shell and tube heat exchanger, simulation, statistical analysis, and modelling.*

1.0 INTRODUCTION

Heat is recovered between two process fluids using heat exchangers in industrial processes. The heat exchangers most frequently used in process industries are shell and tube heat exchangers (STHE). The design of STHEs, including the design of fluid dynamics and thermodynamics, cost estimation, and optimization, represents a complex process consisting of an integrated set of design guidelines and empirical knowledge from lots of fields (Kern 1950, Selbas *et al.* 2006). As part of exploring an exchanger geometry that satisfies the heat duty requirement and a specific set of design constraints, the design of STHEs involves a significant number of geometric and operating variables. For operations like process liquid or gas cooling, process refrigerant vapour or steam condensing, process liquid, steam, or refrigerant evaporation, process heat removal and preheating of feed water, thermal energy conservation effort, heat salvaging, hydraulic and lube oil cooling, shell and tube

heat exchangers are frequently used (Kuye *et al.* 2011) There have been numerous prior studies on heat exchanger optimization. Several researchers have used various optimisation techniques, to improve heat exchanger design, while reflecting multiple objective functions. Selbas *et al.* (2006) used a genetic algorithm (GA) to create STHEs with the best possible design parameters. Ozcelik (2007) considered the STHE's size

and energy cost when analysing the mixed integer nonlinear programming problem. Using GA, Caputo *et al.* (2009) developed a heat exchanger based on financial optimization. By using the harmony search algorithm, Fesanghary *et al.* (2009) optimized an STHE influential parameter from an economic perspective. Ani *et al.* (2010) used experimental data from a heat exchanger that is operated co-currently and counter-currently at a fixed entry temperature to describe the rating method of the design of a multi-tube one shell pass one tube pass heat exchanger. In addition to using GA to reduce costs, Wildi-Tremblay *et al.* (2007) took STHE maintenance into account. The particle swarm optimization (PSO) algorithm was used by Rao *et al.* (2010) to optimize the design of shell and tube heat exchanges. Caputo *et al.* (2015) compared the equipment configurations produced by a genetic algorithm-based software tool created for the best heat exchanger design to the actual patented heat exchangers created using a top commercial software tool. Asadi *et al*. (2014) embarked on the STHE design optimization problem. To solve the STHE problem from an economic perspective, Hadidi *et al.* (2013) use the biogeography-based algorithm and imperialist competitive algorithm. Other researchers' approaches to improving the design of shell and tube heat exchangers varied depending on their goals (Raja et al. 2016, Ani et al 2010, Thirumarimurugan *et al.* 2008). The fluid travels in complicated and irregular flow patterns through a packed bed and other process equipment. Due to this, it is challenging to obtain exact solutions and accurate fluid flow representations. The irregularity of the packing material results in highly varied flow routes and significant variations in local and average velocities, which makes the radial fluid velocity important (Atmakidis *et al.* 2009). The experimental correlations created by (Ergun 1952, Trupti et al. 2012) or other similar correlations are typically used to forecast the pressure decrease across a packed bed (Tema 1999). Similar methods are employed by the majority of Ergun equation extensions, however, some (Atmakidis *et al.* 2009, Pope et al. 2011) also include additional parameters (Chase *et al.* 2005, Radojkovic *et al.* 2003). To broaden the link to other systems, this also takes into account the effects of the vessel walls (Atmakidis *et al.* 2009). By creating correlations for a wider range and lower Reynolds number limit than in earlier studies (Pope *et al.* 2011) and other correlations (Tallmadge 1970) broaden the flow regimes and flow circumstances.

Previously, the effect of corrugated shell and corrugated tube (Dizaji *et al.* 2017), geometry parameters (Alimoradi *et al.* 2017), and helix angles (Gao *et al.* 2015) on the entropy generation and heat transfer performance of shell and tube heat exchanger (STHE) has been investigated. Abd *et al.* (2018) examined the influence of shell diameter, tube length, cutting space, and baffle spacing on pressure drop and heat transfer coefficient for shell sides having triangular and square pitches. An increase in heat transfer coefficient by 3% was recorded for a 0.05 m increase in shell diameter. A decrease in heat transfer coefficient by 15.15% with an increase in baffle space by 0.2 m from shell diameter was noticed with a pressure drop of 41.25%. Hysys v8.8 program was used together with Peng-Robinson as a fluid package to execute the task. The study conducted by Seralathan *et al*. (2020) revealed the thermal conductivities of Ag-W and CuO-W nanofluids enhanced the heat transfer ability of the shell and tube heat exchanger examined with the highest convective heat transfer coefficients and actual heat transfer obtained using CuO-W nanofluid with 0.06% volume concentration.

Recently, Kunjuraman *et al.* (2021) applied Adaptive Neuro-Fuzzy Inference System (ANFIS) and Artificial Neural Network (ANN) models to predict the accuracy of a Shell and Tube Heat Exchanger designed purposely for the treatment of wastewater from the textile industry. The ANFIS model was effective in predicting the condensate temperature over the ANN with an Absolute fraction of variance of 0.9998. Masoumpour *et al*. (2021) investigated the effect of mass flow rate recovery using reflux direction on thermo-economic optimisation of the shell and tube heat exchanger. The result revealed an increase in mass flow rate recovery and total annual cost compared to the conventional heat exchanger without stream recovery. MWCNT/water nanofluid at 0.1%, 0.3%, and 0.5% volume concentration and coiled tubes were simultaneously applied to improve the thermal performance of a shell and helical coil heat exchanger (Shafiq *et al* 2022). An increase in the Nusselt number of the fluid flowing through the coil was noticed as the coil Reynolds number and nanofluid volume concentration were increased (Jamal-Eddine *et al.*, 2022). Sharifat *et al.* (2022) applied computational analysis to investigate the influence of tube pass ratio, helical baffle, and Al_2O_3-water nanofluid on the heat transfer efficiency of an STHE. An increase in Reynolds number caused a reduction in the friction factor. The

simultaneous increase in Reynolds number and tube pass ratio together with the reduction in the baffles space ratio improved the heat transfer performance of the STHE. The effect of using elliptical dimples in a shell and tube heat exchanger on its heat transfer performance has been studied with the application of the P-NTU thermal analysis method (Mehrjardi *et al*. 2023). The result revealed an increase in the heat capacity of the STHE by 40.6% and a 9% error was obtained using an analytical approach. The various available methods for heat transfer enhancement in shell and tube heat exchangers have been presented (Marzouk *et al.* 2023).

In all the examined literature, little consideration has been given to the statistical evaluation of the heat transfer performance of an STHE to the best of the author's knowledge. Many authors focused majorly on the design and modelling of shell and tube heat exchangers with the application of numerous equations which makes the techniques ambiguous and time-consuming (Lona *et al.* 2000). There is a need to bridge the gap between the models developed and their subsequent validation for sustainable industrial application by Engineers. This study statistically analyzes the modelling and simulation of a shell and tube heat exchanger for methanol cooling with the aid of the Aspen HYSYS Process simulator and linear regression ANOVA.

2.0 MATERIALS AND METHODS

The Aspen simulation steady state model was used as the method for performance evaluation of the shell and tube heat exchanger in this paper, and the variation of the hot stream flow rate was used to study the overall performance of the shell and tube heat exchanger (overall heat transfer coefficient and heat transfer area) (methanol). Methanol is cooled from a very high temperature to the surrounding air's 25 °C temperature. The cooling water flow rate necessary to achieve the required methanol outlet temperature is obtained upon convergence of the process simulation. This demonstrates unequivocally that simulations mimic real-world processes (Fadayini, *et al.,* 2018). The steady-state model from the Aspen simulation was employed in this paper to evaluate the performance of the shell and tube heat exchanger. The overall performance of the exchanger, specifically the overall heat transfer coefficient and heat transfer area, was analyzed by varying the hot stream flow rate. Methanol is cooled from a very high temperature to the surrounding air's 25 °C temperature. The cooling water flow rate necessary to achieve the required methanol outlet temperature is obtained upon convergence of the process simulation. This demonstrates unequivocally that simulations mimic real-world processes (Fadayini, *et al.,* 2018). The shell and tube heat exchanger can be utilized in the recovery of essential chemicals, and steam-stripping of hydrogen Sulfide from natural gas during purification production of industrial gases. Hence, the cooling water rate and overall heat transfer coefficient could be predicted from this simulation model. The diagrammatical representation of the simulated shell and tube heat exchanger in the simulation environment is given in Figure 1.

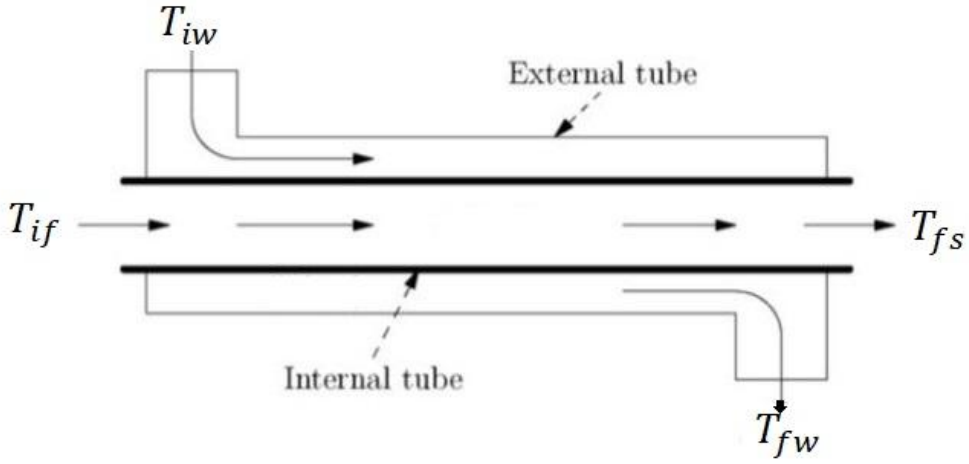

Figure 1: Simulated Shell and Tube Heat Exchangers for Methanol Cooling

The configuration parameters used in the Aspen environment for the simulated and modelled shell and tube heat exchanger are presented in Table 1. This indicates the stream conditions, overall performance, detailed performance, and configuration of the shell and tube heat exchanger.

Table 1: Simulation parameters for the Shell and tube heat exchanger

Stream parameters	Temperature ˚C	Pressure (kPa)
Tube in	120	790.8
Shell in	25	997.6
Tube out	30	997.6
Shell out	30	790.8
Configuration		
Number of shell passes	1	
Number of shells in series	1	
Number of shells in parallel	1	
Tube passes per shell	2	
Exchanger orientation	Horizontal	
Tube volume per shell (m^3)	0.1930	
Tube volume per shell (m^3)	2.272	
Overall performance		
Duty (kJ/h)	2.248×10^4	
Heat leak (kJ/h)	0.0000	
Heat loss (kJ/h)	0.0000	
UA	9.04×10^2	
Min. Approach (˚C)	5.00	
LMTD (˚C)	24.87	
Detailed performance		
UA Curvature error	0.0000	
Hot Pinch Temperature	30.0000	
Cold Pinch Temperature	25.0000	
Ft Factor	0.842	
Uncorrected LMTD	29.537	

3.0 RESULTS AND DISCUSSION

Aspen HYSYS Process simulator, version 8.8, was used to simulate under the steady-state assumption. Methanol flow rate is the predicting variable, and cooling water flow rate and overall heat transfer coefficient are the response variables. The heat transfer area generated by the simulation is 60.32 m^2, which demonstrates that the heat transfer area of a shell and tube heat exchanger is independent of the flow rates of the hot and cold streams. However, as presented in Table 2, the quantity of cooling water required to achieve cooling and the corresponding overall heat transfer coefficient is reliant on the hot fluid flow rate (120 °C). Ordinarily, methanol boils at 68 ˚C, and owing to this temperature, it exists in the vapour phase having a high tendency to vaporize. Hence, this need to simulate and model a shell and tube heat exchanger to lower the temperature of this hot methanol stream.

Table 2: Aspen Simulation Results

Predicting variable	Response variable			
Methanol flow (L/d)	**Cooling water flow (L/d)**	**U (kJ/h = m^2-°C)**	**UA (kJ/°C-h)**	**Heat Trasf. A (m^2)**
1000	12540	7.493	452	60.32
2000	25080	14.99	903.9	60.32
3000	37610	22.48	1356	60.32
4000	50150	29.97	1808	60.32
5000	**62690**	**37.46**	**2260**	**60.32**
6000	75230	44.96	2712	60.32
7000	87770	52.45	3164	60.32
8000	100300	59.94	3616	60.32
9000	112800	67.44	4068	60.32
10000	125400	74.93	4520	60.32

3.1 Statistical Analysis

These mathematical models aid in deciphering the data generated by the model (pilot) plant. This helps when examining process alternatives under various operating circumstances. When these model equations are compared, both are very credible for predicting the heat transfer rate (U) and heat transfer coefficient (UA).

According to Tables 2 and 3, the overall heat transfer coefficient and the heat transfer coefficient per unit area were both statistically significant at R R-squared value of 1.0 in the linear regression model's ANOVA due to a perfect linear change in the independent and dependent variables. This demonstrates how well the model fits the outcomes of the simulation. Therefore, it implies that this mathematical model could be used to describe the response's overall variance (Fadayini, *et al.,* 2018). The significance and statistical correlation between the independent variable and the response variable are demonstrated by the regression analysis results. The correlation coefficient, or R^2, measures how much of the variation in the cooling water flow rate and overall heat transfer coefficient is explained by its independent variable, the flow rate of the chemical compound methanol. As a result, for the number of independent variables in the model, the R^2 (adjusted) is the percentage of cooling water flow rate and overall heat transfer coefficient variation that is explained by its relationship with the flow rate of methanol. This modification is essential because the R^2 for this model rises whenever a new predictor is included. As a result, the adjusted R^2 is a useful tool for assessing how well models with various predictors explain the data. P-values of 0.000 for each coefficient were used to test the null hypothesis and show that there is no relationship between the coefficient and the outcome (Akintola *et al.,* 2020; Wildi-Tremblay & Gosselin, 2007), Minimizing shell and tube heat exchanger expense with genetic algorithms and considering maintenance.

Table 3: Analysis of Variance for U (kJ/h=m²-°C)

Source	DF	Adj SS	Adj MS	F-Value	P-Value
Regression	2	4631.80	2315.90	2.35796E+08	0.00
Methanol flow, L/d (A)	1	0.00	0.00	91.46	0.00
Cooling water flow, L/d (B)	1	0.00	0.00	0.55	0.483
Error	7	0.00	0.00		
Total	9	4631.80			
		Model Summary			
S	R-sq	R-sq (adj)	R-sq (pred)		
0.0031339	100.00%	100.00%	100.00%		
		Coefficients			
Term	Coef	SE Coef	T-Value	P-Value	VIF
Constant	0.00067	0.00215	0.31	0.765	6057801.22
A	0.008121	0.000849	9.56	0.000	6057801.22
B	-0.000050	0.000068	-0.74	0.483	

Table 4: Linear Regression Analysis: UA (kJ/°C-h) versus A, B

Source	DF	Adj SS	Adj MS	F-Value	P-Value
Regression	2	16855396	8427698	7.89506E+09	0.000
Methanol flow, L/d (A)	1	3	3	2627.09	0.000
Cooling water flow, L/d (B)	1	0	0	0.04	0.847
Error	7	0	0		
Total	9	16855396			
		Model Summary			
S	R-sq	R-sq (adj)	R-sq (pred)		
0.0326721	100.00%	100.00%	100.00%		
		Coefficients			
Term	Coef	SE Coef	T-Value	P-Value	VIF
Constant	-0.0330	0.0224	-1.47	0.185	
A	0.45378	0.00885	51.26	0.000	6057801.22
B	-0.000142	0.000706	-0.20	0.847	6057801.22

The Linear Regression Model, Non-Linear Regression Model, and Non-Linear Exponential Regression Model developed with the aid of an in-built solver tool in Minitab Software version 2017 are presented in equations (1) - (3) in that order for heat transfer rate and equations (4) - (6) respectively for heat transfer coefficient. The developed models were used to predict the experimental data. Table 2 reveals the experiment and the predicted data for each of the established models. Regression Equation

$$R_{1LRM} = 0.00067 + 0.008121A - 0.000050B \quad (1)$$

$$R_{1NLRM} = -0.00233 + 0.0383A - 0.00246B - 0.000009A^2 \quad (2)$$

$$R_{1NLERM} = e^{5.5003+0.07A-0.0058B-0.000012A^2} \quad (3)$$

$$R_{2LRM} = -0.0330 + 0.45378A - 0.000142B \quad (4)$$

$$R_{2NLRM} = -0.0927 + 0.673A - 0.0177B - 0.000010A^2 \quad (5)$$

$$R_{2NLERM} = e^{1.401+0.07A-0.006B-0.000013A^2} \quad (6)$$

3.1.1 Graphical Representation of the Statistical Model

A graphic illustration makes it simple to explain experimental results (Ekpotu, *et al.,* 2019; Amodu *et al.* 2019). These findings scrutinize how the heat transfer rate and overall heat transfer coefficient of a shell and tube heat exchanger are affected by the flow rates of cooling water and methanol. The practical implication demonstrates the independence of the independent variables on the response variables were analyzed statistically and this shows the viability of the independent variables in the performance of a shell and tube heat exchanger. Figures 2a and 2b show the surface plots for heat transfer rate and overall heat transfer coefficient, respectively. Figures 3a and 3b describe the contour plots for heat transfer rate and overall heat transfer coefficient, respectively. The results show that the heat transfer rate and overall heat transfer coefficient both depend on the flow rates of cooling water and methanol, as shown in Figures 2 and 3, respectively. These plots explain the strength of agreement between independent variables (methanol flow rate and cooling water flow rate) and response variables (heat transfer rate and overall heat transfer coefficient). As a result, in the absence of an experimental model, predictions of the both heat transfer rate and overall heat transfer coefficient could be tested on the plots at typical streams (methanol and cooling water) flow rates.

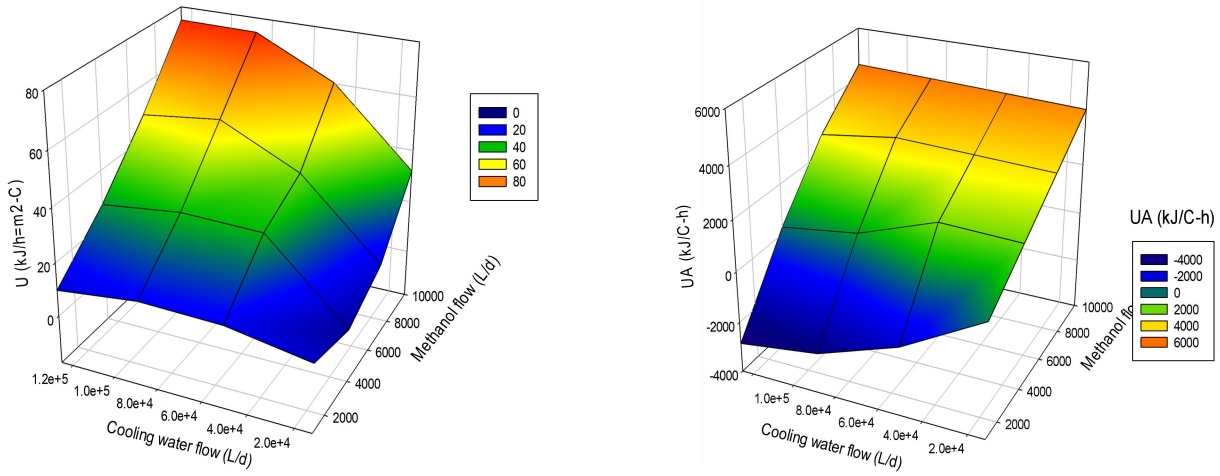

(a) (b)

Figure 2: Surface plot for 'U, kJ/h=m^2-°C (A)' and 'UA, kJ/°C-h (B)' versus Methanol flow rate and Cooling water flow rate

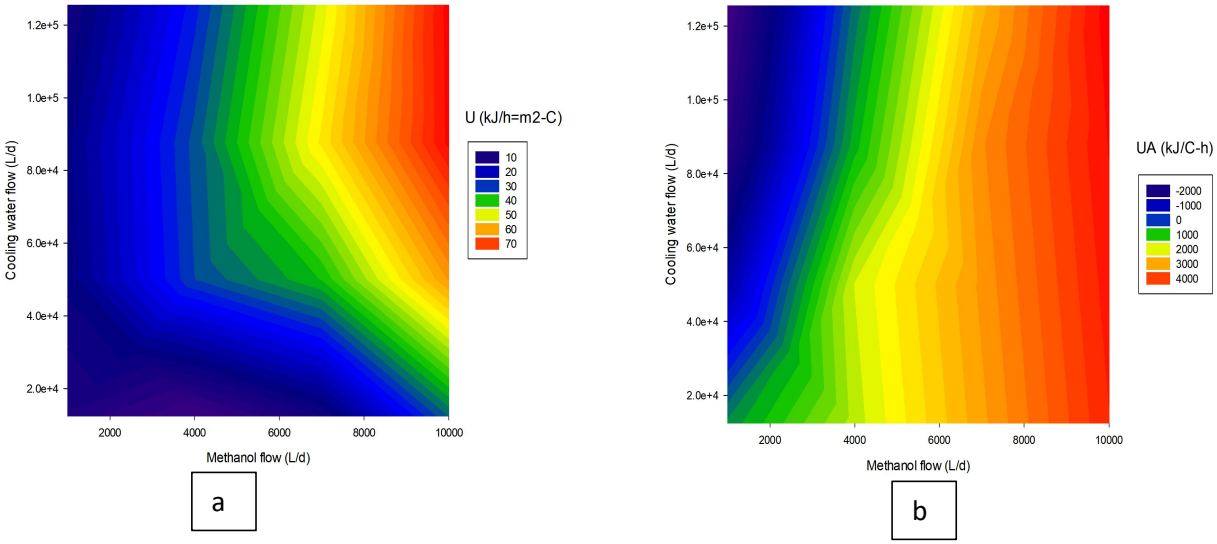

Figure 3: Contour plot for 'U, kJ/h=m^2-°C (A)' and 'UA, kJ/°C-h (B)' versus Methanol flow rate and Cooling water flow rate

3.2 Multiphase Flow Analysis

The Computation Fluid Dynamics Software, COMSOL 5.3, is used to simulate the fluid systems' multiphase phase flow. To replicate or foresee a real-time process, simulation is used. Typical flow parameters would be produced by a typical heat exchange process using a counter-current process.

Figure 4 shows the contour plots of the heat exchanger's interior and the water flow system. At the inlet and outlet points, which are far from the tube wall, higher water flow system velocities are seen. However, a high-velocity profile for water flow is seen inside the heat exchanger; the maximum velocity is seen there between 0.1 m and 0.95 m in length, indicating the ideal length of the shell and heat exchanger for the highest velocity flow. A roughly equal fluid velocity flow is seen at the inlet and exit, and these points of maximum velocity profile also point to a decrease in velocity profile as the water flow crosses the heat exchanger.

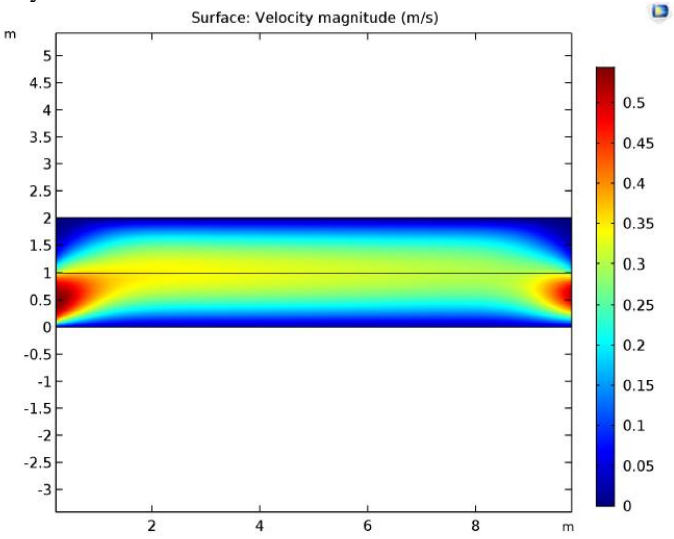

Figure 4: Scatter surface for velocity magnitude water flow system

Figure 5 provides the water flow system's contour plot. At 1 mm from the entrance, the profile of water-hydrogen and water pressure becomes uniform. However, 17.8 Pa is the maximum pressure flow for water fluids.

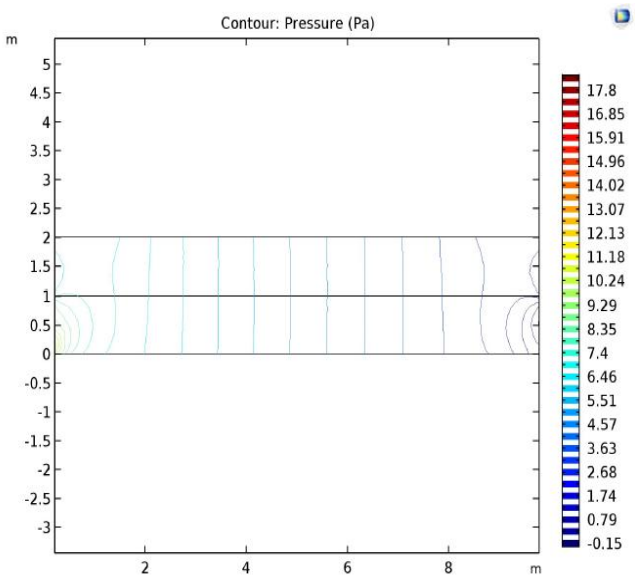

Figure 5: Scatter surface for pressure water flow system

From the simulated profile of the velocity, pressure, shear stress, etc. across the arc length, line graphs are created.

Figure 6 shows a line graph that plots the magnitude of velocity versus the length of the arc in a water flow system. From 0 to 0.125 m (arc length), the velocity rises sharply; however, from 0.125 to 4 m, the velocity decreases sharply.

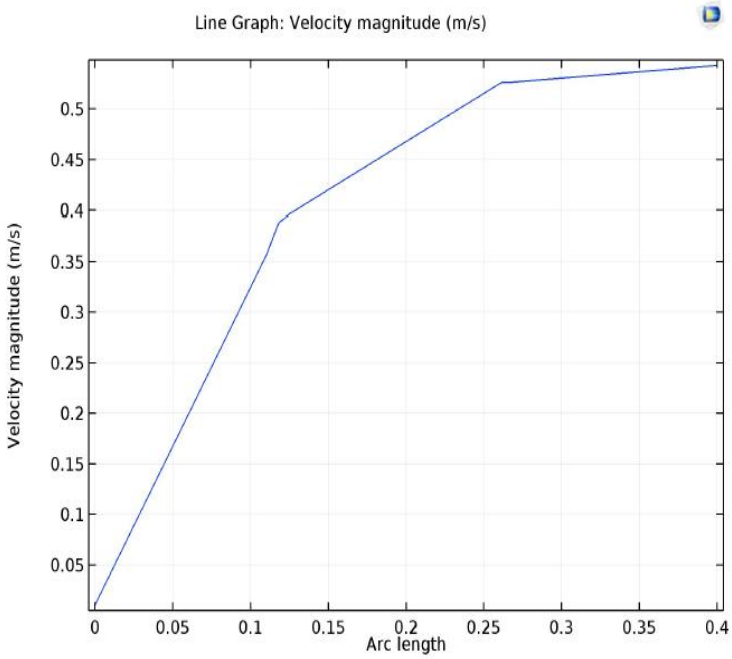

Figure 6: Velocity magnitude versus Arc length for Water flow

Assessing the line plots for this process, Figure 7 reveals a drastic decrease in the pressure, 0 to 0.4, the exit of the shell and tube heat exchange system.

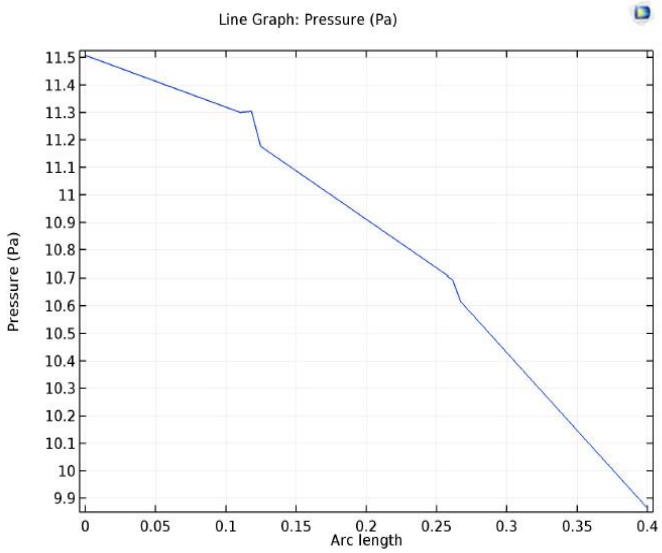

Figure 7: Pressure versus Arc Length for Water Flow System

Figure 8 depicts the shear stress for a water flow system. The gradient in velocity is described by the shear rate. It describes the variations in fluid-containing surface velocities, multiplied by their separation. The plot shows an abrupt increase from 0 to 0.12 Pa, followed by a constant shear rate at this point, a subsequent decrease to 0.265, and then an increase to 0.27, with the share rate (0.3 s-1) at this point to exit. The shear rate of water is seen to haphazardly decline, falling from 3.9 to 0.3 s^{-1}.

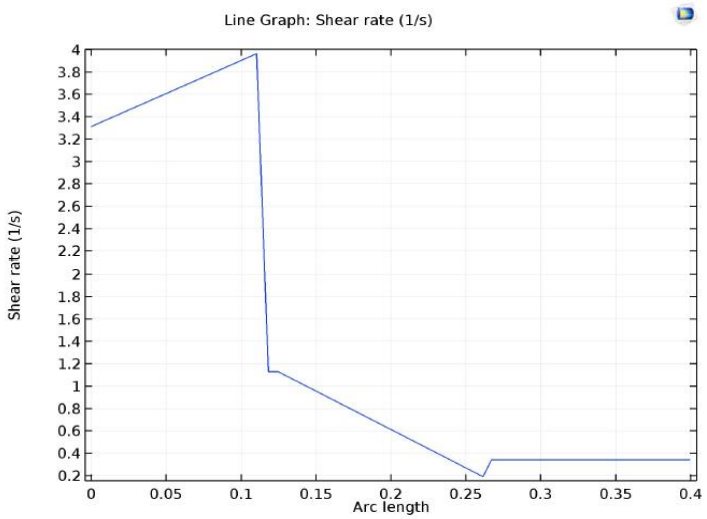

Figure 8: Shear rate versus Arc Length for Water flow System

4.0 DESIGN ALGORITHM

The design research presents, the developed algorithm which describes the pathway to model the process, performance evaluation, and predicted estimation, following the process route is presented as an algorithm in Figure 9, While, Figure 10 shows a flow chart for estimating shell and tube film transfer coefficient. Figure 9 is the algorithm for the Heat Exchanger. Matlab 2018a code for solving the algorithm is presented. At the input of the parameters as stated in the script (code), the compiler compiles and solves the inputs. The input and final output parameters are represented with a parallelogram. However, each step is symbolically represented with a rectangular box. The algorithm calculates the mass flow rate of the cooling water for cooling the methanol fed into the shell and tube heat exchanger, as well as the overall heat transfer coefficient of the shell and tube heat exchanger. The Matlab codes

are available for global computation of the cooling water mass flow rate and overall heat transfer coefficient of the shell and tube heat exchanger. The input parameters as stated are the mass flow rate of the methanol, specific

heat capacity of methanol, specific heat capacity of water, initial and final temperatures of methanol, initial and final temperatures of water, correction factor, heat transfer coefficient of methanol, internal and external diameter of the tube, length of the tube, film transfer coefficient for the shell and tube sides, outside dirt coefficient (fouling factor), thermal conductivity of the tube wall material. The calculated or output parameters are heat load, log-mean temperature difference, heat transfer area, area of transfer units, number of tubes, and overall heat transfer coefficients. Hence, with the available input parameters stated above, the output parameters that indicate the performance of the shell and tube heat exchanger could be predicted.

This program calculates the overall heat transfer coefficient of a shell and tube heat exchanger.

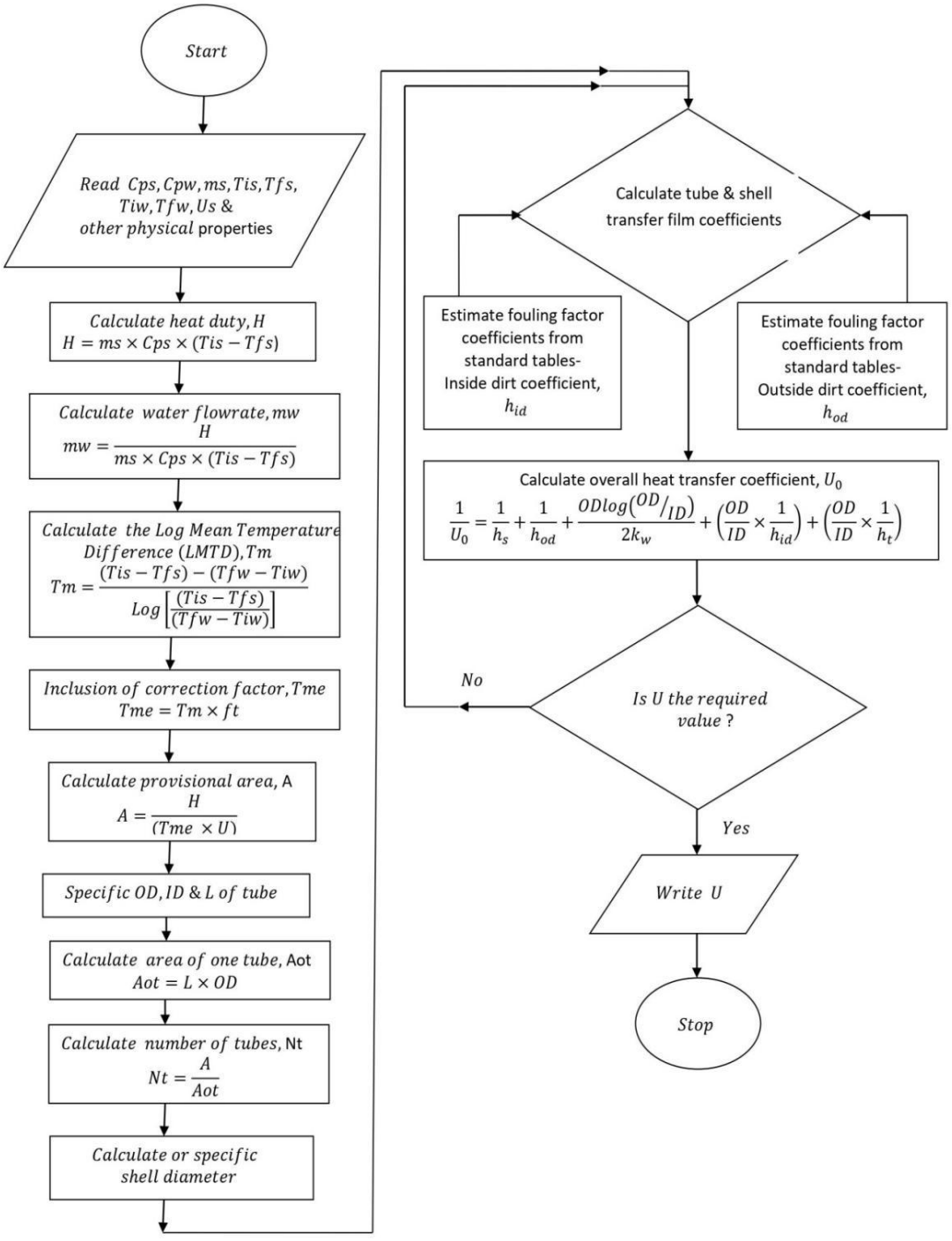

Figure 9: Algorithm for the Heat Exchanger

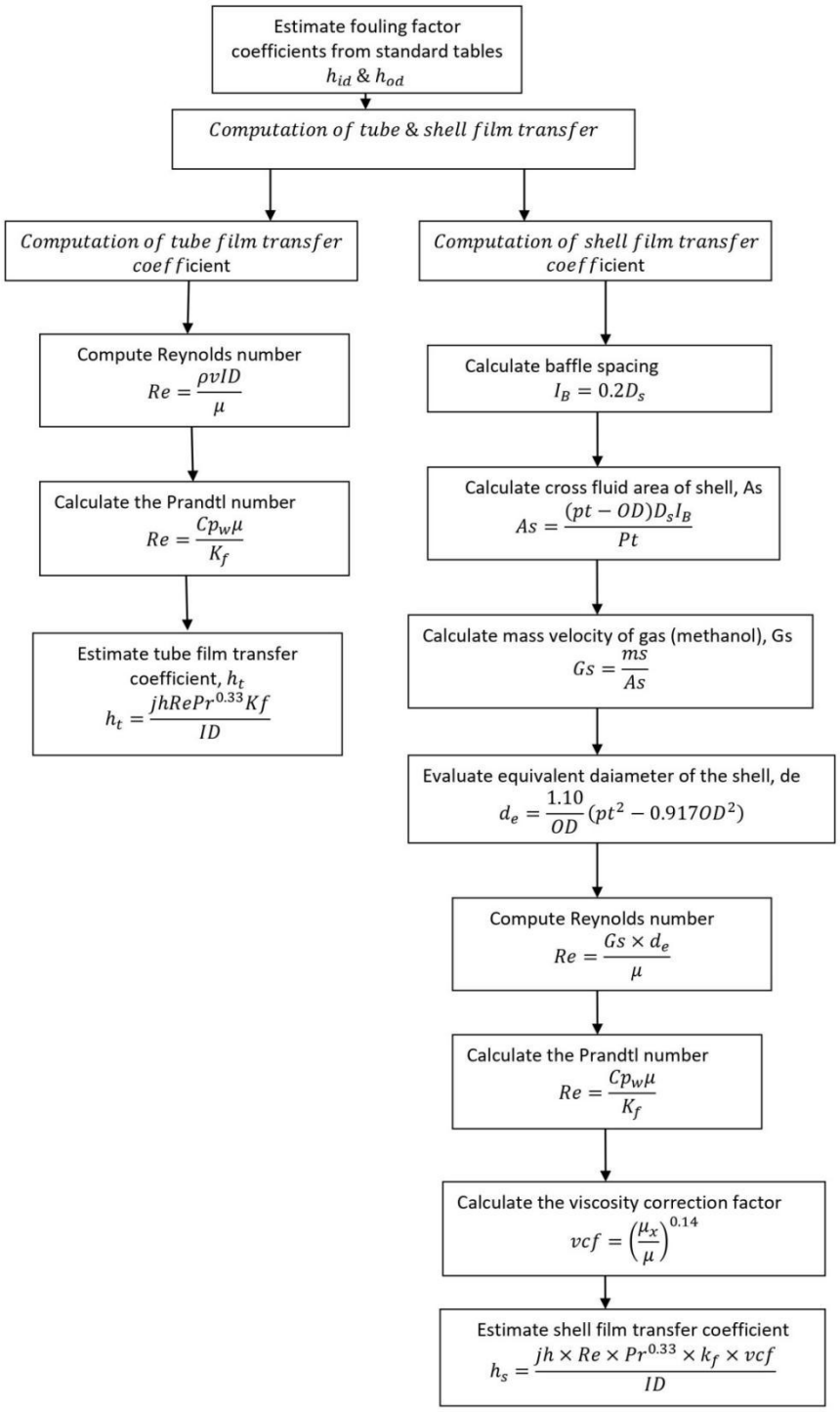

Figure 10: Flow chart for estimating shell and tube film transfer coefficient.

5.0 CONCLUSION

This research exercise has investigated the simulation, modelling, and multiphase flow analysis of the prediction and performance evaluation of a shell and tube heat exchanger for cooling and energy conservation of hot stream methanol, with cooling water. Within the limit of this research study, it can be concluded that the process simulation could be done before a pilot setup of process equipment to replicate a real-time process. Statistical analysis reveals that the correlation coefficient (R^2) values of 100.00 % for both the heat transfer coefficient and overall heat transfer coefficient

reveal the fitness of the model to the simulation results. The performance parameters of a shell and tube heat exchanger can be evaluated via process simulation. Performing computation fluid dynamics of the water-methanol system reveals that higher velocity magnitudes of the water flow system are observed at the inlet and outlet points and are far away from the tube wall, and the profile of methanol and water pressure becomes uniform at a distance of 1 mm from the entrance. Hence, the maximum pressure flow for water fluids pressure is 17.8 Pa. The shear stress analysis for the water-methanol system reveals a sharp increase from 0 – 0.12 pa, then a constant shear rate at this point, before a further decrease to 0.265 and then an increase to 0.27. However, it may be difficult to show complex processes that require multiple attributes in a simple flowchart, so a cross-functional flowchart would be a solution for that situation. Designing the process algorithm will contribute to understanding where the problem is in the process. However, the heat exchangers system can be extended to the scrutiny and conditions where the state variables describing the system are ultimately bounded under some other conditions rather than temperature changes and quantities of heat.

THE MATLAB CODE

```
% MATLAB Code for Estimating the Overall Transfer Coefficient
% Initial Values of physical properties of water and methanol
ms=1000/86400; % mass flowrate of the methanol,ms in L/d change to kg/s.
cpw=4.2; % Specific heat capacity of water, in KJ/KgoC
cps=2.84; % Specific heat capacity of methanol,cps in KJ/Kg0C
pw=995; % density of water
pm= 750; % density of methanol
kf=0.59; % fluid thermal conductivity of water in W/moC
km=0.19; % Fluid thermal conductivity of methanol in W/moC
Tis=120; % Initial temperature of methanol in Celcius, Tis.
Tfs=30; % Final temperature of methanol in Celcius, Tfs.
Tiw=25; % Initial temperature of water in Celcius, Tiw.
Tfw=30; % Final temperature of water in Celcius, Tfw.
ft=0.85; % correction factor, ft.
x=0.0008; % Viscosity of water in Ns/m^2
xm=0.0034; %Viscosity of methanol in Ns/m^2
U=600; % heat transfer coefficient of methanol, U in W/m^2_oC
ID=14*0.001; % Internal Diameter of the tube in metres
OD=19*0.001; % External Diameter of the tube in metres
L=4.83; % Length of the tube, L in m.
kw=50; % thermal conductivity of the tube wall material(cupro-nickel alloys),kw.
pr=(cpw*x)/kf; % Prandtl number
jf=0.0039; %Friction factor for pipes for 25% baffle cut
H=ms*cps*(Tis-Tfs); % Calculate heat load, H in kW.
mw=H/(cpw*(Tfw-Tiw)); % Calculate mass flow rate of water,mw.
Tm=((Tis-Tfs)-(Tfw-Tiw))/log((Tis-Tfs)/(Tfw-Tiw)); % calculate Log Mean Temperature Difference,Tm.
Tme=Tm*ft; % Inclusion of Correction Factor, Tme.
A=(H*1000)/(Tme*U); % Calculate the area or provisional area, A in m^2.
Aot=L*OD*3.142; % Calculate the area of one tube, Aot.
Nt=A/Aot; % Calculate the number of tubes, Nt.
hod=6000; % outside dirt coefficient(fouling factor),W/m2oC
hid=3000; % Inside dirt coefficient, W/m^2oC
% Film transfer coefficient for the tube side, ht.
Db= OD*((Nt/0.249)^(1/2.207)); % Bundle diameter for 1.25 triangular pitch in m
mwt=(Tfw+Tiw)/2; %Mean water temperature
tca=(3.142/4)*ID^2; % Tube cross-sectional area in metres
TPP=Nt/2; % Tubes per pass
TFA=TPP*tca; % Total flow area
WMV= mw/TFA; % Water mass velocity in kg/sm^2
```

```
v=WMV/pw; %Water linear velocity
Re=(pw*v*ID)/x; % Reynolds number
% Estimating film transfer coefficient for the shell and tube side, hsm
Ds= 0.894; % shell inside diameter in m
pt=25; % tube pitch
Ib=0.2*Ds; % Baffle spacing
As=(pt-OD)*Ds*Ib/pt; % Shell cross flow area in m^2
Gs=ms/As; % Mass gas velocity of methanol
de=1.10*(pt^2-0.917*OD^2)/OD; % equivalent diameter in mm
Rem=Gs*de/xm; % Reynolds number of methanol
prm=(cps*xm)/km; % Prandtl number of methanol
vcf=0.99; % viscosity correction factor
hs=jf*Rem*prm^0.33*vcf/OD; % Film transfer coefficient for the shell side, hs.
ht=(jf*Re*pr^0.33*kf)/ID; % Film transfer coefficient for the tube side, ht.
Uoverall=((1/hs)+(1/hod)+((OD*log(OD/ID))/(2*kw))+((OD/ID)*(1/hid))+((OD/ID)*(1/ht)))^-1;
if 500<Uoverall&&Uoverall<600
disp ('overall heat transfer coefficient of the heat exchanger is the required value:');
disp (overall);
else
disp ('overall heat transfer coefficient of the heat exchanger is not the required value:');
disp(Uoverall);
end.
```

AUTHOR CONTRIBUTION STATEMENT

All authors listed have significantly contributed to the development and the writing of this article.

DATA AVAILABILITY STATEMENT

The data used to support the findings of this study are available from the corresponding author upon request at olufeday@gmail.com

DECLARATION OF INTEREST'S STATEMENT

The authors declare no conflict of interest.

REFERENCES

Abd AA, Kareem MQ, Naji SZ (2018) Performance analysis of shell and tube heat exchanger: Parametric study. Case Studies in Thermal Engineering, 12, Pages 563-568.

Akintola, J. T., Ayoola, A. I., Abdulkareem, Y. T., Akintola, O. E., & Etisioro, C. O. (2020). Simulation and Modeling of an Integrated Process Route for the Synthesis of Vinyl Chloride Monomer from Acetylene: Factorial Design Method and Artificial Neural Network. International Journal of Advances in Scientific Research and Engineering (ijasre), Vol 6 (12), 83-93.

Alimoradi A, Veysi F (2017) Optimal and critical values of geometrical parameters of shell and helically coiled tube heat exchangers. Case Stud. Therm. Eng., 73–78.

Amodu, O. S., Ntwampe, S. K., & Ojumu, T. V. (2014). Optimization of biosurfactant production by Bacillus licheniformis STK 01 grown exclusively on Beta vulgaris waste using response surface methodology. BioResources, 9(3), 5045-5065.

Amodu, O. S., Odunlami, M. O., Akintola, J. T., & Ntwampe, S. K. (2019). Exploring Musa Paradisiaca Peel Extract as a Green Corrosion Inhibitor for Mild Steel Using the Factorial Design Method. United Kingdom: IntechOpen.

Ani, J. U., Aneke, L. E., & Oyoh, K. B. (2010). Design and Operatio of a Multitube One Shell Pass One TubePass Heat Exchanger. Journal of the Nigerian Society of Chemical Engineers, 151-157.

Asadi, M., Song, Y., Sunden, B., & Xie, G. (2014). "Economic optimization design of shell-and-tube heat exchangers by a cuckoo-search-algorithm," Appl Therm Eng, vol. 73, 1032-1040.

Atmakidis, T., & Kenig, E. Y. (2009). CFD-based analysis of the wall effect on the pressure drop in packed beds with moderate tube/particle diameter

ratios in the laminar flow regime. Chem. Eng Journal, Vol.155, 404-410.

Caputo, A. C., Pelagagge, P. M., & Salini, P. (2009). "Heat exchanger design based on economic optimization."Appl Therm Eng, vol. 28, 1151-1159.

Caputo, A. C., Pelagagge, P. M., & Salin, P. (2015). "Heat exchanger optimized design compared with installed industrial solutions". Appl Therm Eng, vol. 87, 371-380.

Chase, G. G., & Dachavijit, P. (2005). A correlation for yield stress fluid flow through packed beds. Rheol Acta, Vol. 44, 495-501.

Dizaji HS, Jafarmadar S, Asaadi S (2017) Experimental exergy analysis for shell and tube heat exchanger made of corrugated shell and corrugated tube. Exp. Therm. Fluid Sci., 475–481.

Ekpotu, W. F., Ighalo, J. O., Nkundu, K. B., Onu, P. O., & Adeniyi, A. G. (2020). Analysis of factor effects and interactions in a conventional drilling operation by response surface methodology and historical data design. Petroleum and Coal. 62(4), 1356-1368.

Ekpotu, W., Akintola, J., Obialor, M., Ayoola, A., Asama, M., & Abdulkareem, Y. (2021). Least squares modelling of the depth of cut of reservoir rock from real-time drilling parameters. Petroleum Science and Technology, 1-19.

Ergun, S. (1952). Fluid flow through packed columns. Chem Eng Prog. Vol. 48, 89-94.

Fadayini, O., Madu, C., Oso, A. O., Ugba, E., Ajayi, S. J., & Akintola, J. T. (2018). Simulation and Synthesis of Toluene by Dehydrogenation of N-heptane. Journal of Industrial Research & Technology (JIRT), Federal Institute of Industrial Research, 110-120.

Fesanghary, M., Damangir, E., & Soleimani, I. (2009). "Design optimization of shell and tube heat exchangers using global sensitivity analysis and harmony search algorithm," Appl Therm Eng, vol 29, 1026-1031.

Gao B, Bi Q, Nie Z, Wu (2015) Experimental study of effects of baffle helix angle on the shell-side performance of shell-and-tube heat exchangers with discontinuous helical baffles. Exp. Therm. Fluid Sci., 48–57.

Hadidi, A., & Nazari, A. (2013). "Design and economic optimization of shell-and-tube heat exchangers using biogeography-based (BBO) algorithm," Appl Therm Eng, vol. 51, 1263-1272.

Hadidi, A., Hadidi, M., & Nazari, A. (2013). "A new design approach for shell-and-tube heat exchangers using the imperialist competitive algorithm from an economic point of view. Enter Conver Manag, vol. 67, 66-74.

Jamal-Eddine S, Tarik Z, Ahmed A. M, Merzouki S, Najim S. (2022). Numerical Investigations of the Impact of a Novel Turbulator Configuration on the Performances Enhancement of Heat Exchangers, Journal of Energy Storage, vol. 46, 1038. https://doi.org/10.1016/j.est.2021.103813

Kern, D. Q. (1950). "Process heat transfer," New York: McGraw-Hill.

Kunjuraman S, Velusamy B (2021) Performance evaluation of shell and tube heat exchanger through ANN and ANFIS model for dye recovery from textile effluents. Energy Sources, Part A: Recovery, Utilization, and Environmental Effects, 43(13):1600-1619.

Kuye, A., & Edeh, I. (2011). Educational Software for Shell and Tube Heat Exchanger Design. Journal of the Nigerian Society of Chemical Engineers, 26-35, Vol. 26 (2).

Lona, L. M., Fernandes, F. A., Roque, M. C., & Rodrigues, S. (2000). Developing an Educational Software for Heat Exchangers and Heat Exchanger Networks Projects. Computer and Chemical Engineering by Elsevier Science Ltd, vol. 24, (2-7), 1247-1251.

Marzouk S.A, Abou Al-Sood M.M, El-Said E.M.S, Younes M.M, El-Fakharany M.K (2023). A comprehensive review of methods of heat transfer enhancement in shell and tube exchangers. J Therm Anal Calorim 148, 7539–7578.

Masoumpour B, Ataeizadeh M, Hajabdollahi H, Dehaj MS (2021) Performance evaluation of a shell and tube heat exchanger with the recovery of mass flow rate. Journal of the Taiwan Institute of Chemical Engineers, 000, 1-13.

Mehrjardi SAA, Khademi A, Said Z, Ushak S, Chamkha AJ (2023) Effect of elliptical dimples on heat transfer performance in a shell and tube heat exchanger. Heat Mass Transfer. https://doi.org/10.1007/s00231-023-03367-7

Ozcelik, Y. (2007). "Exergetic optimization of shell and tube heat exchanger using a genetic-based algorithm". Appl Therm Eng, vol. 27, 1849-1856.

Pope, K., Naterer, G. F., & Wang, Z. (2011). Pressure drop of packed bed vertical flow for multiphase hydrogen production. International Journal of Hydrogen Energy, Vol. 36, 11338-11344.

Radojkovic, N., Llic, G., Stevanovic, Z., Vukic, M., Mitrovic, D., & Vuckovic, G. (2003). Experimental Study on Thermal and Flow Processes in Shell and Tube Heat Exchanger Series: Mechanical Engineering. pp. 1377-1284.

Raja, B. D., & Jhala, R. L. (2016). Optimization of Shell and Tube Heat Exchangers using Teaching-Learning based Optimization Algorithm. International Journal of Engineering Research & Technology (IJERT), Volume 4, Issue 10, 1-5.

Rao, R. V., & Patel, V. K. (2010). "Design optimization of shell and tube heat exchangers using particle swarm optimization, M algorithms."Appl Therm Eng, vol 30, 1417-1425.

Selbas, R., Kizilkan, O., & Reppich, M. (2006). "A new design approach for shell-and-tube heat exchanger using the genetic algorithm from an economic point of view," Chem Eng Process, vol. 45, 268-275.

Seralathan S, Vijay R, Aravind S, Sivakumar S, Devaraj G, Hariram V, Raghavan P.S, Premkumar T.M (2021). Nanofluids in Improving Heat Transfer Characteristics of Shell and Tube Heat Exchanger. In: Akinlabi, E., Ramkumar, P., Selvaraj, M. (eds) Trends in Mechanical and Biomedical Design. Lecture Notes in Mechanical Engineering. Springer, Singapore.

Shafiq M.B, Allauddin U, Qaisrani M.A, Rehman T.U, Ahmed N, Mushtaq M.U, Ali H.M (2022) Thermal Performance Enhancement of Shell and Helical Coil Heat Exchanger using Mwcnts/Water Nanofluid. J Therm Anal Calorim 147, 12111–12126. https://doi.org/10.1007/s10973-022-11405-5

Sharifat F, Marchitto A, Solari M.S, Toghrale D (2022) Analysis, Prediction, and Optimization of Heat Transfer Coefficient and Friction Factor Of Water-Al_2O_3 Nanofluid Flow in Shell and-Tube Heat Exchanger with Helical Baffles (Using RSM). Eur. Phys. J. Plus, 137, 991.

Tallmadge, J. A. (1970). Packed bed pressure drops an extension to higher Reynolds numbers. AIChE J, Vol. 16, 1092-1093.

Tema. (1999). Standards of the Tubular Heat Exchanger Manufacturers Association. New York: Tubular Heat Exchanger Manufactures Association.

Thirumarimurugan, M., Kannadasan, T., & Ramasamy, E. (2008). Performance Analysis of Shell and Tube Heat Exchanger using Miscible System. American Journal of Applied Sciences, 548-552, Vol. 5(5).

Trupti, A., Tyagee, C., Manali, K., & Walke, S. M. (2012). Simulation of Process Equipment by using HYSYS. International Journal of Engineering Research and Applications (IJERA), 41-44.

Wildi-Tremblay, P., & Gosselin, L. (2007). "Minimizingshell and tube heat exchanger cost with genetic algorithms and considering maintenance," Int J Energy Res, vol. 31, 867-885.

10.51975/24390206.som
Journal of the Nigerian Society of Chemical Engineers, 39(2), 2024

CHARACTERIZATION OF PALM OIL MILL SLUDGE, PALM OIL MILL EFFLUENT AND RICE HUSK FOR BIOGAS PRODUCTION

Ubani O. AMUNE*[1], Amos O. ISHAKU[1], Jane-Francess O. ILUOKHAUNO, Wilfred O. IKHALUMHE[2], Justus T. OMOYAKHI[3], Kevin S. OTOIKHIAN[1]

[1]Department of Chemical Engineering, Edo State University Uzairue, Edo State, Nigeria
[2]Department of Mechanical Engineering, Edo State University Uzairue, Edo State, Nigeria
[3]Production Department, BUA Cement PLC, Obu-Okpella, Edo State, Nigeria.
***Corresponding Author(s): ****ubani.amune@edouniversity.edu.ng|+2348137147909*
amos18.ishaku@edouniversity.edu.ng|+2348024943595

ABSTRACT

In this study, rice husk (RH), palm oil mill sludge (POMS), and palm oil mill effluent (POME) were characterized for biogas production and then co-digested using cow dung at mesophilic temperatures. RH and POMS were sun-dried, ground, and sieved as mechanical pretreatment methods for digestible particles. The characterization of the POME showed an acidic pH, with BOD, COD, TSS, and TDS values of 57.0mg/l, 84.0mg/l, 19.7mg/l, and 8200mg/l, respectively. RH had a pH of 5.30, C/N, TS, VS, MC, and ash content of 28.64, 90.56%, 72.78%, 9.45%, and 17.78%, respectively. The Lignin, Cellulose, and hemicellulose contents are 16.47%, 55.53%, and 27.54%. POMS also had a pH of 5.95 with C/N, MC, and ash content of 64.1, 5.07%, and 4.73% and Lignin, Cellulose, and hemicellulose contents of 44.88%, 24.67% and 30.46% respectively. Preliminary co-digestion of the samples at room temperature (27.8°C) revealed cumulative biogas production potentials, i.e., 280 ml and 170 ml from POME+RH and POME+POMS respectively, proving the potency of POME, RH, and CD as potential candidates for biogas production.

Keywords: Lignocellulosic materials, POME, Rice husk, Palm oil mill sludge, co-digestion

1.0 INTRODUCTION

The heavy reliance on fossil fuels as the primary energy source has led to critical energy crises and environmental challenges, including greenhouse gas emissions and fossil fuel depletion. This has prompted a global pursuit of greener, more sustainable, and renewable energy production methods to mitigate the far-reaching impacts of fossil fuels (Sokowocin, 2020). Numerous countries are investing in research and development of alternative fuels to address these concerns.

Biogas, a combustible gas mixture resulting from the anaerobic digestion or decomposition of organic waste materials like plant-based (lignocellulosic) and animal-based materials, emerges as a promising alternative to fossil fuels (Hai et al., 2023). Unlike other renewable energy sources such as wind and solar, biogas production is natural and does not require additional energy input. Lignocellulosic materials (LMs) have recently gained attention as a sustainable alternative for waste management and energy production (Nwaneri, 2022; Sittijunda et al., 2022).

Anaerobic digestion of LMs stands out as a sustainable approach for biogas production. This economically feasible, environmentally friendly method employs renewable raw materials such as animal manure, food crops, industrial waste effluents, and crop residues that generate large amounts of methane-rich biogas while aiding waste management by reducing landfill waste (Karki et al., 2021). Anaerobic digestion can occur under different conditions, including dry anaerobic digestion (DAD) and wet anaerobic digestion (WAD), with temperature ranges of psychrophilic (– 1°C to 10°C), mesophilic (11°C to 45°C) and thermophilic (46°C to 75°C) (Okolie et al., 2022). While mesophilic and thermophilic temperatures are usually employed, mesophilic systems are favoured for business applications due to their stability against temperature fluctuations and lower operating costs (Ishmael et al., 2017; Olugbemide et al., 2022). Other factors like pH, substrate type, temperature, loading rate, carbon-nitrogen ratio (C/N), particle size, and dilution ratio affect these stages (Enaboifo, 2020).

Lignocellulose biomass, such as Rice Husk (RH), Palm Oil Mill Sludge (POMS), Palm Oil Mill Effluent (POME), sugarcane bagasse (SCB), and empty fruit bunches (EFB) contains biomass in the form of lignocelluloses, which have the potential to generate energy (Hai et al., 2023) has a high energy content and can help alleviate the looming energy crisis. It is an organic material derived from biological sources, specifically plant biomass, which is the most abundant global source of renewable materials, with an estimated annual global production of 1010 MT (Ajala et al., 2021; Schmatz et al., 2020).

Olugbemide et al. (2016) used a rice husk sample (RH218) to produce 885 ml of biogas on the first day of monodigestion. Also, according to Ahmed et al. (2015), $1m^3$ of POME produces approximately $28m^3$ of biogas in the treatment facility under mesophilic (30–40 °C) conditions. Chan et al. (2021) revealed that co-digestion of POME and EFB at an optimal ratio of (1:0.6) yielded 2.36 times the methane produced from POME mono-digestion. Biogas can also be produced from the co-digestion of palm oil mill effluent (POME). Several other researchers have co-digested POME and Kitchen waste (Hai et al., 2023), POME and Decanter Cake (DC) (Lim et al., 2021), POME and EFB (Suksong et al., 2020); however, little or no work has explored the digestion of POMS or the co-digestion of POMS, RH, and POME for biogas production. Therefore, this research is centred on characterizing Palm Oil Mill Effluent (POME), Rice Husk (RH) and Palm Oil Mill Sludge (POMS) to evaluate their biogas production potentials via co-digestion critically.

2.0 MATERIALS AND METHODS

2.1 Materials collection and storage

The materials used in this work are Palm Oil Mill Effluent (POME), Palm Oil Mill Sludge (POMS), Rice husk (RH), and cow dung (CD). POME and POMS were obtained from Leventis farm, Weppa, Agenebode, Edo State, while RH was obtained from David Akinola Olugbemide Biogas laboratory, Auchi, Edo State. The CD was gotten from cattle rearers at Auchi, Edo state. The POME was stored in a gallon and kept in a temperature-controlled laboratory (15–20°C) to reduce microbial activities.

2.2 Methods

2.2.1 Material Pretretament

POMS was mechanically pretreated by drying under sunlight, grinding, and sieving to ensure homogeneous particles and increase biomass biodegradation accessibility (Bruni et al., 2010). POME was filtered to remove large or unwanted solid particles like shells, EFB particles, stone, and lumps of sand. Rice husk was also sieved using the same mesh size (0.710mm)

2.2.2 Substrates Characterization

The physicochemical characterization of POME was carried out to determine pH, Total Suspended Solids (TSS), BOD, COD, Total Dissolved Solids (TDS), Bicarbonates, etc. were determined using the APHA (2017) revised methods. These results are summarized in Table 1.0

Rice husk (RH) and POMS were characterized for their lignocellulose content, moisture, total organic content (TOC), and carbon-nitrogen (C/N) ratio, amongst others, using methods described by Darmawan et al., 2016 and Toribio-Cuaya et al., 2014. The results are summarized in Table 2.0.

2.2.3 Biogas experimental set-up and production

The preliminary anaerobic co-digestion of the samples took place at an atmospheric temperature of 28.7°C and a digestion time of 21 days. The co-digestion employed a batch water displacement method to measure biogas production according to the procedure by Chan et al. (2021). Four (4) samples, namely POME+POMS (6.5:1), POME+RH (6.5:1), POME+POMS+CD (13:1:1), and POME+RH+CD (13:1:1) were set-up, each with a total co-substrate volume of 300ml. A manual air suction pump was used to extract air from the collection cylinders, and those escaped into the bioreactor. Biogas gas was collected over a salt solution to prevent CO_2 dissolution with daily readings over the co-digestion period.

3.0 RESULTS AND DISCUSSION

3.1 POME Characterization

Table 1 shows the physicochemical results of the palm oil mill sludge (POME) obtained after pretreatment and storage prior to co-digestion.

Table 1: Physicochemical Characteristics of POME

Parameters	Units	Value	Method	NESREA, 2011 & WHO, 1993
pH		4.2		6.5 – 8.5
Chemical Oxygen Demand COD	mg/L	84.0	APHA 5220C	≤ 10.0
Biochemical Oxygen Demand BOD	mg/L	57.12	APHA 5210C	3.0
Total Suspended Solid (TSS)	mg/L	19.7	APHA 2540D	0.25 – 5.0
Total Dissolved Solid (TDS)	mg/L	8200	APHA 2540C	0.3 – 0.5
Turbidity (Turb.)	NTU	10.0	APHA 2310B	≤ 10.0
Salinity (Sal)	mg/L	7.454	APHA 2520C	-
Colour	Pt.Co	11.2	APHA 2120C	≤ 10.0
Bicarbonate (HCO_3)	mg/L	1159	APHA 4500	-

The physicochemical characteristics of palm oil mill effluent (POME) revealed an acidic pH of 4.2 and a total dissolved solids (TDS) of 8200 mg/L. This acidic nature of POME, as also seen from previous literature (Fikri Hamzah et al., 2020; Trisakti et al., 2015), can be attributed to the substrate's volatile fatty acids (VFAs). The optimal pH range for anaerobic co-digestion has been recommended as 6.5–7.5 (Singkhala et al., 2021; Trisakti et al., 2015) to support microbial activities; hence lower values would require the addition of cheap alkaline-based materials to counter-balance as explored by Kalansuriya et al., (2016) and Singkhala et al., (2021) or recycling the treated substrates (Yap et al., 2020). Satyavolu & Lupitskyy (2021) argued that the pH should not add cost to the plant; however, in a study by Pfeiffer et al. (2020), it was discovered that the cost of adjusting pH by adding Na_2CO_3 was approximately 22% of the cost of the chemical used in the anaerobic digestion, thereby adding to the cost of the plant. Hence, adjusting the pH of the substrate using alkaline materials might not be cost-effective on an industrial scale (Lim et al., 2021b). Alternatively, the presence of bicarbonates in the POME increased and stabilized the substrate's pH (Rohma et al., 2021). POME's colour, measured as 11.2 Pt.Co on the Pt/Co scale holds significance as it influences light penetration and the growth of microorganisms in anaerobic digestion (Kamaruddin et al., 2018; Nur et al., 2021). Although no established colour standard exists for POME, some researchers have aimed to minimize colour due to potential negative effects on biogas production. The total suspended solid (TSS) content was 19.7 mg/L, considerably lower than values reported in other studies. This indicates variations due to factors such as palm fruit quality and processing techniques (Trisakti et al., 2015). While the pH and TSS values differ from previous research, the biodegradability of POME is supported by a suitable BOD/COD ratio (0.68), making it conducive for biological treatment. According to Yap et al. (2020), the BOD/COD ratio indicates the biodegradability of the wastewater, and it should exceed the ratio of 0.5 to suit biological treatment. The BOD/COD ratio of the POME obtained is greater (0.68) than the mentioned threshold; hence, the POME used in this study fits this anaerobic digestion treatment method.

3.2 Lignocellulose Characterization

The Lignocellulosic characterization values are presented in Table 2. The moisture content for RH and POMS recorded as 5.95 and 9.45, respectively, are by nature, far lower than other biomass (banana – 84.3% and cassava – 85.3%) explored for biogas production (Ore et al., 2023) but closer to other rice husk results from other regions (Uganda – 9.2 to 11.2%).

Table 2: Characteristics of POMS and RH

Parameters	POMS	RH (Olugbemide et al., 2022)
pH	5.95	5.30
Moisture content (MC) (%)	5.07	9.45
Ash Content (%)	4.73	17.78
Total Organic Content (TOC) (%)	4.70	–
Total Nitrogen (TN) (%)	0.81	1.60
Carbon Nitrogen Ratio (C/N)	64:1	28.64
Total Solid (TS) (%)	97.34	90.56

Parameters	POMS	RH (Olugbemide et al., 2022)
Volatile Solid (VS) (%)	94.51	72.78
VS/TS Ratio	0.97	0.80
Lignin (%)	44.88	16.47
cellulose (%)	24.67	55.53
Hemicellulose (%)	30.46	27.54

The Moisture Content (MC) of co-substrates affects methanogenic bioconversion to biogas; hence, optimal moisture levels are required.

The TS values reported in this study were more than those reported for raw sugarcane bagasse (79.64) (Budiyono et al., 2021) and rice straw (0.94) (Alemahdi et al., 2015). VS values of POME were also higher than rice straw values (0.75) and raw sugarcane bagasse (0.79) (Alemahdi et al., 2015; Budiyono et al., 2021) but similar to the rice husk values in this study. Furthermore, the VS/TS ratio values in this study were higher than those reported by Olugbemide & Likozar (2022) for rice husk (0.80), food waste and fruit, vegetable, and flower waste (0.85) (Alkanok et al., 2014; Batool et al., 2020), and sugar waste (0.93) (Alkanok et al., 2014). The TS content and VS contents of POMS and RH were relatively high, which is advantageous to the co-digestion process, as reported by Olugbemide & Likozar (2022).

Carbon/Nitrogen ratios are also critical in anaerobic digestion (AD) and the production of biogas. RH has a nitrogen content of 1.60%, while POMS has a nitrogen content of 0.81%. RH accounted for a suitable C/N ratio (28.64:1). At the same time, POMS results were far higher (64:1) than the C/N optimal range of 10:1 – 40:1 for the anaerobic digestion described by (Omondi et al., 2019; Suksong et al., 2020; Teghammar et al., 2013). It has been noted that a low C/N ratio might cause ammonia buildup, while a high C/N ratio can cause nitrogen deficiency; both of these scenarios are unhealthy for the smooth operation of a biogas plant. Although the C/N value for RH obtained in this study was higher than the referenced optimal, it was still within the range of RH varieties C/N ratios obtained by Olupot et al. (2016) (55:1–87:1) for biogas and biofuels production.

The lignin, cellulose, and hemicellulose content obtained in the characterization of RH were 35.40%, 40.52%, and 23.69%, respectively, while that of POMS are 44.88%, 24.67%, and 30.46%, respectively. Comparing RH results to similar results obtained by Izzati et al. (2020) and Olupot et al. (2016), the lignin, cellulose, and hemicellulose contents obtained in this study were notably lower (10.6–19.2%, 11.4–34.4%, and 29.3–37%) than their results. Higher cellulose and hemicellulose amounts compared to corresponding lignin contents in a Lignocellulosic material have a higher potential for biogas and biomethane production, while a higher lignin content relative to cellulose and hemicellulose, reduce the biodegradability of the biomass and, generally, the anaerobic digestion potential (Ma et al., 2019; Olatunji et al., 2021).

3.3 Biogas Production

The codigestion of POMS and RH was facilitated by the use of POME, which is composed of over 95% water (Lee et al., 2019) and cow dung (CD). The low moisture content of POMS and RH required an increase in moisture content to about 87% moisture, as done by Chu et al. (2015) (80%) and Olugbemide et al. (2020) (88.9%).

Figure 1 illustrates the daily biogas production for the 21 days of anaerobic digestion. Only three of the four samples co-digested produced measurable biogas, namely POME+POMS, POME+RH, and POME+RH+CD, while POME+RH+CD was insufficient to be measured.

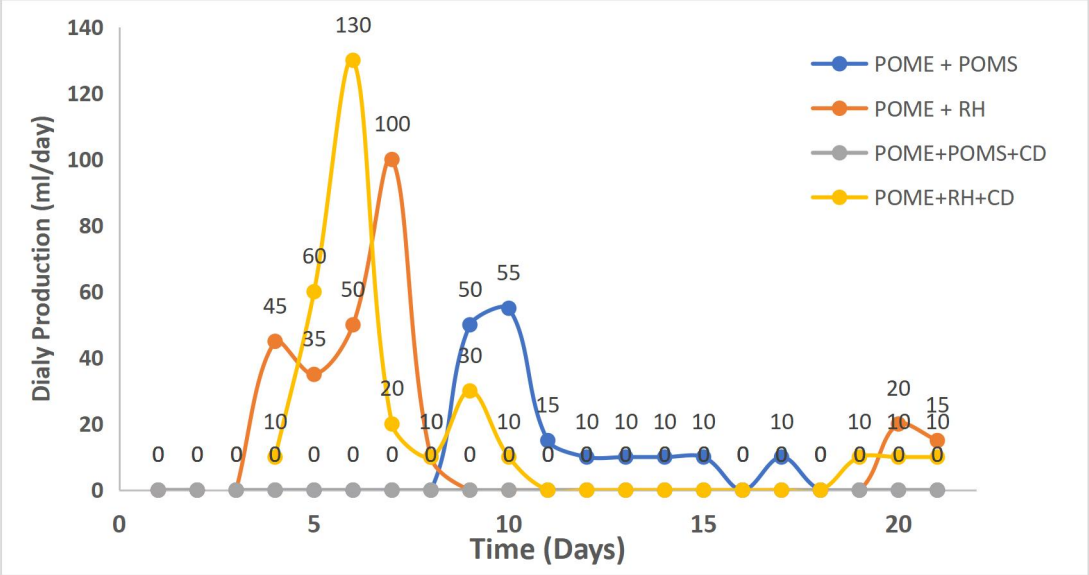

Figure 1: Daily production with time for samples

At the earliest start of production (day 4), as shown in Fig 1, POME+RH started with the highest production of 45ml compared to POME+RH+CD, which produced 10ml biogas. Other samples (POME+POMS+CD and POME+POMS) did not record any notable biogas produced on day 4. POME+RH production, however, grew exponentially on days 5 and 6 by 50 ml and 70 ml, respectively, while POME+POMS started with a notable initial biogas production value of 50 ml on day 9. Similar results were obtained by Latinwo & Agarry (2015) and Okonkwo et al. (2018), with their earliest biogas production date being day 7 and day 5, respectively, in all anaerobic digestion setups. Biogas production on the first few days of anaerobic digestion is low because lignocellulosic components and complex polysaccharides hydrolyze slowly as a result of the lignin that forms a protective barrier that prevents plant breakdown (Latinwo & Agarry, 2015). POME+RH+CD and POME+RH also experienced a notable decline till 0ml on day 9, similar to the results obtained by Lim et al. (2021) and Okonkwo et al. (2018), who used POME+DC and plantain peels in their codigestion processes.

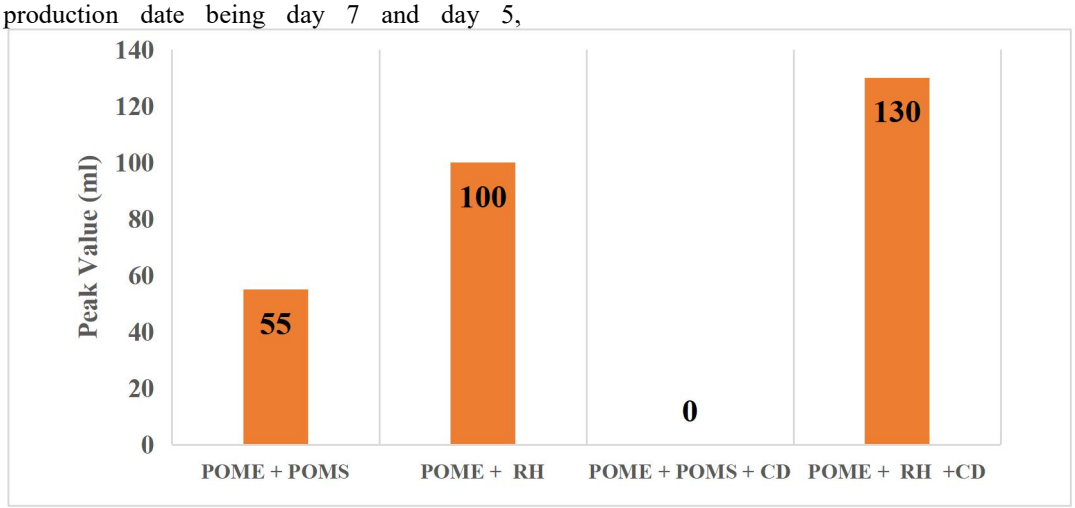

Figure 2: Peak Value of the co-digestion for POME solvent samples

Peak values and cumulative values of the samples co-digestion are shown in Figures 2 and 3. POME+POMS, POME+RH, POME+POMS+CD, POME+RH+CD reached their peak production as 55ml, 100ml, 0ml, and

130ml respectively while the cumulative peak production alues were 170ml, 275ml 0ml and 280ml respectively. Figure 1 shows that POME+POMS reached its peak value on day 10 (one day after production started), which was earlier than others. POME+RH reached its peak value on day 7 (4 days after production started), while POME+RH+CD reached its peak value on day 6 (3 days after production started). Olugbemide et al. (2016) reported that having a shorter time of attaining the peak value would reduce the cost of operation on a large scale. The lag phases for each of the digesters are 4 days for each of the RH samples, 9 days for POME+POMS samples, and 21 days lag phase with no production for POME+POMS+CD sample. The lag phase is a function of the biodegradability of the biomass because the lignin protection over the cellulose and hemicellulose contents is inaccessible by the microbes present (Olatunji et al., 2021). Olugbemide et al. (2020) demonstrated that the pretreatment of lignocellulosic biomass significantly reduces the time lag as all but one digester setup had zero phase lags. Also, the use of carbonaceous materials like activated carbon to improve the direct interspecies electron transfer (DIET) could significantly improve the phase lag (Deng et al., 2023). The lignocellulose biomasses (POMS and RH) subjected to the same conditions, such as feed ratio, solvent, and temperature, have demonstrated that RH has the highest biogas potential with a production value of 130ml as its peak daily production.

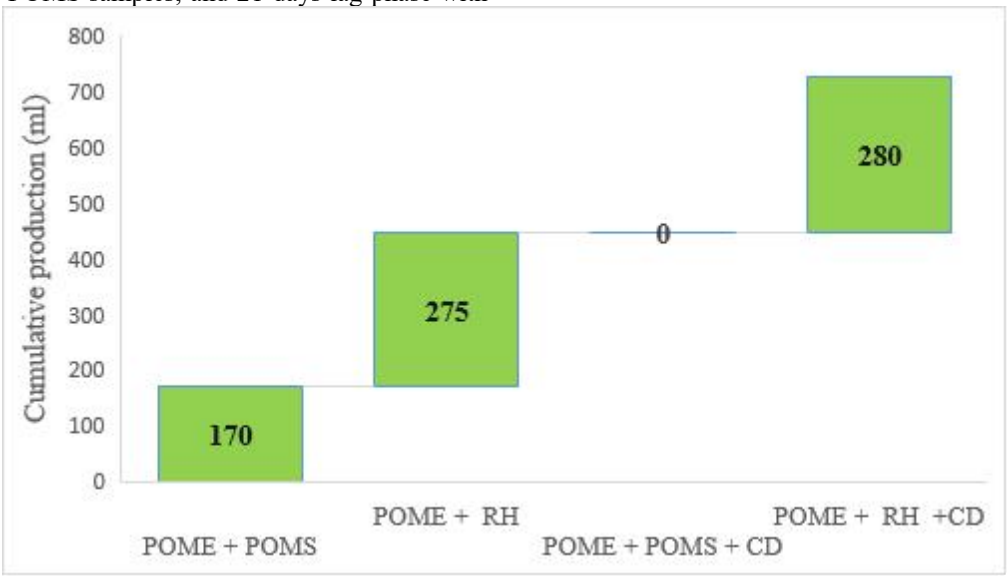

Figure 3: Cumulative co-digestion values of the POME-based samples

From the cumulative production table, POME+RH+CD had the highest cumulative production within the 21 days (280ml) with just a 5ml difference from the same setup, but without cow dung (CD). This signifies that the presence of cow dung (CD) as inoculum had little effect on the production of biogas. The same result was obtained by Olugbemide et al. (2020) and Alkanok et al. (2014), who proved that adding inoculum did not necessarily translate into improved biogas production or delayed phase lag, but rather as a backup for the anaerobic digestion to avoid process failure. POME+POMS had the least cumulative biogas production, with the exception of POME+POMS+CD, which did not produce any measurable quantity of biogas, further buttressing Alkanok et al. (2014) and Olugbemide et al. (2020)'s argument.

The biogas production experiments exhibited a declining trend over time, potentially due to possible factors such as pH, temperature, and lack of lignin-degradable pretreatment. In anaerobic digestion, biogas production

operates optimally within the mesophilic temperature range of 30–40°C (Chu et al., 2015b; Ramaraj & Unpaprom, 2016). However, the conducted experiments took place at room temperature (27.8°C), which is

significantly lower than the recommended range. This suboptimal temperature likely contributed to the low biogas production rates observed. Studies have shown that higher temperatures, closer to 35°C, led to substantial biogas production (Babaei & Shayegan, 2020). The relationship between temperature and biogas generation is complex, as temperature affects microbial metabolic activity, enzymatic processes, and the pace of microbial metabolism, influencing overall biogas production efficiency (Wang et al., 2019). Methanogenic bacteria's activity is particularly affected by temperature, where extremely low temperatures suppress metabolic activity and result in poor biogas production. Conversely, temperatures beyond 25°C tend to boost methanogen metabolic activity, ensuring operational stability and enhanced biogas production (Wang et al., 2019). While different microorganisms thrive within specific temperature ranges, maintaining the microbial community's balance is crucial for efficient anaerobic digestion.

Several studies have validated that biogas production varied with TS, VS, and C/N values; for instance, it has been argued that the TS concentration affects the amount of biogas produced. In a study by Maamri & Amrani (2014), biogas potential and production rates were attributed to be largely dependent on TS concentration as biogas yield increased with an increase in TS concentration. However, in a study by Song et al. (2020), the TS values were ruled out as a determinant of biogas yield.

Another crucial parameter influencing anaerobic digestion is the Carbon-to-Nitrogen (C/N) ratio. The optimal C/N ratio varies based on the feedstock used and the participating microorganisms. In context, POME, POMS, and RH exhibited varying C/N ratios, with POMS displaying higher ratios due to its lower nitrogen content. Excessive nitrogen compared to carbon can lead to volatile fatty acids (VFAs) accumulation from excessive nitrogen, causing process instability. Conversely, nitrogen scarcity due to high C/N ratios can limit microbial activity due to insufficient nitrogen for microbial nutrition, resulting in reduced biogas production (Sarker et al., 2019). The high nitrogen content of RH contributed to its favourable biogas production in comparison to POMS, emphasizing the role of the C/N ratio in biogas yield. Therefore, getting optimal values of the C/N ratio and VS/TS ratio is paramount in biogas production (Mrosso et al., 2023; Rashwan et al., 2013; XuGuang et al., 2018).

The inability of the POME+POMS+CD sample to record any notable biogas could be attributed to the reasons mentioned earlier, i.e., the high lignin content of POMS (44.88%) and the high C/N ratio of POME (64:1) which would have meaningfully inhibited the methanogenesis process and the methanogenic bacteria as explained by (Baksi et al., 2023).

4, CONCLUSION

Anaerobic co-digestion of POME, RH, and POMS is a promising strategy for energy recovery and effective waste management while promoting economic and environmental sustainability. The results from the experiment have proven that the biogas can be produced from the co-digestion of rice husk, palm oil mill sludge, and POME using cow dung as inoculum within 21 days of digestion at ambient conditions. High lignin content POMS (44.88%) emphasized the need for a pretreatment process to break down the recalcitrance and gain access to the cellulosic material. The rice husk–based sample resulted in a more favourable biogas production for the POME+RH and POME+RH+CD samples with cumulative values of 275ml and 280ml, respectively, due to its low lignin and high cellulose content, indicating an almost “ready to use” waste material. Finally, other factors, such as selected pretreatment methods, optimal temperature, and pH of POME, amongst others, contributed to the low (170ml) and negligible (0ml) yield of the biogas. However, these results create opportunities for the exploration of POME, POMS, RH, and CD as potent bioenergy carriers.

REFERENCES

Ajala, E. O., Ighalo, J. O., Ajala, M. A., Adeniyi, A. G., & Ayanshola, A. M. (2021). Sugarcane bagasse: A biomass sufficiently applied for improving global energy, environment and economic sustainability. *Bioresources and Bioprocessing*, *8*(1), 87. https://doi.org/10.1186/s40643-021-00440-z

Alemahdi, N., Che Man, H., Abd Rahman, N., Nasirian, N., & Yang, Y. (2015). Enhanced mesophilic bio-hydrogen production of raw rice straw and activated sewage sludge by co-digestion. *International Journal of Hydrogen Energy*, *40*(46), 16033–16044. https://doi.org/10.1016/j.ijhydene.2015.08.106

Alkanok, G., Demirel, B., & Onay, T. T. (2014). Determination of biogas generation potential as a renewable energy source from supermarket wastes. *Waste Management*, *34*(1), 134–140. https://doi.org/10.1016/j.wasman.2013.09.015

Babaei, A., & Shayegan, J. (2020). Effects of temperature and mixing modes on the

performance of municipal solid waste anaerobic slurry digester. *Journal of Environmental Health Science and Engineering*, *17*(2), 1077–1084. https://doi.org/10.1007/s40201-019-00422-6

Baksi, S., Sarkar, U., Villa, R., Basu, D., & Sengupta, D. (2023). Conversion of biomass to biofuels through sugar platform: A review of enzymatic hydrolysis highlighting the trade-off between product and substrate inhibitions. *Sustainable Energy Technologies and Assessments*, *55*, 102963. https://doi.org/10.1016/j.seta.2022.102963

Batool, N., Qazi, J., Aziz, N., Hussain, A., & Shah, S. (2020). Bio-Methane Production Potential Assays of Organic Waste by Anaerobic Digestion and Co-Digestion. *Pakistan Journal of Zoology*, *52*, 971–976. https://doi.org/10.17582/journal.pjz/20190322170334

Bridgewater, L. L., Baird, R. B., Eaton, A. D., Rice, E. W., American Public Health Association, American Water Works Association, & Water Environment Federation (Eds.). (2017). *Standard methods for the examination of water and wastewater* (23rd edition). American Public Health Association.

Bruni, E., Jensen, A. P., & Angelidaki, I. (2010). Steam treatment of digested biofibers for increasing biogas production. *Bioresource Technology*, *101*(19), 7668–7671. https://doi.org/10.1016/j.biortech.2010.04.064

Budiyono, B., Riyanta, A. B., Sumardiono, S., Jos, B., & Syaichurrozi, I. (2021). Optimization of Parameters for Biogas Productionfrom Bagasse Using Taguchi Method. *Polish Journal of Environmental Studies*, *30*(5), 4453–4461. https://doi.org/10.15244/pjoes/129914

Chan, Y. J., Lee, H. W., & Selvarajoo, A. (2021). Comparative study of the synergistic effect of decanter cake (DC) and empty fruit bunch (EFB) as the co-substrates in the anaerobic co-digestion (ACD) of palm oil mill effluent (POME). *Environmental Challenges*, *5*, 100257. https://doi.org/10.1016/j.envc.2021.100257

Chu, X., Wu, G., Wang, J., & Hu, Z.-H. (2015). Dry co-digestion of sewage sludge and rice straw under mesophilic and thermophilic anaerobic conditions. *Environmental Science and Pollution Research*, *22*(24), 20143–20153. https://doi.org/10.1007/s11356-015-5074-6

Darmawan, S., Wistara, N. J., Pari, G., Maddu, A., & Syafii, W. (2016). Characterization of Lignocellulosic Biomass as Raw Material for the Production of Porous Carbon-based Materials. *BioResources*, *11*(2), 3561–3574. https://doi.org/10.15376/biores.11.2.3561-3574

Deng, C., Kang, X., Lin, R., Wu, B., Ning, X., Wall, D., & Murphy, J. D. (2023). Boosting biogas production from recalcitrant lignin-based feedstock by adding lignin-derived carbonaceous materials within the anaerobic digestion process. *Energy*, *278*, 127819. https://doi.org/10.1016/j.energy.2023.127819

Enaboifo, M. A. (2020). *Comparative study of biogas production from cocoa pod, maize husk, orange peels, pineapple peels, and coconut fiber co-digested with yeast*. Association of Deans of Agriculture in Nigeria Universities (ADAN).

Fikri Hamzah, M. A., Abdul, P. M., Mahmod, S. S., Azahar, A. M., & Jahim, J. Md. (2020). Performance of Anaerobic Digestion of Acidified Palm Oil Mill Effluent under Various Organic Loading Rates and Temperatures. *Water*, *12*(9), 2432. https://doi.org/10.3390/w12092432

Hai, T., Mishra, P., Mohamad Zain, J., Saini, K., Manoj Kumar, N., & Ab Wahid, Z. (2023). Co-digestion of domestic kitchen food waste and palm oil mill effluent for biohydrogen production. *Sustainable Energy Technologies and Assessments*, *55*, 102965. https://doi.org/10.1016/j.seta.2022.102965

Ishmael, M. R., Esther, T. A., & Robert, H. (2017). *Mesophilic temperature range effect on anaerobic digestion of residential grass cuttings using simple batch digester*. Int. J. Renewable Energy Technology.

Izzati Dyah Lantasi, A., Syafrudin, & Budiyono. (2020). Rice husk as renewable energy for biogas production from biomass: Prospect and challenges. *E3S Web of Conferences*, *202*, 06024. https://doi.org/10.1051/e3sconf/202020206024

Kalansuriya, M. H., Mowjood, M. I. M., & Dharmasena, D. A. N. (2016). *Investigation on Neutralizing Agents for Palm Oil Mill Effluent (POME)*. 7th

International Conference on Sustainable Built Environment, SriLanka.

Kamaruddin, M. A., Ismail, N., Tan, H. K., & Alrozi, R. (2018). Sustainable Treatment of Palm Oil Mill Effluent (POME) by using Pectin and Chitosan in Jar Test Protocol – Sequential Comparison. *International Journal of Integrated Engineering*, *10*(9), 63–68. https://doi.org/10.30880/ijie.2018.10.09.012

Karki, R., Chuenchart, W., Surendra, K. C., Shrestha, S., Raskin, L., Sung, S., Hashimoto, A., & Kumar Khanal, S. (2021). Anaerobic co-digestion: Current status and perspectives. *Bioresource Technology*, *330*, 125001. https://doi.org/10.1016/j.biortech.2021.125001

Latinwo, G. K., & Agarry, S. E. (2015). Modelling the Kinetics of Biogas Production from Mesophilic Anaerobic Co-Digestion of Cow Dung with Plantain Peels. *International Journal of Renewable Energy Development*, *4*(1), 55–63. https://doi.org/10.14710/ijred.4.1.55-63

Lee, Z. S., Chin, S. Y., Lim, J. W., Witoon, T., & Cheng, C. K. (2019). Treatment technologies of palm oil mill effluent (POME) and olive mill wastewater (OMW): A brief review. *Environmental Technology & Innovation*, *15*, 100377. https://doi.org/10.1016/j.eti.2019.100377

Lim, Y. F., Chan, Y. J., Hue, F. S., Ng, S. C., & Hashma, H. (2021). Anaerobic co-digestion of Palm Oil Mill Effluent (POME) with Decanter cake (DC): Effect of mixing ratio and kinetic study. *Bioresource Technology Reports*, *15*, 100736. https://doi.org/10.1016/j.biteb.2021.100736

Ma, S., Wang, H., Li, J., Fu, Y., & Zhu, W. (2019). Methane production performances of different compositions in lignocellulosic biomass through anaerobic digestion. *Energy*, *189*, 116190. https://doi.org/10.1016/j.energy.2019.116190

Maamri, S., & Amrani, M. (2014). Biogas Production from Waste Activated Sludge Using Cattle Dung Inoculums: Effect of Total Solid Contents and Kinetics Study. *Energy Procedia*, *50*, 352–359. https://doi.org/10.1016/j.egypro.2014.06.042

Mrosso, R., Mecha, A. C., & Kiplagat, J. (2023). Characterization of kitchen and municipal organic waste for biogas production: Effect of parameters. *Heliyon*, *9*(5), e16360. https://doi.org/10.1016/j.heliyon.2023.e16360

NESREA (2011). *National Environment (Surface and Groundwater Quality Control) Regulation* (Vol. 98). Federal Republic of Nigeria Official Gazette.

Nur, M. M. A., Garcia, G. M., Boelen, P., & Buma, A. G. J. (2021). Influence of photodegradation on the removal of color and phenolic compounds from palm oil mill effluent by Arthrospira platensis. *Journal of Applied Phycology*, *33*(2), 901–915. https://doi.org/10.1007/s10811-020-02341-8

Nwaneri, C. B. (2022). *Batch Mode Biomethane Production from Anaerobic Digestion of Palm Oil Mill Effluent (POME) with Cassava Peels and Cabbage Waste*. https://www.sdiarticle5.com/review-history/89393

Okolie, J. A., Epelle, E. I., Tabat, M. E., Orivri, U., Amenaghawon, A. N., Okoye, P. U., & Gunes, B. (2022). Waste biomass valorization for the production of biofuels and value-added products: A comprehensive review of thermochemical, biological and integrated processes. *Process Safety and Environmental Protection*, *159*, 323–344. https://doi.org/10.1016/j.psep.2021.12.049

Okonkwo, U. C., Onokpite, E., & Onokwai, A. O. (2018). Comparative study of the optimal ratio of biogas production from various organic wastes and weeds for digester/restarted digester. *Journal of King Saud University - Engineering Sciences*, *30*(2), 123–129. https://doi.org/10.1016/j.jksues.2016.02.002

Olatunji, K. O., Ahmed, N. A., & Ogunkunle, O. (2021). Optimization of biogas yield from lignocellulosic materials with different pretreatment methods: A review. *Biotechnology for Biofuels*, *14*(1), 159. https://doi.org/10.1186/s13068-021-02012-x

Olugbemide, A. D., Lajide, L., Adebayo, A., & Owolabi, B. J. (2016). *Production of Second-Generation Biofuel from Five Tropical Lignocellulosic Materials: Effects of Particle Size and Dilution Ratio*.

Olugbemide, A. D., Lajide, L., Adebayo, A., & Owolabi, B. J. (2020). Enhanced Biogas Production from Rice Husk Through Solid-State Chemical Pretreatments. *Waste and Biomass Valorization*, *11*(6), 2397–2407. https://doi.org/10.1007/s12649-018-00567-9

Olugbemide, A. D., & Likozar, B. (2022). Assessment of Liquid and Solid Digestates from Anaerobic

Digestion of Rice Husk as Potential Biofertilizer and Nutrient Source for Microalgae Cultivation. *Processes*, *10*(5), Article 5. https://doi.org/10.3390/pr10051007

Olugbemide, A. D., Likozar, B., Oberlintner, A., Novak, U., & Ekebafe, L. (2022). Reaction kinetics modeling for dry anaerobic digestion of lignocellulosic Hura crepitans leaves. *Chemical Papers*, *76*(10), 6263–6269. https://doi.org/10.1007/s11696-022-02312-y

Olupot, P. W., Candia, A., Menya, E., & Walozi, R. (2016). Characterization of rice husk varieties in Uganda for biofuels and their techno-economic feasibility in gasification. *Chemical Engineering Research and Design*, *107*, 63–72. https://doi.org/10.1016/j.cherd.2015.11.010

Omondi, E. A., Ndiba, P. K., & Njuru, P. G. (2019). Characterization of water hyacinth (E. crassipes) from Lake Victoria and ruminal slaughterhouse waste as co-substrates in biogas production. *SN Applied Sciences*, *1*(8), 848. https://doi.org/10.1007/s42452-019-0871-z

Ore, O. T., Akeremale, O. K., Adeola, A. O., Ichipi, E., & Olubodun, K. O. (2023). *Production and Kinetic Studies of Biogas from Anaerobic Digestion of Banana and Cassava Wastes*.

Pfeiffer, W., Nguyen, V. T., Neumann, J., Awe, D., & Tränckner, J. (2020). Operation and Control of a Full-Scale Biogas Plant Treating Wastewater from the Cleaning of Car Tanks. *Chemical Engineering & Technology*, *43*(1), 84–94. https://doi.org/10.1002/ceat.201900398

Ramaraj, R., & Unpaprom, Y. (2016). *Effect of temperature on the performance of biogas production from Duckweed*.

Rashwan, M. A., Elsoury, H. A., & Omara, A. I. A. (2013). Effect of Total Solids Content on Biogas Production in a Family Scale Biogas Digester. *Misr Journal of Agricultural Engineering*, *30*(4), 1195–1210. https://doi.org/10.21608/mjae.2013.99941

Rohma, N. A., Suhartini, S., & Nurika, I. (2021). Chemical pretreatments on oil palm empty fruit bunches: Impacts on characteristics and methane potential. *IOP Conference Series: Earth and Environmental Science*, *924*(1), 012071. https://doi.org/10.1088/1755-1315/924/1/012071

Sarker, S., Lamb, J. J., Hjelme, D. R., & Lien, K. M. (2019). A Review of the Role of Critical Parameters in the Design and Operation of Biogas Production Plants. *Applied Sciences*, *9*(9), Article 9. https://doi.org/10.3390/app9091915

Satyavolu, J., & Lupitskyy, R. (2021). Evaluation of Physical and Chemical Pretreatment Methods to Improve Efficiency of Anaerobic Digestion of Waste Streams from Grain Processing. In A. Sikora (Ed.), *Anaerobic Digestion in Built Environments*. IntechOpen. https://doi.org/10.5772/intechopen.98321

Schmatz, A. A., Tyhoda, L., & Brienzo, M. (2020). Sugarcane biomass conversion influenced by lignin. *Biofuels, Bioproducts and Biorefining*, *14*(2), 469–480. https://doi.org/10.1002/bbb.2070

Singkhala, A., Mamimin, C., Reungsang, A., & O-Thong, S. (2021). Enhancement of Thermophilic Biogas Production from Palm Oil Mill Effluent by pH Adjustment and Effluent Recycling. *Processes*, *9*(5), 878. https://doi.org/10.3390/pr9050878

Sokowocin, E. V. (2020). *CONVERSION OF BIO-WATSE TO BIOMASS*.

Song, Z., Li, Y., Yang, G., Qin, J., Ren, G., & Feng, Y. (2020). Effect of total solid concentration and temperature on biogas yields of mixture of chicken manure and corn straw. *Transactions of the Chinese Society of Agricultural Engineering*, *26*(7), 260–265. https://www.ingentaconnect.com/content/tcsae/tcsae/2010/00000026/00000007/art00045#trendmd-suggestions

Suksong, W., Tukanghan, W., Promnuan, K., Kongjan, P., Reungsang, A., Insam, H., & O-Thong, S. (2020). Biogas production from palm oil mill effluent and empty fruit bunches by coupled liquid and solid-state anaerobic digestion. *Bioresource Technology*, *296*, 122304. https://doi.org/10.1016/j.biortech.2019.122304

Teghammar, A., Castillo, M. D. P., Ascue, J., Niklasson, C., & Sárvári Horváth, I. (2013). Improved Anaerobic Digestion by the Addition of Paper Tube Residuals: Pretreatment, Stabilizing, and Synergetic Effects. *Energy & Fuels*, *27*(1), 277–284. https://doi.org/10.1021/ef301633x

Toribio-Cuaya, H., Pedraza-Segura, L., Macías-Bravo, S., Vasquez-Medrano, R., & Favela-Torres, E. (2014). Characterization of Lignocellulosic Biomass Using Five Simple Steps. *Journal of*

Chemical, Biological and Physical Sciences, *4*(5), 28–47.

Trisakti, B., Manalu, V., Taslim, I., & Turmuzi, M. (2015). Acidogenesis of Palm Oil Mill Effluent to Produce Biogas: Effect of Hydraulic Retention Time and pH. *Procedia - Social and Behavioral Sciences*, *195*, 2466–2474. https://doi.org/10.1016/j.sbspro.2015.06.293

Wang, S., Ma, F., Ma, W., Wang, P., Zhao, G., & Lu, X. (2019). Influence of Temperature on Biogas Production Efficiency and Microbial Community in a Two-Phase Anaerobic Digestion System. *Water*, *11*(1), Article 1. https://doi.org/10.3390/w11010133

WHO (1993). *Guidelines for drinking-vvater quality* (2nd ed., Vol. 1). World Health Organization.

XuGuang, M., Tao, J., Qiong, T., JiaLi, C., Tao, L., & ZiLi, M. (2018). Effect of total solid content on biogas production from rape stalk and chicken manure with different mixing ratios. *Transactions of the Chinese Society of Agricultural Engineering*, *34*(12), 236–244. https://www.cabdirect.org/cabdirect/abstract/20183321952

Yap, C. C., Chan, Y. J., Loh, S. K., Supramaniam, C. V., Soh, A. C., Chong, M. F., Chew, C. L., & Lim, L. K. (2020). Comparison of different industrial scale palm oil mill effluent anaerobic systems in degradation of organic contaminants and kinetic performance. *Journal of Cleaner Production*, *262*, 121361. https://doi.org/10.1016/j.jclepro.2020.121361

10.51975/24390207.som
Journal of the Nigerian Society of Chemical Engineers, 39(2), 2024

COMPARATIVE ANALYSIS OF IMPORTED AND LOCALLY SOURCED GYPSUM FOR CEMENT PRODUCTION

Justus T. OMOYAKHI[1], *Kenneth K. ADAMA[1], Ubani O. AMUNE[1], Francis A. OLUWADAYO[1], Shegun K. OTOIKHIAN[1], Emmanuel O. ALUYOR[1]

[1]Department of Chemical Engineering, Edo State University Uzairue, Edo State, Nigeria

Correspondence: *omojust1988@gmail.com[1], ubani.amune@edouniversity.edu.ng[1], adama.kenneth@edouniversity.edu.ng[1], and otoikhian.kevin@edouniversity.edu.ng[1] +234(0)8137147909*

ABSTRACT

The availability and use of local gypsum for cement production have become imperative in the Nigerian cement industry. In this research, local and imported gypsum were analyzed comparatively using different characterization techniques: X-ray fluorescence (XRF), Fourier Transform Infrared Spectroscopy (FTIR) and Brunauer-Emmett-Teller (BET). Dry and wet-beneficiation techniques were employed on different samples identified as Spain-A, Warake-B, Afuze-C, Avilele-D, Warake-B1, Afuze-C1 and Aviele-D1, respectively. The initial samples were crushed and sieved to 2 mm, and 500 g of each sample was heated to 45 °C for 24 hrs as dry-beneficiated. Three hundred grams (300 g) of each sample was then soaked for 24 hrs as wet-beneficiated. The dry and wet-beneficiated samples were further heated to 120 °C for 30 mins, and 10 g of each sample was ground and sieved to 45 µm for analysis. The XRF results showed improvement in the active component and SO_3 purity of Warake gypsum, ranging from 72.26% and 86.93% to 75.45% and 91.59%, respectively, using wet-beneficiation. The various local gypsum samples had higher purity levels than Spain gypsum after wet-beneficiation. The FTIR analysis revealed the presence of different functional groups for all samples consisting of –COOH, −OR, CO−NH_2, −C≡N, −OH, C=O, C−I, Br, F, C=C and −C≡C−, which are involved in ionic interaction with clinker mineral. BET analysis revealed improvement in surface area and pore size of 204.515 m^2/g and 1.853 nm to 265.156 m^2/g and 2.108 nm for Aviele wet-beneficiated gypsum. Investment cost analysis for local gypsum production revealed a profit of ₦ 25,104.20 when the cost of producing local gypsum is compared to the cost of importing Spain gypsum per ton, establishing the quality and potentials of different local gypsum for cement production in Nigeria.

Keywords: *Gypsum; Beneficiation; Characterization; Purity composition; Cost*

1 INTRODUCTION

Gypsum is a naturally occurring mineral with the chemical formula ($CaSO_4.2H_2O$) known as calcium sulfate dihydrate. (Al-Ridha *et al.,* 2020; Layr and Hartlieb, 2019). As a set-retarder, gypsum is widely employed in the manufacture of cement. When added to cement, it prolongs the process of hydration and delays the setting time of the cement (Abdul-Wahab *et al*., 2021). By forming ettringite, gypsum addition slows down the tri-calcium aluminate $3CaO.Al._3/C_3$ A's rapid exothermic reaction (Muhammad *et al.,* 2021). In order to create cement with a high compressive strength and minimal concrete expansion, gypsum is added to the clinker (Xiaodi *et al.,* 2022). Gypsum can take a variety of forms when heated, such as Gypsum, $CaSO_4.2H_2O$, hemihydrate $CaSO_4.0.5H_2O$ (mortar), and anhydrates $CaSO_4$ (Adams *et al.,* 2021; Gaharwar *et al.,* 2016; Muhammad *et al*., 2021).

The global gypsum production in 2016 was estimated at 252 million tonnes, valued at $1.49 billion, with 33.3 % and 60.9 % being consumed in the plasterboard and cement industries, respectively (Uriah, 2016). Gypsum output, according to Uriah (2016), is expected to increase at a compound annual growth rate of 9.9% and will reach about $3.8 billion by 2026. For instance, there are more than a billion tons of gypsum deposits in Nigeria, which are dispersed across a number of the nation's states, including Taraba, Sokoto, Borno, Bauchi, Adamawa, Edo, Yobe, Gombe, Ogun, Ebonyi, and Cross River State (Dogara & Aloa, 2017; Muhammad et

al., 2021). Despite these substantial resources, Nigeria imported $56 million worth of gypsum over the past three years (Adams et al., 2021). An estimated 4,000,000 tons of gypsum are located in several local government areas of Edo State (Uriah, 2016).

Gypsum is widely used in cement production to control cement settings and to provide cement with less drying shrinkage and non-excessive expansion in concrete. It is always added to clinker at an optimal level during grinding (Dafni *et al.,* 2019; Mohammad *et al.,* 2022). The purity of gypsum for cement production is required to be between 85-90 %, and where the purity of the gypsum produced locally does not meet this requirement, beneficiation is expected to be carried out to upgrade its purity (Uriah, 2016).

Very few research articles have attempted to analyze the quality of locally sourced Gypsum in Nigeria and its effect on cement production. For instance, Adams *et al.* (2021) worked on the facile purification of locally mined gypsum and its use for preparing nano-hemihydrates using $CaCl_2$-based solvent and achieved high gypsum purity (94.05%). Their work failed to carry out physical beneficiation and non-chemical-based investigation as a cheaper means of solvent beneficiation. Also, Muhammad *et al*. (2021) investigated the effect of locally sourced Nigerian Gypsum (Warake) on the strength and microstructure of Portland cement mortar. They obtained a similar range for foreign and local gypsum content for optimal Portland cement (5 to 6%). However, an intricate analysis of the locally sourced and foreign gypsum prior to its use for ordinary Portland cement, amongst other uses, was not covered in their report. Hence, this study characterized Local Gypsum and compared it to gypsum imported from Spain in order to understand its properties and suitability for cement production while considering its cost of production. The purity, composition, and physiochemical properties of the local and imported gypsum samples were compared along with the industrial cost of importation and local production. Beneficiation methodology was used to fully explore the suitability of warake gypsum over popularly imported (Spain) gypsum for cement production.

2 MATERIALS AND METHODS

2.1 Materials

The materials used in the study include gypsum samples from Warake (randomly selected from Alagbon, Iyekhara, and Akagbe villages), Afuze (Oke, Eme, and Afuji villages), and Aviele in Owan East and Etsako West Local government areas of Edo State, Nigeria. The Warake gypsum was located approximately between Latitudes 6° 58' 54"N and 6° 56' 27"N and between Longitude 6° 13' 25"E and 6°11' 25" E. Avielle gypsum was also located at Latitude 6° 56’ 51" N and Longitude 5° 59’ 38.04" E, while Avielle gypsum was located at Latitude: 7° 0’ 51.57" N and Longitude: 6° 16’ 42.4884" E. Random depths of 1.5m, 4m, and 7m were used to retrieve samples (2, 3, and 4 pieces) at each of these locations. Spain gypsum was obtained from Spain through a gypsum vendor. Table 1 and Plate 1 present different materials used in the study.

Table 1: List of Materials Used for the Experiment

Material	Source	Colour comments
Spain gypsum	Spain	Light brown
Warake gypsum	Warake (Edo state – Nigeria)	Dark brown

2.2 Methods

2.2.1 Preparation of the Spain imported gypsum

The Spain-imported Gypsum (SIG) was prepared using the ASTM (C471) method. Three hundred grams (300 g) of the SIG was crushed with a laboratory crusher and dried in an oven at 45℃ for 24 hrs to remove the moisture content. The SIG was subjected to heat treatment at 120℃ for 30 mins. After that, the samples were pulverized into powder using an ASTM 45 μm mesh-sized sieve and compacted on a ring in a manual press machine. Ten grams (10 g) of prepared sample was then collected and analyzed using XRF, XRD, FTIR, and BET techniques.


Plate 1: Samples of the Warake (left) and Spain-imported Gypsum (SIG Right) used for the study

2.2.2 Preparation of the Local Gypsum

The Warake gypsum sample was equally prepared using the ASTM (C471) method. Five hundred grams (500 g) of gypsum sample from Warake, Afuze, and Avielle (Edo State) Nigeria was crushed into smaller sizes and dried in an oven at 45℃ for 24 hrs to remove the moisture content. The gypsum was then homogenized, and 300g was weighed using a laboratory scale and beneficiated using the dry and wet methods.

2.2.3 Beneficiation of the Local Gypsum

The physical methods for dry and wet-beneficiation of Gypsum by Adams et al. (2021), Gunnar and Kristine (2020), and James et al. (2008) were used. The Dry-beneficiation method involved crushing the sample material into the desired size and sieving with a mesh of 2-micrometer size. In contrast, in the wet-beneficiation method, the samples were soaked with ordinary tap water at a room temperature of 27 ± 2 °C for 24 hours, thoroughly washed and heated to 45 °C for 24 hours, and then sieved using 2-mm mesh to separate smaller particles from larger particles and impurities. The dry-beneficiated samples of the Warake, Afuze, and Avielle samples were labeled as B, C, and D, respectively while the wet-beneficiated samples were equally labeled as B1, C1, and D1, respectively.

2.2.4 Preparation of hemihydrate

The method adopted for the preparation of hemihydrate was that reported by Adams *et al. (*2021). The four gypsum samples were further heated in an oven to 120 °C for 30 minutes to eliminate some of the water of crystallization for hemihydrate determination. After this, the samples were pulverized into powder using an ASTM 45 µm mesh-sized sieve and compacted on a ring in a manual press machine, just as done for the SIG. Ten grams (10 g) of prepared sample was then collected and analyzed using XRF, XRD, FTIR, and BET techniques.

2.2.5 Characterization using XRF, XRD, FTIR and BET

The elemental composition of the gypsum samples was determined using X-ray fluorescence (XRF). A Switzerland Thermo Scientific ARL 9900 XRF equipment was utilized to determine the elemental composition of the different samples and the percentage of CaO, SO_3, and impurities in the different samples. A Rigaku Mini-flex 600 XRD equipment from Tokyo, Japan, was employed for structural analysis of the gypsum samples. The equipment parameter consisted of CuK radiation operated at a wavelength of 1.5406 λ, 40 kV, 30 mA, and a scanning speed of 8 °/min. The 2Θ angle of measurement was in the range of 5° to 70°. Fourier Transform Infrared Spectrometer (FTIR) measurements were performed using an Agilent Cary 630 instrument, Agilent Technologies Inc., USA, to ascertain the phase composition and functional groups. The equipment was operated on 100-240 VAC with a frequency of 50-60 Hz. Brunauer-Emmett-Teller (BET) analysis was used to determine the specific surface area, pore volume, and pore size distribution of the samples. This was accomplished using a Nova 4200e U.S.A BET device. The surface areas were computed by counting the number of N_2 molecules adsorbed at monolayer coverage. Prior to BET analysis, the samples were degassed at 300 °C for 3 hrs to eliminate any physically adsorbed water molecules.

2.2.6 Density determination

ASTM (D792) methodology was employed to determine the density of the samples. The gypsum powder samples sieved with 45 µm ASTM-graded mesh were placed in a weighted density bottle, compressed, and reweighed in a weighing balance. The density of each sample was then estimated using the volume of the density bottle (25 ml) as in Equation 1.0 (Bouzit *et al.,* 2019)

$$\text{Density} = \frac{m_2 - m_1}{v_2 - v_1} \quad (1)$$

Where m_1 and m_2 are the initial and final weight of the samples on the bottle, and v_1 and v_2 are the initial and final volume of the bottle, respectively.

2.2.7 Moisture Content Determination

The moisture content of each sample was determined using the ASTM (D2216-19) method. On a weight balance, the weight of an empty laboratory container was recorded, and 500 g of each sample was weighed into the container, with the total weight recorded. The weighted mass was placed in a 45°C oven for 24 hrs. The new weight of the samples was recorded after 24 hrs, deducted from the initial weight, and the findings were determined using Equation 2.0 (Randazzo *et al.,* 2016).

$$\text{Moisture content} = \frac{w_1 - w_2}{w_1} \times 100\% \qquad (2)$$

Where w_1 and w_2 are the initial and final weight of gypsum after heating, respectively.

3 RESULTS AND DISCUSSION

3.1 Physical Properties of Investigated Gypsum Samples

The results of the investigations conducted on the different samples in terms of their physical properties, which include moisture content, density, surface area, pore size and pore volume, are presented in Table 2.

Table 2: Physical Properties of Different Gypsum Samples

Sample		Moisture content (%)	Density (g/ml)	Surface area (m^2/g)	Pore size (nm)	Pore volume (cm^3/g)
SIG A		1.2	2.86	257.272	2.123	0.143
Warake	B	0	2.98	289.924	2.144	0.180
Afuze	C	0	2.78	270.108	2.122	0.149
Aviele	D	0	2.69	204.515	1.853	0.135
Warake	B1	2.8	2.82	316.747	2.153	0.162
Afuze	C1	2.8	2.30	292.598	2.101	0.179
Aviele	D1	2.8	2.34	265.156	2.108	0.130

3.1.1 Moisture content analysis

Table 2 above shows the results of the moisture content of dry- and wet-beneficiated investigated gypsum samples. Moisture content measurement reveals the water binding ability and hydration behaviour of gypsum samples for consistency testing and performance assessment. It is an important physical characteristic that reveals the amount of water in gypsum and its relationship with the environment. No moisture content was observed in all local dry-beneficiated samples, as seen in Table 2, while a variation in moisture content between the SIG and the wet-beneficiated gypsum. The wet-beneficiated samples, because of their beneficiation process, have more water content, i.e. 2.8 %, while the SIG sample is 1.2 %. The variations in Table 2 can be attributed to the nature of occurrence in different regions and exposure to water, which might have caused changes in moisture content (Gunnar and Kristine, 2020). Several studies by Ahmad *et al*. (2021), Abdul-Wahab *et al.* (2021) and Mohamad *et al.* (2022) revealed that moisture levels should not be more than 2–3 % to avoid problems like clogging of the grinding mill or agglomeration of mineral particles. Zmemla *et al.* (2016) also noted moisture content ranging from 1–2 % for natural gypsum.

3.1.2 Density analysis

Gypsum has a relatively low weight per unit volume due to the presence of impurities (Cordon *et al.,* 2021). Table 2 shows the density values of the investigated SIG and local gypsums. The diverse percentages of crusts and impurities present in the various samples may be responsible for this variance. However, though wet-beneficiation was shown to decrease the density of the local gypsum samples by reducing the impurities present (Mohamad *et al.* 2022), the resulting densities were still in accordance with gypsum density values reported by different authors (Onat *et al.,* 2018; Mohammad *et al.,* 2022; Mohamad *et al*., 2022). As shown in Table 2, the total sample density ranges between 2.30 and 2.98 g/ml.

3.1.3 BET analysis

3.1.3.1 Surface area, pore size and pore volume of dry-beneficiated Gypsum Samples

The pore sizes of gypsum have a significant impact on the estimation of hydration and hydraulic characteristics. Increased dissolution rates, higher adsorption capacity, and free energy available for bonding are all benefits of a solid with a high surface area (Adamas *et al.,* 2021; Ghumman *et al.,* 2022). The surface area, pore size, and pore volume of dry-beneficiated gypsum samples (SIG and local) are shown in Table 2. The BET technique was used to analyze the weak forces of attraction using gas adsorption on particulate materials (Cordon *et al.,* 2021). The dry-beneficiated SIG-A, Warake-B and Afuze-C were all mesoporous materials. In contrast, the dry-beneficiated Aviele gypsum sample D showed a microporous property showing close matching pore diameters as presented in Table 2. This observation is consistent with the result reported by Amenaghawon *et al.* (2021). Gypsum's reactivity and hydraulic characteristics in the manufacture of cement are impacted by higher surface area and pore size (Cordon *et al.,* 2021; Gunnar and Kristine, 2020).

3.1.3.2 Surface area, pore size and pore volume of wet-beneficiated Gypsum

The surface area, pore size, and pore volume of the wet-beneficiated local gypsum samples are displayed in Table 2. The wet-beneficiated Warake gypsum sample B1 improved in surface area from 289.924 m^2/g to 316.747 m^2/g with an increment of 26.823 m^2/g after wet-beneficiation. The pore size increases while the pore volume decreases from 0.180 cm^3/g to 0.162 cm^3/g. The surface area of Afuze wet-beneficiated local gypsum sample C1 increases from 270.108 m^2/g dry-beneficiated to 292.598 m^2/g. This shows an improvement in the surface area due to wet-beneficiation with 22.49 m^2/g increment. The pore size decreases after wet-beneficiation from 2.122 to 2.101 nm while the pore volume increases, which also indicates the effect of its hardness. Wet-beneficiated Aviele gypsum sample D1 also shows improvement in the surface area from 204.515 to 265.156 m^2/g. The microporous nature of the dry-beneficiated Aviele local gypsum sample (1.853 nm) becomes mesoporous (2.108 nm) after wet-beneficiation with a decrease in the pore volume. High pore size and surface area are needed for effective reaction, and this reaction is within the crevices of the material.

3.2.1 XRF analysis

3.2.1.1 XRF Analysis Result of Dry-Beneficiated Gypsum samples

The elemental compositions and active components of dry-beneficiated SIG and Local gypsum samples are shown in Tables 3 and 4, respectively, while Table 5 compares the elemental compositions of gypsum obtained from literature with the present study. These compositions show the requirement in terms of gypsum purity.

Table 3: Elemental Compositions of Dry-Beneficiated SIG and Local Gypsum

Elemental Compositions	SiO_2 (%)	Al_2O_3 (%)	Fe_2O_3 (%)	CaO (%)	MgO (%)	K_2O (%)	Na_2O (%)	SO_3 (%)	Cl (%)
SIG A	2.57	0.74	0.72	31.72	0.81	0.11	0.09	41.83	0.003
Warake B	3.35	1.05	1.05	31.81	1.41	0.11	0.03	40.45	0.008
Afuze C	1.72	0.72	1.36	31.60	0.93	0.07	0.02	42.93	0.002
Aviele D	1.61	0.66	1.11	31.58	0.88	0.07	0.00	43.44	0.000

Generally, gypsum contains oxides of silicon, aluminium, iron, calcium, magnesium, sulphur, potassium, chlorine, and sodium, as well as trace amounts of nickel, barium, phosphorus, titanium, and a few others in varying quantities, depending on their sources and pretreatment methods. The highly active component (CaO) and SO_3 indicate purity and efficiency in cement setting time (Muhammad *et al*., 2021). The high presence of impurities can degrade the quality of cement. The active component levels in the gypsum samples from SIG and Local conform to previously studied local and foreign samples and are even higher in some others (England sample). Overall, the composition of active components in the Local gypsum samples is favourable, making them appropriate for cement manufacture. Table 4 presents the active components of the dry-beneficiated SIG and Local gypsum sources and the requirement in terms of gypsum purity.

Table 4: Active Components of Dry-Beneficiated SIG and Local Gypsum ($CaO+SO_3$) and (SO_3) purity of the content.

Samples	$CaO+SO_3$ (%)	SO_3 Purity (%)	Impurities (%)	Water of crystallization (%)
SIG A	73.55	89.93	5.043	21.407
Warake B	72.26	86.97	7.008	20.732
Afuze C	74.53	92.30	4.822	20.648
Aviele D	75.02	93.40	4.330	20.650

Table 5: Elemental Compositions of Dry-Beneficiated SIG, Local Gypsum, and previously studied literature.

Constituents	Strydom et al., (1997)		Ajayi & Dugbe, (2004)					López-Delgado et al., (2014)	SIGA	WB		
	SG	PG	B	G	S	T	IG				AC	AD
SiO_2	0.5	0.5	3.85	5.08	4.00	0.37	2.68	*2.88 – 3.95	2.57	3.35	1.72	1.61
Al_2O_3	0.4	0.1	1.55	1.56	1.19	0.14	0.81	*0.85 – 1.10	0.74	1.05	0.72	0.66
Fe_2O_3	0.8	0.1	0.60	0.59	0.49	0.01	0.30	*0.36 – 0.53	0.72	1.05	1.36	1.11
CaO	32.2	31.7	31.30	29.45	30.20	32.36	33.61	*42.10 – 43.31	31.72	31.81	31.60	31.58
MgO	0.6	0.1	0.54	0.56	0.54	0.57	0.60	*2.65 – 4.81	0.81	1.41	0.93	0.88
SO_3	45.4	44.8	40.96	40.15	40.00	44.73	38.66	*46.31 – 49.06	41.83	40.45	42.93	43.44
Combined H_2O	NR	NR	NR	NR	NR	NR	NR	NR	21.41	20.73	20.65	20.65
K_2O	0.04	0.0	0.10	0.13	0.15	0.01	0.40	*0.16 – 0.24	0.11	0.11	0.07	0.07
Na_2O	0.0	0.04	0.02	0.00	0.1	0.00	0.01	NR	0.09	0.03	0.02	0.00
Cl	0.00	0.00	NR	NR	NR	NR	NR	NR	0.003	0.008	0.002	0.00

*values are dependent on particle size; NR – Not reported; SG & PG – Synthetic & Phosphogypsum; B, G, S, T, IG – Borno, Gombe, Sokoto, Thailand, and England sourced gypsum; SIGA – Spain imported gypsum A, WB – Warake B, AC – Afuze C & AD – Aviele D.

The dry beneficiated SIGA gypsum sample is slightly purer than the Warake B gypsum sample, as seen in Table 4 and is within the required percentage content of gypsum for cement production (85-90%), according to Uriah (2016). SIG sample has an active component of 73.55% and SO_3 purity of 89.93% with combined impurities (SiO_2, Al_2O_3, Fe_2O_3, MgO, K_2O, Na_2O and Cl) of 5.043% and water of crystallization of 21.407%. Warake gypsum sample shows similar characteristics with 72.26% active component, 86.97% SO_3 purity, 7.008% combined impurities and 20.732% water of crystallization. The number of active components present in the gypsum and the high percentage of SO_3 indicate its purity and effectiveness in regulating cement setting time, and the above results correspond to the report findings by Muhammad *et al.* (2021). The presence of a high percentage of CaO and SO_3 content in Table 3, in comparison with those standard values, shows that the major components in gypsum are Calcium oxide and Sulfur trioxide while minimizing the presence of other compounds as impurities when considering gypsum for cement production.

3.2.1.2 Wet-Beneficiated Local Gypsum XRF Analysis

The elemental compositions and active components of wet-beneficiated local gypsum using X-ray fluorescence spectrometry are shown in Tables 6 and 7.

Table 6: Elemental Compositions of Wet-Beneficiated Local Gypsum

Elemental Compositions	SiO_2 (%)	Al_2O_3 (%)	Fe_2O_3 (%)	CaO (%)	MgO (%)	K_2O (%)	Na_2O (%)	SO_3 (%)	Cl (%)
Warake B1	1.19	0.37	0.60	32.85	1.30	0.06	0.03	42.60	0.006
Afuze C1	0.35	0.31	0.70	32.24	0.87	0.04	0.00	44.38	0.002
Aviele D1	0.37	0.30	0.59	32.38	0.83	0.04	0.01	44.38	0.003

Table 7: Active Components of Wet-Beneficiated Local Gypsum ($CaO+SO_3$) and Purity of the SO_3 Content.

Samples	$CaO+SO_3$ (%)	SO_3 purity (%)	Impurities (%)	Water of crystallization (%)
Warake B1	75.45	91.59	3.556	20.994
Afuze C1	76.63	95.44	2.272	21.098
Aviele D1	76.76	95.42	2.143	21.097

Wet-beneficiation reduced impurities in locally sourced gypsum, as shown in Table 6, with a subsequent increase in purity due to water washing. The results, when compared with previous studies from literature in Table 5, showed that Warake gypsum (B1) exhibited 32.85 % CaO, 42.60 % SO_3 and 75.45 % active component, influencing cement setting time. Impurities dropped from 7.008 % to 3.556 %, while the active component and SO_3 purity increased, as seen in Table 7. Afuze gypsum (sample C1) displayed 32.24 % CaO and 44.39 % SO_3 with 76.63 % active component. Similar findings were reported by Moalla *et al.* (2017) and Wang *et al.* (2020). Aviele gypsum exhibited analogous improvements, including higher SO_3 purity and lower impurities after wet-beneficiation. The purity level of the local gypsum after wet-beneficiation with water shows a remarkable improvement, and this confirmed the reported findings of Adams *et al.* (2021). In conclusion, local gypsum outperformed SIG counterparts in both dry and wet-beneficiated forms. This highlights the benefits of wet-beneficiation in increasing gypsum purity and discouraging gypsum importation.

3.2.2 FTIR analysis

Figure 1(a, b, c, and d) below shows the FTIR spectra of the dry-beneficiated Spain Imported & local gypsum samples. Significant absorption peaks were seen in the dry-beneficiated Spain gypsum, as shown by the different functional groups. The functional groups present include (−COOH) group, hydroxyl (−OH) group, cyano (−C≡N) group with strong C≡N stretch, carbonyl (−C=O) group with strong C=O, amide ($CO-NH_2$) group with medium to strong N−H stretch, ethoxy group (−OR) with medium to strong (C−O and =C−O−C symmetric), halides group with strong C−F, C−Br and C−I stretch, and stretching band linking to C=C and −C≡C− functional groups. Similar functional groups were observed for the Warake gypsum sample. This observation agrees with the findings reported by Akhabue *et al.* (2020) and Xiaodi et (2022*).*

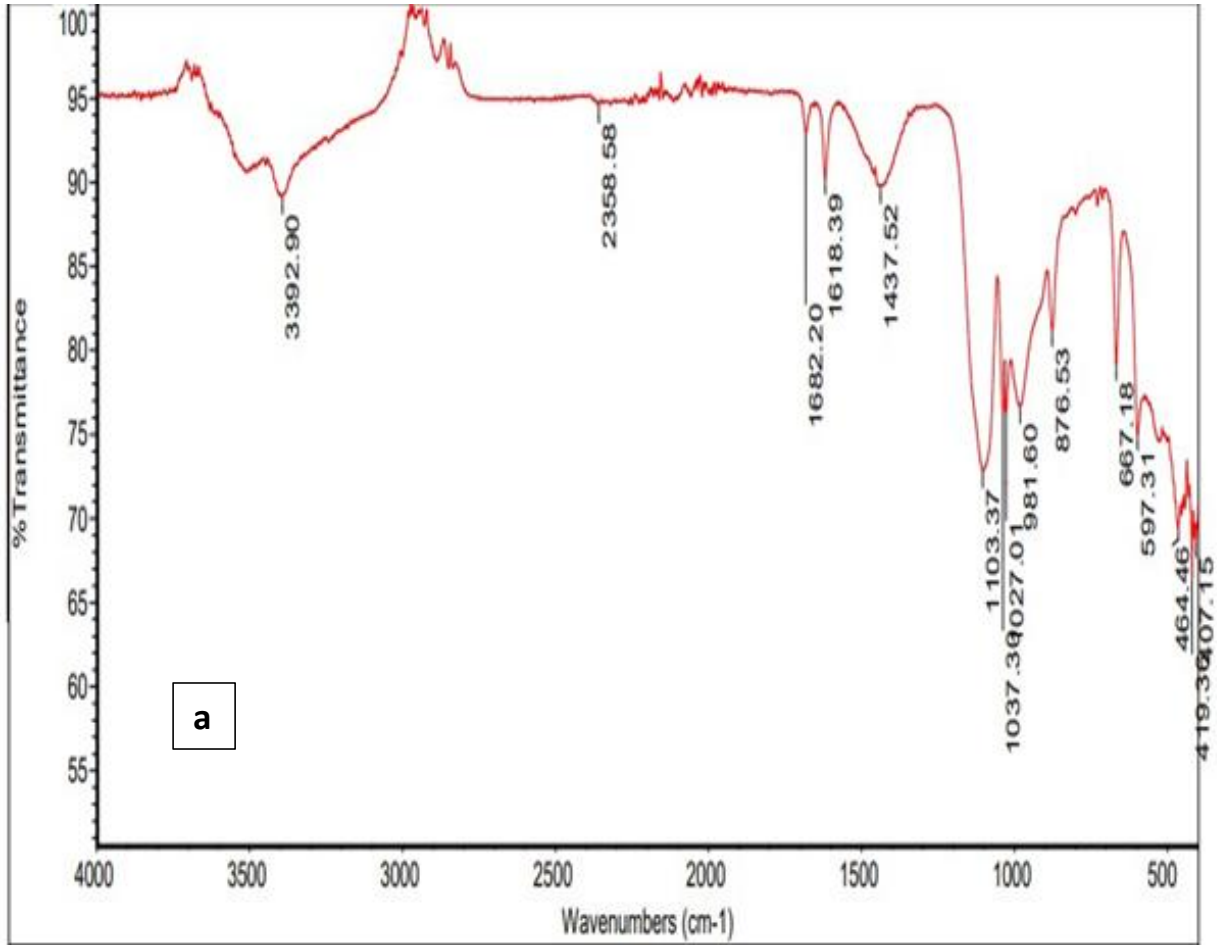
%Transmittance
Wavenumbers (cm-1)
3392.90
2358.58
1682.20
1618.39
1437.52
1103.37
1037.39
1027.01
981.60
876.53
667.18
597.31
464.46
419.36
407.15
a

.

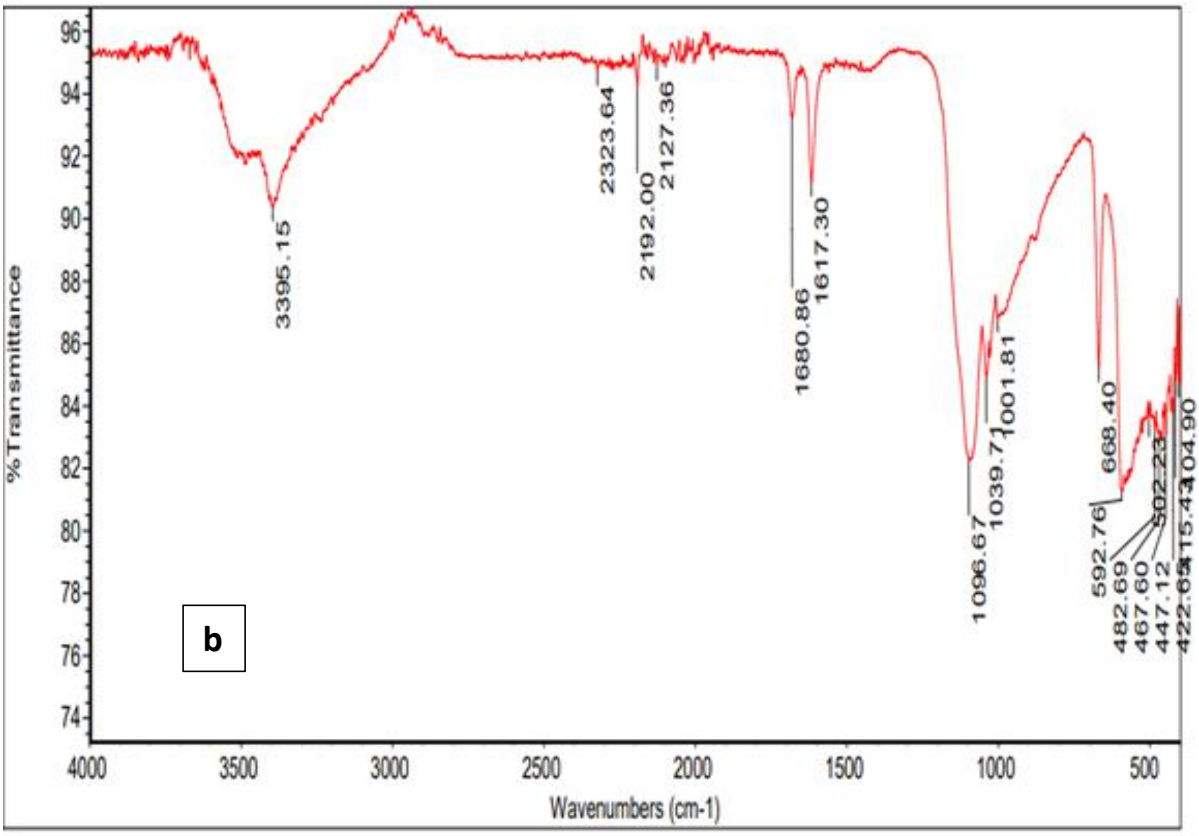

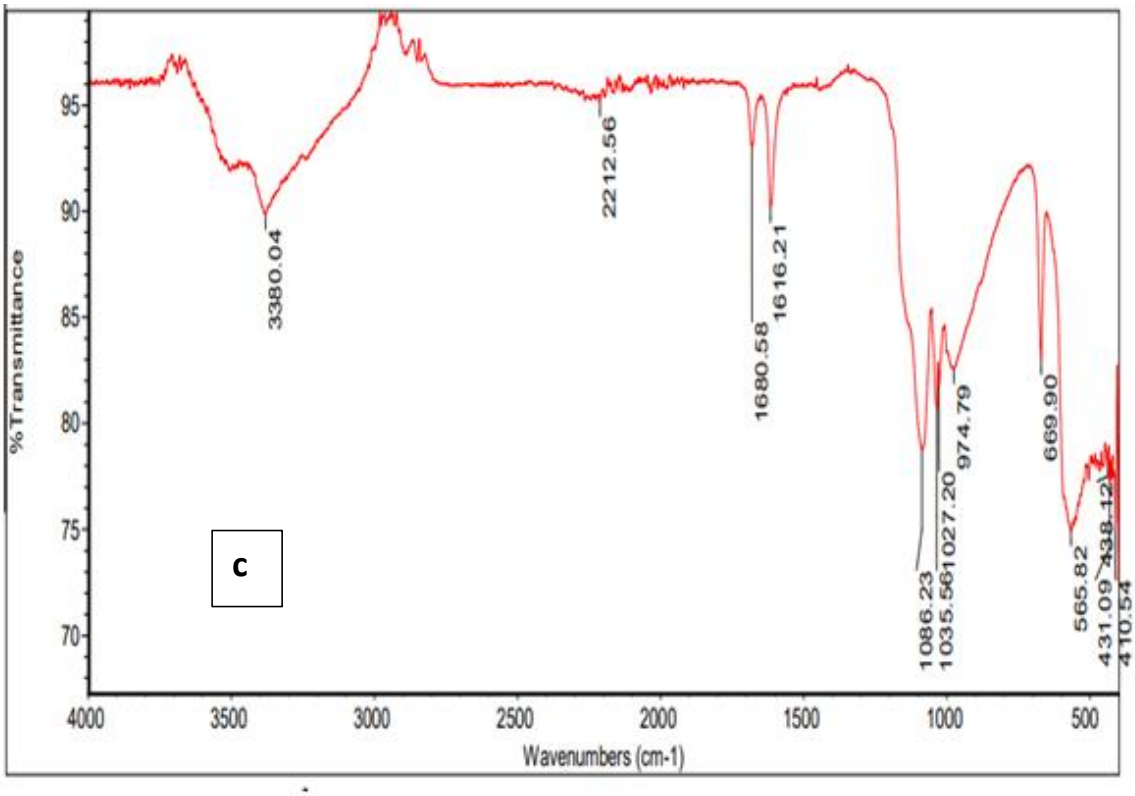

Similar functional groups were observed for the wet-beneficiated local gypsum samples at different wavenumbers from those of the dry-beneficiated.

When the occurring functional groups interact with clinker minerals and other positively charged components during cement blending, these diverse functional groups in dry-beneficiated Spain and Warake

gypsum enable chemical reactions and excellent homogeneity (Xiaodi *et al.,* 2022). These polar, hydrophilic functional groups improve cement's ability to bind water and hydrate it during chemical reactions. These functional groups interact with other gypsum constituents, including MgO, CaO, and SO_3, to produce hydrated salts (Ma *et al.,* 2021).

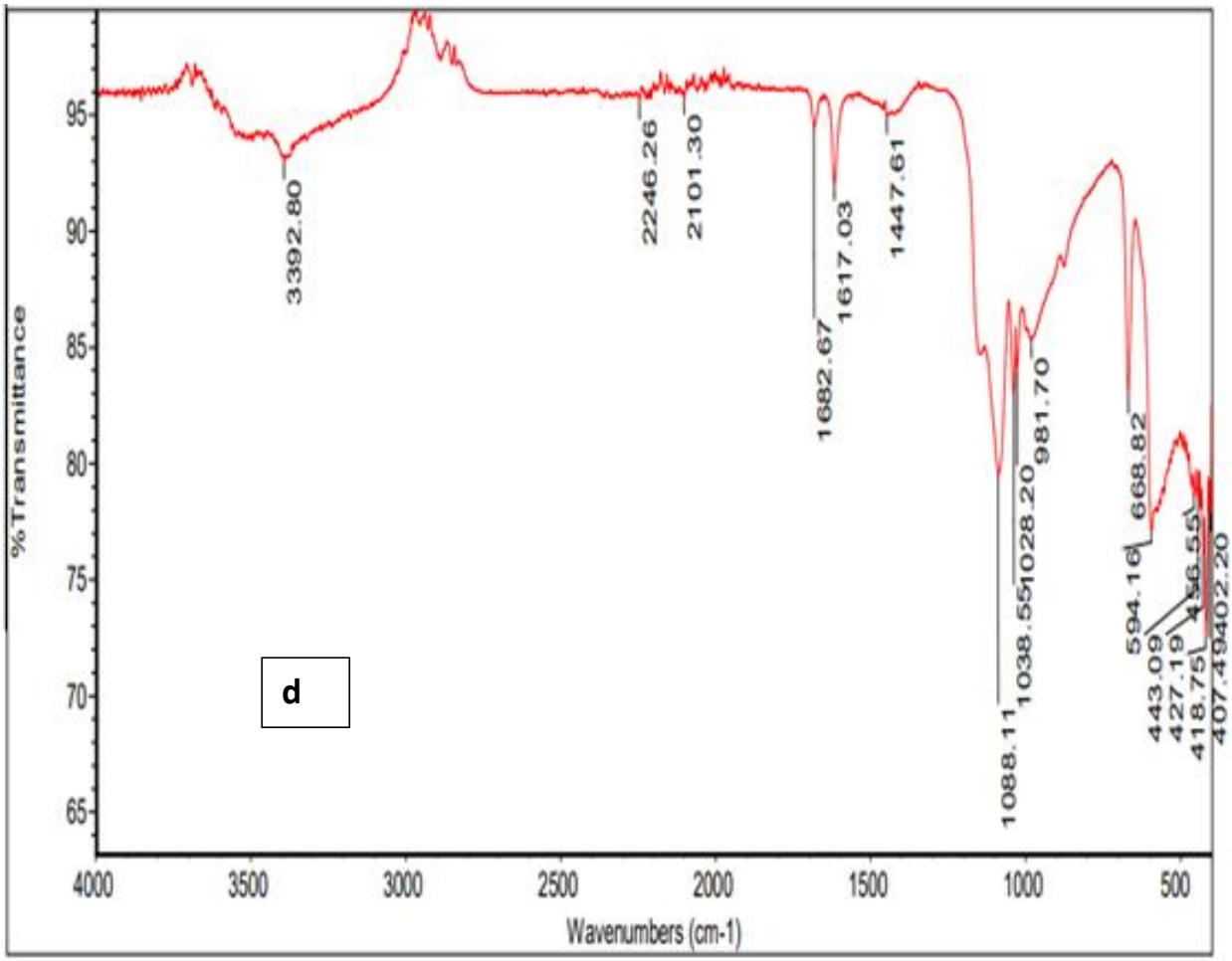

Figure 1: FTIR Spectra of Dry-beneficiated (a)Imported Gypsum, (b)Warake Gypsum, (c)Afuze Gypsum and (d)Aviele Gypsum Samples

The functional groups in the dry-beneficiated and wet-beneficiated local gypsum samples remained unchanged, though the wavenumbers decreased in values after wet-beneficiation. The polarity and hydrophilic nature of these functional groups in gypsum create a medium for the ionic interactions with the positively charged clinker minerals (C_2S, C_3S, C_3A, C_4AF). These ease the hydration process, thereby giving enough time for chemical reaction, homogenization and proper regulating of the setting time of the cement (Xiaodi *et al.,* 2022).

4 COST ANALYSIS FOR LOCAL GYPSUM PRODUCTION

The cost analysis of both SIG and locally sourced gypsum was done in line with the principles and fundamentals highlighted in plant design (Towle & Sinnott, 2008). Table 8 shows the cost of importing SIG to Nigeria.

Table 8: Cost of Imported Gypsum

Ton	Value (₦)	Cost of Transportation (₦/ton)	Value (₦/ Ton)
1.00	64,231.09	17,000.00	47,231.09

A unit (1 ton) of gypsum cost ₦47,231.09 in the year 2022, while the cost of transportation within the country is ₦ 17,000.00. Therefore, the cost of Spain's imported gypsum, including the cost of transportation within Nigeria, is ₦ 64,231.09.

4.1 Cost of Local Gypsum

The cost of producing locally sourced gypsum from the beginning of the land purchase license to startup operations is highlighted in this study. This cost is in line with the principles and fundamentals highlighted in plant design (Towle & Sinnott, 2008). Table 9 illustrates the cost of production of local gypsum at the time of carrying out this study.

Table 9: Overall production cost for Local Gypsum in Edo State

S/N	Item	Quantity	Cost/Unit (₦)	Cost/Month (₦)	Cost/Year (₦)
1	**LAND**				
i	Procurement and development		50,000,000.00	50,000,000.00	50,000,000.00
2	**EQUIPMENT/INSTALLATION**				
i	Grader	2	75,000,000.00	150,000,000.00	150,000,000.00
ii	Drilling Machines	2	50,000,000.00	100,000,000.00	100,000,000.00
iii	Dump Trucks	10	42,000,000.00	420,000,000.00	420,000,000.00
iv	Hydraulic Excavators	2	75,000,000.00	150,000,000.00	150,000,000.00
v	Wheel loader	4	55,000,000.00	220,000,000.00	220,000,000.00
vi	Jaw Crusher	1	23,000,000.00	23,000,000.00	23,000,000.00
vii	Hammer Milling Machine	1	8,000,000.00	8,000,000.00	8,000,000.00
viii	Conveyors	1	6,000,000.00	6,000,000.00	6,000,000.00
ix	Bulldozer	2	70,000,000.00	140,000,000.00	140,000,000.00
x	Hopper and Screen	1	3,000,000.00	3,000,000.00	3,000,000.00
	Total Cost of Equipment			**1,220,000,000.00**	**1,220,000,000.00**
3	**COST OF INSTALLATION**				
i	Installation of Equipment		20,000,000.00	20,000,000.00	20,000,000.00
	Total Cost of Installation			**20,000,000.00**	**20,000,000.00**
4	**CIVIL/DESIGN**				
i	Design and Civil		50,000,000.00	50,000,000.00	50,000,000.00
	Total Cost of Design and Civil			**50,000,000.00**	**50,000,000.00**
5	**COST OF OFFICE VEHICLES**				
i	Office Hilux	3	15,000,000.00	45,000,000.00	45,000,000.00
ii	Office Bus	2	20,000,000.00	40,000,000.00	40,000,000.00
	Total Cost of Official Vehicles			**85,000,000.00**	**85,000,000.00**
6	**OFFICE, FURNITURE AND FITTINGS**				
i	6 Bedroom flat Building	1	12,000,000.00	12,000,000.00	12,000,000.00

S/N	Item		Quantity	Cost/Unit (₦)	Cost/Month (₦)	Cost/Year (₦)
ii	Office Chairs		20	15,000.00	300,000.00	300,000.00
iii	Air conditioning		6	150,000.00	900,000.00	900,000.00
iv	Office Printers		4	130,000.00	520,000.00	520,000.00
	Total Cost of Office, Furniture				**13,720,000.00**	**13,720,000.00**
7	**COST OF MANPOWER**					
i	Quarry Manager		1	400,000.00	400,000.00	4,800,000.00
ii	Mining Engineers		2	200,000.00	400,000.00	4,800,000.00
iii	Geologists		2	200,000.00	400,000.00	4,800,000.00
iv	Accountants		2	150,000.00	300,000.00	3,600,000.00
v	Sales		2	190,000.00	380,000.00	4,560,000.00
vi	HR/Admin		2	190,000.00	380,000.00	4,560,000.00
vii	Operators		10	100,000.00	1,000,000.00	12,000,000.00
viii	Drivers		6	70,000.00	420,000.00	5,040,000.00
ix	Driller Man		2	90,000.00	180,000.00	2,160,000.00
x	Blaster man		4	100,000.00	400,000.00	4,800,000.00
xi	Security		10	100,000.00	1,000,000.00	12,000,000.00
xii	Cleaners		4	40,000.00	160,000.00	1,920,000.00
	Total Cost of Manpower				**5,420,000.00**	**65,040,000.00**
8	**COST OF UTILITIES**					
i	AGO	₦ 800/L	20,000.00	800.00	16,000,000.00	192,000,000.00
ii	Petrol	₦ 270/L	2,000.00	270.00	540,000.00	6,480,000.00
iii	Electricity			4,000,000.00	4,000,000.00	48,000,000.00
iv	Water expenses			1,000,000.00	1,000,000.00	12,000,000.00
	Total Cost of Utilities				**21,540,000.00**	**258,480,000.00**
9	**COST OF EXPLOSIVES**					
i	Ammonium nitrate	₦ 2000/KG	200.00	2,000.00	400,000.00	4,800,000.00
ii	Dynacord	₦350/Meter	4,000.00	350.00	1,400,000.00	16,800,000.00
iii	Electric Detonator	₦ 1200/pc	4,000.00	1,200.00	4,800,000.00	57,600,000.00

S/N	Item	Quantity	Cost/Unit (₦)	Cost/Month (₦)	Cost/Year (₦)
iv	High Gelatine ₦2300/KG	10,000.00	2,300.00	23,000,000.00	276,000,000.00
	Total Cost of Explosives			**29,600,000.00**	**355,200,000.00**
10	**STARTUP COST /MISCELLANEOUS**				
	Miscellaneous		10,000,000.00	10,000,000.00	120,000,000.00
	Cost of Miscellaneous			**10,000,000.00**	**120,000,000.00**
	TOTAL COST OF PRODUCTION PER YEAR			**1,505,280,000.00**	**2,237,440,000.00**

Considering large-scale mining of local gypsum especially in Edo state, the cost of production per ton of the local gypsum as at the time of carrying out this research is summarised in Table 9. This cost is done considering the current Nigeria's 2022 economy. This costing covers land and land development, equipment, installation, civil/design, cost of official vehicles, office furniture and fittings, cost of workforce, cost of utilities, cost of explosives for blasting and startup/miscellaneous costs. Since gypsum processing involves excavating, crushing, screening and grinding, the need for the purchase of the equipment, as mentioned earlier, is necessary. This gives a total cost of production of two billion, two hundred and thirty-seven million, four hundred and forty-four thousand naira only per year while the cost of production per month is one billion, five hundred and five million, two hundred and eighty million naira only for new investment on a largescale production.

4.2 Sales of Local Gypsum

The sales of the local gypsum after production on a large scale are highlighted to determine the profit margin per ton of gypsum. Table 10 shows the sales at a unit price of ₦35,000.00 per ton of the local gypsum.

Table 10: Sales of Local Gypsum

S/N	Description	Quantity	Amount ₦
i	Number of trucks per day	19.00	
ii	Number of trucks per month (19 Trucks x 30 days)	570.00	
iii	Average tonnage per truck	35.00	
iv	Sales unit price per ton		35,000.00
v	Sales for a day (19 trucks x ₦35,000 x35)		23,275,000.00
vi	Sales for a month (570 Trucks x 35Tons x ₦35,000)	30.00	698,250,000.00
vii	Sales for a year (340 days x 19 Trucks x35Tons x ₦35,000)	340.00	7,913,500,000.00
viii	Gross profit per year (Total sales/yr. - total cost of prod/yr.)		5,676,060,000.00
	Cost of Producing 1 Ton		
i	Total tonnage per year (19 trucks x 340 days x 35tons)	226,100.00	
ii	Cost of production per year		2,237,440,000.00
iii	Cost of producing 1 Ton (Cost of prod/yr. / Tons/yr.)		9,895.80
	Profit Margin		
i	Profit margin per Ton (Sales unit price - Cost of prod/tons)		25,104.20

From the production and sales analysis of all the locally sourced gypsum in comparison with the cost of importation of gypsum, it is imperative to note that producing gypsum on a large scale in Nigeria, including transportation to proximate cement industries in Nigeria, will be more viable. Therefore, it is preferable to buy locally sourced gypsum at the selling price of ₦35,000.00 than depending on imported gypsum at the cost of ₦64,231.09, including the cost of transportation.

5.0 CONCLUSION

Gypsum samples from both imported and local sources were prepared using dry and wet-beneficiation methods to determine their moisture content, eliminate impurities, and prepare the desired hemihydrate. XRF, XRD, BET, and FTIR characterizations of the local gypsums showed that

the elemental composition, surface chemistry, functional groups, and textural qualities were similar to those of the imported Spanish gypsum and better than other gypsums obtained from other countries, as shown from various studies. The cost analysis of the entire production and sales process narrowed down to the profit margin of local production per tonne of gypsum produced and sold, showed a profit margin of ₦25,104.20 per tonne of local gypsum sold to cement manufacturers at the 2022 purchase index compared to the cost of gypsum imported from Spain by manufacturers. This indicates that local gypsum samples are a viable substitute for imported Spanish gypsum in the production of cement due to the required quality, compliance with purity standards, and cost efficiency.

REFERENCES

Abdul-Wahab, S. A., Al-Dhamri, H., Ram, G., and Chatterjee, P. V. (2021). An overview of alternative raw materials used in cement and clinker manufacturing. *International Journal of Sustainable Engineering*, 14(4), 743–760.

Adams, L. A., Enobong, Reginald. E., Taiwo, A., Stella, O., and John, M. (2021). Facile purification of Warake mined gypsum and its use for preparing nano-hemihydrates. *Journal of Metals*, *Materials and Minerals*, 106110.

Ahmad, A. (2021, July 6). Comminution a heart of mineral processing. Retrieved February 5,2023,fromTechnologyTimeswebsite:https://www.technologytimes.pk/2021/07/06/comminution-a-heart-of-mineral-processing/

Ajayi, O. O., & Dugbe, S. A. (2004). Chemical Analysis of some Nigerian Gypsum and Limestone Samples Utilized by a Leading Cement Manufacturing Industry. *Global Journal of Pure and Applied Sciences*, *10*(1), 87–90. https://doi.org/10.4314/gjpas.v10i1.16363.

Akhabue, E. C., Evidence, O. O.-B., Eghe, A. O., and Otoikhian, S. K. (2020). Development of a bio-based bifunctional catalyst for simultaneous esterification and transesterification of neem seed oil: Modeling and optimization studies. *Renewable Energy*, *152*(2020), 724–735.

Al-Ridha, A. S. D., Abbood, A. A., Elaiwi, E. H., Hussein, H. H., and Dheyab, L. S. (2020). Increasing the setting time of Warake gypsum (Joss) by the use of TGP additive. *IOP Conference Series: Materials Science and Engineering*, *888*(1), 012078.

Amenaghawon, N. A., Nelson, I. E., and Kessington, O. (2021). Optimum biodiesel production from waste vegetable oil using functionalized cow horn catalyst: A comparative evaluation of some expert systems. *Cleaner Engineering and Technology*, *4*(100184), 1–14.

ASTM D792: Standard Test Methods for Density and Specific Gravity (Relative Density) of Plastics by Displacement. (2020, July 29). https://www.astm.org/standards/d792

ASTM-C471 | Chemical Analysis of Gypsum & Gypsum Products, Standard Testmethods For | Document Center, Inc. (1991, February 22). [ASTM C471]. https://www.document-center.com/standards/show/ASTM-C471

Bouzit, S., Laasri, S., Taha, M., Laghzizil, A., Hajjaji, A., Merli, F., and Buratti, C. (2019). Characterization of natural gypsum materials and their composites for building applications. *Applied Sciences*, *9*(2443), 15. https://doi.org/doi:10.3390/app9122443

Cordon, H. C. F., Ferreira, M. S., and Ferreira, F. F. (2021). Comparative analysis of recycled plaster composition determined by X-ray powder diffraction and thermogravimetric analyses. *Construction Materials*, 1(2), 105–121.

Dafni, F., Stergios, A., Eleni, V., Elias, V., Costas, P., Stephen, O., and Geofrey, D. (2019). Microstructure and compressive strength of gypsum-bonded composites with papers, paperboards and Tetra Pak recycled materials. *Journal of Wood Science*, *65*(42), 1–8.

Dogara, M. D., and Aloa, J. O. (2017). Preliminary estimate of gypsum deposit based on Wenner and Schlumberger electrical resistivity methods at Ikpeshi, Edo State, Nigeria. *Science World Journal*, *12*(2).

Ghumman, S. A., Mahmood, A., Noreen, S., Rana, M., Hameed, H., Ijaz, B., and Rehman, M. F. (2022). Formulation and evaluation of quince seeds mucilage – sodium alginate microspheres for sustained delivery of cefixime and its toxicological studies. *Arabian Journal of Chemistry*, *15*(6), 103811.

Gunnar, H., and Kristine, K. (2020, September 23). Beneficiation of raw gypsum ore. Retrieved January 21, 2023, from 2021 SURP Symposium website: https://surp.calpoly.edu/2020/beneficiation-of-raw-gypsum-ore/

James, O. O., Mesubi, M. A., Adekola, F. A., Odebunmi, E. O., and Adekeye, J. I. D. (2008). Beneficiation and Characterization of a bentonite from North-Easter Nigeria. *Journal of the North Carolina Academy of Science*, *124*(4), 154–158.

Layr, K., and Hartlieb, P. (2019). Market analysis for urban mining of phosphogypsum. *BHM Berg- Und Hüttenmännische Monatshefte*, *164*(6), 245–249.

López-Delgado, A., López-Andrés, S., Padilla, I., Alvarez, M., Galindo, R., & José Vázquez, A. (2014). Dehydration of Gypsum Rock by Solar Energy: Preliminary Study. *Geomaterials*, *04*(03), 82–91. https://doi.org/10.4236/gm.2014.43009.

Ma, H., Chen, S., Song, Y., Yin, D., LI, X., and Li, X. (2021). Experimental investigation into the effects of composition and microstructure on the tensile properties and failure characteristics of different gypsum rocks. *Scientific Reports*, *11*(14517), 1–13.

Moalla, R., Gargouri, M., Khmiri, F., Kamoun, L., and Zairi, M. (2017). Phosphogypsum purification

for plaster production: A process optimization using full factorial design. *Environmental Engineering Research*, 1–29. https://doi.org/10.4491/eer.2017.055.

Mohamad, N., Muthusamy, K., Embong, R., Kusbiantoro, A., and Hashim, M. H. (2022). Environmental impact of cement production and solutions: A review. *Materials Today: Proceedings*, *48*, 741–746.

Mohammad, A., Hoang, N., Tapio, F., Harisankar, S., Ville-Veikko, T., Anu, K., and Paivo, K. (2022). On the hydration of synthetic aluminosilicate glass as a sole cement precursor. *Cement and Concrete Research*, *159*(106859), 1–12. https://doi.org/doi.org/10.1016/j.cemconres.2022.106859

Muhammad, A. D., Amartey, Y. D., Kaura, J. M., Ijimdiya, T. S., and Lawan, A. (2021). Effect of Warake sourced Nigerian Gypsum on the strength and microstructure of portland cement mortar. *Nigerian Journal of Technology*, *39*(4), 1001–1010.

Onat, L. O., Valiyev, K. R., Agapov, R. V., and Kangarli, L. M. (2016). Analysis of anhydrite's effects on quality of cement. *International Research Journal of Engineering and Technology*, 03(09), 7.

Randazzo, L.; Montana, G.; Hein, A.; Castiglia, A.; Rodonò, G.; Donato, D.I. Moisture absorption, thermal conductivity and noise mitigation of clay based plasters: The influence of mineralogical and textural characteristics. *Appl. Clay Sci.* 2016, 132–133, 498–507

Standard Test Methods for Laboratory Determination of Water (Moisture) Content of Soil and Rock by Mass. (2019, March 19). [Html]. https://www.astm.org/d2216-19.html

Strydom, C. A., Groenewald, E. M., & Potgieter, J. H. (1997). Thermogravimetric studies of the synthesis of cas from Gypsum, CaSo4·2H2O and phosphogypsum. *Journal of Thermal Analysis*, *49*(3), 1501–1507. https://doi.org/10.1007/BF01983709.

Towle, W., & Sinnott, R. K. (2008). Chemical engineering design: Principles, practice and economics of plant and process design. Elsevier/Butterworth-Heinemann.

Uriah, L. (2016). Warake sourcing of gypsum for industrial utilization in Nigeria. *Nigeria Society of Chemical Engineers Conference,* 46, 23-32.

Wang, J., Dong, F., Wang, Z., Yang, F., Du, M., Fu, K., and Wang, Z. (2020). A novel method for purification of phosphogypsum. *Physicochemical Problems of Mineral Processing*, *56*(5), 975–983. https://doi.org/10.37190/ppmp/127854

Xiaodi, D., Serdar, A., Mert, Y. Y., and Geert, D. S. (2022). Early structural build-up, setting behavior, reaction kinetics and microstructure of sodium silicate-activated slag mixtures with different retarder chemicals. *Cement and Concrete Research*, *159*(106872), 1–15.

Zmemla, R., Chaurand, P., Benjdidia, M., Elleuch, B., and Bottero, J. Y. (2016). Characterization and pH Dependent Leaching Behavior of Tunisian Phosphogypsum. *American Scientific Research Journal for Engineering, Technology, and Sciences*, *24*(1), 230–244.

10.51975/24390208.som
Journal of the Nigerian Society of Chemical Engineers, 39(2), 2024

INVESTIGATING CALCITE-INDUCED CRACK HEALING TIME-DEPENDENT MODEL FOR BIO-SANDCRETE USING COMSOL MULTIPHYSICS REACTION MODULE

[*]Abdullahi, M.[1], Odigure, J. O.[2], Aliyu, M. B[3]. Aibinu, A. M.[4] and Olarewaju, S. A.[5]

[*1]Department of Chemical Engineering, The Federal Polytechnic, P. M. B 55, Bida, Nigeria

Email: tsowagba@yahoo.com

[2] Department of Chemical Engineering, Federal University of Technology, Minna.

[3]Department of Microbiology, The Federal Polytechnic, P. M. B 55, Bida, Nigeria

[4]Department of Mechatronics Engineering, Federal University of Technology, Minna

[5]Department of Chemistry and Industrial Chemistry, Faculty of Pure and Applied Sciences, Kwara State University, Malete

ABSTRACT

The ability of sandcrete to autogenously heal itself and maintain its physicochemical characteristics is the hallmark of sandcrete technology. Crack healing has become a significant concern in the construction industry, as it directly impacts the durability and longevity of structures. This study aims to developing a 2D Multiphysics model for crack healing in sandcrete using the finite element method (FEM). The research specifically delves into the biochemical reaction profiles and calcite formation utilizing the COMSOL Reaction Engineering Lab (CREL) within the COMSOL Multiphysics software. The findings were validated by comparing the calcite concentration that filled the crack space in a notched physical model (50 x 50 x 50 mm cube) cured for 1 – 28 days under ambient conditions. The simulated concentration profiles of the reactants and products showed increased species concentrations (Ca^{2+}, CH_3COO^-, OH^-, HCO_3^-) at early age. The simulated data also revealed a complete degradation of calcium acetate ($Ca(CH_3COO)_2$) after 15 days post crack formation, with a significant rise in calcium carbonate ($CaCO_3$) concentration as Bacillus sphaericus bacteria metabolized. Both experimental and simulated results demonstrated higher calcite concentrations in the S-B composite (22.31 and 35.01 mol/m^3) under ambient conditions compared to the control bacteria-free standard sandcrete (S-S) composite (8.32 mol/m^3) after 28 days of curing. The concentration of Ca^{2+} ions in the sandcrete crack responsible for healing after 28 days, ranged between 1.53-1.71 mol/m^3 and 0.4-1.76 mol/m^3 for both experimental and simulated S-B composites, while the control specimen exhibited a range of 0.04-0.57 mol/m^3.

Keywords: *Sandcrete, Simulation, FEM, carbonation, crack healing, Modelling*

1. INTRODUCTION

Sandcrete is one of the vital components in the construction industry, playing a significant role in the infrastructural development of a nations and the overall advancement of human civilization. Its susceptible to environmental acidic gases, which infiltrate through microcracks, poses a challenge to the durability of sandcrete structures. The penetration of these acidic gases reduces the service life of sandcrete leading to the degradation and deterioration of the reinforcement, ultimately resulting in costly maintenance and repair work. The need for self-healing sandcrete arises from the detrimental effects of acidic gas ingress on sandcrete durability and resilience. The concept of self-healing in cement composite gained traction in recent years, with various studies focusing on assessing the impact of deterioration on the mechanical and transport properties of cement-based composites (Odigure, 2002; Balazs, 2007; Ghosh, 2009; Samuel De *et al.,*2022).

Research in computational modeling for cement-based self-healing composites is still in its early stages (Bagga *et al.,* 2022). The complexity of developing and simulating a numerical model that involves the complex coupling of chemical, mechanical, biological, and hydraulic equations may explain the limited use of numerical simulation in the bio-mineralization of cement composites. However, progress in this area has the potential to pave the way for the creation and production of smart-cement composites that could adapt to

environmental variations and heal themselves before any structural failure occurs.

Several studies (Balazs, 2007; Hu *et al.,* 2011; Zemskov *et al.,* 2014; Elrasoul and Haniffah, 2020; Chine *et al.,* 2018) highlight the importance of computational models in fluid-structure interactions such as acquiring critical information and predictions regarding dynamic behaviour, determining concentrations of intermediate species and identifying the carbonated front to offer valuable experimental guidelines. A model based on reactive transport properties utilizing biogrout in a 5 m column was reported by Wijngaarden *et al.* (2016). The simulated outcomes exhibited notable differences in the average final concentration of calcium carbonate in the column compared to experimental profiles. The authors suggested that developing a more complex model could help reduce the disparities between experimental and simulated results.

Elrasoul and Haniffah (2020) developed a 1-D numerical model of self-healing concrete by discretizing and simulating a Partial Differential Equation (PDE) using the Galerkin Finite element (GFE). The model was derived based on two nodes of linear elements in conjunction with the specified initial and boundary conditions. The mathematical model they developed was simulated and solved using MATLAB software to determine the time required for the bacteria-based concrete to heal. They observed that with a healing ratio of 60% and an initial urea concentration of 333 mol/m^3, complete crack healing could be achieved in 500 days.

The COMSOL Multiphysics software has been used in earlier studies to simulate the microscale corrosion and cracking process caused by non-uniform corrosion in reinforced concrete (Pan and Lu, 2012). Using COMSOL, the characteristics of porous and fractured media were examined by Perko *et al*. (2011). Richter *et al.* (2011) examined the reaction and diffusion processes occurring in mineral rock neglecting the morphological composition. Chine *et al.* (2018) used the Reaction Engineering Module in COMSOL Multiphysics to model the carbonation process of concrete made with pozzolanic cement with the properties exported to solve the space-dependent model as a function of time. The findings based on the numerical simulation showed the extent of carbonation depth (CD) expressed in terms of age and chemical species concentrations in the concrete. Their findings were validated empirically under a controlled environment.

Zemskov, Jonkers, and Vermeulen (2014) presented a 2-D mathematical model that evaluates the effect of varying technological factors on the efficiency and degree of crack repair with minimal influence on the physicochemical properties of concrete. They incorporated spores of bacteria (*Bacillus cohnii, Bacillus pseudofirmus*) and biochemical healing agents in the concrete mix encased in porous siliceous-clay capsules. The capsules release the encapsulated content when a fissure forms in the concrete matrix. The Galerkin Finite Element Method (GFEM) solved the developed model with the boundary of the computation having two moving fragments. Results show that the time for calcite to reach the center of the crack was 20 hours and 50 minutes. They also observed that the rate of crack healing depended on the width of the crack and capsule size. Shah and Bishnoi (2021) present a sensitivity analysis to explicate the effect of different parameters on the carbonation process in concrete. The developed model predicted carbonation depths and concluded that porosity and pore saturation are key factors controlling the carbonation rate in cement-based composites. In their computational simulations of the integrated mechanism in Microbially Induced Calcite Precipitation (MICP) for soil remediation, Wang and Nackenhorst (2020) demonstrated that the relationship between the mass transit rate and reaction rate, as well as bacterial dispersion, had a significant impact on the geographical distribution of the precipitated calcite's.

There are several models for the intrinsic and autonomous self-curing of non-bacterial concrete. These models have been examined numerous times recently (Mauludin and Oucif, 2019; Schlangen and Joseph, 2013; Fernandez *et al.*, 2021; Bagga *et al.*, 2022), with references to Bacteria Based Self-Healing Concrete (BBSHC) being restricted to Zemskov *et al.* (2014) early work. In these models, self-healing mechanisms for a typical elemental volume (TEV) of the material are described at the constitutive level. The utilization of the Chemical Engineering module (CEM) in the COMSOL Multiphysics simulator to simulate the bioremediation of cracks through carbonation in sandcrete has not been documented. This study aims to model and simulate the time-dependent bioremediation of cracks in sandcrete composite, and to determine the concentration profiles of reactant and product species coupled with calcite concentration using the Chemical Engineering module (CEM) in COMSOL Multiphysics software. The model simulation is based on the finite element method in two dimensions under controlled calcium acetate

concentration, age, and moisture as carbon dioxide (CO_2) and oxygen (O_2) ingress into the sandcrete composite.

2. MATHEMATICAL MODEL

Self-healing in sandcrete is a diffusional control process. The quality of encapsulated sandcrete materials greatly affects the rate of diffusion of metallic ions and oxygen, copious production of bacteria, and subsequent transformation of dissolved carbon dioxide (CO_2) to stable calcite that seals the crack. Fick's law of molecular diffusion and the shell progressive model mechanism were used to derive the reaction rate model for self-healing sandcrete. The healing process hinged on calcium ions, bacteria, water, and nutrients diffusing from a spherical perlite into the crack where calcite is precipitated.

The following suppositions were made to aid the development of the predictive analytic equations:

1. The calcite formed and sandcrete particles are assumed to be spherical and comparatively equal.
2. Microbiological-induced calcite forms under ambient conditions where bacteria act as catalysts, becoming activated as water enters a newly formed fissure, triggering the discharge of encapsulated nutrients and transforming calcium acetate into calcite.
3. The overall microbiological reaction is assumed to be irreversible:
   $CaC_4H_6O_4(s)+Bacteria+4O_2(g) \longrightarrow CaCO_3(s) + 3CO_2(g) +3H_2O(l)$ (1)
4. The rate at which O_2 dissolves in the sandcrete pore solution is equal to the rate it diffuses into the sandcrete particle.
5. Linear isotherm is assumed.

Let the intrinsic reaction rate for the conversion of dissolved calcium acetate (CA) at a constant volume system be equal to the rate of mass transfer of calcium ion from the bulk of fluid to the spherical perlite particle as given by:

$$\therefore \frac{dN_{Ca^{2+},L}}{dt} = 4\pi R_s^{\,2} k_m \left[(C_{Ca^{2+}})_b - (C_{Ca^{2+}})_s\right] \quad (2)$$

The mass transfer of CA through the immobilized bacteria occurs via molecular diffusion.

$$\therefore \frac{dN_{Ca^{2+},L}}{dt} = 4\pi r^2 (D_L)_e \left[\frac{dC_{Ca^{2+},L}}{dr}\right] \quad (3)$$

If the rate of calcium acetate (CA) consumption by the bacteria at the unreacted core is a first-order reaction with respect to the CA reaction at a constant volume, then,

$$r_p = \frac{dN_{Ca^{2+},c}}{dt} = k_1 C_{Ca^{2+},c} \quad (4)$$

The material balance for the spherical shell with product thickness ($CaCO_3$) *dr* is illustrated in Figure 1.

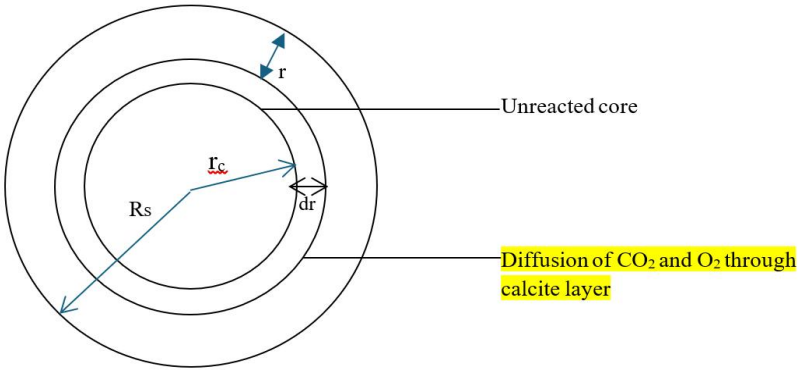

Figure 1: Shell distribute model for Ca^{2+} ion in an immobilized bacterium particle

$$(r+dr)^2 (D_L)_e \left[\frac{dC_{Ca^{2+},L}}{dr} + \frac{d}{dr}\left(\frac{dC_{Ca^{2+},L}}{dr}\right)dr\right] - r^2 (D_L)_e \frac{dC_{Ca^{2+},L}}{dr} + (r^2 dr) r_{\alpha,Ca^{2+}} = 4\pi r^2 dr \frac{dC_{Ca^{2+},L}}{dr} \quad (5)$$

At a steady state, the change of Ca^{2+} ion concentration in the sandcrete matrix equals zero. Simplifying Equation (5) and eliminating all terms containing dr^2 or dr^3 and assuming the $(D_L)_e$ is independent of the Ca^{2+} ion concentration, the differential equation becomes:

$$(D_L)_e\left[\frac{d^2C_{Ca^{2+},L}}{dr^2}+\frac{2}{r}\left(\frac{dC_{Ca^{2+},L}}{dr}\right)\right]+r_{\alpha,Ca^{2+}}=0 \quad (6)$$

$$\therefore \left[\frac{d^2C_{Ca^{2+},L}}{dr^2}+\frac{2}{r}\left(\frac{dC_{Ca^{2+},L}}{dr}\right)\right]+\frac{r_{\alpha,Ca^{2+}}}{(D_L)_e}=0 \quad (7)$$

The rate of Ca^{2+} ion consumption in the sandcrete matrix is assumed to follow first-order kinetics with respect to the concentration of Ca^{2+} ions.

$$r_{\alpha,Ca^{2+}}=k_1C_{Ca^{2+},L} \quad (8)$$

Where:

$r_{\alpha,Ca^{2+}}$ = Intrinsic reaction rate for Ca^{2+} ion (mol/kg s);

v = volume of sandcrete (m^3)

The domain for Equations (7) and (8) is the center of the particle; $\frac{dC_{Ca2+}}{dr}=0$ at $r=0$; symmetry; at the outer surface; $C_{Ca2+}=C_s$ at $r=r_s$

$\frac{N_{Ca^{2+},L}}{dt}$ = mole of Ca^{2+} ion per unit of time, per sandcrete particle in a liquid phase (mol/kg. s).

R_s = initial radius of the immobilized bacteria particle (m)

r = radius of calcite produced (m);

k_m = mass transfer coefficient (m/s)

r_c = radius of unreacted immobilized bacteria particle (m)

$C_{Ca^{2+},b}$ = Ca^{2+} ion concentration in the bulk stream (mol/m^3)

$C_{Ca^{2+},s}$ = Ca^{2+} ion at the surface of the immobilized bacteria particle (mol/m^3)

$(D_L)_e$ =effective diffusion of Ca^{2+} ion in the liquid stream (mol/m^3)

$C_{Ca^{2+},L}$ = Concentration of Ca^{2+} ion in the liquid stream (mol/m^3)

$C_{Ca^{2+},c}$ = Ca^{2+} ion at the unreacted core of the immobilized bacteria particle (mol/m^3)

k_1 = reaction rate constant (m^3/kg s); t = time (s)

3. MATERIALS AND METHOD

Material Characterization

An outcome-based approach was adopted to determine the degree of bio-carbonation through bioremediation time-dependent reactions in sandcrete composite. The intrinsic reaction rate profile for converting calcium acetate by immobilized bacteria was determined, considering the curing age, calcium ion concentration, effective diffusivity, and mass transfer coefficient. The performance of the bio-sandcrete based on carbonate formation was compared with simulated results from COMSOL Reaction Engineering Lab version 1.4. Perlite standard (Sinclair) was obtained from Farm Hydroponics Nigeria store, Abuja with product reference: PERLB and a bulk density of ~100 kg/m^3 with a pH of 7.3 (Figure 2). It is chemically and biologically stable with a surface area of 74.966 m^2/g, a pore radius of 12.11 Å with an average absorption capacity of 169.5%. Silicious sharp sand and sand-perlite mix particle size distribution passing through a 4.75 mm motorized IS sieve shaker (Model: H-4325, ASTM C136) is shown in Figure 3. The result showed that the silt content is less than 0.1 mm, which satisfies the NIS (2007). The fine aggregate (sand) used had a density of 2660 kg/m^3 and an average saturation level of 0.92%, which was sourced from River Landzun in the Bida Local Government Area of Niger State (9°05'N, 6°10'E) following ASTM C33. Ordinary Portland Cement (OPC) purchased from Dangote Cement Company with ISO 9001:2008, was used in the study and compliant with the Nigerian Industrial Standard 444-1:2003-cem 11/B-L 42.5R (NIS, 2007) and has a specific gravity of 3.15. For the investigation, potable water that complied with the standard NIS 554, published in 2007 was utilized to enhance the reaction of cement and calcium acetate with water and to aid binding. The starting materials (Cement, perlite, and Sand) were analyzed using an X-ray diffractometer (XRD) (Thermoscientific model: ARL'XTRA X-ray with serial number 197492086, Thermo Fisher Scientific Company Switzerland) to determine their mineralogical compositions, Scanning Electron Microscopy (SEM)(Field Emission Gun Nova NanoSEM 230) to determine their micro-structure, while Energy Dispersive X-ray Fluorescence (EDXRF) (Model: MiniPal4 embedded with X'pert HighScore Plus Software) to determine the compositions of the oxide respectively.

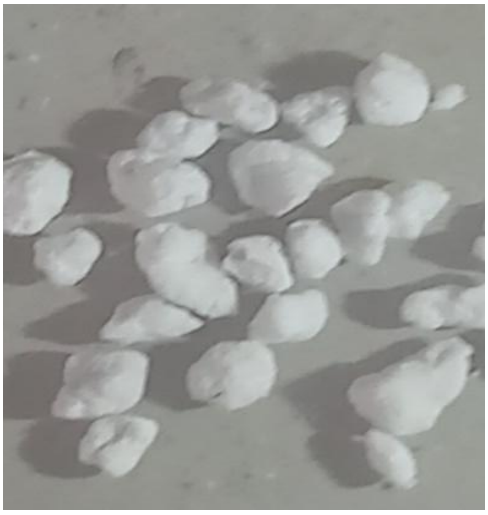

Figure 2: Perlite

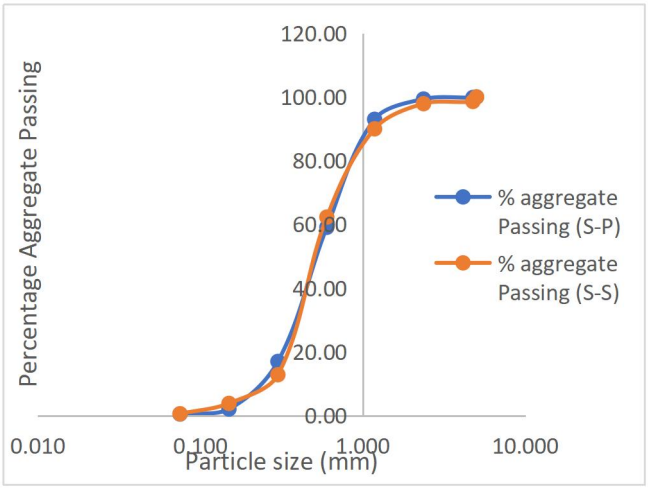

Figure 3: Sieve Analysis of Fine Sand

Preparation of Physical Test Model Specimens

Two groups of sandcrete mortar samples labelled as "P" and "Q" of the same consistency based on the Nigeria Industrial Standard per group were produced. The first set "P" constituted the control and comprised five (5) distinct samples designated P1 to P5 while the second set "Q" was blended mortar whose sand was partially substituted with an encapsulated perlite containing bacteria (10^8 CFU/cm^3) (Bacillus *sphaericus* with NCTC number: NCTC7582, Figure 4) and nutrient precursor (calcium acetate, 0.5% cement weight). The microscopic examination of the bacteria showed a typical rod-shaped structure of *Bacillus* before encapsulation. The optimal concentration and survivability test of bacteria was determined based on Wang *et al*. (2010) at ambient conditions. The encapsulated perlite was impregnated with calcium acetate (1.9 mol/m^3) and bacteria through immersion. To avoid leakage, the perlite was resoaked in sodium silicate solution and dried at 20 °C for 24 hrs in an oven (HUMBOLDT:21-350-ER-1). The proportion of the starting materials in the mix design is presented in Table 1. The mortar specimens were prepared using a fixed ratio of 1:6 for cement to sand, and a water-to-cement ratio (W/C) of 0.5, all by mass. The production process was based on Abdullahi *et al.* (2016) using a 50 x 50 x 50 mm square mould (H-2820 m).

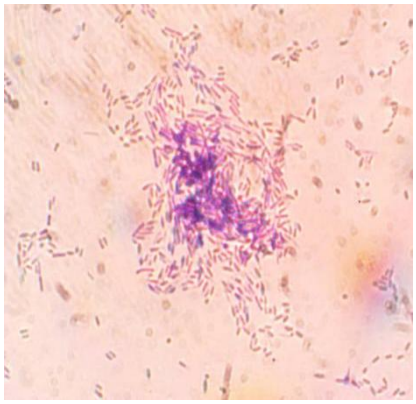

Figure 4: Optical Microscopy of *Bacillus sphaericus* spores

Table 1: Mix ratio for control specimen (S-S) and Sandcrete-Bacteria composite (S-B)

Sample	P1-P5	Q1-Q5
%Replacement	-	10
Cement (g)	33.71	33.71
Sand (g)	202.29	182.06
Perlite (g)	-	20.23
Water (g)	16.85	16.85
Water/Cement ratio	0.5	0.5
Bacteria Concentration (CFU/mL	-	10^8
Relative Humidity	±65%	

Crack Formation and Bio-Healing

After 24 hrs, specimens P1 to P5 and Q1 to Q5 were left to cure and heal for 1, 7, 14, 21, and 28 days at ambient conditions (30 ± 2 °C, 50% RH) following demoulding in the laboratory. A 0.3 mm notch was made at the center of the cubic samples to induce crack formation

using the three-point bending test technique on a compression testing machine. The cracks width was measured using a digital microscope with 1000X zoom capacity and confirmed with Image-J software. Subsequently, the specimens were allowed to heal for 1, 7, 14, 21, and 28 days respectively under ambient conditions in the laboratory with periodic water sprinkling for curing every 24 hours.

Carbonation and Healing Test

The mass of calcite and carbon dioxide sequestered was determined using quantitative analysis (Back-titration method) by dissolving 20 g of pulverized sandcrete samples in 20 ml of 1 M HCl acid and titrating with 0.5 M NaOH using phenolphthalein reagent. The healing capacity was evaluated using an optical microscope. The carbonated healing front was analyzed using an X-ray diffractometer (XRD) (Thermo scientific model: ARLX'TRA X-ray with serial number 197492086, Thermo Fisher Scientific Company Switzerland) to determine their mineralogical compositions, Scanning Electron Microscopy (SEM)(Field Emission Gun Nova NanoSEM 230) and Elemental Diffraction Spectrometer (EDS) (Oxford X-Max Detector using INCA software) to determine their micro-structure and elemental composition, while Energy Dispersive X-ray Fluorescence (EDXRF) (Model: MiniPal4 embedded with X'pert HighScore Plus Software) to determine the compositions of the oxide respectively of the calcite formed in the cracked area. Calcium ion concentrations in the pulverized sandcrete samples were determined based on the absorbance measurement and standard curve using an RT-1904C Chemistry Analyzer with a specific wavelength of 570 nm. Thermogravimetric Analysis (TGA) was conducted to monitor the formation of calcite that heals the crack under ambient conditions. Tweezers were used to extract the calcite formed in the cracks and allowed to dry at 80 ^{o}C for 24 hrs in an oven (HUMBOLDT:21-350-ER-1). The samples were collected in a plastic film to prevent re-carbonation of the sample with atmospheric CO_2 at ambient conditions. The TGA tests were conducted on a PerkinElmer TGA4000 (USA) under a temperature range of 30 to 950 ^{o}C, heated at 10.00 ^{o}C/min, in an N_2 atmosphere to prevent reactions.

Time-Dependent Bio-carbonation Model through Lixiviation of Calcium Acetate using COMSOL Reaction Engineering Lab

Crack healing through sandcrete bioremediation and carbonate formation is solved using COMSOL Reaction Engineering Lab version 1.4. The production of microbial inorganic calcium carbonate in the cracked sandcrete is depicted by the following sequence:

I. Calcium acetate, bacteria, and nutrients are encapsulated in spherical perlite before being incorporated into the sandcrete mix.
II. Upon consolidation of the sandcrete mixture, homogenously dispersed perlite particles will retain the encapsulated healing agents until a crack is created, triggering their release.
III. Water entering the crack subsequently disperses the chemicals over the crack surface and activates the bacterial spores to become metabolically active vegetative cells in the presence of oxygen. The dissolved calcium acetate compound is the converted into insoluble calcite as expressed in Equations 9 - 12.

$$Ca(CH_3COO)_2 \xrightarrow{H_2O} Ca^{2+} + 2CH_3OO^- \quad (9)$$

$$CH_3COO^- + 2O_2 \rightarrow 2CO_2 + H_2O + OH^- \quad (10)$$

$$2CO_2 + OH^- \rightarrow CO_2 + HCO_3^- \quad (11)$$

$$2HCO_3^- + Ca^{2+} \rightarrow CaCO_3 + CO_2 + H_2O \quad (12)$$

The model studies the healing age, and concentration profiles of the reacting and product species as bio-mineral precursor hydrates to form calcite at ambient conditions. The rate constants used for Equations 9 - 12 simulations are 0.36, 0.0024, 0.0003, and 0.0524 s^{-1} respectively, with a porosity of 0.1828 at 25 ^{o}C. The diffusion coefficients in cracks and voids are $2x10^{-9}$ and 0.001 m^2/s, respectively. Figure 5 shows the modelling strategy for crack healing in smart sandcrete using the Reaction Engineering Lab. By employing the Finite Element Method, the software accurately simulates the degree of carbonate formation and the impacts of geometry on the concentration distribution over time. The software is capable of creating models of reacting systems from a set of partial differential equations in time-dependent, diffusion transport in saturated porous media as shown in Equations 2, 3, and 7 respectively.

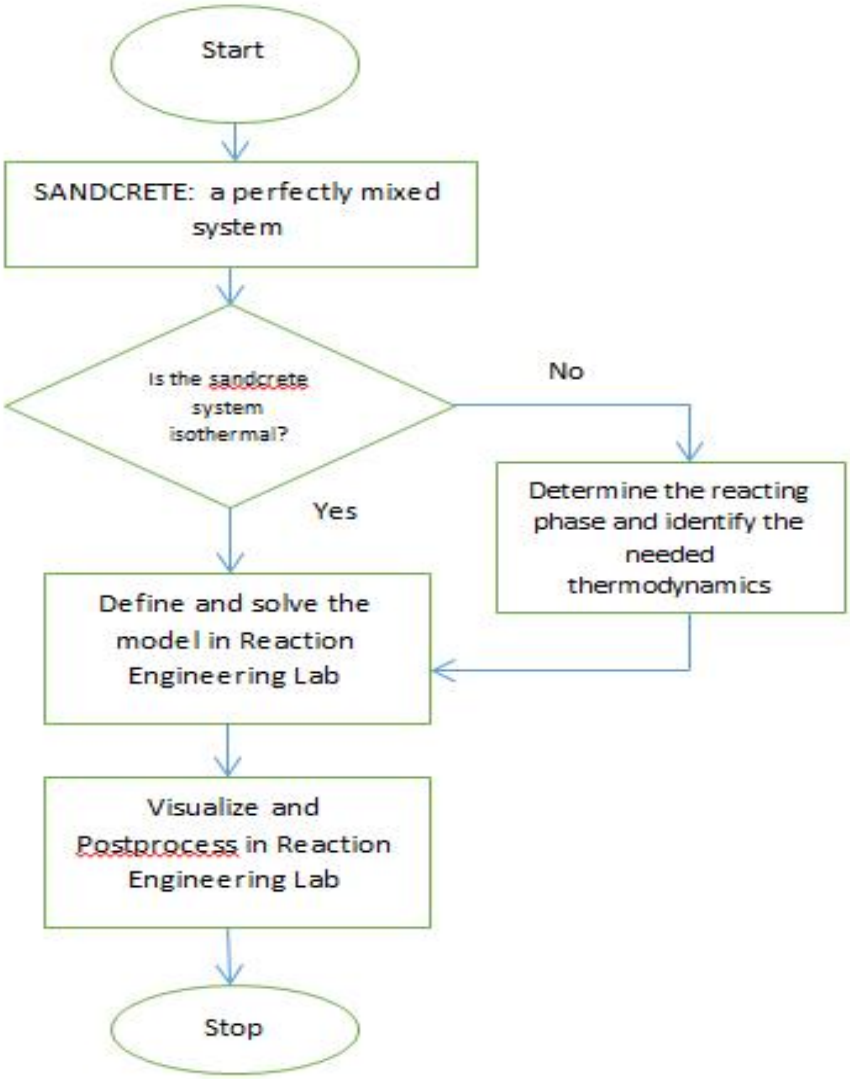

Figure 5: Modelling strategy for crack healing using Reaction Engineering Lab

Mathematical Simulation

Table 2 shows the parameters used in the simulation based on polynomial regression of the experimental to simulated data utilizing the fast-converging Levenberg-Marquardt least square minimization technique. This procedure was employed in finding the mass transfer coefficient (K_m) and effective diffusion of Ca^{2+} ions in the liquid stream (mol/m^3) $(D_L)_e$. The time step used was 10 days for a total simulation time of 80 days with an assumed cracked size between 0.3 mm.

Table 2: Simulation Data

Species	CO_2	O_2	H_2O	$CaC_4H_6O_4$	$CaCO_3$
Initial Concentration (mol/m^3)	1.2e-5			1.9	
Molar Mass (kg/m^3)	44.01	32	18.02	158.17	100
Density (kg/m^3)			1000	1500	2710
Diffusion Coefficient(m^2/s)	1e-8	1.5e-9	6e-9		1e-9

RESULTS AND DISCUSSION

Physicochemical Properties of the Starting Materials

Figures 6 - 11 present a comprehensive characterization of sand, cement and perlite in terms of mineralogy, chemistry, and morphology. The XRF analysis depicted in Figure 6 reveals that the Ordinary Portland cement comprises 61.09% CaO, 5.531% Al_2O_3, and 17.89% SiO_2, meeting the minimum requirement of ASTM C 150. The sand consists of 89.029% SiO_2, 8.415% Al_2O_3, and 2.39% MgO, while perlite includes 74.624% SiO_2, 14.133% Al_2O_3, 0.96% CaO, and 0.7610% Fe_2O_3 along with trace amounts of other oxides. The EDX analysis in Figure 7 reveals a high concentration of oxygen (O) and silicon (Si) in the starting samples. Figure 8 presents the mineralogical composition of the starting materials, displaying varied compositions with peaks of calcite, gypsum, muscovite, and quartz for the cement. The sand exhibited high silica content, while the perlite showed 47 wt% silica. The XRD peak elements align with findings from previous studies (Abdullahi *et al.,* 2016).

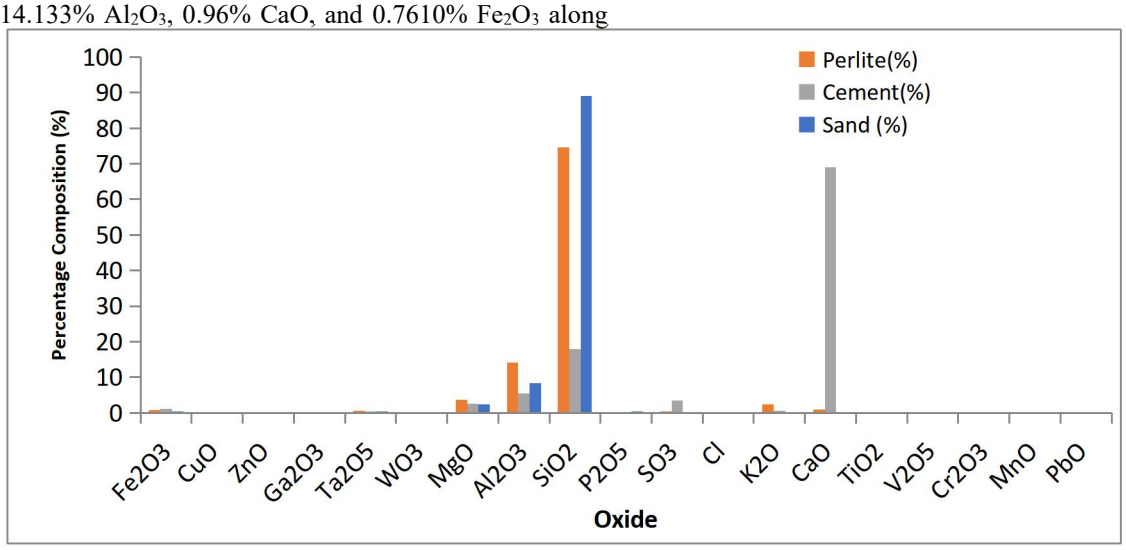

Figure 6: Comparative Oxide Compositions of Sand, Cement and Perlite

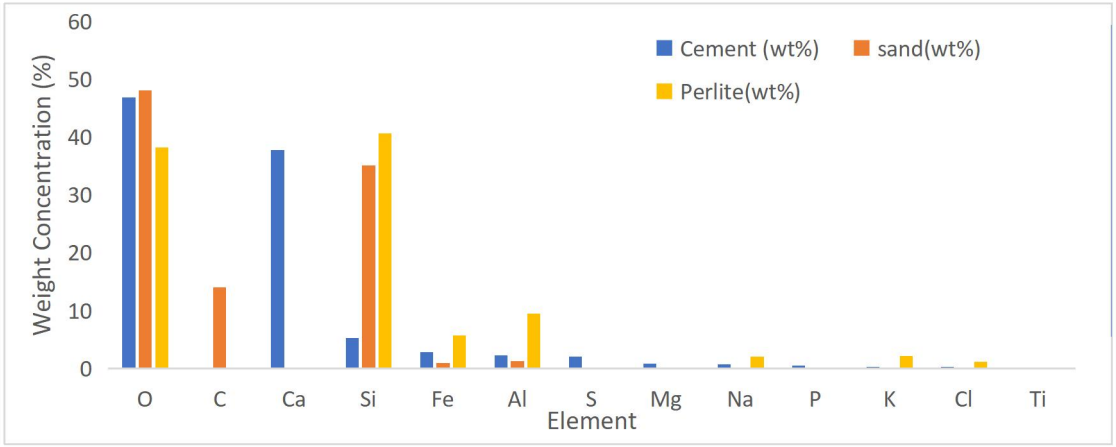

Figure 7: EDS Analysis of Sand, Perlite, and Cement

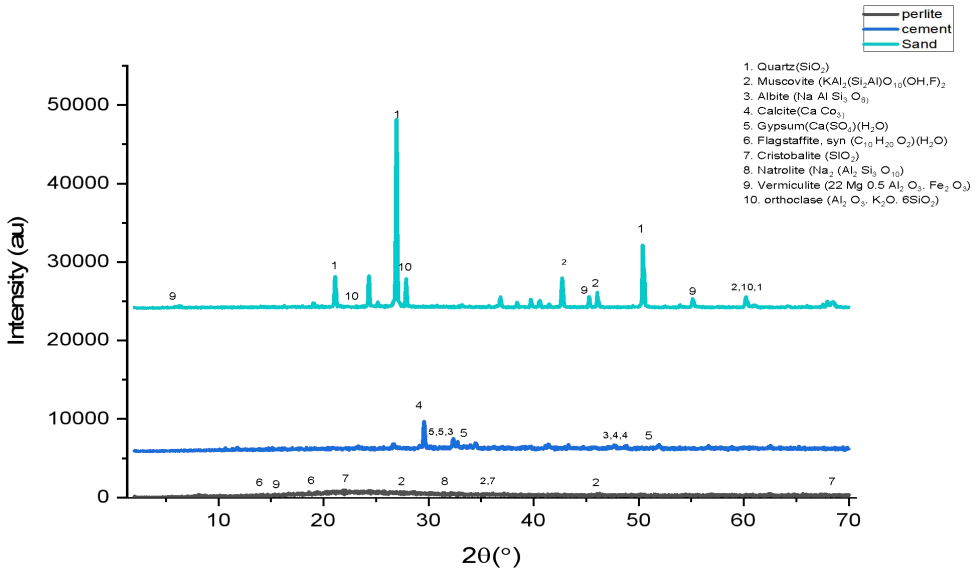

Figure 8: Comparative XRD analysis of Perlite, Cement and Sand

Figures 9 – 11 display typical SEM micrographs of OPC, sand, and cement-sand-perlite mix captured before mixing. The morphology showed an irregular shape similar to cement and sand grits with sizes ranging from 1-20 µm (Kabra *et al.,* 2013; Xue *et al.,* 2020; Hermawan *et al.,* 2021).

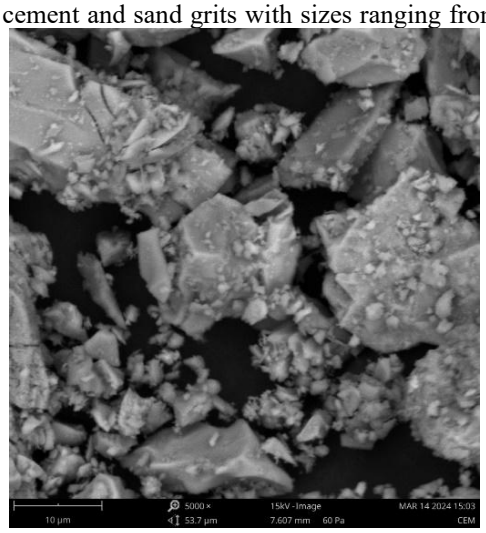

Figure 9: SEM micrograph of Cement grains

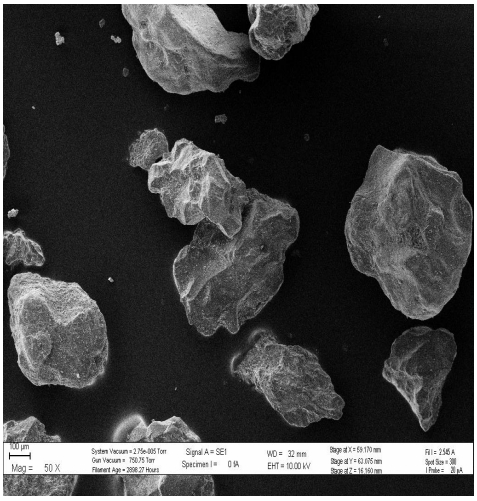

Figure 10: SEM micrograph of sand particles

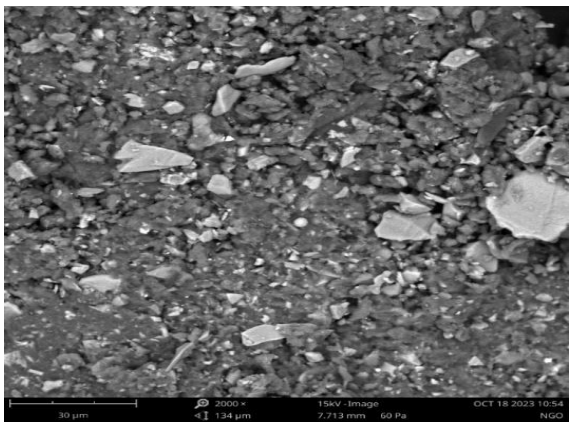

Figure 11: SEM micrograph of Perlite-sand-cement mixture

The simulated concentration profiles of the reactants and product species (calcium acetate, oxygen, carbon dioxide, water, and calcium carbonate) involved in the bioremediation of sandcrete cracks using COMSOL Multiphysics software are displayed in Figure 12. The experimental results for samples Q: S-S(control) and Q: S-B(Healed) are presented in Figure 13. The degradation of $Ca(CH_3OO)_2$ and the formation of $CaCO_3$ are evident as CO_2, O_2, and moisture infiltrate the sandcrete matrix. The simulation indicates a decrease in calcium acetate concentration from 300 g/lit to an infinitesimal level after 15 days, accompanied by noticeable $CaCO_3$ formation after 25 days. This is corroborated by the experimental findings in Figure 13 (b) where a whitish calcite formation was observed visually near the crack mouth and is confirmed by SEM and EDX analysis in Figure 14 after 28 days of curing containing Ca, C, and O. The degradation of calcium acetate and the rise in $CaCO_3$ and Ca^{2+} ion concentration in the crack may be attributed to bacterial cell metabolization as O_2 ingress into the sandcrete composite as seen in Equation 13. Moisture as noted by Shah and Bishnoi (2021) plays a crucial role in carbonation of cement-based composites, while the bacteria's cell wall acts as a nucleus for calcite precipitation, aiding in its crystallization as observed by Saetta *et al.* (1995) and Siddique and Chahal, 2011).

$$Ca(CH_3COO)_2 + 6O_2 \xrightarrow{\text{Bacteria}} CaCO_3 + 3CO_2 + 3H_2O \quad (13)$$

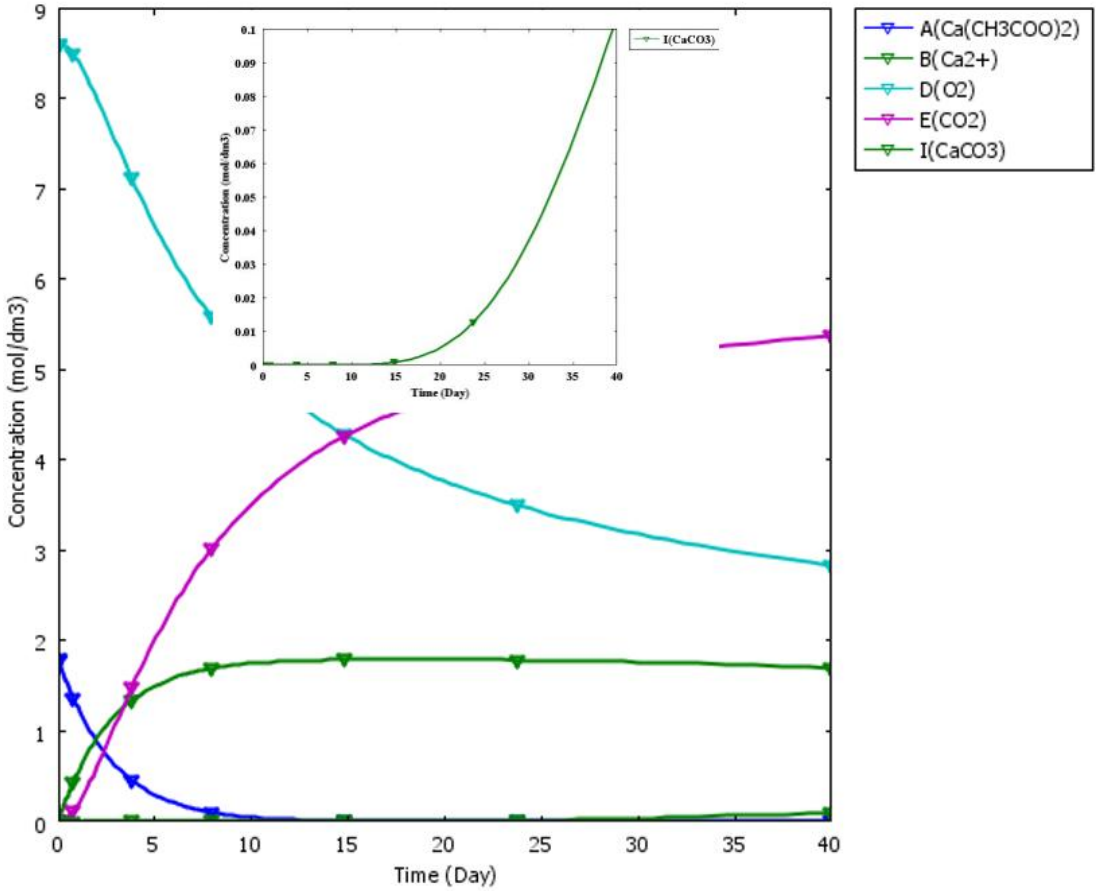

Figure 12: Comparative Simulated Concentration Profiles of Reactants and Products Species Bioremediation of Crack with Age

(a) (b)

Figure 13: Experimental Specimens (P: S-S (control) and Q:S-B(Healed))

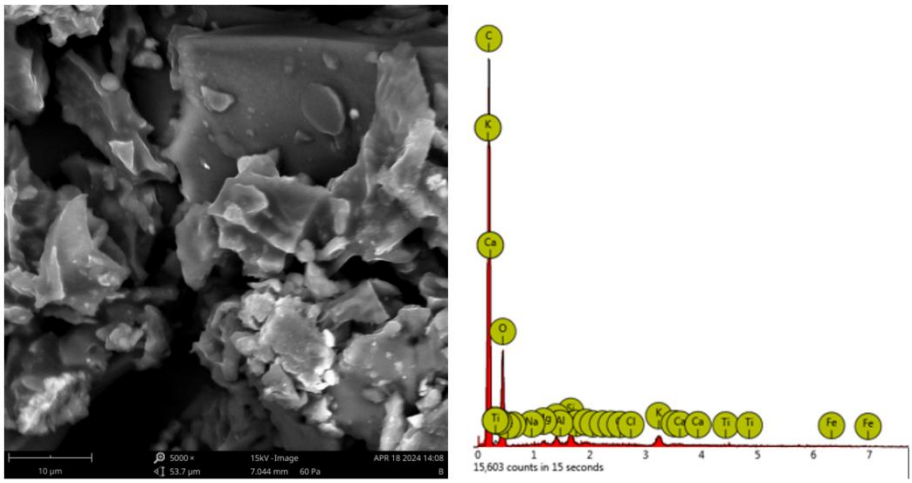

Figure 14: SEM and EDX analysis of Calcite after 28 days for S-B composite

Figure 15 depicts a comparative analysis of the experimental and simulated calcite concentration of S-S (P) and S-B (Q) composites over time under ambient conditions. The results revealed a consistent qualitative pattern as the samples aged from 1 to 28 days. The increase in $CaCO_3$ precipitation can be linked to the complete dissolution of calcium ion precursors in the pore solution due to perlite disintegration upon crack propagation, followed by bacterial reactivation as oxygen and moisture permeate the crack. Moreover, the data indicate a gradual calcite formation within the sandcrete matrix at early age, likely due to the initial curing of the sandcrete composites within 24 hours post-de-moulding, early exposure to air, and activation of bacteria as nutrient precursors dissolved in the sandcrete pore solution. This observation is supported by the SEM/EDX analysis in Figure 14 revealing the precipitation of calcite crystals in conjunction with cement hydrated (C-S-H) gel. Based on the simulated parameters used, the progressive increase in bacteria-induced calcite formation after 25 days under ambient conditions, can be attributed to heightened microbial activities as cells multiply, in conjunction with nutrients-cement hydration reactions facilitated by oxygen and

carbon dioxide ingress into the sandcrete composites. The resulting calcite precipitation is the actual by-product of bacteria metabolism with the cell surface potentially providing a favourable environment for nucleation and crystal growth. This outcome is consistent with findings from Bagga *et al.* (2022), Chine *et al.* (2018) and Jafarnia *et al.* (2020). The comparison between experimental and simulated calcite concentrations demonstrated a strong fit, supported by a high correlation coefficient (R^2) of 0.9951 at a 95% confidence level.

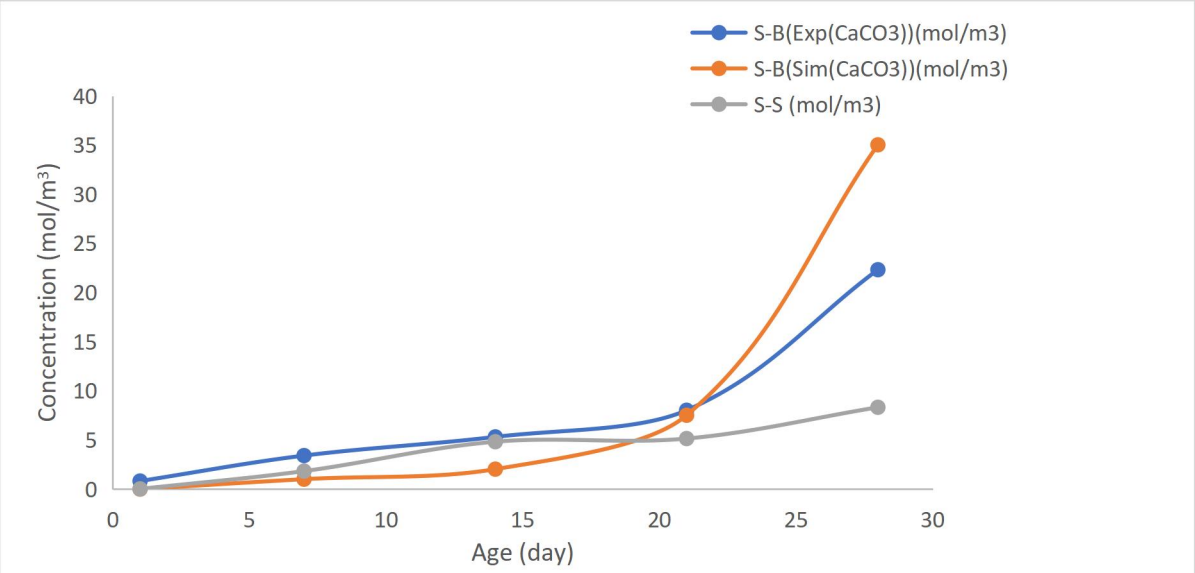

Figure 15: Comparative Experimental and simulated calcite concentration for S-B and S-S with age

The degree of Ca^{2+} ion utilization in the crack healing process in sandcrete based on the simulated data with age is also depicted in Figure 12. The result showed an increased Ca^{2+} ion concentration at an early age and became relatively stable after 15 days under ambient conditions. The high concentration of calcium ions in the sandcrete-bacteria composite at an early age based on the simulated result could be attributed to the release and dissolution of calcium acetate precursor as perlite disintegrates due to crack development, coupled with cement hydrated products (C-S-H and portlandite). The increase in calcium ion concentration at an early age could be responsible for the initial calcite deposition in the sandcrete pores and crack (Hermawan *et al.,* 2021), coupled with increased Ca^{2+} ions adsorption caused by net electronegative charges in bacterial cells resulting in Ca^{2+} ions attraction to CO_3^{2-} and HCO_3^- ions (Siddique and Chahal, 2011). However, the low calcite precipitation at an early age could be due to the slow metabolic activation rate of the dormant bacteria as moisture and O_2 ingress into the crack. As the bacteria cell concentration increases, the calcium ion utilization subsequently increases and becomes relatively stable after 10 days, and starts decreasing slightly as cracks heal, resulting in the densification of the sandcrete composite. Naturally, a high bacteria concentration results in enhanced $CaCO_3$ precipitation. This result is observed by Satyam (2021) and Hermawan *et al.* (2021). Figure 16 shows the comparative analysis of experimental and simulated Ca^{2+} ion concentration profiles with age for S-S (P) and S-B (Q) composites. The result showed increased calcium ion concentration at an early age (1-7 days) and decreased slightly after 14 days. The low calcium ion concentration for the S-S sample could be attributed to the migration of calcium ions encased in lengthy silicate structures which are restricted by the decalcified C-S-H generated during carbonation, and the development of a calcite layer surrounding hydrated phases also prevents the hydrated phases from dissolving further (Shah and Bishnoi, 2021; Morales-Florez *et al.* 2012; Omikrine Metalssi *et al.* 2020; Šavija and Luković 2016). Comparing the experimental and simulated calcium ion concentrations showed a high positive correlation coefficient (R^2) of 0.8851 and *Adj* R^2 (0.8468) at a 95% confidence level.

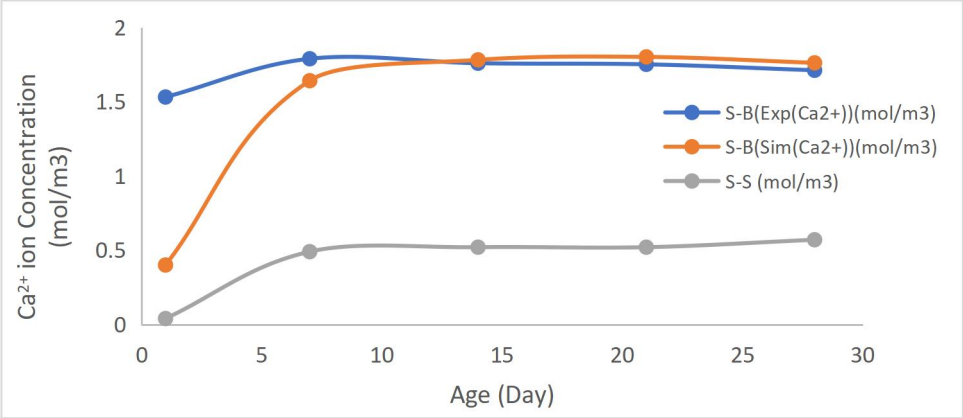

Figure 16: Comparative Experimental and Simulated Calcium Ion Concentration with Age for S-B and S-S composites

The formation of calcite in cracks for S-S and S-B composites after 1 and 28 days is evident in the TGA analysis presented in Figure 17. The results showed the percentage weight loss of the samples as the temperature increased from 30 to 950 ºC. Between 100 and 300 ºC, the loss of water from the sample's spores, spores walls and interlayers occurred (Chang and Chen, 2006). The weight loss between 500 – 950 ºC, is attributed to the decomposition of calcite as depicted in Equation 14. The dehydroxylation of portlandite and C-S-H gel may contribute to the significant weight loss observed in for specimens S-S and S-B after1 day (Singh *et al.,* 2015).

$$CaCO_3\,(s) \longrightarrow CaO\,(s) + CO_2\,(g) \qquad (14)$$

This is corroborated by the dense microstructure of calcite shown in the SEM micrographs in Figure 18 (a and b). Elrasoul and Haniffah (2020) also observed similar results during the ureolysis of urea by bacteria to form carbonate. The metabolically driven transformation surrounding the bacterial cells could be responsible for the active carbonate nucleation and growth that heal the crack. The FT-IR spectroscopic studies of the sandcrete composites (S-S and S-B) after 1- and 28-day healing in ambient conditions are shown in Figure 19, confirming the formation of carbonate as the crack heals. The results showed major absorption bands ranging from 500 - 1550 cm^{-1}. The spectra at 1500 cm^{-1} correspond to the carbonation of sandcrete composites. The S-B composite exhibited a strong peak intensity at this band indicating high calcite formation after 28 days of curing compared with the control sample. The fingerprint of carbon detected in the sandcrete matrix is evident at peaks 1125-1150 cm^{-1} respectively. The sharp absorption bands at 1500, 980, 1000, and 1100 cm^{-1} for all the samples could be attributed to either silicon-oxygen (Si-O) or carbon-oxygen (C-O) bond bending/vibrations primarily characterizing C_3S and C_2S or ether groups. These bands could also be associated with either C-O symmetric and asymmetric stretching vibration (-C-O-C-) ring and anti-symmetrical Si-O-Si stretching mode due to of existing alumina and silica-containing minerals within the control and sandcrete-bacteria composite (Ngally Sabouang *et al.,* 2014). The peaks at 1350 cm^{-1} and 3580 cm^{-1} indicate a strong bond for calcite, $CaCO_3$ (C-O bond), and portlandite ($Ca(OH)_2$) (O-H) respectively.

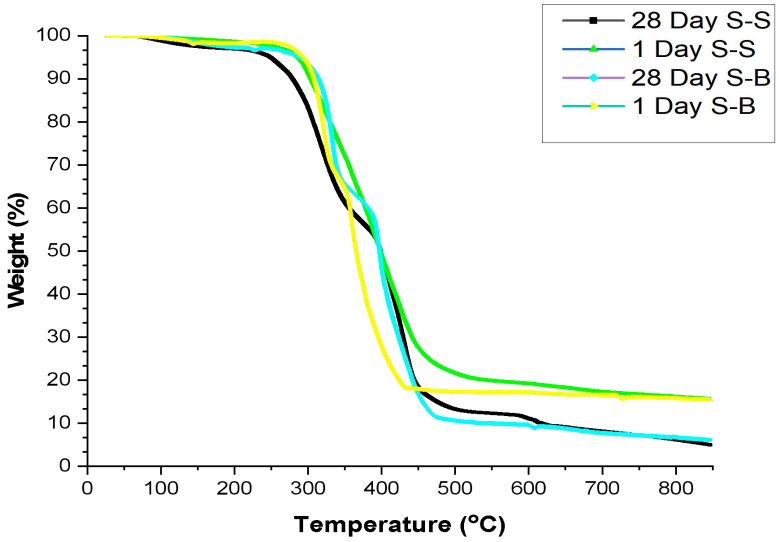

Figure 17: TGA analysis for S-S and S-B composites for 1-28 days

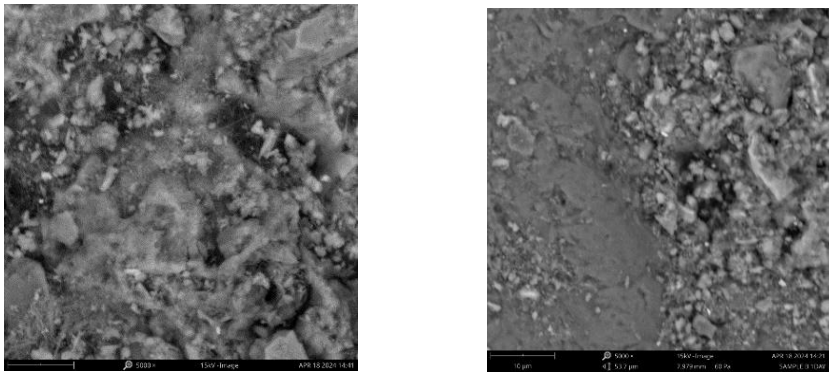

(a) **(b)**

Figure 18: Photomicrographs of S-B for: a (day-1) and b (day-28)

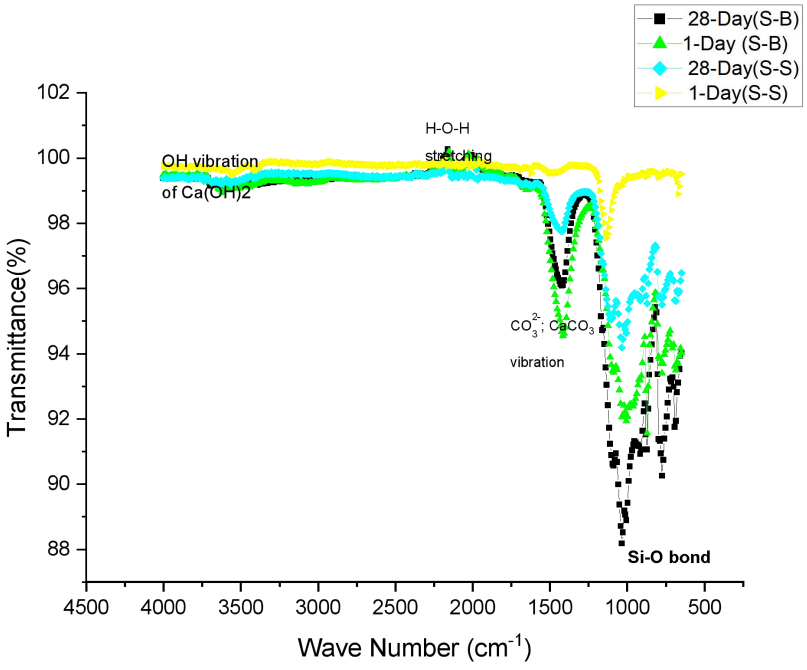

Figure 19: Comparative FTIR analysis of S-S (P) and S-B (Q) for 1-28 days of curing

Figure 20 displays the comparative XRD patterns of samples P (control) and Q (S-B) for 1 and 28-day crack healing at ambient conditions. The result showed the presence of calcite as bacteria metabolized in the sandcrete crack. On the 28th day of healing, the S-B composite showed high calcite intensities compared with the control sample. All samples displayed high silica content attributable to sand and encapsulated perlite content.

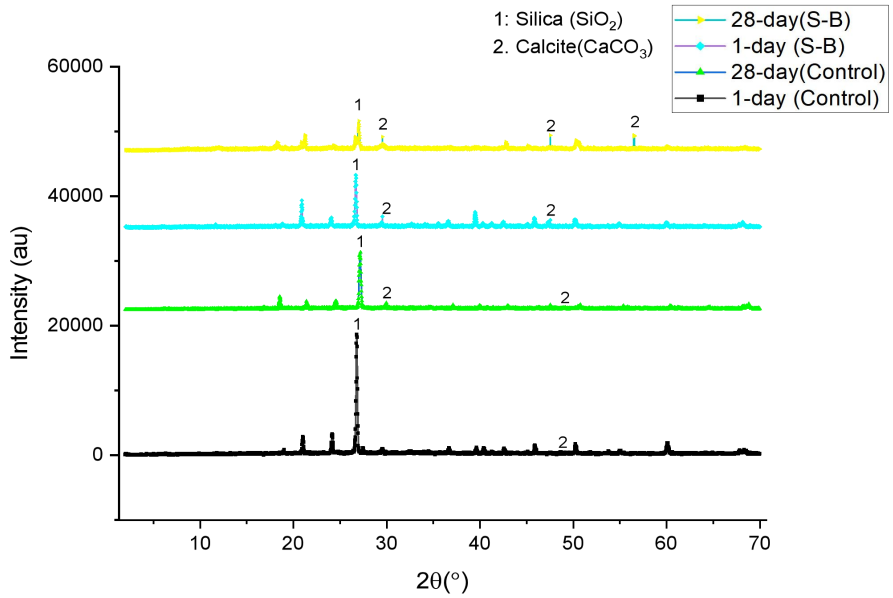

Figure 20: Comparative XRD analysis of S-S (P) and S-B (Q) for 1-28-day crack healing

Figure 21 shows the 2-D contour model simulation of the bioremediation of cracks in sandcrete composite. Mathematically, the bio-remediation process is a dynamic boundary problem for a system of equations that describe diffusion processes (Equations 2, 3, and 7). The result shows the diffusion flux of Ca^{2+} ions toward the crack as O_2, CO_2, and water ingress into the sandcrete through the crack. The result showed the crack healing process as $CaCO_3$ is deposited in the crack.

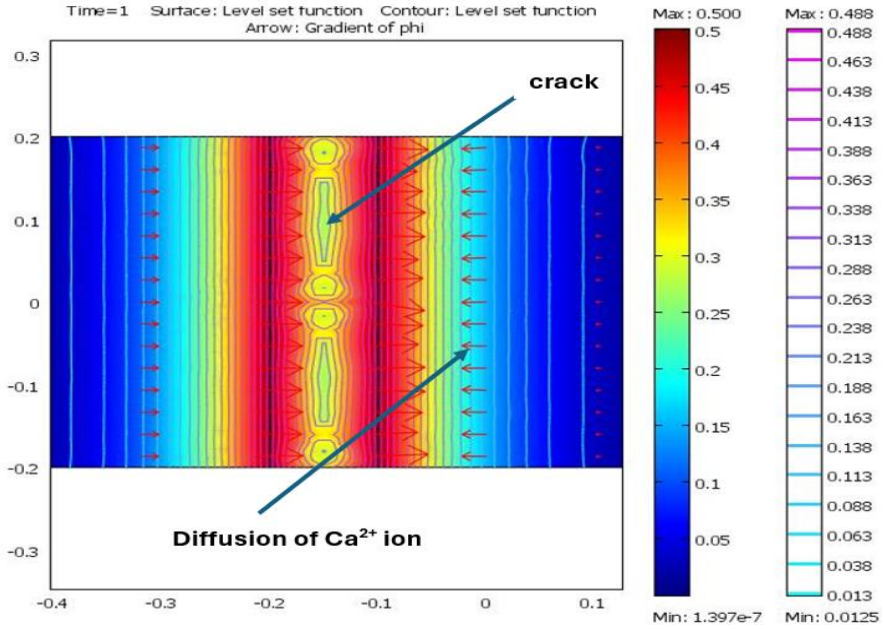

Figure 21: 2-D prediction model of crack healing in sandcrete composite using Moving Boundary

5.0 CONCLUSION

Finite Element Method (FEM) was employed to conduct 2D Multiphysics modelling of crack healing over 1-28 days in sandcrete with focusing on biochemical reactions and calcite formation. The results were validated by comparing the calcite concentration filling the crack space with a notched physical model (50 x 50 x 50 mm cube) cured for 1 – 28 days under ambient conditions. The simulation demonstrated complete degradation of calcium acetate ($Ca(CH_3COO)_2$) after 15 days of crack formation, accompanied by significant rise in calcium carbonate ($CaCO_3$) concentration as *Bacillus sphaericus* metabolized. After 28 days of curing, the experimental and simulated outcomes indicated higher calcite concentrations for the S-B composite (22.31 and 35.01 mol/m^3) under ambient conditions compared to the bacteria-free standard sandcrete (S-S) composite (8.32 mol/m^3). The Ca^{2+} ion concentrations in the sandcrete crack responsible for healing after 28 days, ranged from 1.53-1.71 mol/m^3 and 0.4-1.76 mol/m^3 for the experimental and simulated S-B composites, while the control specimen ranged from 0.04-0.57 mol/m^3. A comparative analysis of experimental and simulated data for calcite and calcium ion concentrations exhibited high correlation coefficients at a 95% confidence level.

ACKNOWLEDGMENTS

The authors wished to acknowledge the Tertiary Education Trust Fund (TETFund) for providing the grant TETF/ES/DR&D-CE/NRF2021/CC/EHU/00045/VOL.1 for this research.

REFERENCE

Abdullahi, M., Odigure, J. O., Kovo, A.S. and Abdulkareem, A. S. (2016). Characterization and Predictive Reaction Model for Cement-Sand-Kaolin Composite for CO_2 Sequestration. *Journal of CO_2 Utilization*, 16 (2016) 169–181.

ASTM (2022). Standard Specification for Portland Cement (C150-22). American Societyfor Testing and Materials, West Conshohocken, Pennsylvania: ASTM International.

ASTM (2023). Standard Specification for Concrete Aggregates, (C33-23). American Society for Testing and Materials, West Conshohocken, Pennsylvania: ASTM International.

ASTM (2019). Standard Test Method for Sieve Analysis of Fine and Coarse Aggregates, (C136-19). American Society for Testing and Materials, West Conshohocken, Pennsylvania: ASTM International.

Bagga, M., Hamley-Bennett, C., Alex, A., Freeman, B. L., Ismael Justo-Reinoso, I., Mihai, I.C., Gebhard, S., Paine, K., Jefferson, A. D., Masoero, E., Ofiteru, I. D. (2022). Review: Advancements in Bacteria Based Self-Healing Concrete and the Promise of Modelling. *Construction and Building Materials*, 358, 129412. https://doi.org/10.1016/j.conbuildmat.2022.129412

Balazs, A. C. (2007). Modelling Self-healing Materials. *Materials Today*, 10 (9), 18-23. Doi: 10.1016/s1369-7021(07)7020.

Chang, C. and Chen, J. (2006). The Experimental Investigation of Concrete Carbonation Depth. *Cement and Concrete Research*, 36, 1760 – 1767. https://doi.10.1016/j.cemconres.2004.07.025

Chine, B., Cuevas, R., H., Jimenez, R. S. and Rodriguez, A. R. (2018). A Model of Concrete Carbonation Using COMSOL Multiphysics, Proceedings of the 2018 COMSOL Conference in Lausanne.

Elrasoul, E. A. and Haniffah, M. R. H. (2020). 1-D Modelling of Healing Agent in Self-Healing Concrete Using Finite Element Method. *Nature and Science,* 18(6), 49-56.

Fernandez, C. A., Correa, M., Nguyen, M.T., Rod, K.A., Dai, G.L., Cosimbescu, L.,Rousseau, R. and Glezakou, V.A. (2021). Progress and Challenges in Self-healing Cementitious Materials. *Journal of Materials Science,* 56 (1), 201–230.

Ghosh, S. K. (2009). Self-Healing Materials: Fundamentals, Design Strategies, and Applications, Wiley-VcH verlag GmbH & co. KGaA, Weinheim, India, Pp. 1-179.

Hermawan, H., Minne, P., Serna, P., Gruyaert, E. (2021). Understanding the Impacts of Healing Agents on the Properties of Fresh and Hardened Self-Healing Concrete: A Review. *Processes,* 9, 2206. https://doi.org/10.3390/pr9122206

Hu, D., Zhang, F., Zhou, H. and Shao, J. (2011). Modeling of Lixiviation-Mechanical Coupling Behaviour of Fiber Reinforced *Proceedings of the 2011 COMSOL* Concrete, Conference in Stuttgart, Germany.

Jafarnia, M.S.; Khodadad Saryazdi, M.; Moshtaghioun, S.M. (2020). Use of Bacteria for Repairing Cracks and Improving Properties of Concrete Containing Limestone Powder and Natural Zeolite. *Construction and Building Materials,* **2020**, 242, 118059.

Kabra, S., Sharma, A., Katara, S., Hada, R., Rani, A. (2013). DRIFT- Spectroscopic Study of Modification of Surface Morphology of Perlite

during Thermal Activation. *Indian Journal of Applied Research*, 3 (4), 40-42.

Mauludin, L.M. and Oucif, C. (2019). Modeling of Self-healing Concrete: A Review, *J. Appl. Comput. Mech*. 5 (3), 526–539.

Morales-Florez, V., Findling, N. and Brunet, F., (2012). Changes on the nanostructure of cementitius calcium silicate hydrates (C-S-H) induced by aqueous carbonation. *Journal of Materials Science*, 47(2), 764-771

Ngally Sabouang, C. J., Mbey, J. A., Liboum, F. T. and Njopwoup, D. (2014). Talc as Raw Material for Cementitious Products Formulation. *Journal of Asian Ceramic Societies*, 2, 263 – 267.

Nigeria Industrial Standard (NIS) (2007). *Draft Code of Practice for Sandcrete Blocks*. Federal Ministries of Industries, Lagos: Nigeria

NIS 444-1. (2003). Cement Part 1- Composition and Conformity Criteria for common

Cements, Nigerian Industrial Standard.

Odigure J. O. (2002). Deterioration of long-serving Cement-based Structures in Nigeria. *Cement and Concrete Research*, 32, 1451 – 1455.

Omikrine Metalssi, O., Aït-Mokhtar, A. and Turcry, P., (2020). A proposed modelling of coupling carbonation-porosity-moisture transfer in concrete based on mass balance equilibrium. C*onstruction and Building Materials*, 230, Article No. 116997.

Pan, T. and Lu, Y. (2012). Stochastic Modeling of Reinforced Concrete Cracking due to Non-uniform Corrosion: FEM: based Cross-Scale Analysis. *Journal of Materials in Civil Engineering*, 24(6), 698-706.

Perko, J., Seetheram, S. and Mallants, D. (2011). Verification and validation of flow and transport in cracked saturated porous media. *Pros., the proceeding of 2011 COMSOL conference* in Stuttgart.

Richter, M., Moenicekes, S., Richter, O., and Schroder, T. (2011). The soil as a bioreactor: reaction-diffusion process and biofilm. *Proceedings, The proceeding of 2011 COMSOL conference* in Stuttgart, Germany.

Siddique, R. and Chahal, N. K. (2011). Effect of ureolytic bacteria on concrete properties Review. *Construction and Building Materials*, 25, 3791–3801. doi:10.1016/j.conbuildmat.2011.04.010

Šavija, B. and Luković, M., (2016). Carbonation of cement paste: Understanding, challenges, and opportunities. *Construction and Building Materials*, 117, 285-301.

Saetta, A. V., Schrefler, B. A. and Vitaliani, R. V. (1995). The carbonation of concrete and the mechanism of moisture, heat and carbon dioxide flow through porous materials, *Cement and Concrete Research*, 23, 761-772.

Samuel De, C. G., John, L. Z., Xiaohui, Z. and Guangcheng, L. (2022). Water treatment Sludge Conversion to Biochar as Cementitious Material in Cement Composite. *Journal of Environmental Management,* 306: 114463. https://doi.org/10.1016/j.jenvman.2022.114463

Satyam, N. (2021). Numerical Modelling of Biocemented Soil Behaviour, Modeling in *Geotechnical Engineering*, 101-117. https://doi.org/10.1016/B978-0-12-821205-9.00015-0.

Schlangen, E. and Joseph, C. (2013). Modelling of self-healing cementitious materials, in: M.de Rooij, K. Van Tittelboom, N. De Belie, E. Schlangen (Eds.), Self-Healing Phenomena in Cement-Based Materials: State-of-the-Art Report of RILEM Technical Committee 221-SHC, Springer, Netherlands, Dordrecht, 2013, pp. 217–240.

Shah, V. and Bishnoi, S. (2021). Understanding the Process of Carbonation in Concrete using Numerical Modeling. *Journal of Advanced Concrete Technology*, 19, 1148-1161. https://doi:10.3151/jact.19.1148

Singh, L. P., Goel, A., Bhattacharyya, S. K., Sharma, U. and Mishra, G. (2015). Hydration Studies of Cementitious Material Using Silica Nanoparticles. *Journal of Advanced Concrete Technology,* 13, 345-354. https://doi.org/10.3151/jact.13.345

Wang, J. Y., Van Tittelboom, K., De Belie, N. and Verstraete, W. (2010). Potential of Applying Bacteria to Heal Cracks in Concrete. *2nd International Conference on Sustainable Construction Materials and Technologies,* The University of Wisconsin, Milwaukee Centre for bye-product Utilization.

Wang, X.F., Yang, Z.H., Fang, C., Wang, W., Liu, J. and Xing, F. (2020). Effect of carbonate-containing self-healing system on properties of a cementitious composite: fresh, mechanical, and durability properties. *Construction and Building Materials,* 235, 117442.

Wang, X. and Nackenhorst, U. (2020). A coupled bio-chemo-hydraulic model to predict porosity and permeability reduction during microbially induced calcite precipitation, *Advances in Water Resources,* 140, 103563

Wijngaarden, W.K. V., Paassen, L.A.V., Vermolen, F.J., Meurs, G.A.M. V. and Vuik, C. (2016). A Reactive Transport Model for Biogrout Compared to Experimental Data, *Transport in Porous Media*, 111 (3), 627–648.

Xue, C., Li,W., Qu, F., Sun, Z. and Shah, S. P. (2020). Self-healing efficiency and crack Closure of smart cementitious composite with crystalline admixture and structural polyurethane. *Construction and Building Materials,* 260, 119955.

Zemskov, S.V., Jonkers, H. M. and Vermolen, F.J. (2014). A mathematical model for bacterial self-healing of cracks in concrete, *Journal of Intelligent Material System and Structures,* 25 (1), 4–12.

10.51975/24390209.som
Journal of the Nigerian Society of Chemical Engineers, 39(2), 2024

HYDRAULIC STUDY OF GAS DISTRIBUTION SYSTEM: CASE STUDY OF KADUNA REFINERY AND PETROCHEMICAL COMPANY (KRPC)

***Salihu M Suleiman, Bello Abdulhanan, Fatima A. Salihu, Jibril A. Ahmed and Yahaya G. Umar**

Department of Chemical Engineering Technology, Federal Polytechnic Nasarawa, Nasarawa State.

Corresponding author:
*Salihu M Suleiman, ssalihum@gmail.com; 09019110605

ABSTRACT

In this study, strategy for utilization off-gas flared in Kaduna Refinery and Petrochemical Company was investigated. The methodology explored hydraulic design of the pipeline system that will deliver the off-gas from the refinery to a gathering system for domestic use. This approach included demand calculation, pipeline sizing through pressure, velocity and wall thickness calculations. Aspen Hysys software package (V8) was used for the design and the results validated using numerical calculations. 4", 6" 8" and 10" sizes of Polyethylene (PE) pipe, SDR11, were compared at current capacity of 35m^3/h. Future demand capacity were captured at 70, 105 and 175 m^3/h volumetric flows and source pressure of 70kPa. The findings indicated; 4" pipe best suit 35m^3/h flow at a delivery pressure of 64.99 and 68.15 kPa for simulation and numerical calculations respectively, and velocity of 2.888m/s (simulation) and 2.665m/s (numerical calculation). At 70m^3/h flow, 4" and 6" may contain the flow at simulated delivery pressure conditions of 50.353 and 63.249 kPa respectively; velocity conditions of 7.472 and 5.714m/s. Numerical values were obtained to be 67.405kPa and 69.045kPa – pressure; and velocity of 2.464m/s and 2.337m/s for 4" and 6" pipes respectively. At 105m^3/h flow, 6" pipe was found to best suit the flow at delivery conditions of; 64.904kPa and 3.850m/s using simulation, and 68.026kPa and 3.540m/s using numerical calculations. However, at an estimated flow of 175m^3/h, 6" pipe was also found to best suit the flow at the delivery conditions of 56.200kPa and 7.420m/s using simulation, and 64.839kPa and 6.183m/s using numerical calculation. Both simulation and numerical calculations results were found to be in close agreement.

***Keywords**: Hydraulics, gas distribution, flared gas, system*

1.0 INTRODUCTION

Gas flaring has been a major concern the world over due to the danger it poses on the environment, and consequently human lives. Nigeria is one of the countries around the world that flares large volumes of both natural, associated and petroleum gases, from both its oil/gas fields and processing/refining facilities. This practice dates back to 1958 (about 50 years ago) when crude oil was first exported from the country (OPEC, 2022), and it has been on the increase since that time. Unconfirmed sources has it that Nigeria is second to none in gas flaring worldwide, leaving its environment with devastating effects. This large volume of gases flared can or would have been put into use to serve the epileptic energy supply, and the increasing energy demand in the country. The abundance or availability of the oil and gas in Nigeria may justify the investment in the sector, but diversification is very crucial to the dilapidating power sector of the country. There is, therefore, the need to channel part of these flared gases to this sector for power generation, and also for domestic use. This will reduce resource 'wastage', and environmental degradation due to gas flaring. Kaduna Refining and Petrochemical Company (KRPC), Kaduna, Nigeria, flares more than 80% of the off gas it produces from its Crude Distillation Units (CDU) I and II giving rise to high rate of gas flaring. This flared gas would have been re-routed to complement domestic energy demand in some part of Kaduna metropolis, thereby reducing environmental degradation due to gas flaring and resource wastage.

This study, therefore, focuses on hydraulic study of gas distribution pipeline system that will deliver off-gas (flare gas) from KRPC to gathering system for domestic consumption. The study estimates the pipeline sizing

requirement that will re-route the off gas from flare line by; deciding the inlet pressure of the line from KRPC, evaluating compression requirement of the off-gas (if supply pressure is adequate), and conduct wall thickness requirement of the sized pipeline. American Petroleum Institute (API 15LE, 1995) standard specification for polyethylene line pipe and American Society of Mechanical Engineers (ASME B31.8, 2012) standard for gas transmission and distribution were selected as standard for the sizing.

Nigeria, just as many other African states, suffers from a phenomenon known as the 'natural resource curse' (CAI, 2012). Though it is endowed with an abundance of other natural energy resources, including natural gas, coal and lignite, hydropower, solar radiation, wind, biomass (such as wood, animal and plant wastes), (Oseni, 2012) indicating the availability of both renewable and non-renewable energy resources.
However, supply of energy from fossil fuels among Africa's developing states is insufficient, with one-third of the continents population dependent upon traditional biomass for cooking and heating (Ajayi, 2009). This is also the trend in Nigeria, where as much as 83% of the country's total energy consumption results from traditional biomass and waste (typically consisting of wood, charcoal, manure, and crop residues), as contained in report of (US EIA, 2013). This high share represents the use of biomass to meet off-grid heating and cooking needs, mainly in rural areas, leaving the urban areas with epileptic grid energy supply. Where the supply is ensured however, it is at great expense.

Energy resource in the country is currently been underutilized. Coal which has been basically source of deriving locomotives and electricity generation in the colonial era has been abandoned owing to the discovery of oil and gas resources in the country. Although Belhre Dolbear (2006) projected coal production for power generation and briquetting to most likely to be about 13 million tonnes in 2010 and increasing to 29 million tonnes by the year 2025, indicated in a report prepared by (Centre for People and Environment,, 2009).
So far, piping systems have proved most efficient in the delivery of oil and gas and their residual products, over a very long distance. As such, the efficiency and durability of these piping systems heavily depends on efficiency, reliability and accuracy of the design, and of course its economics.

Design of pipeline systems depends on a lot of factors, as mentioned in Mohitpour, *et al*., (2003), which include; fluid properties, supply and demand magnitude/locations, codes and standards, design conditions, route, topography and acess, environmental impact and economics. Characteristics (both physical and chemical) of transmitting fluid plays a significant role in the deisgn of transmission and utilization equipments. These fluid properties may include density, specific gravity, viscosity, reactivity and corrosive tendensies, odour and water content. The properties are essentials in determining appropriate material grade and gas behavioural state, and in setting thermodynamic (operating) conditions.
Specific gravity of gas, is defined in Mokhatab *et al*., (2006), as

$$\gamma_g = \frac{M}{M_{air}} \quad (1)$$

where M_{air} is the molecular weight of air. Once the value of molecular weight of the mixture is calculated, the specific gravity of the mixture can be calculated as well. For a given gas mixture, the molecular weight was calculated using equation (2).

$$M = \sum_i^n y_i M_i \quad (2)$$

Where y_i represent the mole fraction of component i in the gas mixture, M_i represent the molecular weight of component i in the mixture and n represent the total number of components.

The pipe length, temperature, pressure, pipe size and other gas properties are interrelated by the given sets of equation known as flow equations. For a given length of pipe, and assuming a horizontal pipe (ie no elevation exist between upstream and downstream ends), a general flow equation, according to (Paulo & Carlos, 2007), may be written, in S.I. unit, as;

$$Q = 7.574 \times 10^{-4} \frac{T_s}{P_s} \frac{1}{\sqrt{f}} \left[\frac{(P_1^2 - P_2^2)d^5}{SZLT}\right]^{0.5} \quad (4)$$

Where
Q represent the gas flow rate, m^3(st)/h; L is pipe length (m); S is the gas specific gravity;
T_s and P_s are standard temperature (K) and standard pressure (bar-absolute) respectively;
f is the (Moody) friction factor, a dimensionless quantity which may be specified or calculated using a Moody diagram as a function of Reynold's number;
P_1 and P_2 are upstream and downstream pressures (barg) respectively;
d is the pipe diameter; and T represent gas temperature (K)

Equation 4 applies over all pressure ranges, and it forms the basis for many of the flow equations used in the analysis of gas transmission and distribution systems.

Equation 5 may be used to further derive equations 6 and 7 for medium and low pressure systems/regimes respectively.

$$Q = 1.269 \times 10^{-2} \frac{1}{\sqrt{f}} \left[\frac{(P_1^2 - P_2^2)d^5}{SL}\right]^{0.5} \quad (6)$$

$$Q = 5.712 \times 10^{-4} \frac{1}{\sqrt{f}} \left[\frac{(P_1 - P_2)d^5}{SL}\right]^{0.5} \quad (7)$$

Equation 6 may be used for systems operating up to maximum pressure of 7 barg, while equation 7 is used for systems operating up to maximum pressure of 75 mbarg.

Gas velocity at standard condition is calculated using the relation

$$u_s = \frac{Q}{A} \quad (8)$$

u_s represent gas velocity at standard condition; Q is gas flow rate at standard condition and A is the pipe cross-sectional area.

Therefore, the velocity of gas at any given length of pipe may be calculated, as suggested by Nasr, (2013), using equation (9).

$$u_2 = 353.68 Q P_s \left[\frac{d}{d^5 P_1^2 - 6211.2 Q^2 f SL}\right]^{0.5} \quad (9)$$

Where every term has it usual meaning as defined previously.

The velocity for treated gas in transmission pipeline may be as high as 15 – 17 m/s, while for untreated gas should be maintain quite low (10 -12 m/s). This is to do away with erosion effect due to high gas velocities. On the other hand, gas velocity may be maintained as low as 2 – 5 m/s in distribution systems. Generally, gas velocity should not exceed erosional velocity.

2.0 MATERIALS AND METHOD

2.1 Design Data

To accomplish the task in this study, data are needed. The data was obtained from KRPC. Among the required data were off gas volumetric flow rate, gas pressure and temperature, gas relative density/ specific gravity. These were summarized in Table 1.

Table 1 Design data from KRPC (KRPC, 2013)

PARAMETER	VALUE
Gas volumetric flow rate, m^3/h	35
Gas pressure (source pressure), kg/cm^2	0.75
Gas temperature, ^0C	28
Route distance, km	3.5

2.2 Future Demand/Capacity Estimate

The intended delivery/utilization domestic area has 649 houses in the estate. This is in addition to one (1) school, 1 club house and 1 clinic. These houses were categorized as shown in Table 2.

Table 2 Gas consumption estimate for consumer estate

Type of house	Quantity (based on consumption)	Cooker units	Times of usage/unit	Times of usage/hour	Unit factor	Daily Usage factor*	Total gas consumption (m^3/h)**
5 bedroom	6 + club house	4	6	24	0.3871	2.7097	5.7660
4 bedroom	30	4	6	24	0.3871	11.613	24.7113
3 bedroom	250 + clinic	2	4	8	0.1290	32.3790	68.8993
2 bedroom	360 + staff school	2	3	6	0.0968	34.9448	74.3590 ≈ 175

* Daily usage factor = unit factor × quantity of houses

** Total gas consumption = standard estimated gas consumption for gas cooker ($75 ft^3/h$) × daily usage factor

2.3 Operating Pressure and Temperature

This defines the pressure condition of the gas at the upstream (source) point. Off-gas from the columns is been transported to the flare at a pressure of 0.75 kg/cm^2

and temperature of 28 ºC. As a consideration for operational changes, the values of 0.7 kg/cm^2 (0.7bar) and 28 ºC were therefore considered as the upstream pressure and temperature respectively.

2.4 Gas Volumetric Flow Rate/Capacity

Table 1 showed that an average 35 cubic meter of gas is been transported to the flare each hour. Therefore, volumetric flow rate was taken to be 35m^3/h. This flow was doubled and tripled to capture future demand and each case, values were simulated and plotted. Theoretical calculations were made, using equations 2 – 9, to validate these results.

2.5 Delivery/Route Distance

This defines the distance between the gas delivery point and the source. It is an important parameter, as it determines the total pipe length to be installed along the route. An approximate distance of 3.5km was measured.

2.6 Pipe grade/specification

These are available and specified by established standards, and choice of one material to another is governed by the intended operational conditions; pressure capacity, stress (either external or internal due to transporting fluid), etc. In this study, and based on available data and operating conditions, ***polyethylene pipe*** with standard dimension ratio 11 (SDR11) was selected, adopting API 15LE specification for Polyethylene Line Pipe. This choice was made based on material strength and wall thickness to withstand the installation environment.

2.7 Pipe Sizes

This is defined by the pipe dimension. Since there were no previous work to develop on, four different pipe sizes were chosen; 4", 6", 8" and 10" PE pipes. Choice of the sizes was made considering the intended application, operating conditions and the installation environment.

2.8 Gas Composition

The gas under study is a petroleum gas with the following composition as shown in Table 2.

Table 2 Gas composition

Component	Molecular Formula	Mole Fraction	Relative Density
Ethane	C_2H_6	0.002	0.3460
Propane	C_3H_8	0.573	0.5170
Butane	C_4H_{10}	0.411	0.5802
Pentane	C_5H_{12}	0.014	0.6107

Source: KRPC, 2013

2.9 Simulation Procedure

Aspen Hysys simulation package (V8) was used to carry out hydraulic simulation of the available data. Data were defined on the simulator and corresponding gas behaviour of parameters was obtained as result. The parameters whose behaviours were studied were pressure, temperature and velocity profiles along the pipe at a given length interval as the gas flows. Plots were made of the values obtained to analyse these behaviours.

2.10 Numerical Calculations

To validate and compare results obtained using simulation software, theoretical calculations were conducted using Equations 4 and 9 to confirm pressure drop and velocity respectively. Plots were also made of the tabulated results.

Pipe wall thickness for the various pipes were calculated and tabulated based on API 15LE specifications for SDR11 pipe material.

3.0 RESULTS AND DISCUSSION

3.1 Flow variations at 35m^3/h Gas Flow Rate

3.1.1 Pressure variations at 35m^3/h Flow

Pressure variations along the chosen pipe sizes, for both simulation and numerical calculation shown in Figures 1 and 2 respectively.

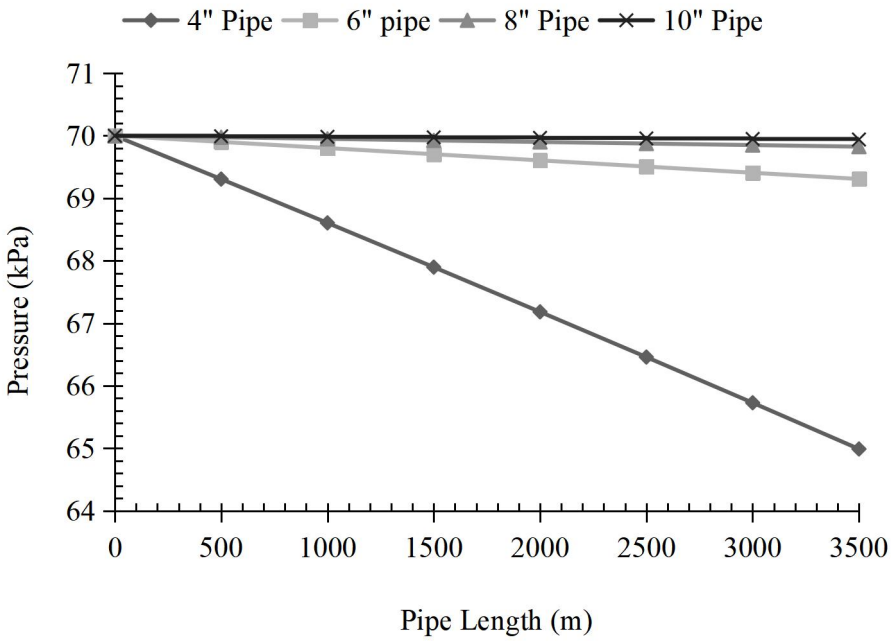

Figure 1 Pressure profiles from simulation at 35m^3/h flow

At 35m^3/h gas flow, 4" pipe showed more promising result for both simulation and theoretical approach with appreciative constant pressure drop of up to 64.987kPa and 68.14kPa for simulation and theoretical respectively. There were minimal pressure drops across 6", 8" and 10" pipes with the lowest being 69.3083kPa and 69.7106kPa respectively from simulation and numerical calculations. These were both obtained from 6" pipe. It is therefore expected that these low pressure drops along 6", 8" and 10" pipes will result in low gas flow (SPE, 2013) as well as low flow velocity.

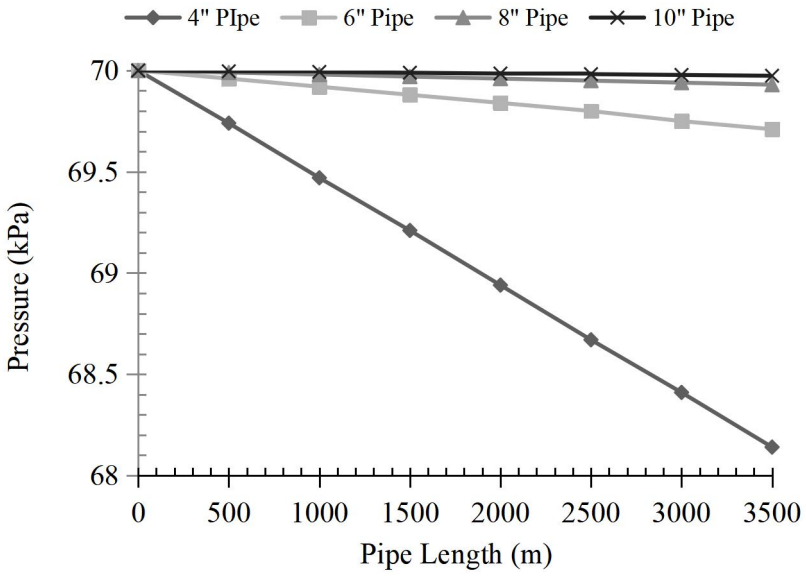

Figure 2 Pressure profiles from numerical calculations at 35m^3/h flow

The fluid behaviour observed in terms of velocity, from simulation, was presented in Figure 3, for each pipe size.

3.1.2 Velocity variations at 35m^3/h gas flow

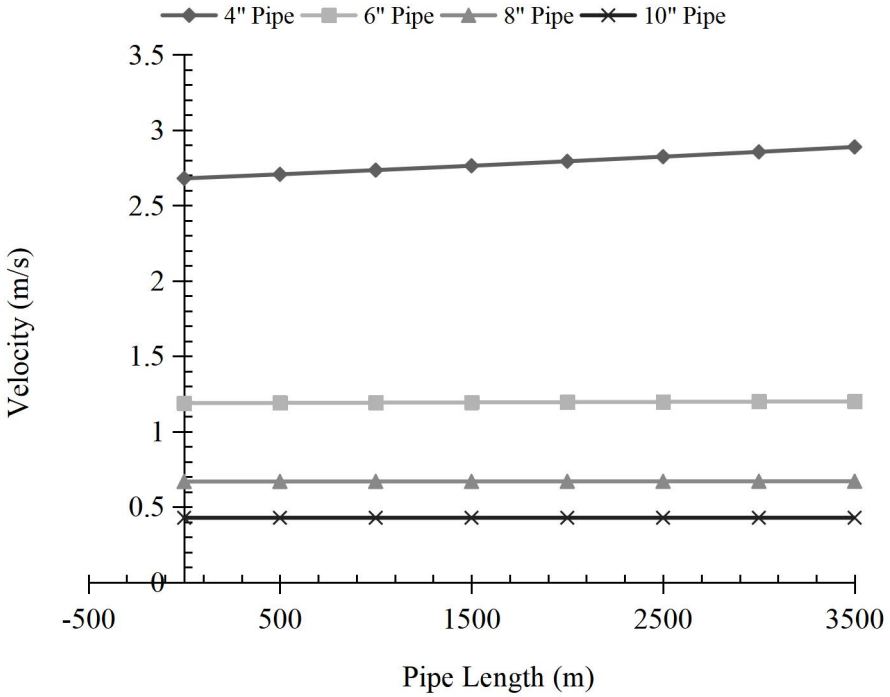

Figure 3 Velocity profiles from simulation at 35m^3/h flow

As predicted earlier, there is minimal flow velocity increase across 6", 8", and 10" pipes, with 10" pipe having a constant value as shown in Figures 3 and 4. Highest velocity value of 2.6652m/s and 2.8884m/s were observed in 4" pipe from both simulation and numerical calculations respectively. These values therefore, indicated that more gas will flow through 4" pipe. Hence, 4" pipe will ensure gas delivery at the downstream gathering point.

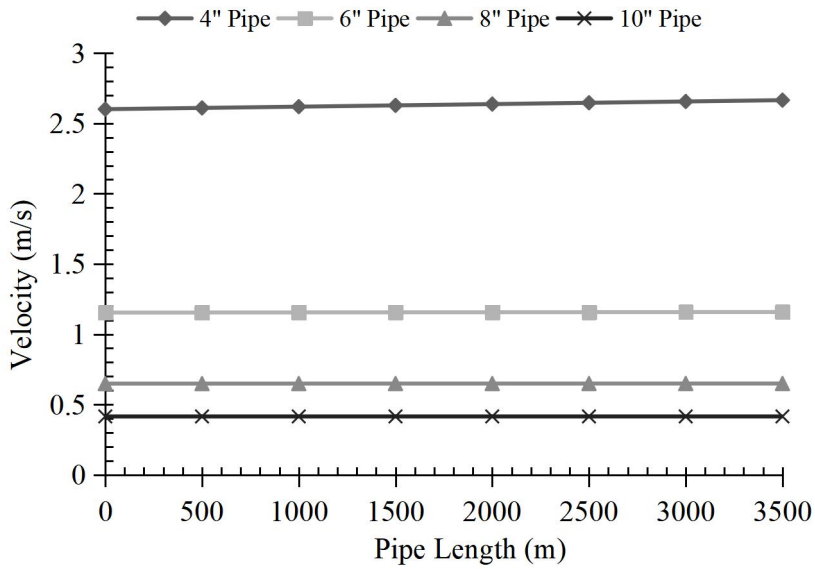

Figure 4 Velocity profiles from numerical calculations @ 35m^3/h flow

3.2 Results obtained when flow was doubled (70m^3/h)

3.2.1 Pressure variations at 70 m^3/h gas flow

When the gas volumetric flow rate was 70 m^3/h, pressure drop along the pipe length, for various pipe sizes considered were generated as shown in Figures 5 and 6.

When flow was doubled to 70m^3/h, the pressure drop continue to increase across all the pipes as shown in Figures 5 and 6 for both simulation and numerical results respectively. The trend follows as at when flow was 35m^3/h. This is expected considering Bournulli's principles and the principles of Law of Continuity. To experience fluid flow, pressure drop must be developed along a pipeline. The pressure drop reduces as the pipe diameter increases. More pressure drop of 70 – 50.3528 kPa was observed in 4" pipe resulting in increased flow through the pipe compared to 6", 8" and 10" pipes.

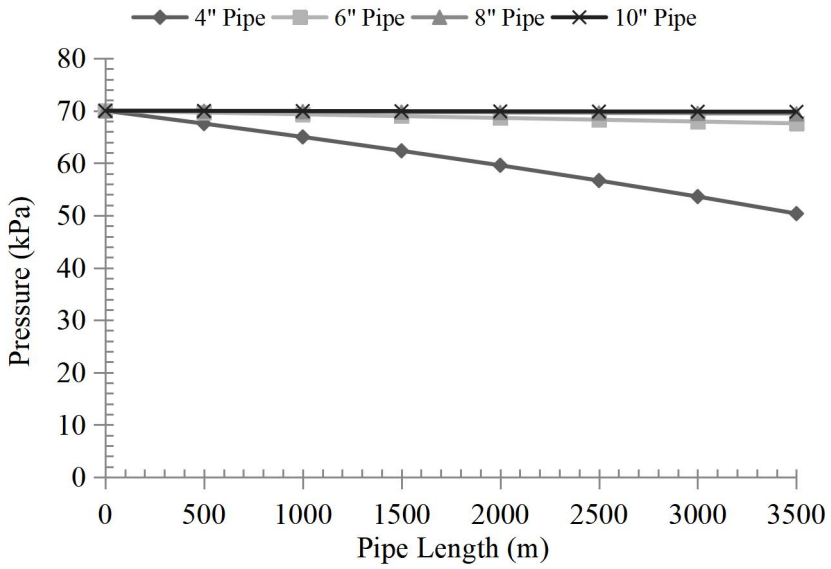

Figure 5 Pressure profiles from simulation at 70m^3/h gas flow

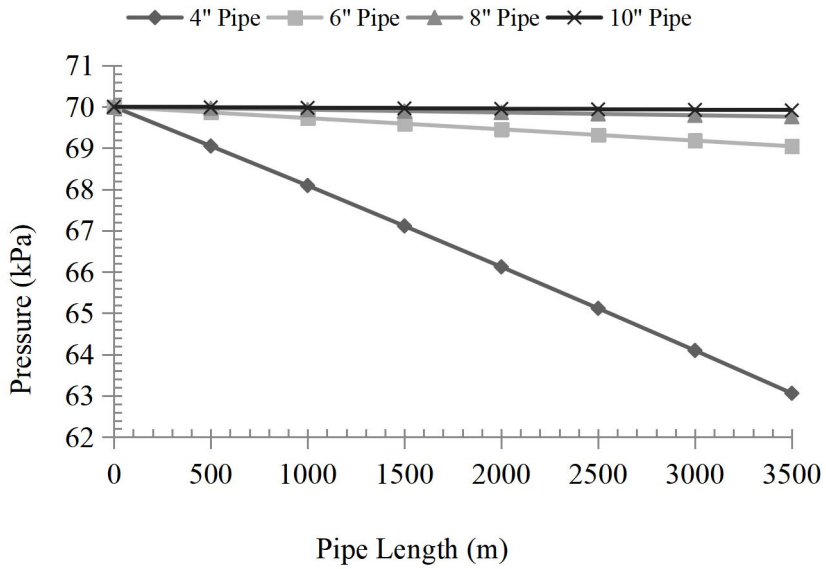

Figure 6 Pressure profiles from numerical calculations at 70m^3/h flow

At double flow, Figures 7 and 8 were generated to establish velocity profiles through each pipe segments from simulation and numerical calculations respectively.

3.2.2 Velocity variations at 70m^3/h

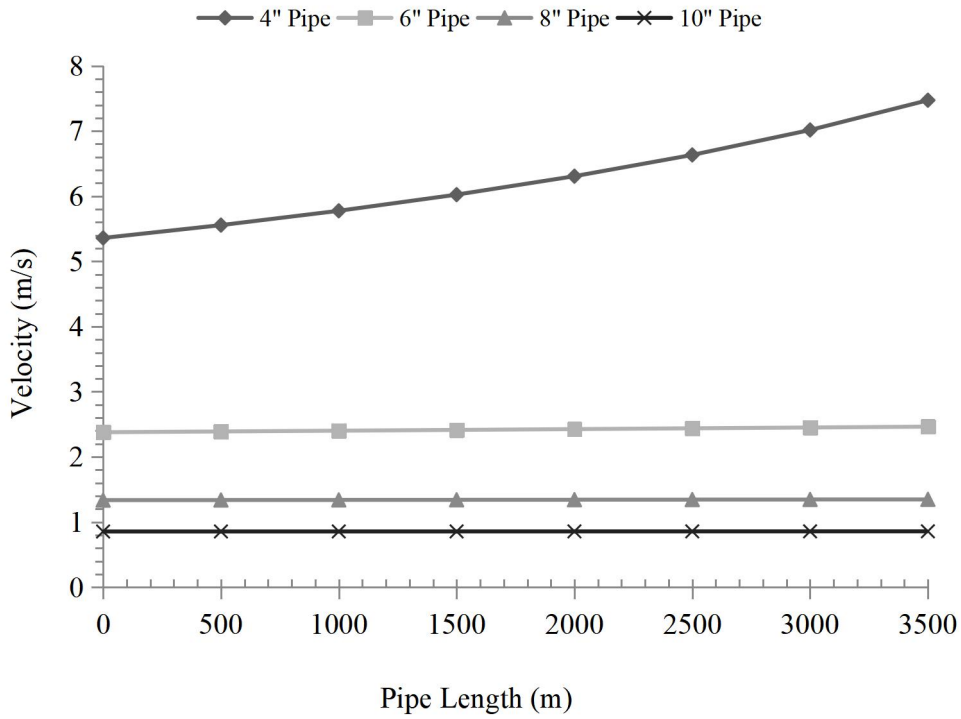

Figure 7 Velocity profiles from simulation at 70m^3/h flow

There is flow increase as a result of increased pressure drop. Consequently the velocity increases through the pipes segments. However, velocity for 4" pipe was becoming undesirably higher (7.4723m/s and 5.7137m/s) than necessary for distribution systems, suggesting an unsuitability to meet further capacity increase. On installation, this will definitely have negative consequence when gas demand increases. In this case, 6" showed more promising results for adoption at this flow capacity and to accommodate future demand. On the other hand, velocities show no appreciable increase through 8" and 10" pipes.

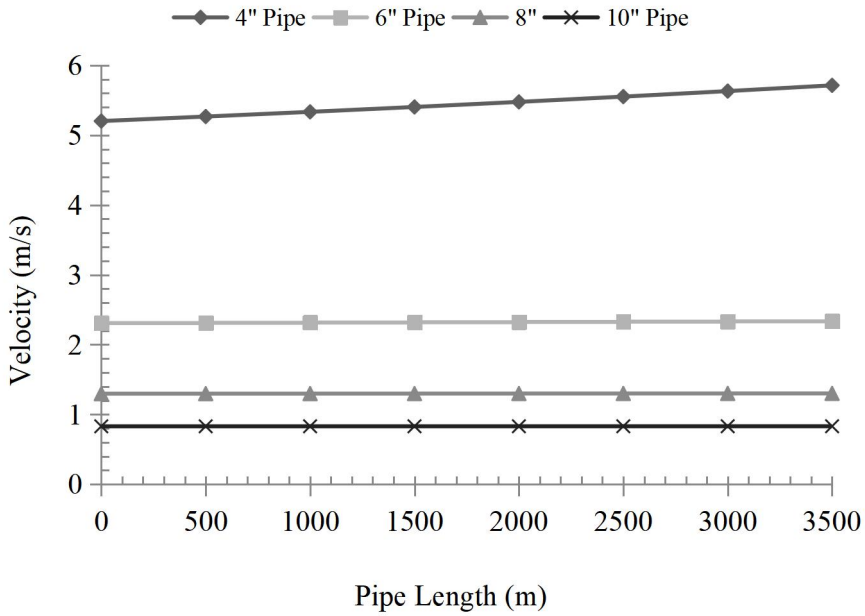

Figure 8 Velocity profiles from numerical calculations at 70m^3/h flow

3.3 Results Obtained at 105 m^3/h gas flow

3.3.1 Pressure variations at 105 m^3/h gas flow

As the gas flow rate was increased to 105 m^3/h, there is exponential increase in pressure drop along 4" pipe compared 6", 8" and 10" pipes as shown in Figures 9 and 10.

\

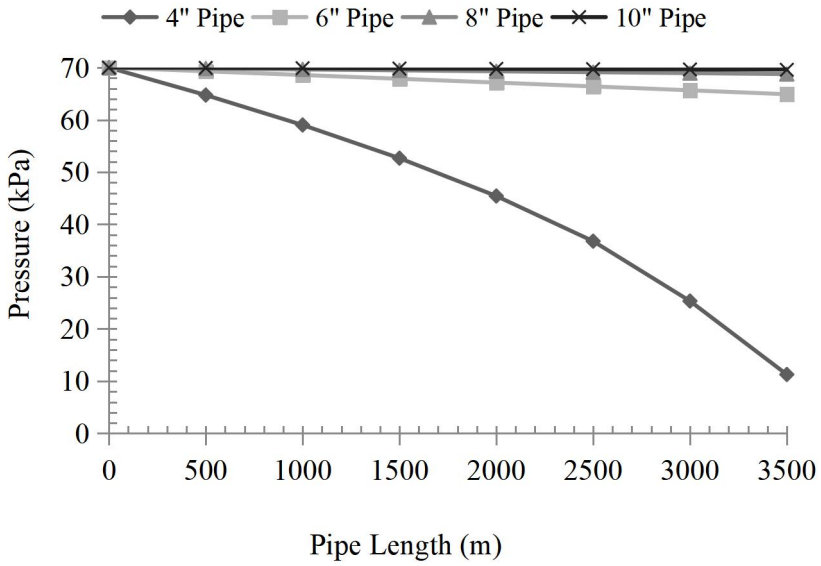

Figure 9 Pressure profiles from simulation at 105m^3/h flow

The pressure has dropped from 70 to 11.27 kPa (simulation) while it dropped from 70 to 54.68 kPa (numerical calculations) across 4". This drastic pressure drop may compromise the integrity of the pipe and safety of ecosystem. Although there was appreciable pressure drop through 8" and 10" pipes, it was less desirable and not appreciable enough to deliver desired gas volume compared to 6" pipe. As such, based on the profiles in the figures, 6" pipe provides a better option for this flow rate.

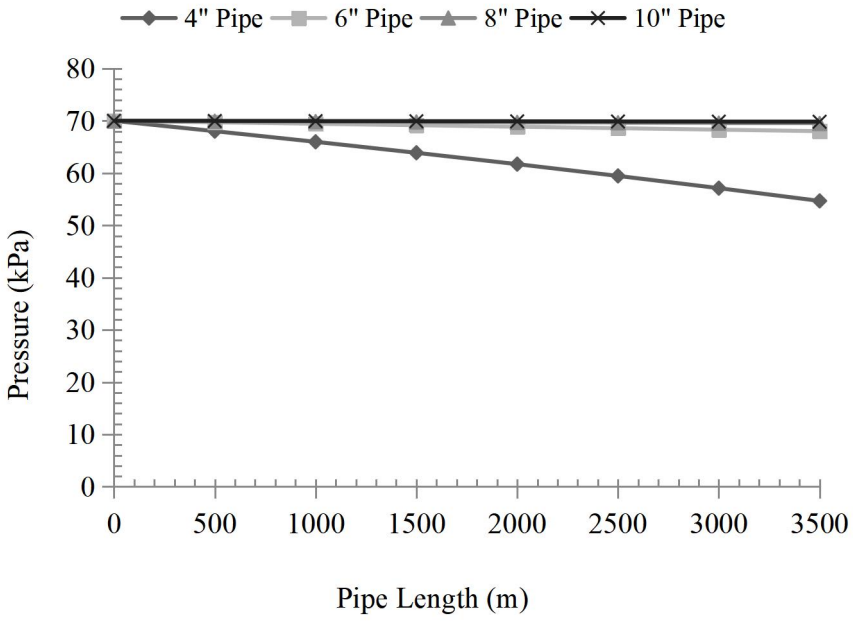

Figure 10 Pressure profiles from numerical calculations at 105m^3/h flow

Additionally, the discrepancy between the values obtained from simulation and numerical calculations may be from choice of Reynolds number.

3.3.2 Velocity variations at 105m^3/h Flow

The drastic pressure drop experienced in 4" pipe led to velocity far exceeding erosional velocity of 20 m/s as indicated in Figures 11 and 12 for simulation and numerical calculation respectively. There is a discrepancy between the values obtained from simulation and theoretical calculations. This may not be far from choice of Reynolds number.

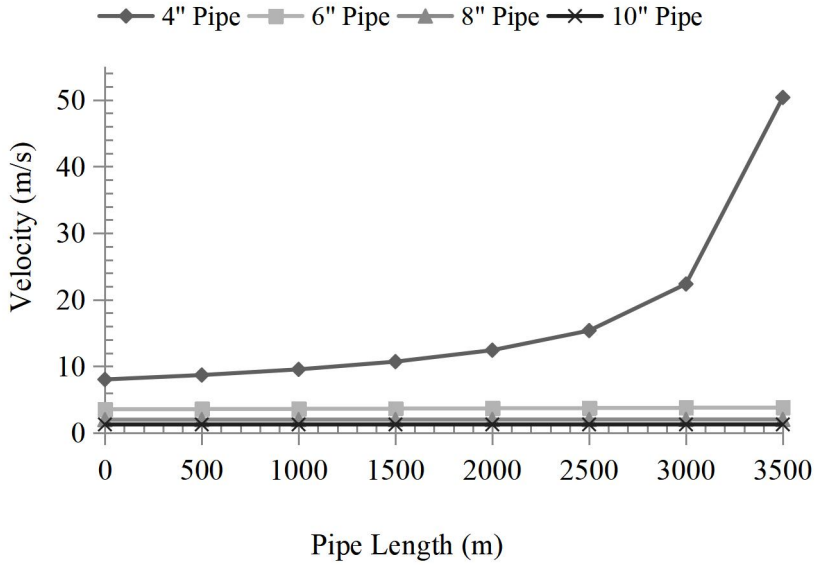

Figure 11 Velocity profiles from simulation at 105m^3/h flow

Either way however, the velocity in each case is intolerable (with values up to 9.7076m/s and 50.3703m/s respectively for theoretical and simulation) for distribution systems where gas will be supplied to homes. As such, 6" will offer best choice, compared to 4", 8" and 10.

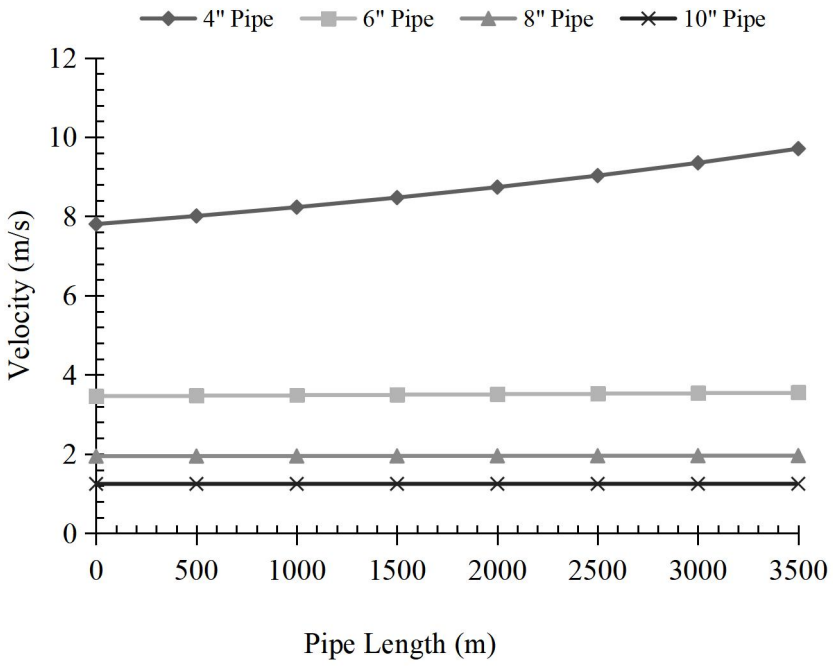

Figure 12 Velocity profiles from numerical calculations at 105m^3/h flow

3.4 Results obtained at 175 m^3/h flow

3.4.1 Pressure drop at 175 m^3/h flow

At estimated gas demand of 175 m^3/h, the pressure drop for 4" pipe increased beyond limit and therefore couldn't converged or be solved by the simulator (Figure 13).

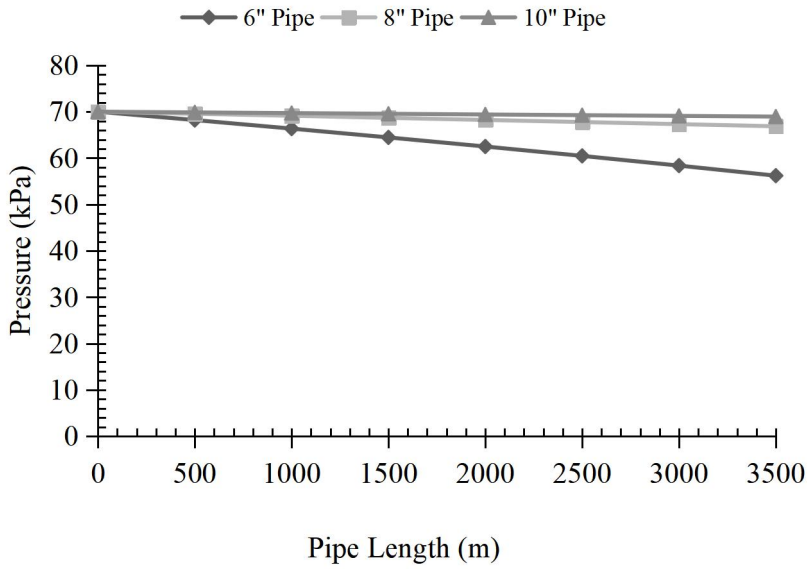

Figure 13 Pressure profiles from simulation at 175m^3/h flow

When solved theoretically however, a negative downstream pressure was obtained as indicated in Figure 14. Therefore, 6" pipe proffer the required solution to the pipe requirement problem, compared to 8" and 10" pipes, with appreciable and tolerable pressure drops of 56.20 and 64.83 kPa from 70 kPa for simulation and numerical calculation respectively.

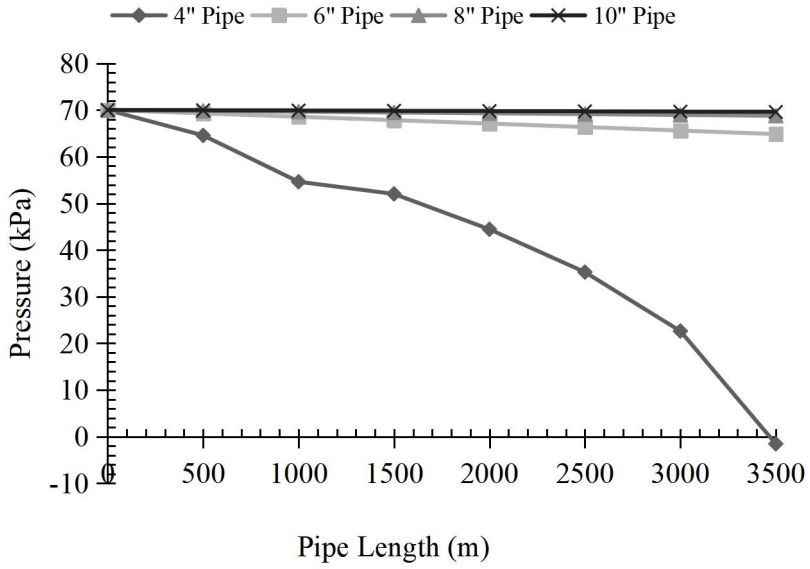

Figure 14 Pressure profiles from numerical calculation at 175m^3/h flow

3.4.2 Velocity Variations at 175m^3/h Flow

Gas velocity at this flow was studied using both simulation and numerical calculations. For flow of 175m^3/h, 6" pipe showed an appreciable and tolerable velocity of 7.420204m/s and 6.1831m/s respectively for simulation and theoretical calculation. The profiles for 8" and 10" shown in Figures 15 and 16 may not be enough to delivery this volume of gas.

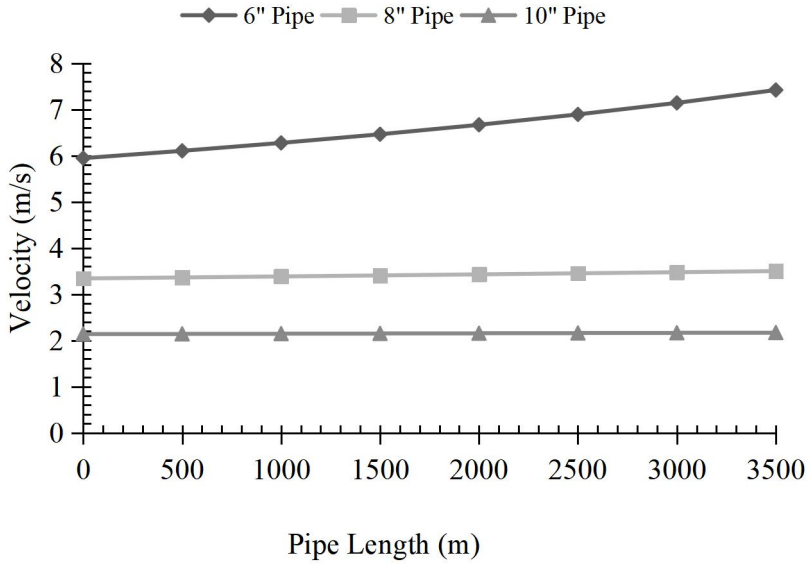

Figure 15 Velocity profiles from simulation at 175m^3/h flow

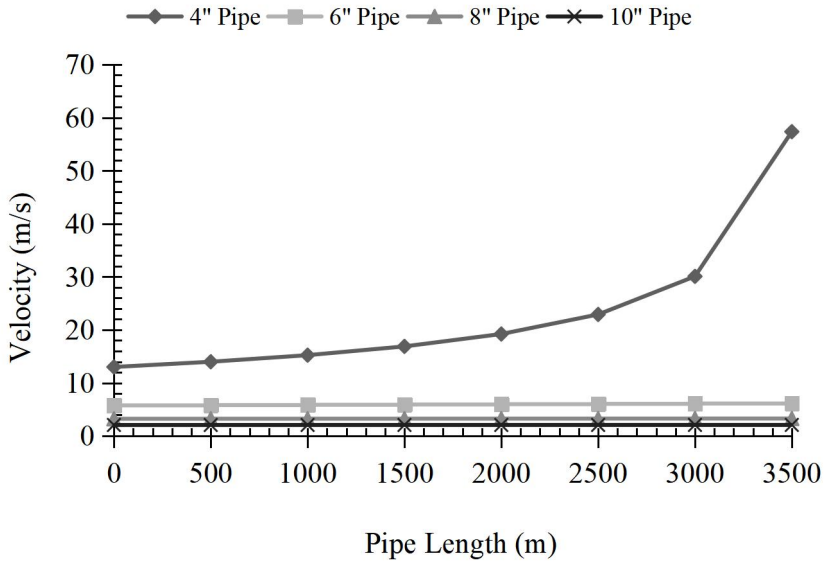

Figure 16 Velocity profiles from numerical calculations at 175m^3/h flow

3.5 Pipeline Integrity Calculations

3.5.1 Wall Thickness

Wall thickness for the pipe nominal sizes were considered for selected SDR11 based API 15LE specification and presented in Table 3.

Table 3 Wall thickness for corresponding nominal pipe size, with tolerance

Nominal Pipe Size in (mm)	Outer Diameter (Average) in (mm)	Minimum Wall Thickness in (mm)
4 (101.6)	4.50 + 0.009 (114.3 + 0.23)	0.409 + 0.048 (10.39 + 1.24)
6 (152.4)	6.63 + 0.011 (168.28 + 0.28)	0.602 + 0.072 (11.53 + 1.83)
8 (203.2)	8.63 + 0.015 (219.08 + 0.38)	0.785 + 0.094 (19.94 + 2.39)
10 (254.0)	10.75 + 0.015 (273.05 + 0.38)	0.978 + 0.117 (24.84 + 2.97)

3.5.2 Pressure Calculation

For 4" Pipe

Taking standard stress rating (HDS) for the selected SDR11 PE material to be 1000psi (Radius System, 2008), the pressure was calculated thus using Equation 10.

$$P = \frac{2S}{SDR-1} \qquad 10$$

$$P = \frac{2 \times 1000 \times 0.366}{4 - 0.366}$$

= 201.43psi (13.89bar)

However, due to commercial availability, standard stress rating (HDS) of 800psi was also considered and pressure calculated as well.

$$P = \frac{2 \times 800 \times 0.366}{4 - 0.366} = 161.14\text{psi (11.11bar)}$$

The same procedure was followed to calculate for 6", 8" and 10" pipes and the result shown in Table 4.

Table 4 Calculated pressure ratings

Nominal Pipe Size (in)	Pressure Rating (bar) HDS	
	800psi	1000psi
4	11.11	13.89
6	11.07	13.84
8	11.05	13.81
10	11.03	13.79

The pressure ratings in Table 2.18, for the given stress, indicate that the selected pipe sizes will withstand pressure of 7bar for medium and intermediate pressure systems.

4, CONCLUSION

The hydraulic simulation of the proposed pipeline was successfully carried out using Aspen Hysys software package (V8). The simulated pipeline sizing was confirmed using numerical calculations. Sizing of the pipeline was studied using PE material of SDR11, having nominal sizes of 4", 6", 8", and 10". Results obtained that both theoretical and simulated results considerably agreed. Additionally, 4" pipe will best suit

delivery of 35 m^3/h flow while 70m^3/h flow will effectively be delivered by 4" and 6". At 105 and 175 m^3/h flow, only 6" pipe will effectively deliver the gas to the downstream at required conditions of pressure and volumetric flow. The findings further indicates that the upstream pressure will be adequate to transport the flare gas the proposed estate without the need for compression.

REFERENCES

Ajayi, O., 2009. Assessment of utilisation of wind energy resources in Nigeria. *Journal of Energy Policy,* 37(2), pp. 750-753.

API 15LE, 1995. *Specification for Polyethylene Line Pie.* 3rd ed. Washington: American Petroleum Institute.

ASME B31.8, 2012. *Gas Transmission and Distribution Piping Systems.* New York: American Society of Mechanical Engineers.

Centre for People and Environment,, 2009. *Pre-Feasibility Study of Electricity Generation from Nigerian Coalmine Methane.* [Online] Available at: http://www.temec5.com/CMM_to_Electricity%20Finall%20Report.pdf [Accessed 11 February 2014].

Consultansy Africa Intelligence, 2012. *Scramble for Energy Resources: The prospects for Sino-Nigerian cooperation.* [Online] Available at: http://www.polity.org.za/article/scramble-for-energy-resources-the-prospects-for-sino-nigerian-cooperation-2012-11-27 [Accessed 11 February 2014].

KRPC, 2013. *Production Log/Data Book.* Kaduna: Kaduna Refining and Petrochemical Company.

Mohitpour, H., Golshan, H. & Murray, A., 2003. *Pipeline design and Contruction: A Practical Approach.* 2nd ed. New York: ASME Press.

Mokhatab, S., Poe, W. A. & Speight, J. G., 2006. *Handbook of Natural Gas Transmission and Processing.* New York: Elsevier Inc.

Nasr, G. G., 2013. *Gas Flow and Network Analysis.* Salford: University of Salford.

Oseni, M. O., 2012. Households' access to electricity and energy consumption pattern in Nigeria. *Renewable and Sustainable Energy Reviews,* 16(1), pp. 990-995.

Radius Systems, 2008. *Natural Gas Pipelines: Polyethylene Pipe Systems for Pressure Classes up to 10bar.* [Online] Available at: http://www.radius-systems.com/uploadedfiles/16-1375443465-gas_technical_manual1.pdf [Accessed 26 January 2014].

SPE, 2013. *Pipeline Design Consideration and Standards.* [Online] Available at: http://petrowiki.org/Pipeline_design_consideration_and_standards [Accessed 27 February 2014].

US Energy Information Administration, 2013. *Country Analysis: Nigeria.* [Online] Available at: http://www.eia.gov/countries/cab.cfm?fips=ni [Accessed 11 February 2014].

MODELING BIOCORROSION OF MILD STEEL UNDER STAGNANT FRESH WATER STREAM CONDITION USING ENVIRONMENTAL FACTORS

[*]Amadi, T.N., Izionworu, V.O., Nwosa, I.G., Altraide, I. and Wami, E.N.
Department of Chemical/Petro-Chemical Engineering,
Rivers State University, Port Harcourt.
Corresponding author's email: titus.amadi@ust.edu.ng

ABSTRACT

This paper provides a mathematical model of predicting corrosion rate in relation with known prevailing environmental factors that promote corrosion processes. In this study, biocorrosion of mild steel in a fresh water environment was investigated under static condition taken into account some of the environmental factors prevailing in the water body. A mathematical model relating weight-loss of the metal to some corrosion determining factors such as, temperature (27.00^0C–30.30^0C), pH (5.92-6.60), conductivity (82.15 µS/cm–120.30µS/cm), dissolved oxygen (4.10mg/l – 5.20mg/l), total dissolved solids (92.16mg/l–178.01mg/l) and total bacterial count ($4.23x10^1$CFU/ml-$1.26x10^5$CFU/ml) was established. The results obtained showed that corrosion rate was most sensitive to temperature with power dependence of 1.21, followed by total dissolved solids with a power dependence of 0.64 as seen in the developed model. The predicted corrosion rate in mils per year (mpy) (0.49, 0.64, 0.94, 1.02, 0.98, 0.94, 1.01, 1.05) compared well with the experimental data (0.51, 0.67, 0.96, 1.05, 1.01, 0.97, 1.05, 1.09) respectively and a mean absolute relative error, ε_a = 3.40%, was obtained. This shows that the model developed is obviously a faster method of predicting corrosion rate than the conventional weight-loss method. Hence, this mathematical model can serve as a proactive measure in mitigating the effects of corrosion in any environment since it can be used to predict corrosion rate before, during and after environmental impact assessment of any engineering materials.

***Keywords**: Modeling, Fresh Water, Mild Steel, Biocorrosion, Environmental factors*

1.0 INTRODUCTION

This study introduces a model that describes the relationship between the environmental factors and corrosion processes in static fresh water environment. Biorrosion modeling is the process of developing a mathematical model that can be used to relate the processes or factors involved during biocorrosion activities (Fernández *et al*., 2022; Hadi *et al*., 2020). Mathematical model is used to determine the relationship between a specific biocorrosion process and a number of influencing parameters. Modeling and simulation often provide efficient and cheap tools for understanding the behavior of considered systems and processes (Moore *et al*., 2022; Javiera *et al*., 2022). Moreover, they simplify results in the development of some correlations that could be used for monitoring, optimization, and control of a given system (Amadi and Wami, 2023; Ruiz-Garcia *et al*., 2024). It is of great importance to develop a relationship between corrosion rate of materials and the various environmental factors that exist in an environment such as the fresh water body so that the modeling of corrosion dynamics can simulate the actual mechanisms as accurate as possible. This would help to reduce the uncertainties associated with some methods used in predicting corrosion rate such as the weight loss method.

Numerous mathematical models have been developed by different authors to simulate biocorrosion processes (Javiera Anguita, *et al*., 2022; Hadi 2020; Sarmasti, 2011; Ruiz-Garcia *et al*., 2024; Shaukat *et al*., 2020; Anees and Baker, 2017; Jose *et al*., 2020; Sergey *et al*., 2020; Agarry and Salam, 2016).

Studies have shown that cellular substances form on the surfaces of metals when immersed in water due to biochemical reaction between the microorganisms and nutrients such as dissolved oxygen (DO) and total dissolved solids (TDS) in the water body (Pan Liu *et al*., 2023; Amadi *et al*., 2011). The physicochemical interaction of metals with their environment undoubtedly causes corrosion problems (Amadi and Wami, 2023; Agarry and Salam, 2016)

The occurrence of Microbiologically Influenced Corrosion (MIC) takes place in diverse environments and not limited to aqueous corrosion under submerged conditions, but also takes place in humid atmospheres (Tsarovtceva *et al*., 2023; Kovacevic *et al*., 2023;Sergey *et al*., 2020).

Biocorrosion is an electrochemical process in which microorganisms are able to initiate, facilitate, or accelerate the corrosion reactions without changing its electrochemical nature (Sutherland *et al*., 2021; Anusuya *et al*,. 2021). Microbiologically mediated reactions do not result in a unique type of corrosion, but they can induce localized corrosion, change the rate of corrosion, and also inhibit corrosion (Harrison *et al*., 2023).

Microorganisms distinguish themselves from other industrial water contaminants by their ability to utilize available nutrient sources, reproduce, and generate intra- and extracellular organic and inorganic substances in water (Ruiyong *et al*., 2021; Amadi, 2015).

Biocorrosion can be described in terms of its effects on processes and products such as material degradation, product contamination, mechanical blockages, and impedance of heat transfer (Deidda *et al*., 2021; Puyate *et al*., 2009). MIC is widely recognized in various industrial fields. Microorganisms are especially abundant in soil and water, which means they can influence the corrosion behavior of metal structures (Smith *et al*., 2021).

Microorganisms add to the corrosion process all the diverse effects derived from microbial interactions with the environment surrounding the metal surface. As this interaction becomes very intense, it can be expected that microbial participation in corrosion will markedly enhance the damage to the metal (Amadi and Wami, 2023; Zhao *et al.,* 2020; Agarry and Salam, 2016).

Over the years, different methods of determining corrosion rate have been developed. The methods include weight loss, Potentiodynamic Polarization (Tafel Extrapolation); Electrochemical Impedance Spectroscopy (EIS)**;** Linear Polarization Resistance (LPR)**;** Zero-Resistance Ammeter (ZRA)**;** Ultrasonic Thickness Measurement**;** Radiographic Techniques; Magnetic Flux Leakage (MFL)**;** Scanning Electron Microscopy (SEM)**;** Energy Dispersive X-ray Spectroscopy (EDX)**;** Electrical Resistance Probes**;** Hydrogen Permeation Technique among others methods (Li *et al*., 2023). It is important to note that these methods listed above are used to monitor corrosion processes during and after installations. However, the present study seeks to provide a proactive measure that could predict corrosion problems before, during and after installation is done through proper analysis of the prevailing environmental factors.

Conventional weight-loss method has been the oldest and most common method used in determining corrosion loss of materials which takes longer time and, in some cases, may not give accurate results (Francisco Malaret, 2022). However, the need for faster, more reliable, and proactive method of predicting corrosion rate to fill this knowledge gap as seen in existing literature prompted the present study.

This study is thus, aimed at generating primary biocorrosion data for mild steel in a static fresh water condition and modeling the effects of these factors in the corrosion of metal which will be useful for impact assessments of engineering materials before, during and after any engineering construction works.

The purpose of this study is to develop an alternative method that is faster, proactive and more reliable in predicting corrosion failures other than the weight loss method.

2.0 MATERIALS AND METHODS

2.1 Materials

The following materials were used during this investigation. They include mild steel coupons, thread, emery paper, ethanol, acetone, oven, desiccator, freshwater sample, plastic container, hydrochloric acid, McCartney glass bottle, water quality monitor, saline, test tubes, glass spreader, nutrient agar, petri dishes, plates, nutrient broth, bowls, polypropylene rope, and weighing balance.

2.2 Method

2.2.1 Preparation of Mild Steel Coupons

The mild steel used was obtained from a corrosion monitoring and control company at Port Harcourt. The chemical composition of the mild steel used for the experiment include C 0.14, Si 0.18, Mn 0.44, S 0.4, Pt 0.7, Sn 0.05, Cr 0.01, Cu 0.05 and Fe 98.03 (Amadi and Wami, 2023). The mild steel sheet was cut into smaller sheets of length 50mm, width 25mm and thickness 1mm. A hole of the same diameter was drilled close to an edge

of each mild steel coupon to allow for passage of a thread. The coupons were thoroughly surface-finished with emery paper. Eight (8) pieces of corrosion coupons were prepared for the study. The method used in preparing the coupons is consistent with known methods (Amadi and Wami, 2023). The prepared coupons were weighed before and after each test period using a weighing balance.

2.2.2 EXPERIMENTAL PROCEDURE

Water was collected from the flowing fresh water stream at Isiokpo and stored in a fifty (50) litres capacity plastic bowl. The bowl was left wide open and kept in the same environment to ensure uniform climatic/weather conditions. A total of eight (8) prepared corrosion coupons (with their initial weights as seen in Table 2 below) were immersed and suspended in the stagnant water with the help of a polypropylene rope. The coupons were retrieved at intervals of 720 hours from the stagnant water. The corrosion product or biofilm formed on the retrieved coupons was carefully removed by washing with de-mineralized water into a beaker. Thereafter, the retrieved coupon was cleaned, dried and re-weighed. The process was repeated every 720 hours for a total period of 5760 hours. The physicochemical properties of the water sample were tested each day of retrieving the coupons. The parameters tested for include temperature, pH, conductivity, total dissolved solids and dissolved oxygen. The biofilm washed off from the retrieved coupon was analyzed to determine total bacterial count as outlined in (Amadi and Wami, 2009).

3.0 RESULTS AND DISCUSSION

Table 1.0 shows the changes in the physicochemical and bacteriological properties of the stagnant water in the course of the experiments.

Table 1.0: Physicochemical and Bacteriological Properties of Stagnant FreshWater Stream

Time (hours)	Temp. (^oC)	pH	Cond. (µS/cm)	TDS (mg/l)	DO (mg/l)	TBC (CFU/ml)
0.00	27.00	6.60	82.15	168.40	4.47	$1.26x10^5$
720	28.60	6.58	90.20	166.70	4.51	$2.82x10^4$
1440	29.30	6.51	98.41	172.40	4.34	$2.16x10^4$
2160	30.30	6.40	108.20	168.70	4.10	$2.52x10^3$
2880	29.20	5.92	120.30	119.40	4.62	$2.32x10^3$
3600	28.40	6.48	112.50	178.01	4.78	$2.18x10^3$
4320	29.80	6.39	120.15	102.58	4.40	$3.78x10^2$
5040	30.10	6.44	104.40	98.36	4.30	$3.54x10^2$
5760	28.80	6.51	118.70	92.16	5.20	$4.23x10^1$

Temperature is an important rate – controlling factor in bacterial activity which directly or indirectly affects all the factors that govern microbial growth in any environment (Edinson *et al*., 2022; Amadi, 2015). The temperature ranged from 27–30.30^{o}C. This temperature range favours the growth and activities of microorganisms in fresh water environment, which in turn promoted biocorrosion of the immersed coupons (Edinson *et al*., 2022; Clarke *et al*., 2022). Electrical conductivity of the stream water samples ranged from 82.15-120.30 µS/cm, indicating the presence of ions in the water body. Studies have shown that higher conductivity values promote metal corrosion (Dheenadhayalan *et al*., 2024; Padmalatha and Lavanya, 2023). The pH of all the water samples ranged from 5.92 - 6.60, indicating a slight acidic medium. Research has shown that acidic media promote corrosion of metals and other engineering materials (Talukdar and Rajaraman, 2020).Total dissolved solids are the amount of organic and inorganic materials, such as metals, minerals, salts, and ions, dissolved in a particular volume of water (Al-Moubaraki and Obot,

2021). Variations of total dissolved solids (TDS) in the water body ranged from 102.58 -178.01mg/l which is a good indicator for an environment that promotes biocorrosion (Amadi, 2015). Dissolved Oxygen (DO) which is the amount of oxygen that is present in water ranged from 4.10 - 5.20mg/l. The presence of oxygen promotes corrosion of metals. The formation of oxide with metal leading to corrosion of the said metal are well documented (Choi *et al*., 2021; Anusuya *et al*., 2021; Shaukat *et al*., 2020). The total bacterial count ranged from $1.26 \times 10^6 – 4.23 \times 10^1$, showing a decline in population of aerobic bacteria in biofilm scrapped off from the retrieved coupons. The decline in population in stagnant water may be attributed to decay of cells in the

biofilm depth due to aging or starvation which leads to a decrease of the adhesive strength (Padmalatha and Lavanya, 2023). The biofilm formation on the surfaces of the mild steel coupons due to metabolic activities occasioned by the consumption of nutrients by microorganisms and their interaction with the metal undoubtedly contributed to the corrosion of the immersed mild steel coupons. However, the population of microorganisms contained in the scrapped biofilm as seen in Table 1 was within the range of microbial population that can promote biocorrosion in any environment (Amadi and Wami, 2023; Agarry and Salam, 2016).

where
$\Delta M = M_0 - M_F$ is the weight-loss (g) of the coupon, A is the total exposed surface Area of the coupon (cm^2), calculated as $A = 2(LW + LH + WH)$, in which L is length of the coupon, H is the thickness of the coupon and W is the width of the coupon, ρ is the density of the coupon (g/cm^3) and t is the time (hours).

3.1 Corrosion Rate Calculations

The results of changes in the weights of the various coupons with respect to the extent of immersion in water are shown in Table 2. The longer the immersion duration of the coupons in water the higher the weight of the metal lost (Padmalatha and Lavanya, 2022).

There are several methods of determining corrosion rate including the weight-loss method which has been used in this study. Corrosion rate (CR) is related to weight-loss (Amadi and Wami, 2023) as:

$$Corrosion \quad Rate = \frac{\Delta M \times 3.45 \times 10^6}{A \rho t} (mpy) \quad (1)$$

The weight-loss and the total surface area of the coupon were calculated and substituted in equation (1) to obtain the corrosion rate values. Table 2.0 shows corrosion rate of mild steel in stagnant water system in which the corrosion rates (mils per year) showed a general trend of increase as the exposure times were increased.

Table 2: Corrosion Rate of Mild Steel in Stagnant Fresh Water

Time (Hrs)	Initial mass (g)	Final mass (g)	ΔM (g)	Corr. Rate (mpy)
0.00	0.00	0.00	0.00	0.00
720	13.25	13.22	0.03	0.51
1440	13.49	13.41	0.08	0.67
2160	13.35	13.18	0.17	0.96
2880	13.42	13.17	0.25	1.05
3600	13.41	13.11	0.30	1.01
4320	13.26	12.92	0.34	0.97
5040	13.28	12.85	0.43	1.05
5760	13.16	12.65	0.51	1.09

The weight-loss of metal continuously immersed in water is a linear function of time (Amadi and Wami, 2009).

However, in this study, it was observed that the weight-loss of mild steel immersed in water under stagnant condition depended on time and the environmental factors contributing to biocorrosion behaviour of mild steel within the environment. The factors affecting biocorrosion in a stagnant fresh water environment are numerous and include parameters such as pH, electrical conductivity, total dissolved solids (TDS), dissolved oxygen (DO), temperature, total bacterial count (TBC), etc. These parameters are good environmental impact indicators for biocorrosion assessment (Lavanya, 2021; Amadi, *et al*., 2010).

Since the weight-loss as seen in this study is a function of time and the prevailing environmental factors present

in the environment, the relationship can be represented mathematically (Rajput, 2005; Amadi and Wami, 2023):

$$\Delta M = f\left(t\ pH\ \lambda\ \beta\ [O]\ \mu\ \eta\right) \quad (2)$$

Where t = time, λ = conductivity, β = TDS, [O] = DO, μ = temperature, η = TBC

Equation (2) can also be written as:

$$\Delta M = K_M \left(t^n \; pH^a \; \lambda^b \; \beta^c \; [O]^d \; \mu^e \; \eta^f \right) \qquad (3)$$

where n, a, b, c, d, e and f, are power dependence of the respective parameters during metal corrosion. K_M is a modified corrosion rate constant whose value depends on other environmental factors that might not have been considered in this analysis.

The values of power dependence of these parameters were evaluated by taking natural logarithm of both sides of equation (3) to give

$$In\Delta M = InK_M + n\ln t + a\ln(pH) + b\ln\lambda + c\ln\beta + d\ln[O] + e\ln\mu + f\ln\eta \qquad (4)$$

In general, equation (4) may be re-written for each experimental run, i, as

$$In\Delta M_i = InK_M + n\ln t_i + a\ln(pH)_i + b\ln\lambda_i + c\ln\beta_i + \mathrm{d}\ln[O]_i + e\ln\mu_i + f\ln\eta_i \qquad (5)$$

Equation (5) was solved by substituting the experimental values in Tables 1 and 2 at each given time. These resultant simultaneous equations were solved using matrix method to give:

$K_M = 5.83 \times 10^{-5}$, n = 1.28, a = −3.86, b = −0.29, c = 0.64, d = −0.04, e = 1.21, f = −0.09

Substituting the power values and K_M in equation (3) gives:

$$\Delta M = 5.83x10^{-5} . t^{1.28} . pH^{-3.86} . \lambda^{-0.29} . \beta^{0.64} . [O]^{-0.04} . \mu^{1.21} . \eta^{-0.09} \qquad (6)$$

where $K_M = 5.83 \times 10^{-5}$, takes care of other prevailing environmental factors that might not have been considered in this model for stagnant water condition.

Substituting equation (6) into equation (1) gives a new corrosion rate expression as:

$$Corrosion\ Rate = \frac{201.14 . pH^{-3.86} . \lambda^{-0.29} . \beta^{0.64} . [O]^{-0.04} . \mu^{1.21} . \eta^{-0.09}}{A . \rho . t^{-0.28}} (mpy) \qquad (7)$$

The effect of each physicochemical property, as shown by the values of their power dependence in equation (6), shows that time has the highest effect, followed by temperature, then slightly by total dissolved solids (TDS). The negative power value of dissolved oxygen (DO) shows that the mild steel coupons were starved of oxygen as the biofilm or corrosion product thickens on the coupons (Amadi and Wami, 2009; Amadi, 2015). The analysis also showed that increase in pH will lead to decrease in corrosion rate. Hence, decrease in pH will increase corrosion rate. Similarly, the negative power value of total bacterial count indicates a declining population of bacteria in the water due to depletion of nutrients in the system.

2. **Comparison between Experimental and Correlated Corrosion Rates**

Table 3 shows the comparison between experimental and correlated corrosion rates results.

Table 3: Comparison between Experimental and Correlated Corrosion Rates.

Experimental corrosion rate	Correlated corrosion rate	Relative error ε_i (%)
0.00	0.00	0.00

Experimental corrosion rate	Correlated corrosion rate	Relative error ε_i (%)
0.51	0.49	3.92
0.67	0.64	4.48
0.96	0.94	2.08
1.05	1.02	2.86
1.01	0.98	2.97
0.97	0.94	3.09
1.05	1.01	3.81
1.09	1.05	3.67
		$\varepsilon_a = 3.40\%$

where $$\varepsilon_i = \frac{(CR)_E - (CR)_C}{(CR)_E} \times 100 \quad , \tag{8}$$

and $$\varepsilon_a = \frac{1}{n}\sum_{i=1}^{n} |\varepsilon_i| \tag{9}$$

$(CR)_E$ = Exprimental Corrosion Rate

$(CR)_C$ = Correlated Corrosion Rate

n = Number of Experiment run

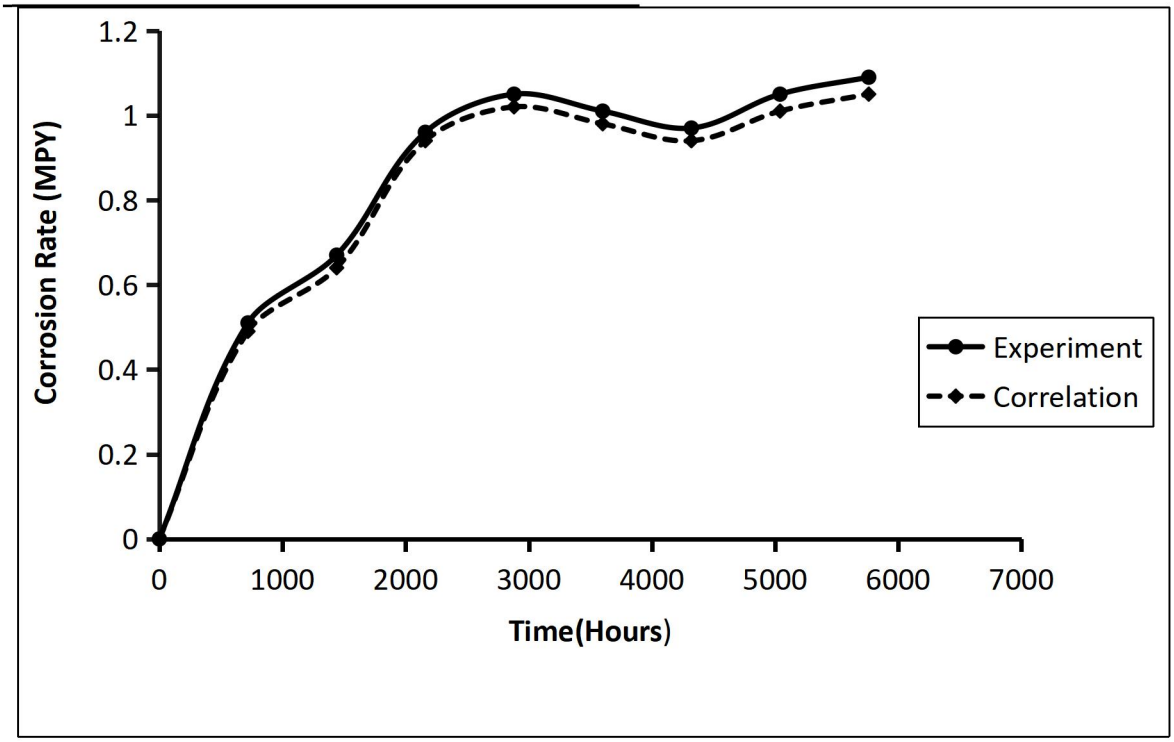

Figure 1: Experimental and Correlated Corrosion Rate Results

The experimental results had been compared with correlated values of corrosion rate in Table 3 and Figure 1 and a mean absolute relative error, ε_a = 3.40%, was obtained. This shows a good agreement, implying that equation (7) can be satisfactorily used to predict the corrosion rate of metals (mild steel) over a period of time in a stagnant water condition, once the dimensions of the metal and the environmental factors are known.

4.0 CONCLUSION

The physicochemical and bacteriological properties of the fresh water body were determined and a correlation relating corrosion rate with the environmental factors was developed. The prediction of corrosion rate with the developed model compared well with the experimental data. This correlation has shown that the corrosion rate of metals under stagnant water conditions can be successfully predicted once the environmental factors and the dimensions of the metal are known.The correlation is very accurate within the range of variations of the parameters investigated. Hence, it is established within the context of this study that the model developed is obviously a faster and more reliable method of predicting corrosion rate than the conventional weight-loss method.

5.0**RECOMMENDATION**

It is recommended that this new model be used as an alternative method of determining corrosion rates before, during and after environmental impact assessment. It is also recommended that further studies be carried out to widen the scope of this study. Constructive criticisms aimed at strengthening this new model are highly recommended.

6.0 ACKNOWLEDGEMENT

The authors are grateful to Prof S.A Wemedo of the Department of Applied and Environmental Biology, Rivers State University, Port Harcourt for his support in the microbiological analysis.

REFERENCES

Al-Moubaraki, A.H. and Obot, I.B. (2021). Top of the line corrosion: causes, mechanisms, and mitigation using corrosion inhibitors. *Arab. J. Chem.* 14; accessible on https://doi.org/10.1016/j.arabjc.2021.103116.Search in Google Scholar

Amadi, T.N., and Wami, E.N. (2023). Correlating The Effect of Some Environmental Factors on Mild Steel Biocorrosion in A Flowing Freshwater Using Dimensional Analysis; *Paper Presented At The 5th International Conference On Engineering For Sustainable Environment* Organised ByThe Nigerian Institution Of Environmental Engineers, Rivers State Chapter, Held On 22nd November, 2023 At Amphitheatre, Rivers State University, PortHarcourt, pp 85 – 90 of the Proceeding.

Amadi, T.N. and Wami, E.N. (2023). Biocorrosion of Mild Steel in Culture of Aerobic Bacteria. *Journal of Newviews in Engineering and Technology (JNET) Volume 5, Issue 1, 2023. Available online at http://www.rsujnet.org/index.php/publications/2023 - edition*

Amadi, T. N. (2015).Investigation of Biocorrosion of Mild Steel in a Fresh Water Environment, *Ph.D Thesis* Submitted to the Post Graduate School, Rivers State University, Port Harcourt.

Amadi, T.N., Puyate, Y.T. and Wami, E.N. (2011). One-Dimensional Model for Convective-Diffusive Transport of Dissolved Oxygen during Biofilm Formation on Mild SteelImmersed in Flowing Fresh Water Body. *Journal of the Nigerian Society of Chemica0lEngineers*, Vol. 26 No.2, pp. 61 – 69.

Amadi, T.N., Amadi, S.A. and Wami, E.N. (2010). Biocorrosion of Mild Steel in Stagnant and Flowing Fresh Water Stream Conditions. *Journal of the Nigerian Society of Chemical Engineers*, Vol. 25 No.1&2, pp. 95 – 108.

Amadi, T.N. and Wami, E.N.(2009); Effect of Physicochemical Properties of Fresh Water Stream on Mild Steel Corrosion, Part 1: under a Stagnant Condition, *Journal of The Nigerian Society of Chemical Engineers*, Vol. 24, No.1&2, pp. 111 – 116.

Choi, S. S., Lee, M. J. and K. J. Kim, K. J. (2021). A review of mathematical models for corrosion of metals in aqueous environments.*Journalof Corrosion Science.*

Clarke, A. M., Nguyen, E. P. H. and Johnson, R. L. (2022). Mathematical modeling of corrosion in high-temperature environments: Application to nuclear reactor materials.*Journal of Nuclear Materials*

Deidda, M. R., Tan, L. S. and Smith, J. A. H. (2021). Predictive modeling of localized corrosion in industrial environments: An application to chloride-induced corrosion of reinforced concrete. *Journal of Construction and Building Materials*

Dheenadhayalan Sivakumar , Rathinam Ramasamy , Yamuna Rangaiya Thiagarajan , Brindha Thirumalairaj , Umapathi

Krishnamoorthy , Md Irfanul Haque Siddiqui , Natrayan Lakshmaiya , Abhinav Kumar and Mohd Asif Shah (2024). Biosurfactants in biocorrosion and corrosion mitigation of metals: An overview. *Journal of Open Chemistry. https://doi.org/10.1515/chem-2024-0036*

Edinson Puentes-Cala; Valentina Tapia-Perdomo; Daniela Espinosa-Valbuena; Maria Reyes-Reyes; Diego Quintero-Santander; Silvia Vasquez-Dallos; Henry Salazar; Pedro Santamaria-Galvis; Ramon Silva-Rodriguez and Genis Castillo-Villamizar (2022). Microbiologically Influenced Corrosion: The gap in the field. *Front. Environ. Sci. Volume 10 https://doi.org/10.3389/fenvs.2022.924842*

Fernández, L. A., Peters, M. E. and Evans, H. L. (2022). Modeling the interactions between corrosion and microbial communities in concrete structures.*Journal of Construction and Building Materials*

Hadi Seddiqiz, Ali Sadatshojaie, Behzad Vaferi, Ehsan Yahyazadeh, Afshin Salehi, David A. Wood (2020). Mathematical model for iron corrosion that eliminates chemical potential parameters. *Chinese journal of chemical engineering, vol. 28, Issue 2.*

Harrison, J. S., Lee, Y. K. and F. R. Wang, F. R. (2023).Machine learning-enhanced models for predicting biocorrosion in industrial environments.*Journal of Corrosion Engineering, Science and Technology*

Javiera Anguita, Gonzalo Pizarro, Ignacio T. Vargas (2022). Mathematical modelling of microbial corrosion in carbon steel due to early-biofilm formation of sulfate-reducing bacteria via extracellular electron transfer. *Bioelectrochemistry, Volume 145, 2022.https://doi.org/10.1016/j.bioelechem.2022.108058*

Jose a. Rodriguez, Julian Cruz-Borbolla, Pablo A. Arizpe-Carreon and Evelin Gutierrez (2020). Mathematical Models Generated for the Prediction of Corrosion Inhibition Using Different Theoretical Chemistry Simulations. *Materials* **2020**, *13*(24), *5656; https://doi.org/10.3390/ma13245656*

Kovacevic, S., Ali, W., Martínez-Pañeda, E., and LLorca, J. (2023). Phase-Field Modeling of Pitting and Mechanically-Assisted Corrosion of Mg Alloys for Biomedical Applications. *Journal ofActa Biomaterialia*, 164, 641-658.

Lee, M. J., Vermeulen, N. T. and Patel, S. J. (2020). Biocorrosion of metals: A Review of Mathematical Models and Simulation Approaches. *Journal of Corrosion Science*

Li, J. X., Zhang, Y. K. and Wang, P. T. (2023). Coupled Electrochemical and Mechanical Modeling of Stress-Corrosion Cracking in Alloys. *Journal of Materials Science and Engineering*

Moore, A. B., Roberts, C. D. and Johnson, T. J. (2022). Computational modeling of sulfate-reducing bacteria and their impact on corrosion in oil and gas pipelines.*Journal of Petroleum Science and Engineering*.

Padmalatha Rao and Lavanya Mulky (2023). Microbially Influenced Corrosion and its Control Measures: A Critical Review. *Journal of Bio- and Tribo-Corrosion; Volume 9, article 57.*

Pan Liu, Haiting Zhang, Yongqiang Fan, and Dake Xu (2023). Microbially Influenced Corrosion of Steel in Marine Environments: A Review from Mechanisms to Prevention. *Journal of Microorganisms, 11(9), 2299.*

Puyate, Y.T., Rim-Rukeh, A. and Ujile, A.A. (2009). One–Dimensional Approximation of Oxygen Transport during Biofilm Formation on X60 Steel Immersed in Static Aqueous Medium. *Journal of the Nigerian Society of Chemical Engineers, Vol. 23, pp. 20 – 28.*

Rajput, R. K. (2005). A Textbook of Fluid Mechanics in S.I Units, 4rd Edition, pp. 294 – 361.

Ruiz-Garcia A., Esquivel-Penna V., Godinez F. A., and Montoya R. (2024).Corrosion Modeling of Aluminum Alloys: A Brief Review. *ChemElectroChem. Volume 11, Issue 9*. https://doi.org/10.1002/celc.202300712

Shaukat Ali Mazari, Lubna Ghalib, Abdul Sattar, Mir Muhammad Bozdar, Abdul Qayoom, Israr Ahmed, Atta Muhammad, Rashid Abro, Ahmed Abdulkareem, Sabzoi Nizamuddin, Humair Baloch and Mubarak, N.M. (2020). Review of modelling and simulation strategies for evaluating corrosive behavior of aqueous amine systems for CO_2 capture. *International Journal of Greenhouse Gas Control. Volume 96.*

Smith, R. L., Davies, J. H. and Brown, P. E. (2021). Mathematical modeling of microbial-induced corrosion in marine environments.*Journal of Biofouling*.

Sutherland, E. G . K., Lopez, A. V and J. L. Park, J. L. (2021). Mathematical modeling of Microbiologically Influenced Corrosion in Oil and Gas Pipelines.*Journal of Corrosion Science*

Tsarovtceva, I. M., Bryukhanov, A. L., Yu Vlasov D. and Maiyorova, M. A. (2023). Biocorrosion of Metal Alloys. *Journal of Power, Technology and Engineering. Volume 57, pp 203 – 208.*Engineeringower Technology and eering

Talukdar, A. and Rajaraman, P.V. (2020). Investigation of acetic acid effect on carbon steel corrosion in CO2–H2S medium: mechanistic reaction pathway and kinetics. *ACS Omega* 5: *11378–11388, https://doi.org/10.1021/acsomega.0c00387. Search in Google Scholar*

Zhao, Jiayue; Csetenyi, Laszlo; Gadd, Geoffrey Michael (2020). Biocorrosion of copper metal by Aspergillus niger. *International Biodeterioration and Biodegradation DOI: 10.1016/j.ibiod.2020.105081*

10.51975/243902011.som
Journal of the Nigerian Society of Chemical Engineers, 39(2), 2024

BIOREMEDIATION OF ENGINE-OIL AND GREASE POLLUTED SOIL USING COMPOST MANURE, FINELY GRANULATED CORNCOB AND BLEND GROUNDNUT SHELL

Alexander Sixtus Eko, Abdullahi Mohammed Evuti, Yetunde M. Aladeitan, Enumah Amarachukwu and Stephen Yakubu

Department of Chemical Engineering
University of Abuja, Abuja. Nigeria
Corresponding email: alexsixalex784@gmail.com

ABSTRACT:

Oil pollution is a major contributor to environmental deterioration. In bioremediation, compost manure, a synergistic blend of finely granulated corncob and groundnut shell can serve as good biostimulants in bioremediating petroleum polluted soils. In this experimental study, all the 14 prepared soil samples used were loamy-sand labelled: Sample A (control soil), Sample B (contaminated soil studied for natural attenuation), Samples C to N (contaminated soil + biostimulant(s)). The variations in soil pH, electrical conductivity, heavy metal (HM) content, total microbial count and total petroleum hydrocarbon content measured at intervals (on days 0, 28, 56, 84, and 112), were used as criteria for evaluating the effectiveness of treatment process. Prior to commencement of experimental studies (at time, t = 0), GC-MS, FTIR, AAS analysis carried out on Sample A showed no petroleum contaminations in them. However, analytical variations across all polluted samples indicated reduction in TPH concentrations at various rates during the span of the experimental studies. Remediation was more enhanced in Sample F (with removal efficiency of 56.79%) and lowest in Sample B (with removal efficiency of 8.642 %). The results obtained were used to develop charts and equations for determining the most suitable treatment regime adoptable based on the given parameters and conditions.

Keywords: *Bioremediation, Petroleum contamination, Compost Manure, Environmental Sustainability*

1.0 INTRODUCTION

Oil pollution in terrestrial and aquatic environment has become a major threat to natural ecosystems and human beings through the transfer of complex toxic materials including polycyclic aromatic hydrocarbons (PAHs) into the food chain (Sharaff *et al*., 2020; Varjani *et al*., 2017, Srivastava *et al*., 2020). Both aquatic and terrestrial habitats have been ravaged by petroleum contamination but, petroleum hydrocarbon contamination in aquatic habitats is more difficult to control than terrestrial habitat. The reason being that concentrating the spill to a particular point is almost impossible because of the nature and instability of the environment (due to the presence of tidal waves) (Lee and Levy, 1989). To stem the effect of these pollutants several techniques including; chemical degradation, physical degradation, thermal degradation, biodegradation, phyto-degradation as well as combined degradation methods have been developed and applied in restoring affected ecosystems to their states prior to contamination (Nyer, 2001). Reported studies have shown that some metabolic intermediates produced from the degradation of petroleum by microbes (bacteria), having relatively high solubility may have greater cytotoxicity then the parent molecules and therefore resulting in bacteria cell damage (van Dorst *et al*., 2014). Indigenous bacteria however form extensive aggregates with each specie performing specific functions. While some bacteria sensitive to petroleum hydrocarbons are inhibited upon exposure to petroleum and environs contaminated by it, those efficient degraders of petroleum hydrocarbons, as well as those resistant and can degrade

cytotoxic metabolites will flourish in such hostile environs. The strength of bioremediation is to a large extent dependent on the size of the remediating

community and so sole reliance on the strength of indigenous microbial communities for clean-up of affected areas will span a longer time. Developing interventionary measures (such as *bioaugmentation* and *biostimulation*) to enhance degradation processes is of paramount importance (New Society Publishers, 2023). This research therefore seeks to show the synergistic effect of compost manure and a blend of finely granulated corncob and groundnut shell biostimulants on the bioremediation of spent engine oil and diesel polluted soil using theoretical and practical machineries as tools for performance analysis and evaluation.

2.0 MATERIALS AND METHODS

2.1 Soil Sampling: The polluted soil samples were collected from the surroundings of University of Abuja-Nigeria main campus generator house. Soil samples were collected at the depths ranging from 0-100mm based on the established claim that bioremediation is ineffective from depths greater than 150mm (Ofoegbu *et al*., 2015). The control sample was obtained from uncontaminated site, 100m away from polluted site (at latitude 8.981277 and longitude 7.179537).

2.2 Experimental Procedures

2.2.1 Determination of Physicochemical Properties

Moisture Content (MC)

The percentage moisture content was determined using established and standardized protocols for soil hydrocarbon (HC) analysis adopted by Usoji and Nwoye (2007). The percentage moisture content ($MC_{\%}$) was calculated using Equation (1);

$$MC_{\%} = \frac{\text{wt. of wet soil (g)} - \text{wt. of dried soil (g)}}{\text{wt. of wet soil (g)}}\% \quad (1)$$

Electrical Conductivity and pH analysis

Electrical conductivity **(**EC) and pH of soil samples were determined using a conductivity meter (Systronics-304) and a digital pH meter (Jenway Model 3015) with a glass-calomel electrode combination respectively following the procedure of Ibitoye (2008).

Soil Organic Matter

Soil organic carbon (OC) concentration was estimated experimentally using modified dichromate wet oxidation method called Walkley-Black procedure (Osuji and Nwoye, 2007; Ibitoye, 2008; Adams *et al*., 2006; Uwem *et al*., 2015).

Bulk density

Bulk density was determined by the method proposed by Verla *et al*. (2012). The volumes of the void (V_v) in the cylinders used were measured by first determining the total volume of each of the cylinders (V_t) which is expressed as:

$$V_t = \pi r^2 h \quad (2)$$

The volumes of used samples (V_s) as shown in Equation (3):

$$V_s = \frac{Ms}{GsPw} \quad (3)$$

Where: r = radius of the cylinder, h = height of the cylinder, M_s = mass of cylinder, G_s = Specific gravity, P_w = density of water. The volume of void was obtained as: $V_v = V_t - V_s$, and bulk density (B_d) was calculated by Equation (4):

$$B_d = \frac{\text{Mass of sample}}{\text{volume}} \quad (4)$$

Oil and Grease Content

Determination of oil and grease content was carried out using the gravimetric method by Cirne *et al.* (2016). And the total oil and grease (TOG) content was calculated using Equation (5):

$$\text{TOG content} = \frac{1{,}000{,}000 \times (M_f - M_i)}{\text{Sample Volume}} \quad (5)$$

Where M_f is is mass of the flask and extract; M_i is mass of empty flask; and sample volume is the volume of analyzed sample.

Particulate Sizing

Soil and biostimulant average particle sizes were determined by sieve analysis: using a 100 µm and a 200µm diameter mesh sieve for biostimulants and 500µm sieve for sample soils.

2.2.2 Composting Process (Backyard composting)

The composting method adopted was simple and executed in a more or less hidden location where proper ventilation and water are accessible, and is partially hidden from the sun to enable conservation of compost water (since it was done during the dry season). To support the composting process, every 7days for a period of 30 days the compost pile is turned using a stick to increase aeration and so oxygen (O_2) is generated into the compost pile.

2.2.3 Gas Chromatography Mass Spectrometer Determination of TPH Residue in Soil Samples

GC-MS (Agilent 7820A- 5975C inert mass spectrometer, Agilent Technologies®) by operating MSD in selective ion monitoring (SIM) applying the procedures of Rosenzweig *et al*. (2022).

2.2.4 Determination of Total Petroleum Hydrocarbon Content by FTIR Spectrophotometer

The total petroleum hydrocarbon concentration was determined using the Fourier-Transform Infrared (FTIR) 7800A (HACH DR/2010) spectrophotometer applying standard solvent extraction method. 1gram of the sieved soil sample was dissolved in carbon tetrachloride (CCl_4) in a test tube. CCl_4 (a non-polar solvent) was used as a solvent in preference to chloroform (a polar solvent) The clear lower layer was thereafter collected with a clean test tube upon which it was dehydrated by the addition of a spoonful of anhydrous sodium sulphate. The clear extract was absorbed at 420 nm and the functional groups present were identified based on their wave lengths.

Total Petroleum Hydrocarbon Removal Efficiency

Total Petroleum Hydrocarbon Removal Efficiency, $TPH_r(\%)$ measures the percentage of TPH removed at any given time in the process and is mathematically expressed in Equation (6) as:

$$TPH_r(\%) = \frac{TPH_i - TPH_f}{TPH_i} \times 100\% \qquad (6)$$

Where Initial Total Petroleum Hrocarbon Concentration (TPH_i) and Final Total Petroleum Hydrocarbon (TPH_f) concentration respectively.

Referring to the Beer-Lambert's equation:

$$A = \varepsilon Cl \qquad (7)$$

Where **A** is Absorbance, $\boldsymbol{\varepsilon}$ is Molar Extinction Coefficient, $\boldsymbol{l}$ is length of path travelled by light, and $\boldsymbol{C}$ is the Concentration of the pollutant in a gram of the sample. Since from our above analysis $\boldsymbol{\varepsilon, l}$ are constants, therefore Equation (7) can be rewritten as:

$$\frac{A}{C} = \varepsilon l \qquad (8)$$

If we have absorbance A_o, A_1, A_2…, An at concentration C_o, C_1, C_2…, C_n respectively, then we have that

$$\frac{A_o}{C_o} = \frac{A_1}{C_1} = \frac{A_2}{C_2} = \ldots = \frac{A_n}{C_n} \qquad (9)$$

Recall that from the First Order Reaction Rate Law:

$$In\frac{C_n}{C_o} = -kt \qquad (10)$$

Or its Integrated Form

$$InC_t = (-kt) + InC_o \qquad (11)$$

Where $\boldsymbol{k}$ is the Reaction Rate Constant

Making $\boldsymbol{C_o}$ (concentration at time, t = 0) and $\boldsymbol{C_n}$ (concentration at time, t = n) subject of the equation from Equation (9) above we have that

$$C_o = \frac{A_o}{\varepsilon l} \qquad (12)$$

Also,

$$C_n = \frac{A_n}{\varepsilon l} \qquad (13)$$

Applying the Equation (11) we have

$$In\left(\frac{\left(\frac{A_n}{\varepsilon l}\right)}{\left(\frac{A_o}{\varepsilon l}\right)}\right) = -kt \qquad (14)$$

Where $\boldsymbol{t}$ is time spent. Simplifying the above Equation (14), we have

$$In\left(\frac{A_n}{A_o}\right) = -kt \qquad (15)$$

From FTIR analysis, since Concentration of TPH is directly proportional to Absorbance, therefore we have that:

$$C_{o(TPH_i)} = \frac{A_o}{\varepsilon l} \qquad (16)$$

$$C_{n(TPH_f)} = \frac{A_n}{\varepsilon l} \qquad (17)$$

Since $\boldsymbol{\varepsilon l}$ is constant (from the above analysis), replacing the above in Equation (7), we have that:

$$TPH_r(\%) = \frac{\left(\left(\frac{A_o}{\varepsilon l}\right) - \left(\frac{A_n}{\varepsilon l}\right)\right)}{\left(\frac{A_o}{\varepsilon l}\right)} \qquad (18)$$

Simplifying the above we have:

$$TPH_r(\%) = \frac{A_o - A_n}{A_o} \qquad (19)$$

Where $\boldsymbol{A_o}$ and $\boldsymbol{A_n}$ are the Absorbance for concentrations of the petroleum hydrocarbon polluted samples for both initial and final. A similar analysis may apply for a second and zero order.

Bio-stimulation efficiency

Biostimulation efficiency (B.E) measures the extent biostimulants enhanced remediation processes compared to natural attenuation process under the same environmental conditions, and is mathematically expressed as:

$$(B.E) = \frac{\text{TPH Conc. in } S_{sample} \text{ at time } t_n - \text{TPH Conc. in } U_{sample} \text{ at time } t_n}{\text{TPH Conc. in } S_{sample} \text{ at time } t_n}(\%) \quad (20)$$

S_{sample} is the stimulated sample and U_{sample} is unstimulated sample.

Half-Life and Kinetic Model of Biodegradation

At $t_{\frac{1}{2}}$, A_t is equal to A_o. A plot of $ln[A_t]$ versus t for a first order reaction is supposed to give a straight line with a slope of $-k$ and a y-intercept of $ln[A_o]$. First-Order Rate equation is expressed in the form of a line equation (Equation (22)) in Equation (21) in terms of Absorbance (from the integrated rate form) as shown below:

$$\ln A_t = (-kt) + \ln A_o \quad (21)$$

$$y = mx + b \quad (22)$$

2.2.6 Enumeration of Bacterial Populations and Subsequent Growth

The total heterotrophic bacterial (THB) and hydrocarbon utilizing bacterial (HUB) counts of the petroleum polluted soil was carried out by ten-fold serial dilution using normal saline by adopting the procedures of (Osobamiro et al., 2019) and the total number of colony forming units (cfu) in a gram of the polluted sample at a particular time. The total number of colonies is multiplied by the dilution factor (10^{-4}) and then divided by the volume of the culture plate, as mathematically expressed in Equation (23) –

$$\text{cfu/ml} = \frac{\text{no. of colonies x dilution factor}}{\text{Volume (or mass) of culture}} (23)$$

And the mean colony forming unit (mean cfu/ml) is given by Equation (24) –

$$\text{Mean cfu/ml} = \frac{B_1 \text{ (cfu/ml)} + B_2 \text{ (cfu/ml)}}{n} \quad (24)$$

Where, n is the number of incubated cultures ($n = 2$).

2.2.7 Isolation and Identification of Hydrocarbon Utilizing Bacteria (HUB)

Culturable bacteria isolates from the hydrocarbon utilizing bacteria plates were sub cultured onto nutrient agar (NA) plates and incubated at 28^0C for 24hrs. The pure isolates were identified on the basis of their cultural, morphological and physiological characteristics (Verla *et al*., 2012).

2.2.8 Bioremediation Experiment (Ex-Situ Remediation)

Glass bottles (each 20 mm in width × 10 mm in height) were used as sample stores. Table 1 and Figure 1 are a data of samples prepared and an illustration of flow of experimental process.

Table 1: The Fourteen Different Samples, their Corresponding Constituents and Total Mass.

S/N	Sample	Sample Constituents	Total Mass of Sample (in grams)
1	A	CS	100g
2	B	PS	100g
3	C	PS + $CM_{(10g)}$	110g
4	D	PS + $CM_{(25g)}$	125g
5	E	PS + $CM_{(50g)}$	150g
6	F	PS + $CM_{(100g)}$	200g
7	G	PS + $GC_{(5g)}$ + $GS_{(5g)}$	110g
8	H	PS + $GC_{(12.5g)}$ + $GS_{(12.5g)}$	125g
9	I	PS + $GC_{(25g)}$ + $GS_{(25g)}$	150g
10	J	PS + $GC_{(50g)}$ + $GS_{(50g)}$	200g
11	K	PS + $CM_{(5g)}$ + $GC_{(2.5g)}$ + $GS_{(2.5g)}$	110g
12	L	PS + $CM_{(12.5g)}$ + $GC_{(6.25g)}$ + $GS_{(6.25g)}$	125g
13	M	PS + $CM_{(25g)}$ + $GC_{(12.5g)}$ + $GS_{(12.5g)}$	150g
14	N	PS + $CM_{(50g)}$ + $GC_{(25g)}$ + $GS_{(25g)}$	200g

Legend for Table 1
PS = 100grams of Contaminated Sample
CS = 100 grams of Control Sample
CM = Compost Manure
GC = Granulated Corncob
GS = Granulated Groundnut Shell

2.2.9 Rationing of Samples for FTIR Analysis

When carrying out the FTIR analysis at first test, 1gram of Sample B was taken from the sample bottle tagged Sample B. Due to the fact that the Samples C-N have mixtures of biostimulants in them, taking the same 1 gram to evaluate the TPH in the FTIR analysis would not give proportionate values to track degradation because naturally the concentration of pollutant in 1gram of Sample B is not the same as that in 1gram of stimulated samples. So, in order to keep near accurate track of degradation samples were taken in equal ration of each samples' mass. Sample C consists of 100 grams of polluted soil and 10grams of stimulant mixed homogeneously, making a total weight of 110gram. Therefore, for every 1gram taken from 100grams of sample B, there will be X-grams taken from 110 grams of C:

$$\frac{1\text{g of B}}{\text{X}} = \frac{100\text{g of B}}{110\text{g of C}} \qquad (25)$$

$$\text{X} = 1.1\text{g of C}$$

Summarily, if 110grams of Sample C contains 100grams of Polluted soil at time, $t = 0$.

Therefore, at time, $t = 0$: 1.1grams of Samples C, G and K would contain 1gram of contaminated soil; 1.25grams of Samples D, H and L would contain 1gram of contaminated soil; 1.50grams of Samples E, I and M would contain 1gram of contaminated soil; 2.00grams of Samples F, J and N would contain 1gram of contaminated soil.

Hydrocarbon polluted soils usually exhibit characteristic low pH values (i.e. are acidic in nature) as a result of their being contaminated with petroleum and its by-products. But the state of a bioremediation process cannot be judged based solely on variations in pH values overtime since the addition of a stimulant can alter soil pH; homogenous alkaline biostimulants can increase soil pH values regardless of the state of a remediation process. Therefore, results from this research will judge its remediation process from the studied trends and characteristic changes in pH, heavy metal content, TPH removal and bio-stimulation efficiencies, as well as intermediate TMC. Table 2 highlights the possible outcomes and inferences that may be drawn at the end of the remediation process.

Table 2: Highlight of the Probable Outcome from Successive TMC and TPH Concentration Analysis

S/N	TMC	TPH Concentration	Probable Outcome
1	Decrease	Constant/Increase	• Microbes are not remediating. • Microbes could not withstand environment.
2	Increase	Constant/Increase	• Microbial life depended on the stimulant and not contaminant to survive.
3	Decrease	Decrease	• Degradation progressed. • Microbes could not withstand harsh environment.
4	Increase	Decrease	• Degradation progressed. • Microbes depended on carbon from contaminant to thrive.

3.0 RESULTS AND DISCUSSION

3.1 Identification of Heterogeneous Bacteria in Polluted Sample.

Crude oil contains hydrocarbons and does not resist attack by microorganisms. The hydrocarbon utilizing microorganisms isolated from the soil were species of: *Bacillus specie, Aspergillus specie, Staphylococcus specie, Pseudomonas specie, Aeromonas specie, Streptococcus specie. Bacillus specie* has been shown to be a good degrader of hydrocarbon in past researches, which might be due to their ability to produce spores, which may shield them from the toxic effects of the HC

(Agu *et al.,* 2015). If the organisms are able to utilize the hydrocarbon as their sole carbon source, they can be used for bioremediation of the polluted sites.

3.2 Physicochemical Analysis of Soil Samples

Physicochemical analysis of soil samples collected at three points were denoted as **A**, **B1** and **B2**. **A** represents the point of control sample collection, which is in a garden of no pollution at a 100 m distance from the polluted site. **B1** and **B2** are the polluted samples collected from different points less than 1m apart at the site of pollution. The results of the physicochemical analysis of polluted soil samples and control are shown in Table 3.

Table 3: Physicochemical properties of soil samples

Parameter	Average Measured Values of Physicochemical Property at Room Temperature (30°C) and 1atm		
	A	B1	B2
pH	7.77	5.32	5.31
Oil and Grease (mg/L)	-	13487	13490
Conductivity (dS/m)	0.8143	0.9779	0.9783
Moisture content (%)	44.5	46.2	46.0
Organic Matter (%)	1.2	3.7	3.8
Texture Class	Sandy Loam	Sandy Loam	Sandy Loam
Particulate Size Range (μm)	50 - 500	50 – 500	50 - 500
Number of Colonies	95	9	11
Colony Forming Units (cfu/g × 10^{-4})	9.5	0.9	1.1

Table 3 shows the pH of the control sample to be slightly alkaline, while those of the polluted samples were mildly acidic. The near neutrality (pH of 7.77) of the control sample could possibly account for the increased volume of the microbe existent in the soil sample while the pH (within the range of 5.32 and 5.31) does not support microbial growth. This accounts for why the size of the colony forming units in the polluted sample (0.9 cfu/g × 10^4 and 1.1 cfu/g × 10^4) was far less than in the control sample (9.5 cfu/g × 10^4) which maybe as a result of the high acidity content caused by the pollutants present in the polluted soil samples. Relative to the adopted method for measuring pH, after mild stirring (to increase homogeneity), pH measurement was taken thrice for each sample with 5minutes interval between successive tests and consecutively obtained results for each sample: sample A (7.77, 7.77, and 7.76); sample B1 (5.31, 5.33, and 5.32); sample B2 (5.31, 5.32, and 5.31) with a deviation ($0 \leq X \leq 0.01$): where X represents the deviation and is highest deviation when it is equal to 0.01. All recorded at standard conditions (average room temperature (30°C) and 1 atm). The conductivity of a sample of soil is best below 1dS/m. Soil samples with higher concentration of metals tend to exhibit high conductivity. The increased conductivity of the polluted samples might be due to the presence of heavy metals in higher concentration from petroleum pollutants. Conductivity test carried at room temperature of 30°C, three times at 5minutes interval between successive analysis gave the results: sample A (0.8143, 0.8142, and 0.8143); sample B1 (0.9779, 0.9779, and 0.9778); sample B2 (0.9785, 0.9784, and 0.9781) with a deviation ($0 \leq x \leq 0.0004$). The moisture content of the polluted soil being higher than that of the control sample is as a result of the high concentrate of grease and oil present in polluted soil. Water is a necessary element for microbial growth but the presence of petroleum hydrocarbon pollutants in soil tends to clog pore spaces, limit the infiltration of water and air (Varges *et al*., 2017). Oil and grease added to the increased moisture content of the contaminated soil but in this case due to their toxicity, insolubility in water and viscous nature they tend to form a *blanket-like* covering over the soil that has led to low soil aeration and therefore microbial activities was restricted from reaching its full potential. The increased organic matter content (OMC) in the contaminated soil than in the control sample could be attributed to many factors such as; population of the microbial community, bio-accessibility of the nutrients, type and nature of organic matter, etc. Low cell density restricts organic activities from reaching full potential, and this in turn would mean higher OMC in affected environments.

3.3 Physicochemical Analysis of Stimulants

As a result of the low pH of the soil, microbes find it hard to adapt and survive in such hostile environment.

According to Varges *et al*. (2017) optimal soil pH for microbial life to thrive ranges between 6.5 - 7.5. Acidic biostimulants will invariably discourage soil remediation. The pH and other of properties of the stimulants analyzed are shown in Table 4.

Table 4: Properties of Stimulants at Standard Conditions (Avg. Room Temperature of 30^{o}C and 1atm)

Parameter	Compost Manure	Granulated Corncob	Granulated Groundnut Shell
pH	6.81	7.63	8.41
Moisture Content (%)	42.1	21.0	19.5
Bulk Density (g/cm^3)	0.8	1.25	1.17
Average Granular Size (µm)	3 - 100	200	200

The pH recorded is the average value gotten from a series of successive three tests with the highest deviation of (0.011) at average room temperature (30^{o}C). The bulk density of the stimulants is a function of its mass and volume. Before the commencement of the composting process, the recorded bulk density of composted manure was recorded to be 1.4g/cm^3, whereas after composting the bulk density recorded was 0.8g/cm^3. This is because the composting process helps in reduction of pathogenic and parasitic load, destroys weed seeds, reduces manure volume and acidity, which is consequential to increased bioavailability and improved soil health and fertility.

3.4 Pollutants level of concentrations using laboratory analysis

The laboratory analysis (including GC-MS and FTIR methods) were carried out with the results in Table 5 indicating of the types of contaminants and their concentrations in the polluted samples with focus limited to only carbon constituting functional groups from FTIR analysis.

Table 5: GC-MS Analysis of Polluted Samples

Component	B1 (ppm)	B2 (ppm)
Naphthalene	29.54	29.76
Acenaphthylene	0.99	21.28
Acenaphthene	1.37	3.82
Flourene	1.22	48.76
Phenanthrene	1114.76	46.59
Anthracene	8.38	82.87
Fluoranthene	2.96	27.23
Pyrene	2.27	22.53
Benzo[c]phenanthrene	9.63	28.75
Benzo[a]anthracene	2.01	97.84
Chrysene	102.86	111.14
Benzo[e]pyrene	19.37	433.65
Benzo[k]fluoranthene	8.66	63.65
3-Methylcholanthrene	79.65	100.28
Indeno[1,2,3-cd]pyrene	17.15	68.45
Dibenzo[a,h]anthracene	33.45	72.41
Benzo[g,h,i]perylene	45.78	15.19
Dibenzo[a,h]pyrene	2.35	14.91
Dibenzo[a,i]pyrene	14.07	10.91
Dibenzo[a,l]pyrene	112.34	6.41
Benzo[a]pyrene	11.98	209.5

The concentration differences at B1 and B2 is as a result of different activities occurring at various points. To know the HMs removal or transformation potential of the biodegraders, a data of recorded metal

concentrations in polluted samples at the beginning and end of the study the AAS analysis carried out showed the concentration of different metals in the soil.

Polluted soil tends to have increased metal content compared to the control soil. Table 6 shows the concentrations of metals in samples collected at A, B1 and B2 at time, t = 0.

Figure 2 below shows the generated graph of absorbance recorded against wave number for the FTIR spectroscopic analysis of Sample B at time, t = 0 days.

Table 6: AAS Analysis of the Soils Collected at A, B1 and B2 at t=0.

Heavy Metal	Corrected Conc. in A (mg/l)	Average Corrected Conc. in B1 and B2 (mg/l)
Cobalt, Co	0.4913	0.6091
Iron, Fe	7.2347	64.7709
Magnesium, Mg	1.6203	11.2404
Zinc, Zn	0.8320	2.0279
Cadmium, Cd	0.0004	0.0313
Lead, Pb	1.3453	21.4664
Nickel, Ni	0.4892	0.6771
Copper, Cu	0.6315	0.8532
Manganese, Mn	1.9915	2.8277
Calcium, Ca	0.8878	1.3451

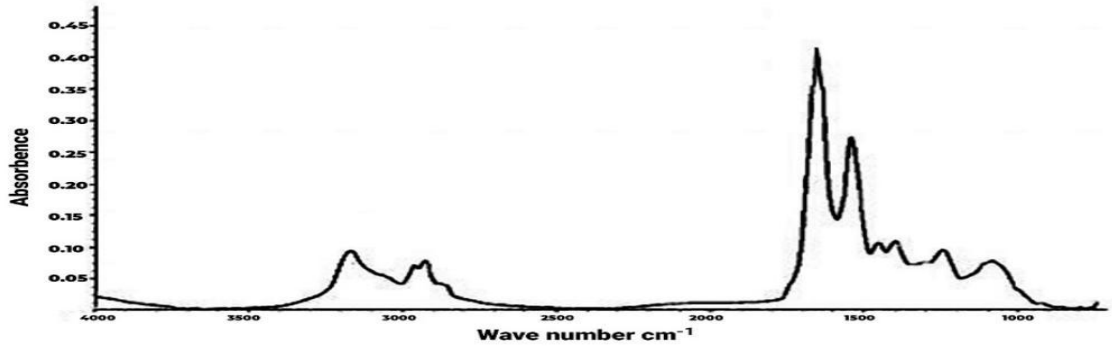

Figure 1. Generated graphical representation of Absorbance recorded against Wave number for FTIR Spectroscopic Analysis of Sample B at time, t = 0 days

FTIR spectroscopy showed that alkanes (C-C) and PAH hydrocarbons constituted the contaminant concentrated in the soil at wavenumber between approximately 1,600-845 cm^{-1} (Khan and Hossain, 2016). The FTIR spectroscopy of the polluted soil sample at time, t = 0 (with highest absorbance of approximately 0.405). The detected concentration of alkanes (about 0.17% of total sample weight from calculations in Equation (5)) cannot be considered negligible compared to the concentration of the PAHs which possess stronger bonds as a result of the multiple benzene rings in their complex structures which makes them more difficult to degrade. The presence of alkane stretch (from about 1500-1000 cm^{-1}) is as a result of higher spent oil and grease contaminant in the environment. The analysis carried out in this project placed focus on the most concentrated hydrocarbon group i.e. straight chain alkanes (paraffin) group. Although, cognizance is given to the least concentrated functional groups which happens to have the stronger bond (C=C) from the presence of PAH since they are most difficult to degrade due to their characteristic nature, environmental persistence and stronger bond. Table 7 below gives the recorded data of FTIR absorbance for all samples recorded on every 28day for the 112day period of study (i.e. four times after t = 0 in the 112day period of study). GC-MS analysis results indicated that there was no presence of petroleum hydrocarbon in the control sample but proved otherwise in the contaminated samples taken from the site of pollution, hence the reason absorbance read zero (0) when analysis on the Fourier-Transform Infrared Spectroscopy (FTIR) with a light wave of 420nm wavelength passed through the prepared sample. The FTIR Calibrations: l = 10mm or 1cm, light wavelength = 420nm.

Calculation of Total Petroleum Hydrocarbon Removal Efficiency (TPH_r (%)) and Bio-Stimulation Efficiency (B.E (%))

Tables 7 and 8 below shows the calculated TPH_r (%) and B.E (%) from the start to finish of the experimental study at different intervals of time.

Table 7: Total Petroleum Hydrocarbon Removal Efficiency (TPH_r (%)) at different Time Intervals of Remediation Process.

Samples	Time Span (days)			
	0-28	0-56	0-84	0-112
A	-	-	-	-
B	1.235	3.704	4.938	8.642
C	3.704	7.407	8.100	13.58
D	7.407	16.05	25.90	29.63
E	4.938	16.05	28.40	37.04
F	7.407	18.52	41.98	56.79
G	1.235	4.938	8.642	13.58
H	3.704	8.642	12.35	16.05
I	2.469	4.938	14.82	18.52
J	4.938	13.58	24.69	32.10
K	1.235	3.704	11.11	14.82
L	2.497	6.173	13.58	19.75
M	2.469	7.407	16.05	24.69
N	3.704	22.22	32.10	46.91

Table 8: Bio-stimulation Efficiency (%) for Stimulated Samples during Remediation Process.

Sample	Time (days)			
	0-28	0-56	0-84	0-112
A	-	-	-	-
B	-	-	-	-
C	2.564	4.000	8.451	5.714
D	6.667	14.71	28.33	29.83
E	3.896	14.71	32.76	45.10
F	6.667	18.18	63.83	111.4
G	0	1.299	4.054	5.714
H	2.564	5.405	8.451	8.824
I	1.266	1.299	11.59	12.12
J	3.896	11.43	26.23	34.55
K	0	0	6.944	7.246
L	1.266	2.632	10.00	13.85
M	1.266	4.000	13.24	21.31
N	2.564	23.81	40.00	72.09

Analysis of Half Life

A second form of the rate law that relates the concentrations of reactants and time i.e. integrated rate law (IRL) can be used to determine the amount of contaminant likely to be present at a particular time and possibly estimate the amount of contaminant present at a particular time. This process can either be straightforward or complex, depending on the complexity of the differential rate law. From the result record of absorbance against time, concentration decreased with increasing time and so did the total microbial count (TMC) overtime, indicating that the environment was becoming favorable and supportive of microbial life. The conducted test for the best fit using the zero, first and second order reaction kinetics in developing a kinetic model that best describes the process showed that first-order kinetic model was best since from the above analysis best described the processes, giving best fit (R^2) values from the graph that were nearest to unity (i.e. 1). The first-order rate

equation in the test for linearity brought about the generated graphs which have been able to describe the remediation process best compared to the zero order and second order rate laws respectively. The coefficient of determination (R^2) is a statistical measure in a regression model that determines the proportion of variance in the dependent variable that can be explained by the independent variable. It shows the goodness of fit in other words. Plotting graphs of t on horizontal axis against $\ln[A]_t$ on vertical axis for Samples B-N gave the following figures:

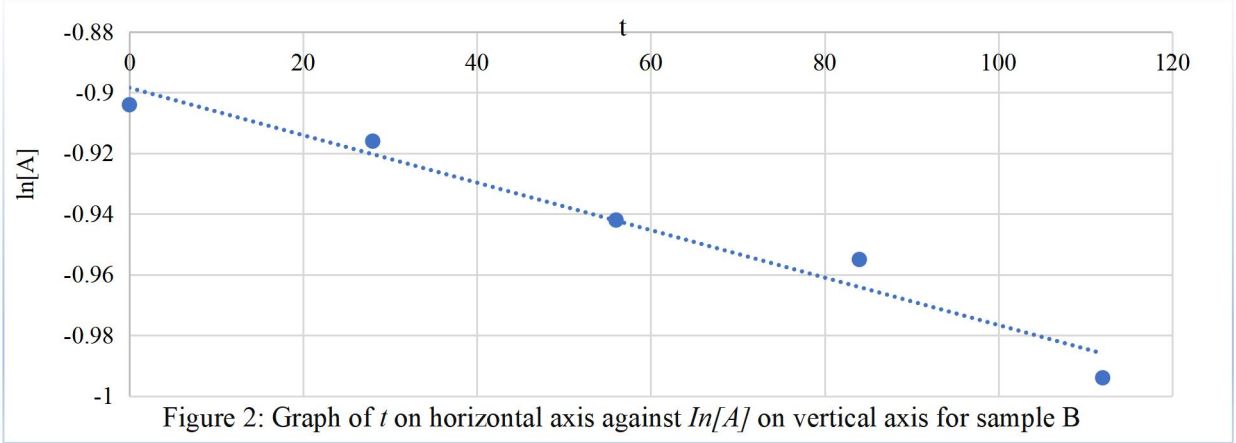

Figure 2: Graph of *t* on horizontal axis against *In[A]* on vertical axis for sample B

Figure 2, is a graphical plot correlating the natural log of recorded absorbance (dependent variable) of sample B on the vertical axis against the time (independent variable) on the horizontal axis. The linear graph of Figure 3 generated the relation:

$$\ln[A] = -0.0008t - 0.8984 \quad (26)$$

The line of best fit represented on the graph gives the best linear correlation of the points with a coefficient of determination (R^2) = 0.9606 (good fit) and k = 0.0008/day, where k is the rate constant in unit per day and with the line of best fit intercepting the vertical axis at a point -0.8984. Anti-log of the intercept gives an approximate value for initial absorbance recorded at t = 0 days.

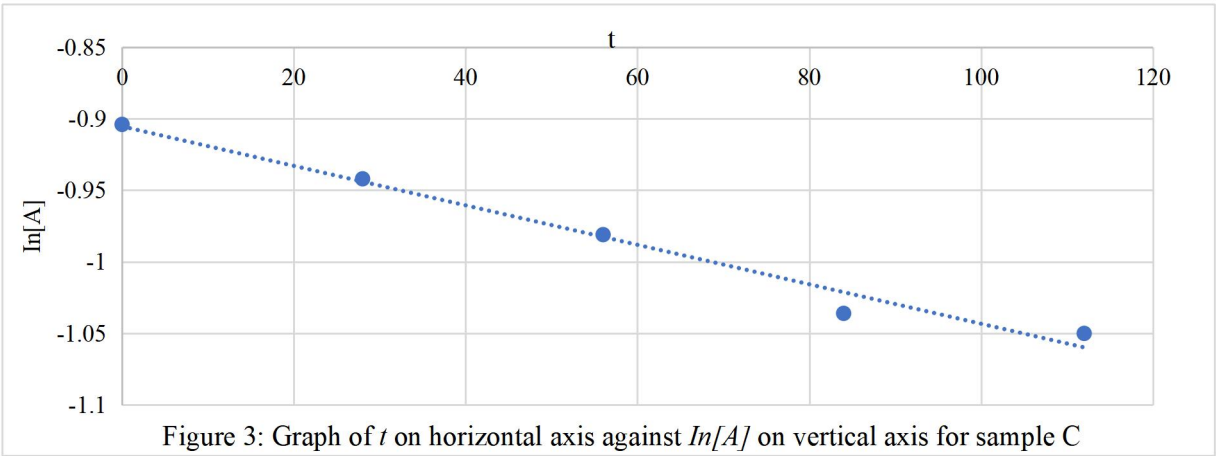

Figure 3: Graph of *t* on horizontal axis against *In[A]* on vertical axis for sample C

Figure 3 is a graphical plot correlating the natural log of recorded absorbance (dependent variable) of sample C on the vertical axis against the time (independent variable) on the horizontal axis. The linear graph of Figure 4 generated the relation below:

$$\ln[A] = -0.0014t - 0.9054 \quad (27)$$

The line of best fit represented on the graph gives the best linear correlation of the points with a coefficient of determination (R^2) = 0.978 (good fit) and k = 0.0014/day, where k is the rate constant in unit per day and with the line of best fit intercepting the vertical axis at a point -0.9054. Anti-log of the intercept gives an approximate value for initial absorbance recorded at t = 0 days.

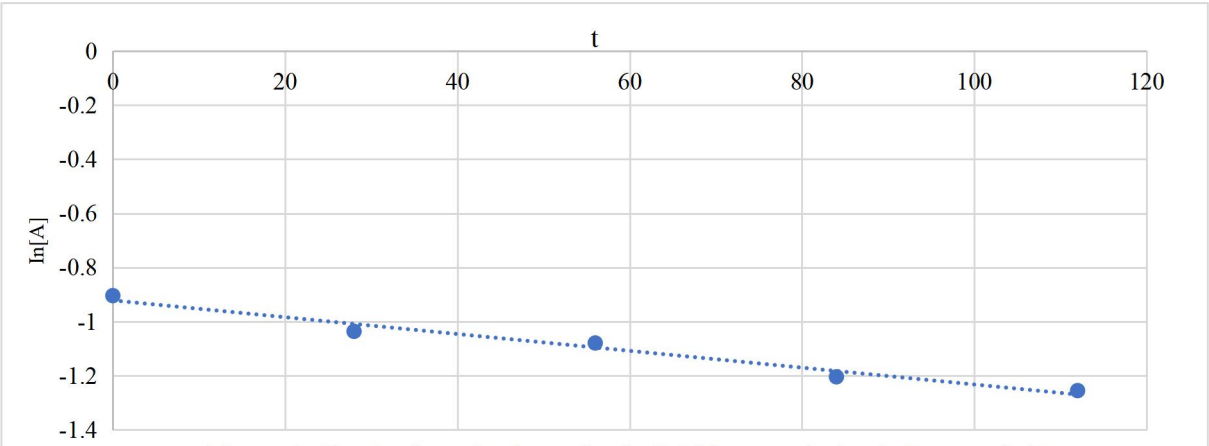

Figure 4: Graph of t on horizontal axis In[A] on vertical axis for sample D

Figure 4 is a graphical plot correlating the natural log of recorded absorbance (dependent variable) of sample D on the vertical axis against the time (independent variable) on the horizontal axis. The linear graph of Figure 5 generated the relation below:

$$\ln[A] = -0.0031t - 0.9216 \quad (28)$$

The line of best fit represented on the graph gives the best linear correlation of the points with a coefficient of determination (R^2) = 0.9742 (good fit) and k = 0.0031/day, where k is the rate constant in unit per day and with the line of best fit intercepting the vertical axis at a point -0.9216. Anti-log of the intercept gives an approximate value for initial absorbance recorded at t = 0 i.e. the initial absorbance before the study began.

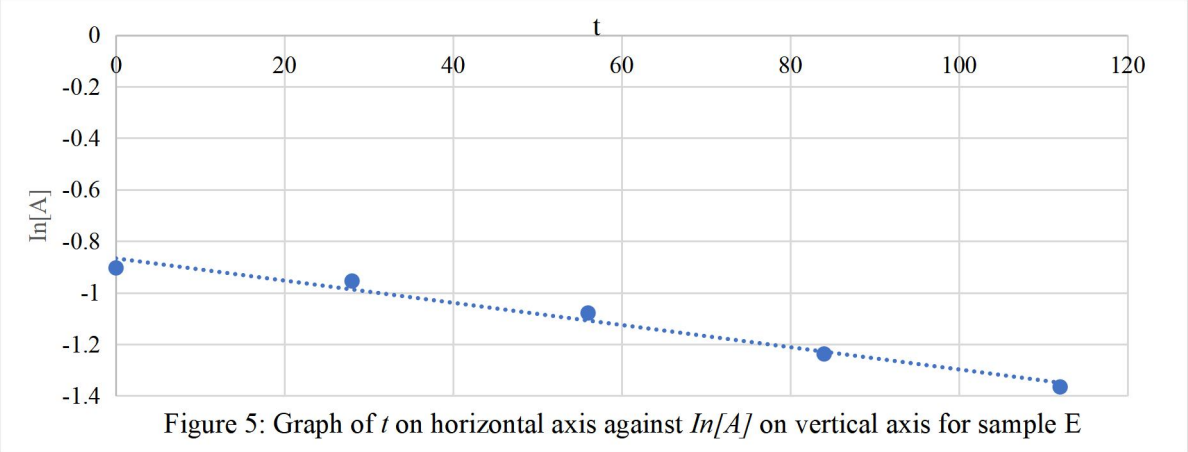

Figure 5: Graph of *t* on horizontal axis against *In[A]* on vertical axis for sample E

Figure 5 is a graphical plot correlating the natural log of recorded absorbance (dependent variable) of sample E on the vertical axis against the time (independent variable) on the horizontal axis. The linear graph of Figure 6 generated the following relation:

$$\ln[A] = -0.0043t - 0.867 \quad (29)$$

The line of best fit represented on the graph gives the best linear correlation of the points with a coefficient of determination (R^2) = 0.9756 (good fit) and k = 0.0043/day, where k is the rate constant in unit per day and with the line of best fit intercepting the vertical axis at a point -0.867. Anti-log of the intercept gives an approximate value for initial absorbance recorded at t = 0 days.

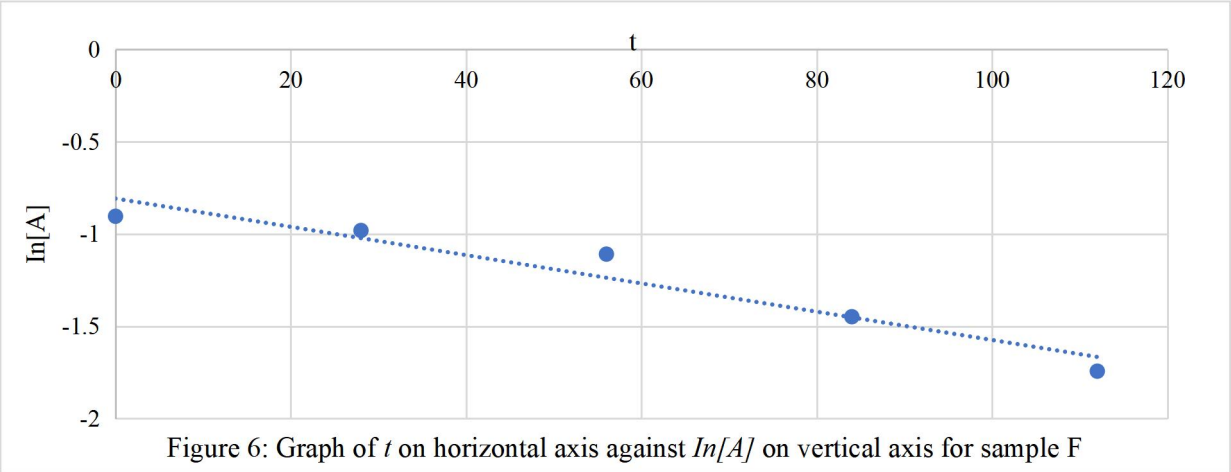

Figure 6: Graph of *t* on horizontal axis against *In[A]* on vertical axis for sample F

Figure 6 is a graphical plot correlating the natural log of recorded absorbance (dependent variable) of sample F on the vertical axis against the time (independent variable) on the horizontal axis. The linear graph of Figure 7 generated the following relation:

$$\ln[A] = -0.0077t - 0.808 \quad (30)$$

The line of best fit represented on the graph gives the best linear correlation of the points with a coefficient of determination (R^2) = 0.9326 (good fit) and k = 0.0077/day, where k is the rate constant in unit per day and with the line of best fit intercepting the vertical axis at a point -0.808. Anti-log of the intercept gives an approximate value for initial absorbance recorded at t = 0 days.

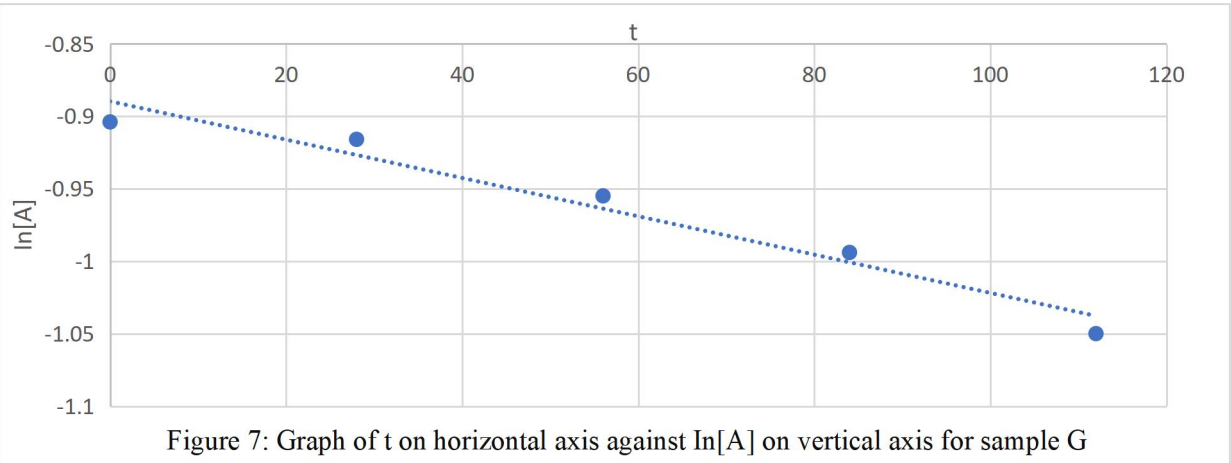

Figure 7: Graph of t on horizontal axis against In[A] on vertical axis for sample G

Figure 7 is a graphical plot correlating the natural log of recorded absorbance (dependent variable) of sample G on the vertical axis against the time (independent variable) on the horizontal axis. The linear graph of Figure 8 generated the following relation:

$$\ln[A] = -0.0013t - 0.8898 \quad (31)$$

The line of best fit represented on the graph gives the best linear correlation of the points with a coefficient of determination (R^2) = 0.9586 (good fit) and k = 0.0013/day, where k is the rate constant in unit per day and with the line of best fit intercepting the vertical axis at a point -0.8898. Anti-log of the intercept gives an approximate value for initial absorbance recorded at t = 0 days.

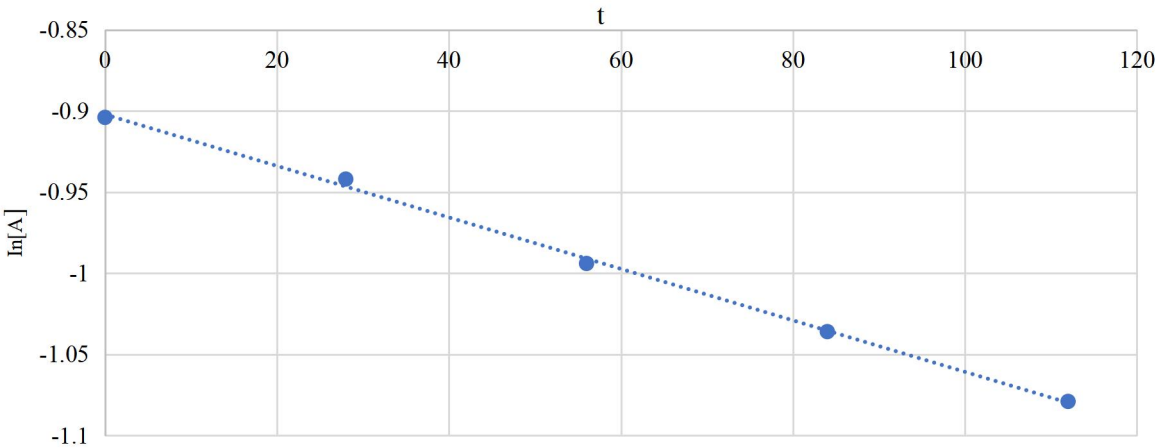

Figure 8: Graph of *t* on horizontal axis against *In[A]* on vertical axis for sample H

Figure 8 is a graphical plot correlating the natural log of recorded absorbance (dependent variable) of sample H on the vertical axis against the time (independent variable) on the horizontal axis. The linear graph of Figure 9 generated the following relation:

$$\ln[A] = -0.0016t - 0.9022 \quad (32)$$

The line of best fit represented on the graph gives the best linear correlation of the points with a coefficient of determination (R^2) = 0.9983 (good fit) and k = 0.0016/day, where k is the rate constant in unit per day and with the line of best fit intercepting the vertical axis at a point -0.9022. Anti-log of the intercept gives an approximate value for initial absorbance recorded at t = 0 days.

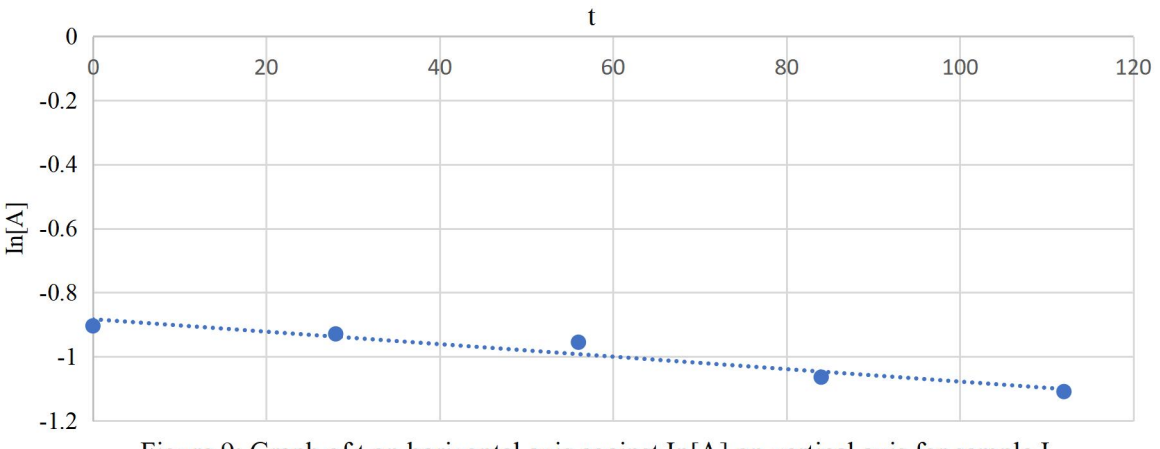

Figure 9: Graph of t on horizontal axis against In[A] on vertical axis for sample I

Figure 9 is a graphical plot correlating the natural log of recorded absorbance (dependent variable) of sample I on the vertical axis against the time (independent variable) on the horizontal axis. The linear graph of Figure 10 generated the following relation:

$$\ln[A] = -0.0019t - 0.8832 \quad (33)$$

The line of best fit represented on the graph gives the best linear correlation of the points with a coefficient of determination (R^2) = 0.9295 (good fit) and k = 0.0019/day, where k is the rate constant in unit per day and with the line of best fit intercepting the vertical axis at a point -0.9022. Anti-log of the intercept gives an approximate value for initial absorbance recorded at t = 0 days.

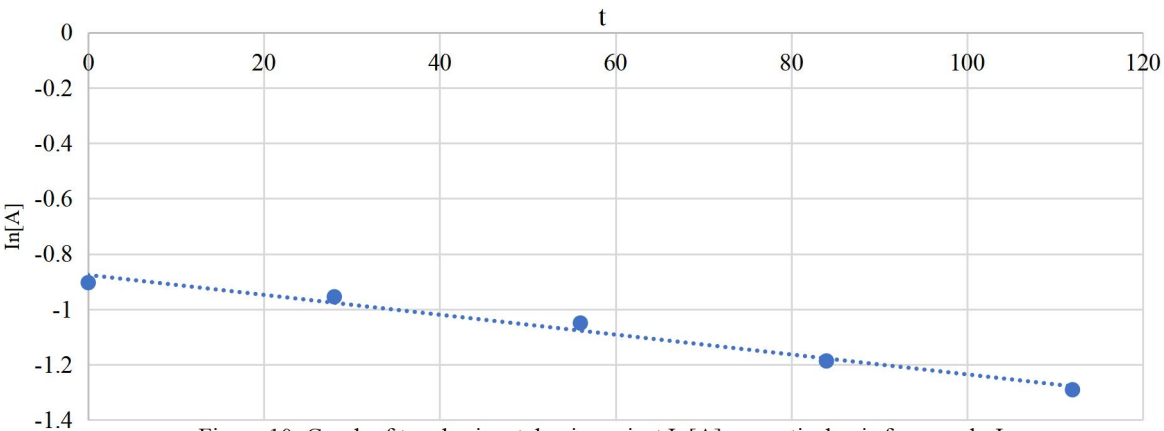

Figure 10: Graph of t on horizontal axis against In[A] on vertical axis for sample J

Figure 10 is a graphical plot correlating the natural log of recorded absorbance (dependent variable) of sample J on the vertical axis against the time (independent variable) on the horizontal axis._The linear graph of Figure 11 generated the following relation:

$$\ln[A] = -0.0036t - 0.8762 \quad (34)$$

The line of best fit represented on the graph gives the best linear correlation of the points with a coefficient of determination (R^2) = 0.9784 (good fit) and k = 0.0036/day, where k is the rate constant in unit per day and with the line of best fit intercepting the vertical axis at a point -0.8762. Anti-log of the intercept gives an approximate value for initial absorbance recorded at t = 0 days.

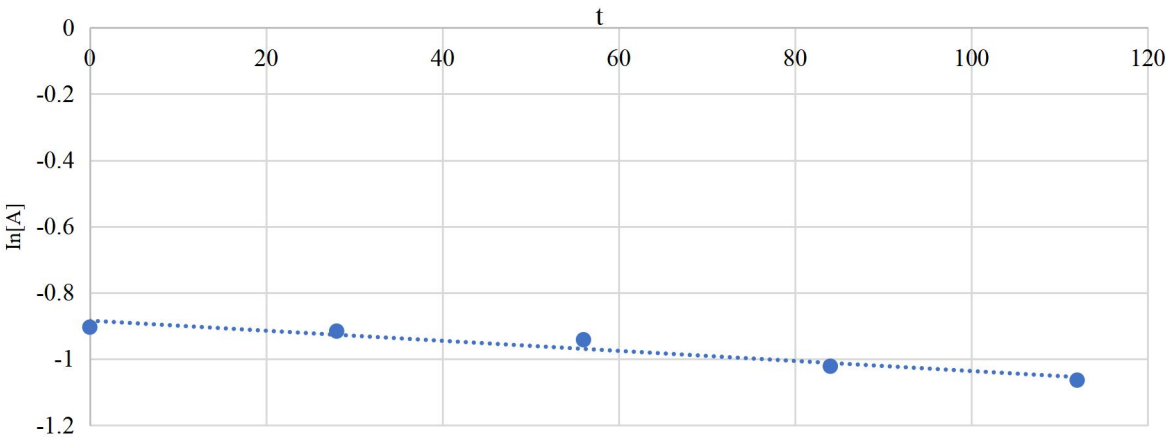

Figure 11: Graph of t on horizontal axis against In[A] on vertical axis for sample K

Figure 11 is a graphical plot correlating the natural log of recorded absorbance (dependent variable) of sample K on the vertical axis against the time (independent variable) on the horizontal axis. The linear graph of Figure 12 generated the following relation:

$$\ln[A] = -0.0015t - 0.8844 \quad (35)$$

The line of best fit represented on the graph gives the best linear correlation of the points with a coefficient of determination (R^2) = 0.9261 (good fit) and k = 0.0015/day, where k is the rate constant in unit per day and with the line of best fit intercepting the vertical axis at a point -0.8844. Anti-log of the intercept gives an approximate value for initial absorbance recorded at t = 0 days.

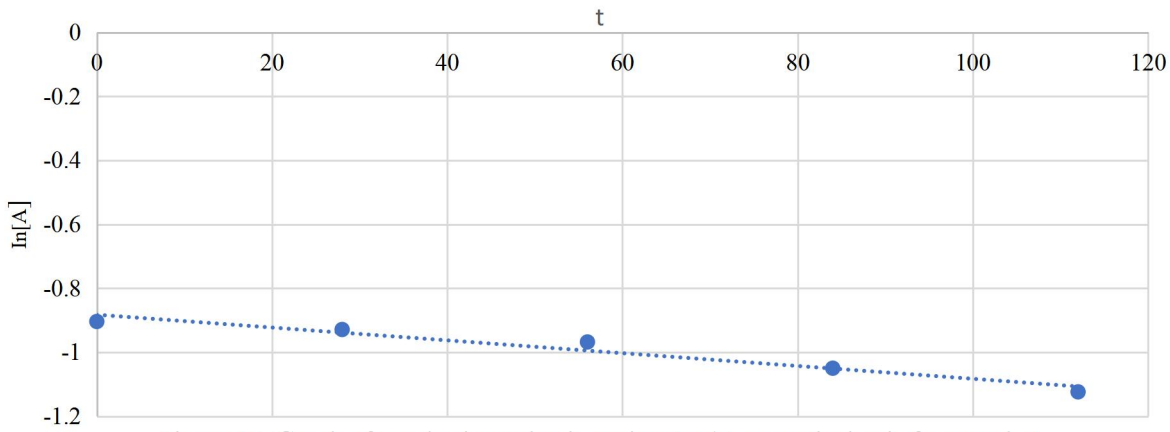

Figure 12: Graph of t on horizontal axis against In[A] on vertical axis for sample L

Figure 12 is a graphical plot correlating the natural log of recorded absorbance (dependent variable) of sample L on the vertical axis against the time (independent variable) on the horizontal axis. The linear graph of Figure 13 generated the following relation:

$$\ln[A] = -0.002t - 0.8828 \quad (36)$$

The line of best fit represented on the graph gives the best linear correlation of the points with a coefficient of determination (R^2) = 0.9528 (good fit) and k = 0.002/day, where k is the rate constant in unit per day and with the line of best fit intercepting the vertical axis at a point -0.8828. Anti-log of the intercept gives an approximate value for initial absorbance recorded at t = 0 days.

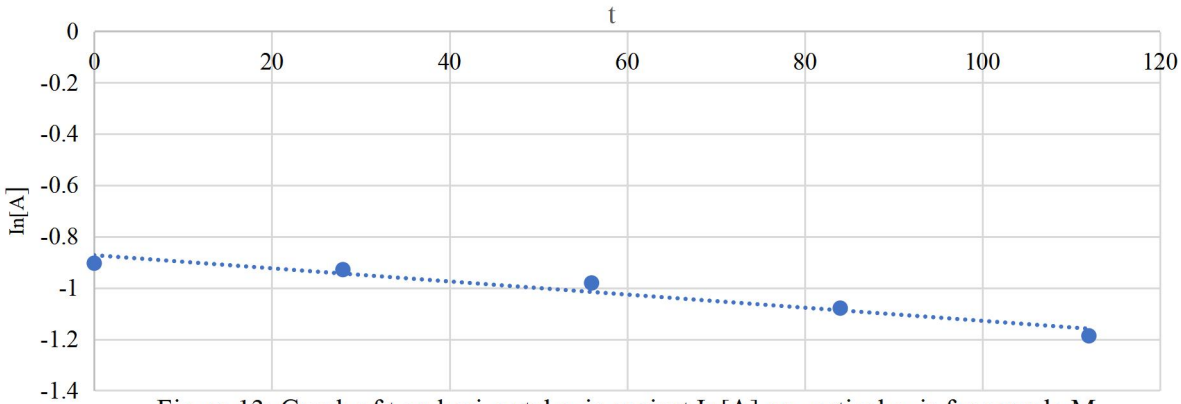

Figure 13: Graph of t on horizontal axis against In[A] on vertical axis for sample M

Figure 13 is a graphical plot correlating the natural log of recorded absorbance (dependent variable) of sample M on the vertical axis against the time (independent variable) on the horizontal axis. The linear graph of Figure 14 generated the following relation:

$$\ln[A] = -0.0026t - 0.8728 \quad (37)$$

The line of best fit represented on the graph gives the best linear correlation of the points with a coefficient of determination (R^2) = 0.9398 (good fit) and k = 0.0026/day, where k is the rate constant in unit per day and with the line of best fit intercepting the vertical axis at a point -0.8728. Anti-log of the intercept gives an approximate value for initial absorbance recorded at t = 0 days.

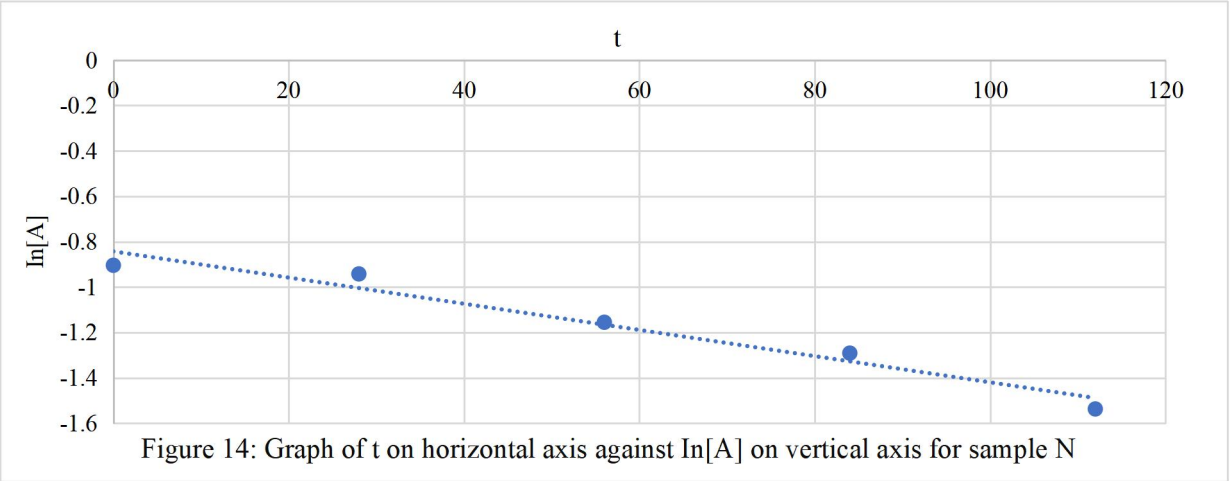

Figure 14: Graph of t on horizontal axis against In[A] on vertical axis for sample N

Figure 14 is a graphical plot correlating the natural log of recorded absorbance (dependent variable) of sample N on the vertical axis against the time (independent variable) on the horizontal axis. The linear graph of Figure 15 generated the following relation:

$$\ln[A] = -0.0058t - 0.8428 \quad (38)$$

The line of best fit represented on the graph gives the best linear correlation of the points with a coefficient of determination (R^2) = 0.9582 (good fit) and k = 0.0058/day, where k is the rate constant in unit per day and with the line of best fit intercepting the vertical axis at a point -0.8428. Anti-log of the intercept gives an approximate value for initial absorbance recorded at t = 0 days.

Laboratory Determination of Microbial Cell Density and Growth

At time, t = 0 days, after carrying out serial dilution, culturing of isolates from samples in nutrient agar and incubating isolates for 48hrs on two plates for each sample, the data collated for each sample every 28days was used to generate the chart in Figure 15 below:

Similarly, the corresponding TPH concentrations in each of the samples overtime used to generate the chart in Figure 16 below. The results obtained from FTIR analysis were used to plot the chart shown in Figure 16. Of all the 14 samples prepared the rate of degradation was highest in sample F and lowest in sample B, which was the sample studied for the natural attenuation of the polluted soil where the site was left fallow for a period of time.

Graphically, Figures 15 and 16 illustrates the resultant effect of stimulation on the interaction between the microbial communities and pollutants constitutes in the

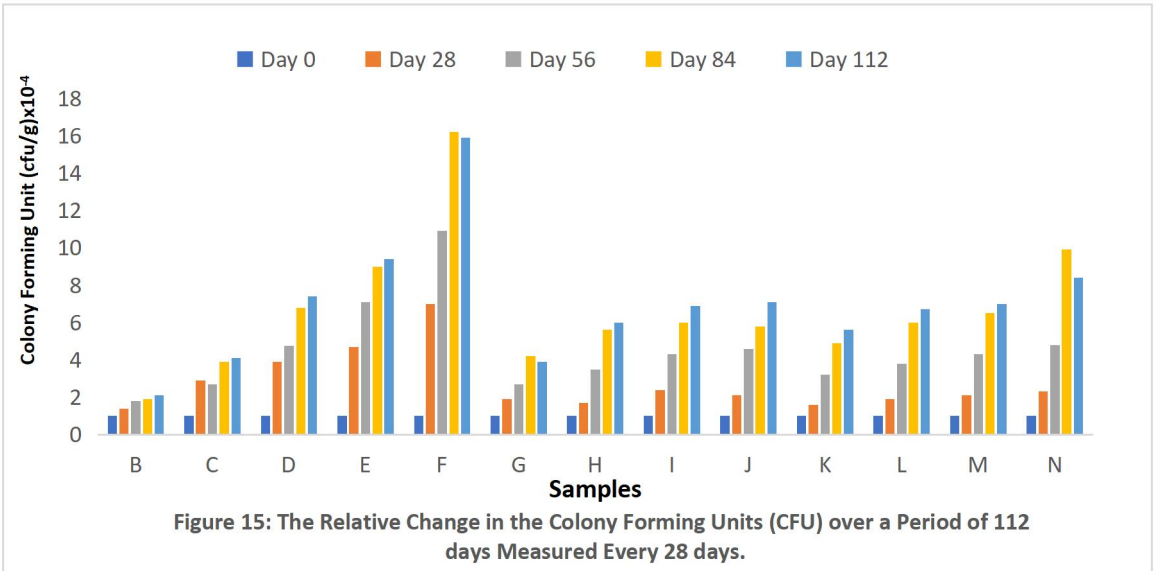

Figure 15: The Relative Change in the Colony Forming Units (CFU) over a Period of 112 days Measured Every 28 days.

environment and the relationship between TMC and TPH concentration (in the form of Absorbance) overtime respectively. TMC increased overtime with decreasing TPH concentrations, implying an inverse relationship between the properties. In addition, the relationship between TMC and TPH concentrations does not entail all microbial communities and species benefited or participated in remediation under the influence of the biostimulants, but may be as a result of predominance of a few species using the biostimulants. This is likely to be so for all microbial species if there is individual increase across all microbial species cell density, so that hydrocarbon utilizing bacteria (HUB) count is inversely related to the TPH concentration overtime.

This may be known if research has been carried out prior to this using the same microbes in the soil. Nonetheless, the response to biostimulation was positive and through further studies the dominant microbial specie may be known for future studies and the possible creation of metagenomic libraries.

Physicochemical Analysis of soil samples after remediation

The Table 14 below shows the experimental outcome of test for pH and Conductivity of the samples on 112th day with greatest experimental deviation recorded for pH as 0.01, and for conductivity as 0.0002 for all samples.

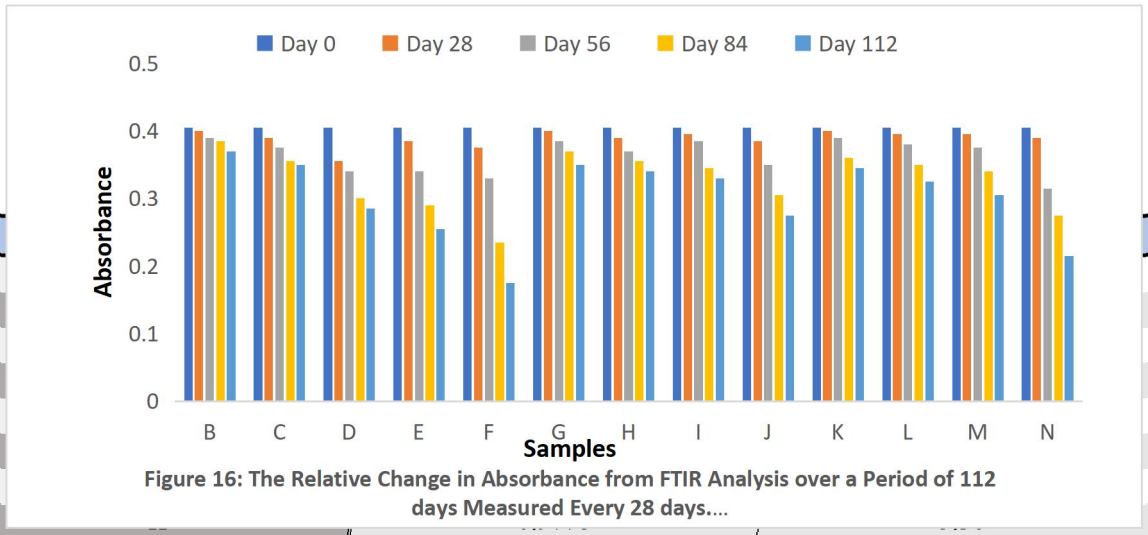

Figure 16: The Relative Change in Absorbance from FTIR Analysis over a Period of 112 days Measured Every 28 days....

I	0.9801	5.42
J	0.9790	5.90
K	0.9779	5.33
L	0.9811	5.32
M	0.9800	5.31
N	0.9777	6.11

Table 9 reveals that the hydrocarbon polluted soils are known to exhibit lower values in pH (i.e. below 7.0) and conductivity as a result of their being non-polar which explains the partial distribution of electron in hydrocarbon structures. Furthermore, as pH values tend towards neutrality (7.0 pH) remediation became more progressive, hence the reason the TMC of samples F and N increased more than in sample B. Also, high conductivities is an indication of high metal concentration. With the concentration of other components being negligible, the wetter the soil the higher the electrical conductivity (since water is polar). Low pH (below 7.0) exhibited by polluted soils is as a result of the acidity added to the soil by the pollutant and low conductivity is exhibited by non-polar materials such as hydrocarbons. However, the use of slightly alkaline and homogenous biostimulants may encourage microbial activities through soil pH modification. Therefore, one indication of a remediating soil is a pH shift towards neutrality and lowering conductivity which indicates HM reduction with time. Furthermore, Table 15 showed the results of AAS analysis carried out on samples B – N at the end of 112 days.

Table 10: Result of AAS analysis for all Samples at the End on the Remediation Study (112th day)

Sample	Heavy Metals Concentration (mg/L)									
	Co	Fe	Mg	Zn	Cd	Pb	Ni	Cu	Mn	Ca
A	0.4913	7.2347	1.6200	0.8320	0.0004	1.3453	0.4892	0.6315	1.9910	0.8878
B	0.6091	84.771	11.240	2.0280	0.0313	21.466	0.6671	0.8532	2.8270	1.3451
C	0.6088	84.760	11.201	1.9199	0.0313	20.456	0.6770	0.8011	3.0020	0.7552
D	0.6095	84.791	11.212	1.9199	0.0310	18.464	0.6730	0.7912	2.8310	0.7256
E	0.6061	85.112	11.250	2.0293	0.0305	19.121	0.6730	0.8013	2.9920	0.6999
F	0.6088	82.570	11.209	2.0311	0.0314	19.199	0.6690	0.9121	3.0010	0.6219
G	0.6092	80.211	11.208	1.9980	0.0309	11.124	0.6720	0.7518	2.9550	1.2511
H	0.6110	79.112	10.990	0.9835	0.0315	10.129	0.6770	0.7215	2.2130	1.1193
I	0.6091	77.820	10.125	0.8121	0.0312	11.121	0.6010	0.8183	2.8000	1.0129
J	0.5990	55.998	9.5150	0.4222	0.0212	8.5291	0.5011	0.7171	2.7990	0.7218
K	0.6089	72.112	11.235	1.2154	0.0219	14.815	0.6771	0.8251	2.7110	1.3446
L	0.6059	80.117	11.121	1.3254	0.0301	14.911	0.6801	0.7818	2.1130	1.1127
M	0.6079	74.999	11.101	0.9931	0.0317	10.312	0.5991	0.7282	2.7180	1.1215
N	0.6071	77.314	11.209	0.7919	0.0299	11.314	0.5717	0.6212	2.1130	1.0010

The results gathered in Table 10 affirmed the general knowledge that metals are non-biodegradable by microbes but can be mineralized into their complexes or absorbed by plants and fungi through their roots (Naeim *et al*., 2021). The AAS analysis carried out showed that HMs concentration fell mildly in samples with high concentration of granulated groundnut shell and corncob which suggests that they might be good absorbers of HMs or good stimulants and facilitators of HM conversion. Temitope *et al.* (2019) noted that according to World Health Organization (WHO) standard, the effective concentration of HMs in soil identified as Cr - 100mg/kg, Cd - 0.8mg/kg, Pb – 85mg/kg, Cu – 36mg/kg and Zn – 50mg/kg. The results were below the acceptable limit as identified by WHO, thus annulling the effect of HMs concentration on the remediation process. Generally, aliphatic compounds (e.g. diesel, grease) are more amenable to biodegradation than aromatic compounds, and the higher the number of rings, the more difficult is the biodegradation (Nzila, 2018), therefore, it will not be erroneous to infer that PAH toxicity level did not affect the remediation process. This implies that as the CFU/g increased overtime, the FTIR absorbance decreased from the FTIR analysis within the wavenumber range of 1000 to 800cm^{-1}**.** Bioremediation of PAHs in HMs loaded soils is difficult as their toxicity is capable of inhibiting microbial growth. This was not so in this research study because the HMs toxicity levels was unable to suppress microbial activities.

CONCLUSION

Increasing soil nutrients necessary for microbial life support reduces the concentration of contaminants,
increases microbial activity and the soil becomes habitable and enriched for agricultural activities as remediation is increased. Across all samples synergistically or singly treated with compost manure the remediation speed was more enhanced. For sustainability of microbial life and increased rate of remediation there
is need to maintain a level of nutrition in the soil, water content, pH, sunlight, temperature, etc. Compost manure, corncob and groundnut shell are good stimulants for bioremediation of petroleum contaminated soils.

REFERENCES

Alexis Nzila (2018): Current Status of the Degradation of Aliphatic and Aromatic Petroleum Hydrocarbons by Thermophilic Microbes and Future Perspectives. *2018 Dec; 15(12):2782.*

Florida Department of Environmental Protection (2023): "Commonly Encountered Petroleum and Petroleum Products for Florida Storage Tank Systems". *Section 376. 301 (30 – 31).*

Ibitoye A. A (2008). Laboratory Manual for Soil Analyses 3rd Edition *Scientific Research* 1:10-34.

Ilma Cirne, Jaime Boaventura, Yuri Guedes and Elizabete Lucas (2016): Methods for Determination of Oil and Grease Contents in Wastewater from the Petroleum Industry. *Chemistry and Chemical Technology, vol. 10. No.4.*

Josefina Perez Varges, Sergio Esteban, Vigueras Carmona, Enid Zamudio Moreno, Noemi Araceli Rivera Casado, and Graciano Calva Calva: (2017) 'Bioremediation of Soils from Oil Spill Impacted Sites using Bio-augumentation with Bio-surfactants Producing, Native, Free-living Nitrogen Fixing Bacteria'. *Rev Int. Contam. Ambie.33 (Especial Biotecnologia e ingenieria ambiental) 105 – 114.*

Kingsley Chukwuebuka Agu, Bassey Effiong Edet, Iloanusi Confidence Ada, Awah Nsikak Sunday, Okeke Benjamin Chidi, Anaukwu Chikaodili Gladys, Ezenwa Chinaemelum Uche, Orji Michael Uchenna, and Okafor Arthur Chinedu (2015). "Isolation and Characterization of Microorganisms from Oil Polluted Soil in Kwata, Awka South, Nigeria." *American Journal of Current Microbiology.* Vol.3 Issue1.

Lee K. and Levy E. M. (1989) a Biodegradation of Petroleum in the Marine Environment and its Enhancement. In: Nriagu JA, editor;, Lakshminarayana JSS, editor., eds. Aquatic Toxicology and Water Quality Management. New York: Wiley & Sons Inc. p217-243.

Li Zheng, Ravid Rosenzweig, Fengxian Chen, Ji Qin, Tianyi Li, Jincheng Han, Paula Istvan, Damiana Diaz-Reck, Faina Gelman, Gilboa Arye and Zeev Ronen, (2022) "Bioremediation of Petroleum-Contaminated Soils with Biosurfactant-Producing Degraders Isolated from the Native Desert Soils", *Microorganisms*. 10: 2267.

M.Z.H Khan and Md. Ikram Hossain (2016). Fuel Properties of Pryolytic Tyre Oil and its Blends with Diesel Fuel – Towards Waste Management. *Int. J. Environment and Waste Management.* Vol. 18, No. 4.

Manish Srivastava, Anamika Srivastava, Anjali Yadav, Varum Rawat: (2020) "Source and Control of Hydrocarbon Pollution" *Intechopen.* 8:64 – 87.

Naeim A.H., Baharlouei J., Ataabadi M. (2021): Different Biological Strategies for the Bioremediation of Naturally Polluted Soils. *Plant, Soil and Environ*. 67:337-342.

New Society Publishers (2023):'What are the Different Types of Bioremediation?' *Vol.1, Chpt. 4.*

Nyer E: *In situ* Treatment Technology (2001). *Lewis Publishers, USA.*

Osuji I. C., and Nwoye I. (2007). "An Appraisal of the Impact of Petroleum Hydrocarbons on Soil Fertility: The Owaza Experience." *African Journal of Agricultural Research,* 2(7):318-324.

Rowland U. Ofoegbu, Yusuf O.L. Momoh, and Ify L. Nwaogazie. (2015). "Bioremediation of Crude Oil Contaminated Soil Using Organic and Inorganic Fertilizers." *J Pet Environ Biotechnol 2015,* 6.1.

Sharaff, M.M., Subrahmanyam, G., Kumar, A., Yadav, A.N., 2020. Mechanistic understanding of the root microbiome interaction for sustainable agriculture in polluted soils. In: New and Future Developments in Microbial Biotechnology and Bioengineering. *Elsevier*, pp. 61–84.

TB Adams, DC Sinclair, AR West. (2006). Influence of Processing Conditions on the Electrical Properties of Ceramics. *Journal of the American Ceramic Society.* 89 (10), 3129-3135.

Temitope M. Osobamiro, Oluwafemi Awolesi, Oluwatobi M. Alabi, Abiodun Y. Oshinowo, Mujeebat A. Idris, Farouq A. Busari (2019): Heavy Metal Levels of Soil Samples Collected from a Major Industrial Area in Abeokuta, South-western Nigeria. *International Journal of Scientific and Research Publications,* Volume 9, Issue 8.

Useh Mercy Uwem, Etuk-Udo Godwin Akpan and Dauda Mary S, (2015) "Evaluating the Physico-Chemical Properties and Heavy Metals in Soils of Municipal Waste Dumpsites at Kubwa, Abuja, Nigeria." *Journal of Chemistry and Chemical Sciences, Vol. 5(11), 654-662.*

van Dorst, J., Siciliano, S. D., Winsley, T., Snape, I., and Ferrari, B. C. (2014). Bacterial Targets as Potential Indicators of Diesel Fuel Toxicity in Subantarctic Soils. *Appl.Environ.Microbiol.* 80,4021–4033. https://doi:10.1128/AEM.03939-13

Varjani SJ, Upasani VN (2017) A new look on factors affecting microbial degradation of petroleum hydrocarbon pollutants. *Int Biodeterior Biodegradation* 120:71–83. https://doi.org/10.1016/j.ibiod.2017.02.006

Verla, AW; Horsfall, M (Jnr). Verla, E.N. Spiffl, A.I. Ekpete, O.A. (2012): Preparation and Characterization of Activated Carbon from Fluted Pumpkin (*Telfaria Occidentalis Hook. F)* Seed Shell. *Asian J. Nat. Appl. Sci.* 39-50.

MODELLING AND SIMULATION OF WASTEWATER TREATMENT PLANT

[*]Praise T. OBASEKI[1], Joseph O. AJAYI[2], Mufliah G. OMOFOYEWA[3], Idowu I. OLATEJU[4], Abel A. ADEYI[5], Saidat O. GIWA[6], Abdulwahab GIWA[7,8]

[1,2,3,4,5]Department of Chemical and Petroleum Engineering, Afe Babalola University, Ado-Ekiti, Ekiti State, Nigeria
[6]Department of Chemical Engineering, Abubakar Tafawa Balewa University, Bauchi, Nigeria
[7]Department of Petroleum Engineering, Abubakar Tafawa Balewa University, Bauchi, Nigeria
[8]Department of Chemical Engineering, University of Abuja, Abuja, Nigeria
[1]obasekipraise@gmail.com, [2]ajayijo@abuad.edu.ng, [3]omofoyewamg@pg.abuad.edu.ng, [4]iolateju@abuad.edu.ng, [5]abeladeyi@abuad.edu.ng, [6]sogiwa@atbu.edu.ng, [7,8]agiwa@atbu.edu.ng
+2348148053959, +2347032819336, +2348101820340, +2348060847941, +2348060921556, +2347055649325, +2347010900875
[*]Corresponding author: obasekipraise@gmail.com

ABSTRACT

Maintaining environmental sustainability and public health requires effective management of wastewater treatment plants. Computer-based modelling and simulation tools have become crucial in designing, optimizing, and operating these plants. This study presents a comprehensive approach to wastewater treatment plant modelling and simulation using commercially available software for prediction and optimization of plant performance. Sensitivity analysis was performed to examine the impact of different operational and design parameters on plant performance. Furthermore, optimization techniques were employed to identify cost-effective operational strategies and potential areas for improvement. The influent concentration values of alkalinity, COD, BOD, volatile suspended solid and total suspended solid were reduced to 3.92, 78.74, 10.95, 8.08, and 10 mg/L respectively at the effluent. The findings from this research provided valuable insights into the wastewater treatment plant's performance and offered recommendations to enhance its efficiency and environmental sustainability.

***Keywords**: Wastewater, modelling, simulation, BioWin, effluent quality.*

1. INTRODUCTION

In a water treatment system, the removal of turbidity, taste, colour, iron, odour, chlorine, and other specific chemicals is achieved. The system can include one or more filters, which can be in the form of cartridge devices or loose media tank-type systems. The water treatment process involves chemical, physical, and sometimes biological procedures to eliminate impurities. Chemical and physical methods are the most commonly used approaches for treating drinking water. Wastewater treatment primarily employs biological processes (Gerba and Pepper, 2019). Water treatment facilities employ various physical and chemical techniques to purify and enhance the quality of waste or contaminated water. The objective of wastewater treatment processes is to improve the quality of the wastewater (Sokolowski *et al.,* 2009).

The different treatment methods focus on:
(a) Removing suspended solids, which are physical particles that can cause blockages in rivers or channels when they settle under gravity.
(b) Breaking down biodegradable organic substances, such as Biochemical Oxygen Demand (BOD), which can serve as “food” for microorganisms in the receiving body of water.
(c) Eliminating pathogenic bacteria and other disease-causing organisms.
(d) Removing nutrients, including nitrates and phosphates (Xiao *et al*., 2019).

Before water enters residential, commercial, or educational buildings, it undergoes a water treatment process to ensure it is safe to drink and free from odours. Water is extracted from the ground or a reservoir, such as a lake, and transported to water treatment plants. At

these plants, various processes involving chemical, physical, and biological agents are employed to remove contaminants and pathogens from the water before they reach the consumers (de Lemos *et al.*, 2005).

Water is the most vital substance for the survival of all living organisms on Earth. The intelligent and effective use of water resources is crucial at all times. A large portion of the population is affected by the consumption and use of contaminated water. Drinking impure and polluted water can lead to waterborne diseases, which can affect anyone and even result in death. Treating available water is the solution to this problem (Fazal-ur-Rehman*,* 2019). Since providing clean and safe drinking water is a significant technical challenge, water treatment, which establishes and regulates water quality, plays a crucial role as a chemical process. Water treatment refers to utilizing a water source to produce high-quality water that meets specific criteria. Raw water treatment involves multiple procedures such as coagulation, sedimentation, and filtration, which are commonly conducted in water treatment facilities for chemical clarification purposes. It is essential to have a reliable model of the treatment process for control purposes to ensure the accurate operation of water treatment (Hoslett *et al.,* 2018).

Water treatment systems are essential for purifying drinking water and treating wastewater, serving as a preventive measure against the spread of diseases. The treatment of drinking water can occur at various stages, including the water source, distribution points, or centralized processing plants. In the United States, centralized treatment facilities handle the majority of water treatment operations (Venugopal *et al.,* 2020). In countries with limited water resources, waterborne diseases caused by pathogens pose significant public health challenges. Such countries often rely on cost-effective treatment methods like chlorination, although this approach may not effectively address all contaminants, such as heavy metals (Pichel *et al*., 2019). Developing nations commonly employ methods like solar disinfection, utilizing natural UV light, and sand filters due to their simplicity and ease of maintenance. Wastewater treatment is equally crucial in disease control. In the United States, centralized sewage processing plants are responsible for treating most wastewater before its release back into the environment (Ray and Jain, 2011).

Wastewater treatment plants use the activated sludge process, which involves the use of microorganisms containing sludge to remove pollutants from sewage. Mathematical models are also used to analyze the activated sludge process and find solutions to control or operating problems. Temperature plays a significant role in the growth of microorganisms and the nitrification process, and it can be influenced by various factors, including climate change. Advanced control algorithms, such as model predictive control, can be used to manage wastewater treatment plants effectively, but the effect of temperature needs to be investigated (Dadrasnia *et al.,* 2017).

Hence, this paper investigates the influent temperature effects on the concentration of pollutants in the effluent of a municipal wastewater treatment plant using mathematical modelling and simulation.

2. METHODOLOGY

2.1 Process Modelling and Simulation

BioWin is a widely used software tool for modelling and simulating wastewater treatment plants. It employs the Activated Sludge Model No. 1 (ASM1) to simulate the biological processes in the treatment plant. Figure 1 shows the step-by-step methodology employed for modelling and simulation, and the data used are in Table 1.

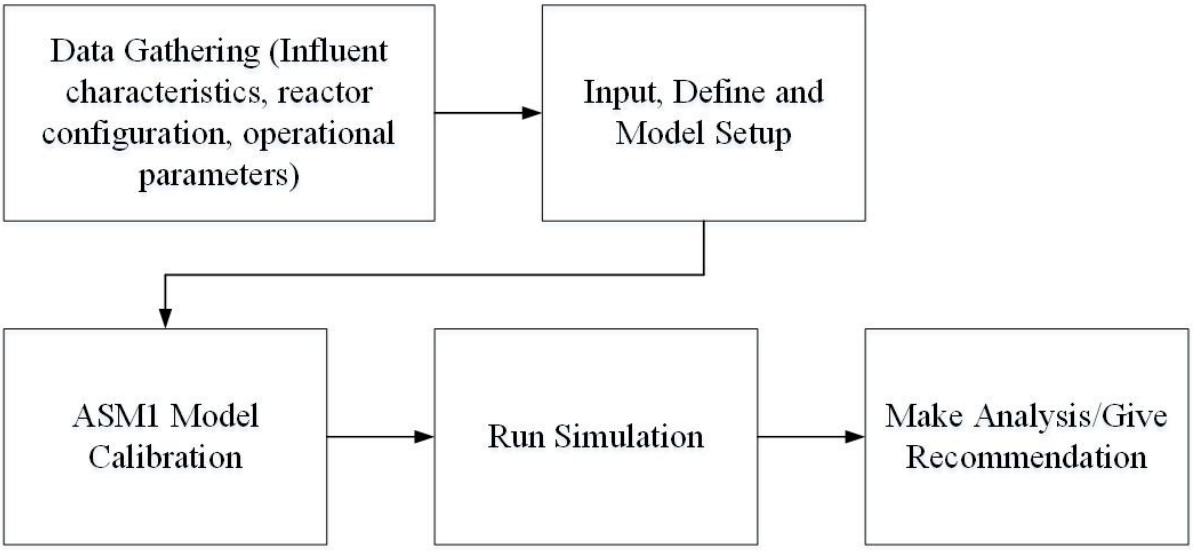

Figure 1: BioWin Process Flow Chart

Remember that modelling and simulation using BioWin are iterative processes. Continuous refinement and validation of the model against real-world data are essential to improve the accuracy and reliability of the predictions.

Table 1: Influent Input Data of Paint Industry for Simulation

Parameter	Value
COD (mg/L)	1101
DO (mg/L)	0
BOD (mg/L)	1101
Nickel (mg/L)	7.5
Chlorine (mg/L)	159.5
TDS (mg/L)	980
TSS (mg/L)	8090
TS (mg/L)	9070
pH	6.9
Conductivity (µS/cm)	122

The TSS value for the raw wastewater from paint in the paint industry was 8090 mg/L.

2.2 Process Description

An initiative was launched within the BioWin platform. In the context of wastewater treatment, an Activated Sludge Design Module (ASDM) was employed for a wastewater treatment plant, as shown in Figure 2, and the parameters used as the influent data were as given in Figure 3. The essential components of the model, encompassing key unit processes like influent traits, reactors, clarifiers, pumps, and disinfection units, were defined. Details about influent attributes such as flow rate, temperature, COD, BOD, nutrient concentrations, and other pertinent parameters were also established. The specifications for each reactor, including volume, depth, and other relevant factors, were provided. Specifics regarding the operational aspects of the aeration tank were elucidated. The mixing tank played a role in integrating amalgamating incoming influent with recycled activated sludge. It is noteworthy that the absence of oxygen was intentional to prevent microorganism proliferation.

Bioreactor-type mixing and aeration tanks were introduced. Parameters like aeration method, temperature, and mixing conditions for aeration were input. The size and characteristics (volume and depth) of the aeration tank were explicitly outlined, based on a predefined geometric configuration. In the mixing tank,

aeration was omitted, whereas the aeration tank was governed by a designated dissolved oxygen (DO) set point. The arrangement of the clarifier, sometimes referred to as a settler, was outlined in the model. Tank geometry, which influences the settling process, along with recycled activated sludge or other pertinent streams, was specified. The final treated effluent configuration was established, encompassing a disinfection unit (e.g., chlorination). This entailed specifying parameters like chlorine dosage for disinfection and flow rate for filtration.

Configuration for the pump responsible for circulating and recycling activated sludge was also defined. This stage involved outlining how waste-activated sludge was distributed or diverted within the system. The flow rate for waste-activated sludge was established during this process. The pump's power calculation was determined, and the simulation was set up to estimate the requisite pump power. The flow rate for the waste-activated sludge was also defined. Analogous to the pump handling recycled activated sludge, a similar process was undertaken for the pump managing waste-activated sludge. The power calculation for this pump was also detailed. Essential simulation parameters such as simulation time, time step, and solver options were configured. The simulation was initiated to observe the functioning of the treatment plant over time, and the resultant trends and data were examined.

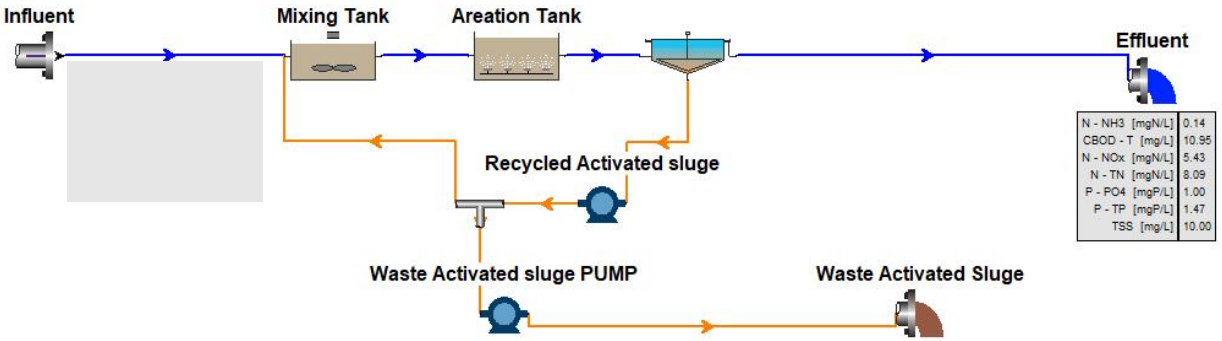

Figure 2: Process Flow Diagram of Simple Wastewater Treatment Plant

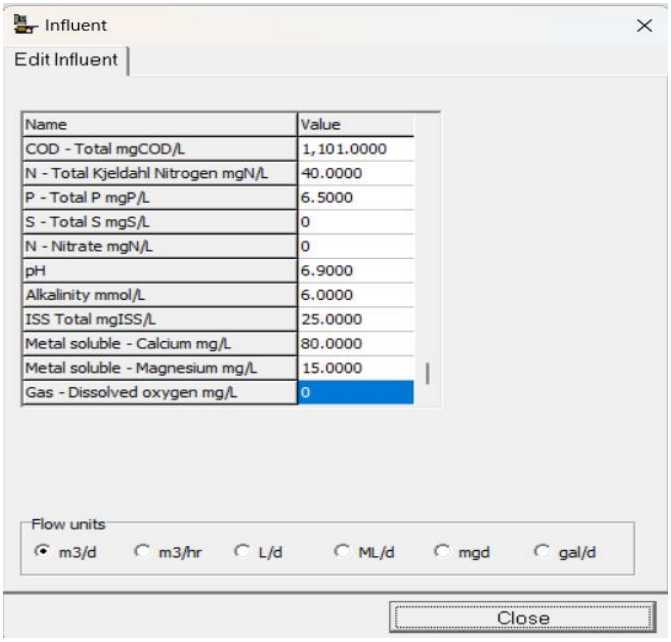

Figure 3: Influent Data Input

3. RESULTS AND DISCUSSION

Elements	COD - Total [kg /d]	COD - Filtered [kg /d]	BOD - Total Carbonaceous [kg /d]	Volatile suspended solids [kg /d]	Total suspended solids [kg /d]
Influent	110,100.00	40,714.98	53,994.69	43,525.34	46,025.34
Effluent	7,604.38	6,472.37	1,057.81	780.65	965.70
Waste Activated Sluge	17,603.87	229.89	5,993.96	11,981.33	14,821.44

Elements	P - Total P [kg P/d]	P - Soluble PO4-P [kg P/d]
Influent	650.00	325.00
Effluent	142.05	96.57
Waste Activated Sluge	701.45	3.43

Figure 4: Mass Flowrate of Influent, Effluent and Activated Sludge Result

In summary, thes kg/d, 6,472.37 kg/d, 1,057.81 kg/d, 780.65 kg/d, and 965.70 kg/d as shown in Figure 4 respectively. The reduction in COD, BOD, and suspended solids from influent to effluent indicates the successful removal of pollutants, while the waste-activated sludge values indicate the amount of residual solids generated during treatment.

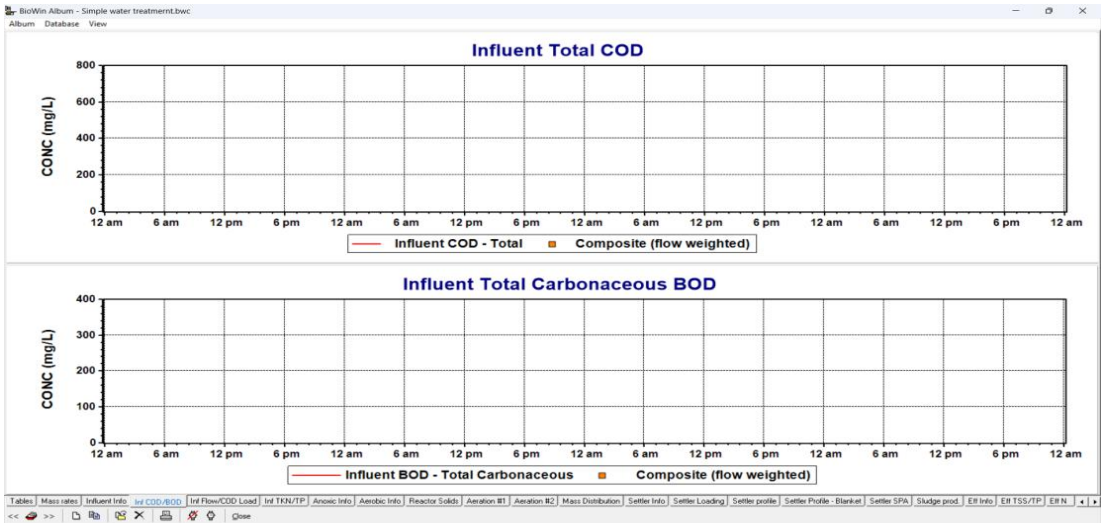

Figure 5: Influent Total COD and BOD Result

Figure 5 illustrates the initial treatment of influent total COD and influent total carbonaceous BOD with varying times of 12 to 6 am for 4 days. It means there is no initial treatment of effluent at the beginning of the process.

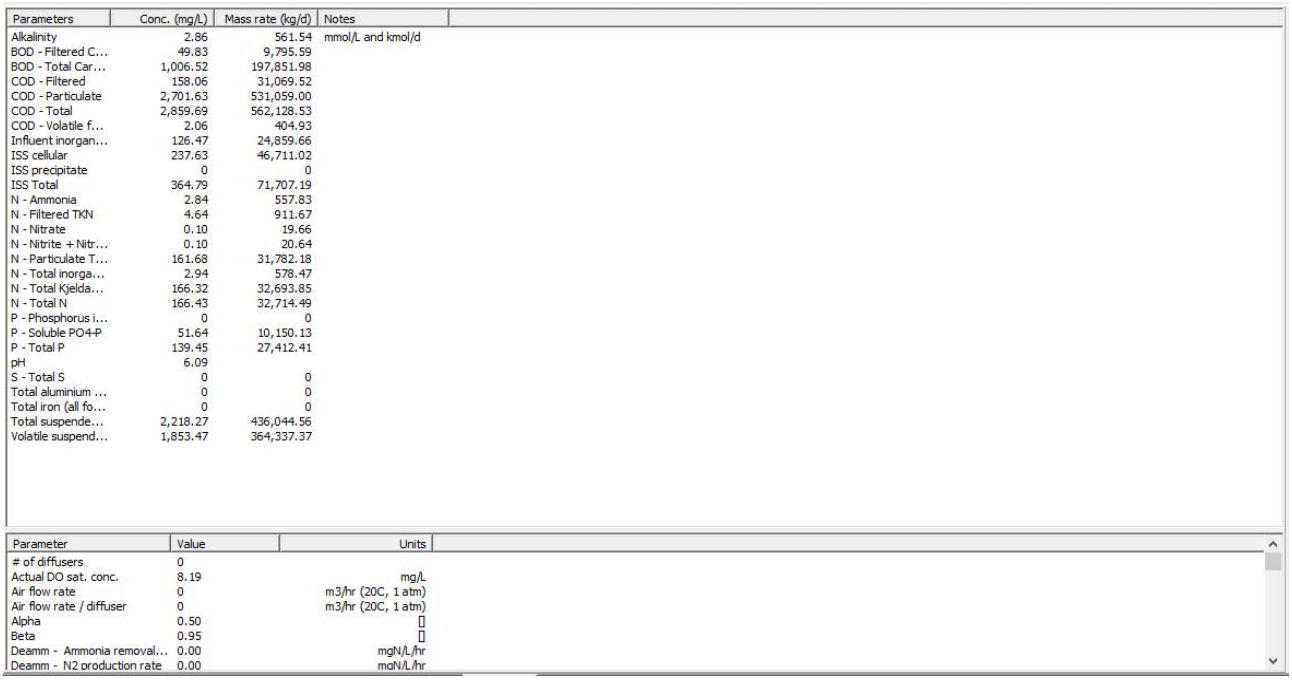

Parameters	Conc. (mg/L)	Mass rate (kg/d)	Notes
Alkalinity	2.86	561.54	mmol/L and kmol/d
BOD - Filtered C...	49.83	9,795.59	
BOD - Total Car...	1,006.52	197,851.98	
COD - Filtered	158.06	31,069.52	
COD - Particulate	2,701.63	531,059.00	
COD - Total	2,859.69	562,128.53	
COD - Volatile f...	2.06	404.93	
Influent inorgan...	126.47	24,859.66	
ISS cellular	237.63	46,711.02	
ISS precipitate	0	0	
ISS Total	364.79	71,707.19	
N - Ammonia	2.84	557.83	
N - Filtered TKN	4.64	911.67	
N - Nitrate	0.10	19.66	
N - Nitrite + Nitr...	0.10	20.64	
N - Particulate T...	161.68	31,782.18	
N - Total inorga...	2.94	578.47	
N - Total Kjelda...	166.32	32,693.85	
N - Total N	166.43	32,714.49	
P - Phosphorus i...	0	0	
P - Soluble PO4-P	51.64	10,150.13	
P - Total P	139.45	27,412.41	
pH	6.09		
S - Total S	0	0	
Total aluminium ...	0	0	
Total iron (all fo...	0	0	
Total suspende...	2,218.27	436,044.56	
Volatile suspend...	1,853.47	364,337.37	

Parameter	Value	Units
# of diffusers	0	
Actual DO sat. conc.	8.19	mg/L
Air flow rate	0	m3/hr (20C, 1 atm)
Air flow rate / diffuser	0	m3/hr (20C, 1 atm)
Alpha	0.50	[]
Beta	0.95	[]
Deamm - Ammonia removal...	0.00	mgN/L/hr
Deamm - N2 production rate	0.00	mgN/L/hr

Figure 6: Data in the Mixing Tank of Anoxic Process

In Figure 6, the data shows the result in the mixing tank of anoxic process. In the mixing tank activated sludge is mixed with influent flow into the tank, because activated sludge is rich in microorganisms that play a crucial role in removing nutrients, such as nitrogen and phosphorus, from the wastewater. By recycling the activated sludge into the influent stream, these microorganisms are reintroduced into the treatment process, enhancing their population and improving nutrient removal efficiency. The recycled activated sludge helps maintain a stable and consistent microbial population within the treatment system. This stability is important for maintaining the desired treatment performance, especially during fluctuating influent conditions or variations in organic load. The presence of an adequate population of microorganisms ensures the availability of sufficient biomass to degrade organic pollutants effectively. Recycling activated sludge aids in maintaining an adequate solids retention time (SRT) in the treatment process. SRT refers to the time solids spend in the system before being removed. By recycling a portion of the activated sludge, the SRT is increased, allowing for better settling of solids and improved clarification in subsequent treatment steps, such as sedimentation or filtration. In Figure 7, the data shows the concentrations of the influent and recycled activated sludge mixing process. The figure also displayed the geometry of the tank along with the data.

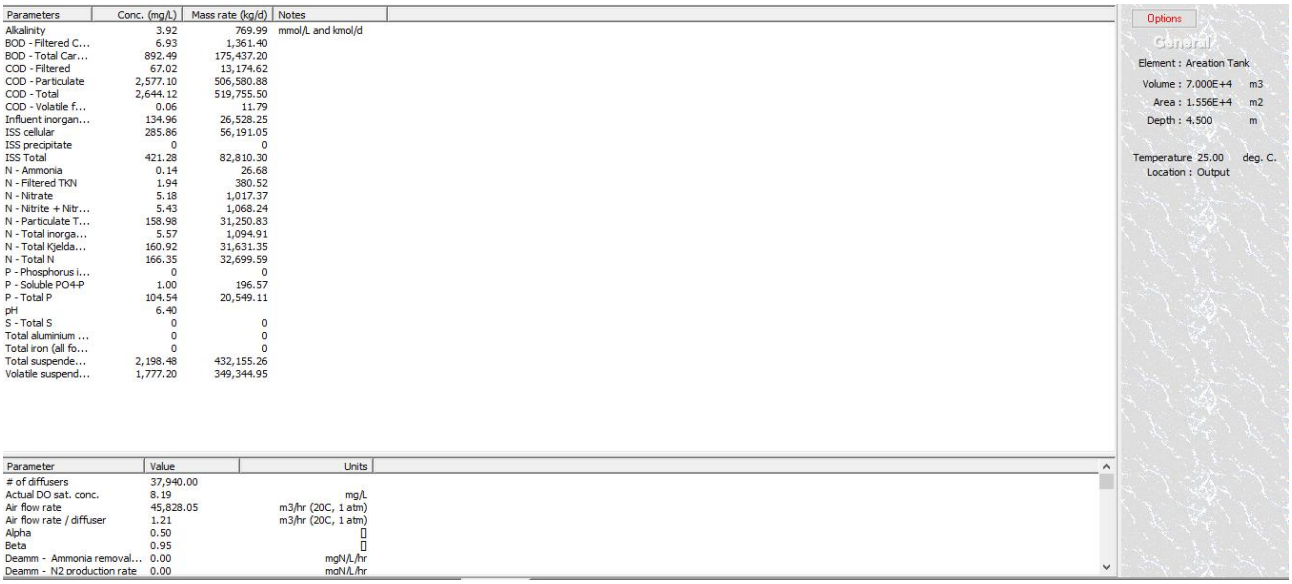

Figure 7: Mixing Tank for Aerobic Process

After equalization in the mixing tank, the Aerobic tank is diffused with oxygen into the system to support microbial activity, enable aerobic biodegradation, enhance process efficiency, and facilitate proper sludge management. It ensures optimal e results provide insights into the effectiveness of the wastewater treatment process. COD, BOD, Volatile suspended solid and the total suspended solid were reduced to 7,604.38treatment performance, efficient removal of organic pollutants, and the production of high-quality effluent in compliance with regulatory standards. Figure 7 shows the data obtained after the simulation.

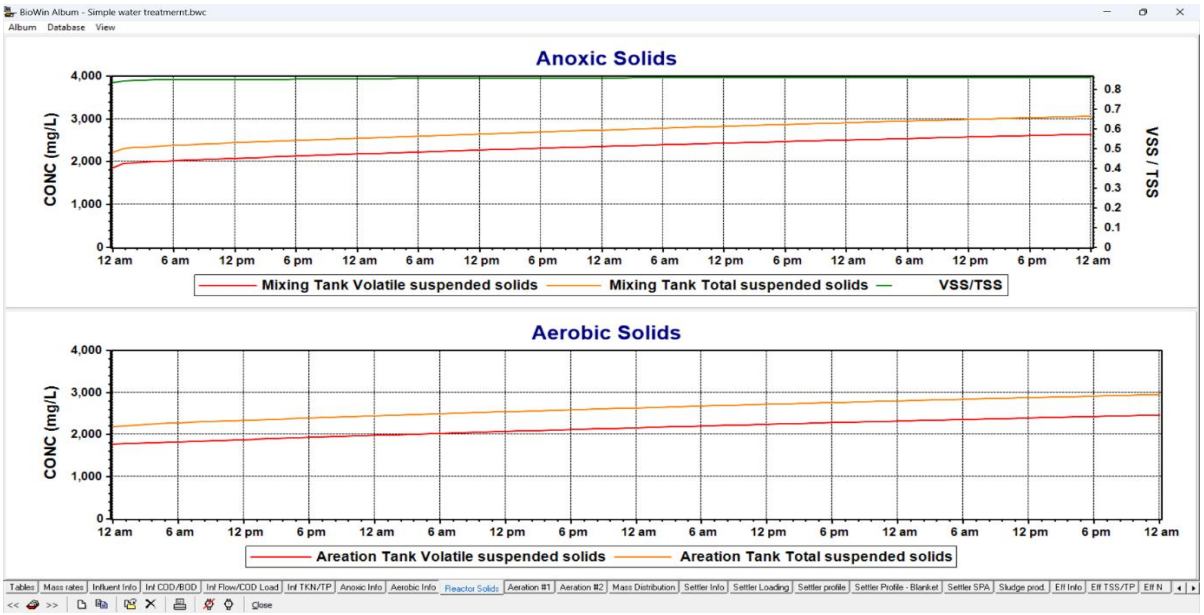

Figure 8: Anoxic and Aerobic Solids

Figure 8 shows the plot of the total suspended solids and volatile solids in the mixing tank and aerobic tank. Figure 9 shows the plot of the aerobic reactor air flow.

Elements	OUR - Total [mgO/L/hr]	OUR - Total [kg/d]	OUR - Carbonaceous [mgO/L/hr]	OUR - Carbonaceous [kg/d]	OUR - Nitrification [mgO/L/hr]	OUR - Nitrification [kg/d]	Denit - N2 production rate [mgN/L/hr]	Denit - N2 production rate [kg/d]	OTE [%]	OTE [%]
Mixing Tank	0	0	0	0	0	0	10.65	6,389.64	100.00	100.00
Areation Tank	19.53	32,803.10	15.39	25,863.13	4.13	6,939.98	0.30	507.39	10.83	10.83

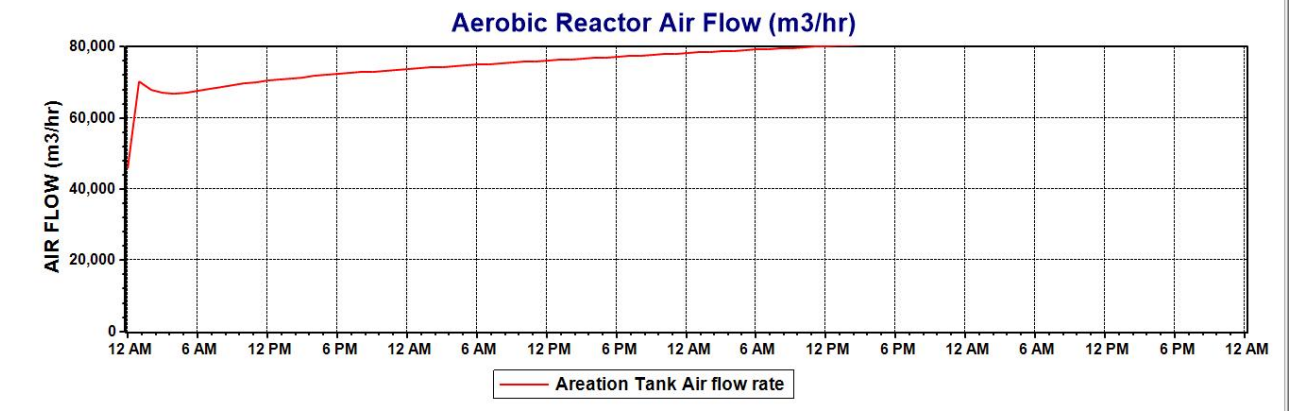

Figure 9: Aerobic Reactor Air Flow

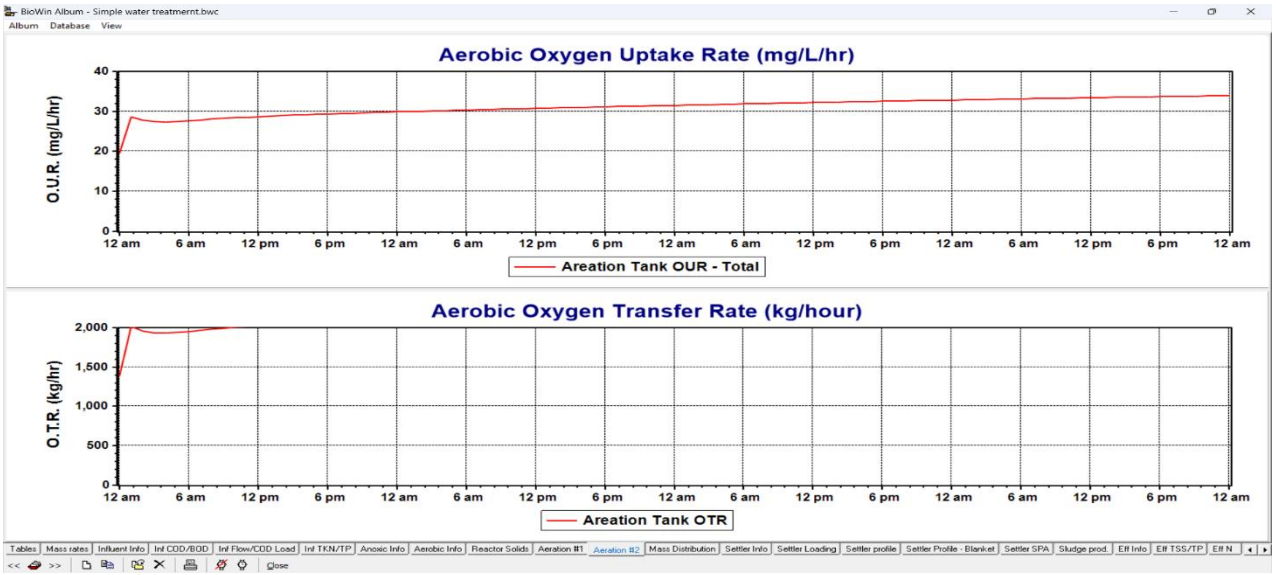

Figure 10: Aerobic Oxygen Uptake Rate and Aerobic Oxygen Transfer Rate

Figure 10 illustrates the oxygen transfer mechanism within the system, highlighting its role in supporting the activity of micro-organisms. Figure 11 presents the mass distribution across key components, including the mixing tank, aeration tank, and clarifier, offering a clear view of the system's operational flow. Figure 12 displays the data generated for the secondary settler, showing key metrics relevant to its performance. Figure 13 visualizes the performance of the secondary settler through plots that depict both the solids loading rate and the surface overflow rate. Figure 14 features plots that represent the relationship between the number of layers and concentration levels within the system. Figure 15 indicates the general effluent data, showing the value of the pH, BOD, COD, alkalinity etc. Figure 16 showcases effluent data, with plots showing the variation in total suspended solids and total phosphorus concentration.

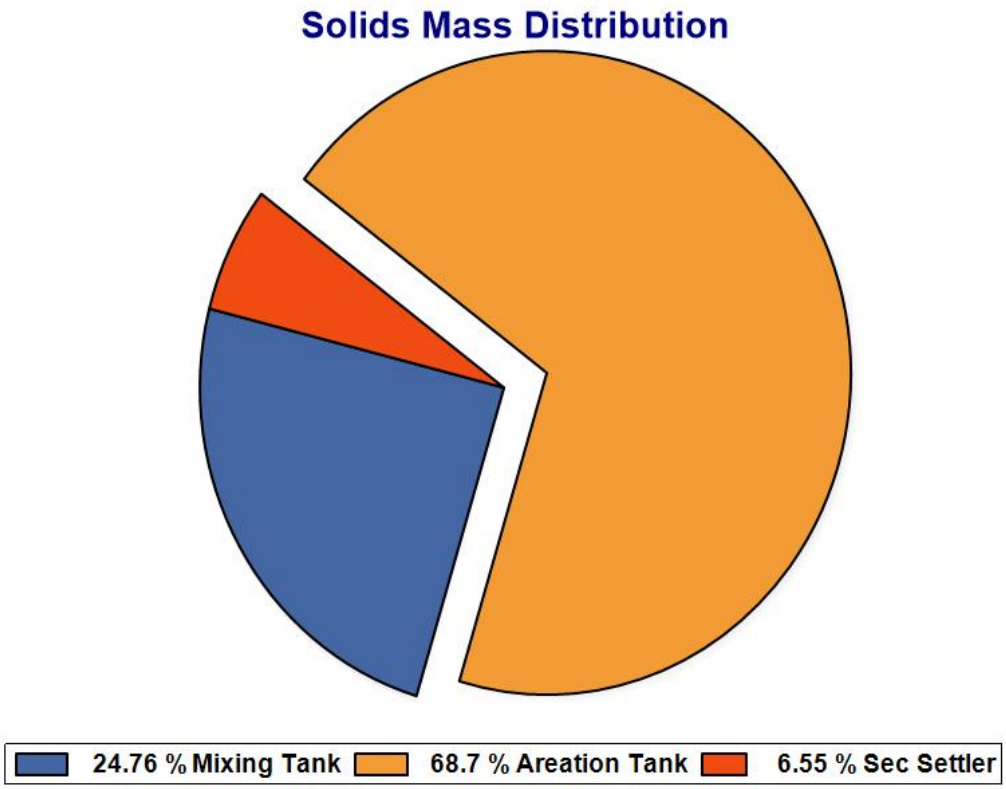

Figure 11: Mass Distribution across the Mixing Tank, Aeration Tank and The Clarifier

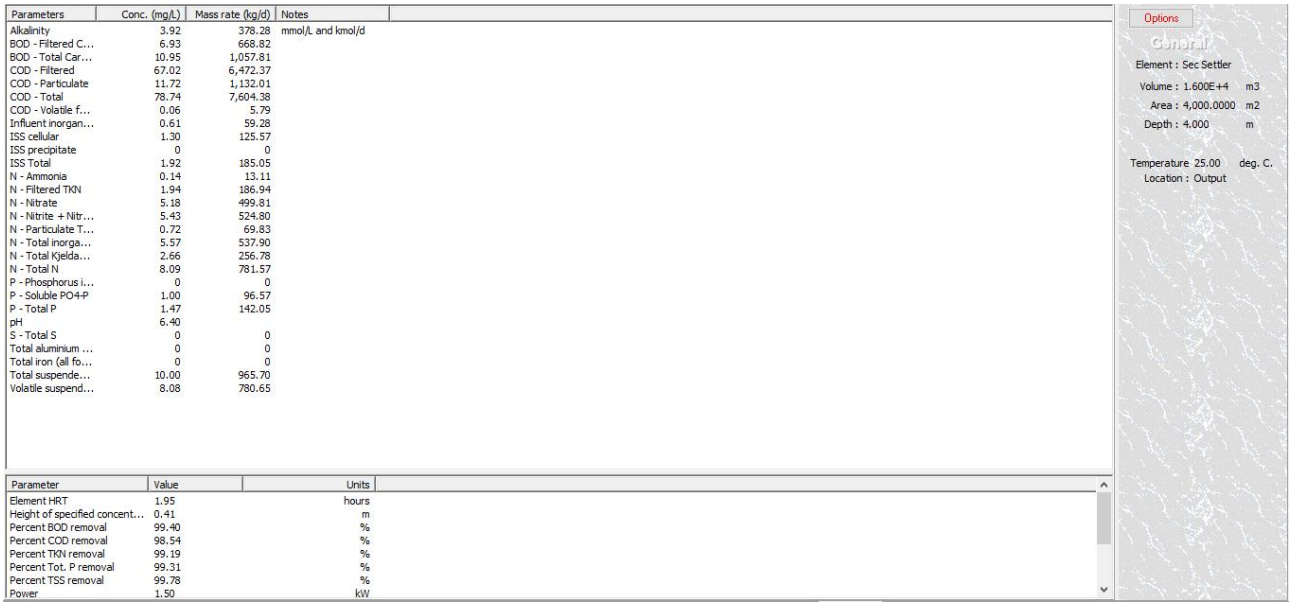

Parameters	Conc. (mg/L)	Mass rate (kg/d)	Notes
Alkalinity	3.92	378.28	mmol/L and kmol/d
BOD - Filtered C...	6.93	668.82	
BOD - Total Car...	10.95	1,057.81	
COD - Filtered	67.02	6,472.37	
COD - Particulate	11.72	1,132.01	
COD - Total	78.74	7,604.38	
COD - Volatile f...	0.06	5.79	
Influent inorgan...	0.61	59.28	
ISS cellular	1.30	125.57	
ISS precipitate	0	0	
ISS Total	1.92	185.05	
N - Ammonia	0.14	13.11	
N - Filtered TKN	1.94	186.94	
N - Nitrate	5.18	499.81	
N - Nitrite + Nitr...	5.43	524.80	
N - Particulate T...	0.72	69.83	
N - Total inorga...	5.57	537.90	
N - Total Kjelda...	2.66	256.78	
N - Total N	8.09	781.57	
P - Phosphorus i...	0	0	
P - Soluble PO4-P	1.00	96.57	
P - Total P	1.47	142.05	
pH	6.40		
S - Total S	0	0	
Total aluminium ...	0	0	
Total iron (all fo...	0	0	
Total suspende...	10.00	965.70	
Volatile suspend...	8.08	780.65	

Parameter	Value	Units
Element HRT	1.95	hours
Height of specified concent...	0.41	m
Percent BOD removal	99.40	%
Percent COD removal	98.54	%
Percent TKN removal	99.19	%
Percent Tot. P removal	99.31	%
Percent TSS removal	99.78	%
Power	1.50	kW

Figure 12: Generated Data for the Sec Settler

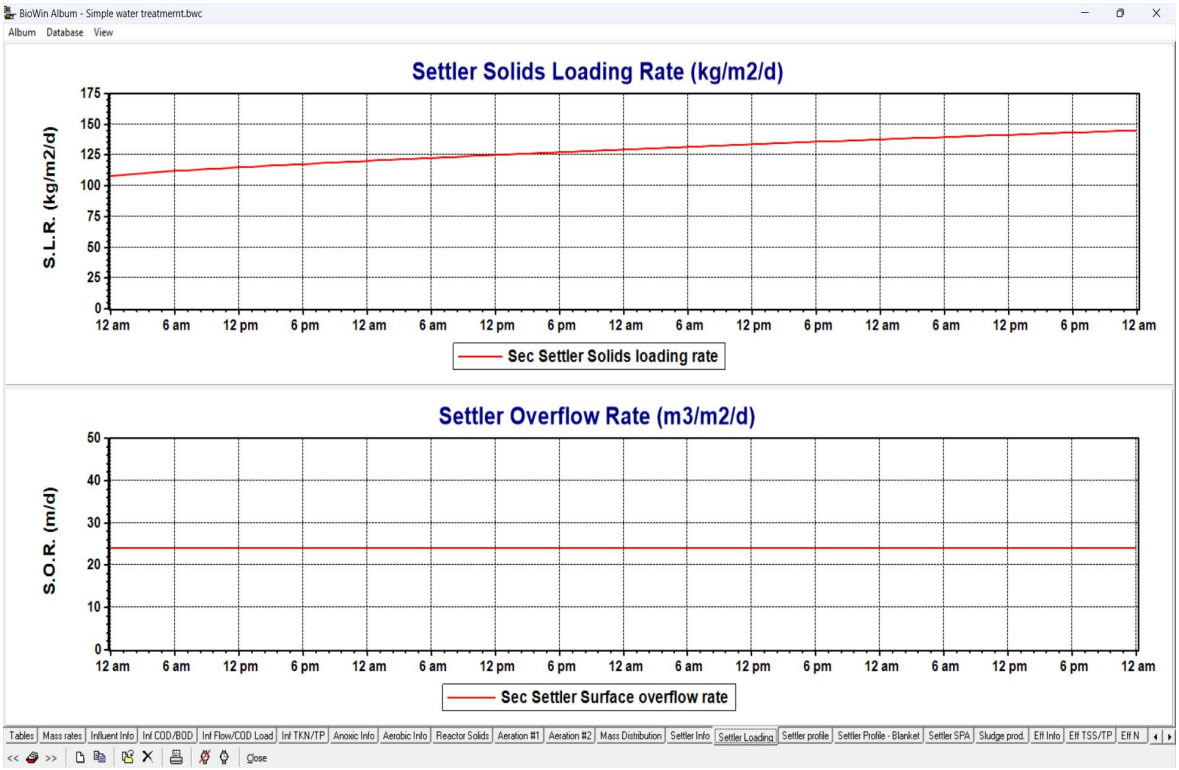

Figure 13: Plots of the Sec Settler

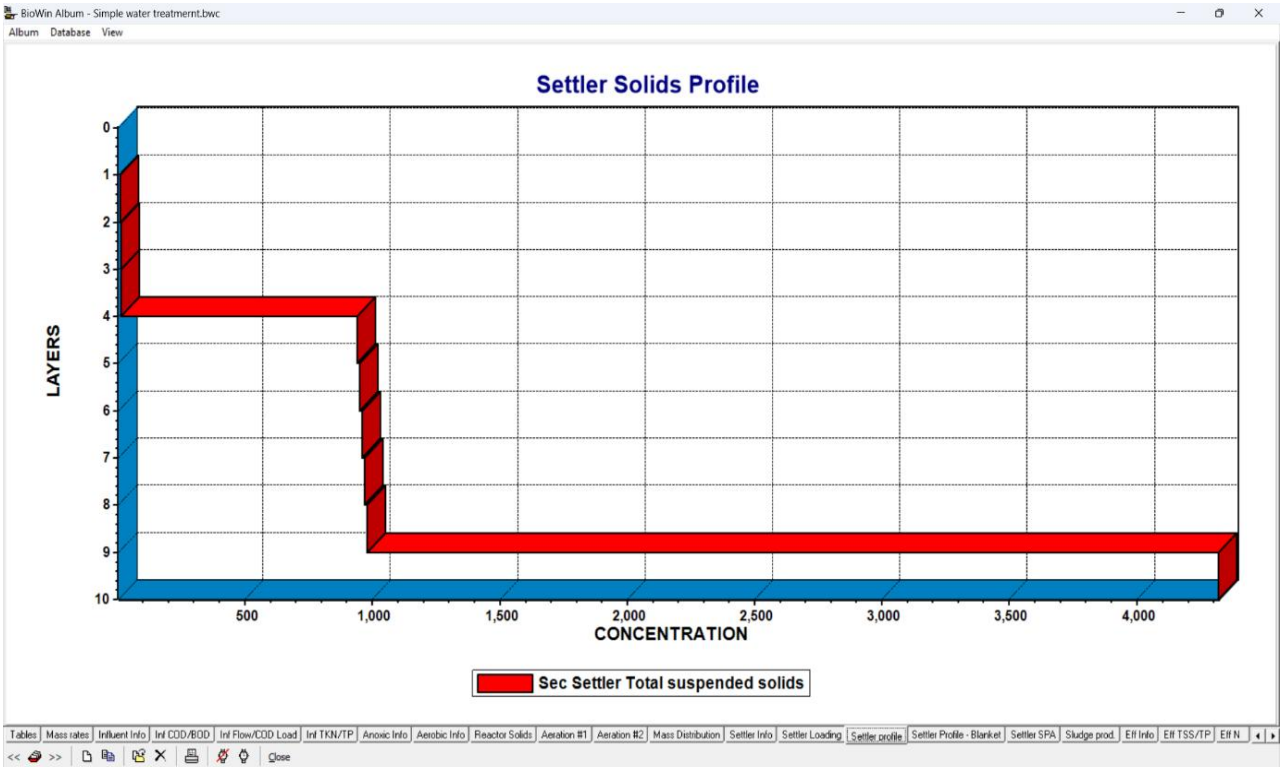

Figure 14: Plots of the Number of Layers against the Concentration

Parameters	Conc. (mg/L)	Mass rate (kg/d)	Notes
Alkalinity	3.92	378.28	mmol/L and kmol/d
BOD - Filtered C...	6.93	668.82	
BOD - Total Car...	10.95	1,057.81	
COD - Filtered	67.02	6,472.37	
COD - Particulate	11.72	1,132.01	
COD - Total	78.74	7,604.38	
COD - Volatile f...	0.06	5.79	
Influent inorgan...	0.61	59.28	
ISS cellular	1.30	125.57	
ISS precipitate	0	0	
ISS Total	1.92	185.05	
N - Ammonia	0.14	13.11	
N - Filtered TKN	1.94	186.94	
N - Nitrate	5.18	499.81	
N - Nitrite + Nitr...	5.43	524.80	
N - Particulate T...	0.72	69.83	
N - Total inorga...	5.57	537.90	
N - Total Kjelda...	2.66	256.78	
N - Total N	8.09	781.57	
P - Phosphorus i...	0	0	
P - Soluble PO4-P	1.00	96.57	
P - Total P	1.47	142.05	
pH	6.40		
S - Total S	0	0	
Total aluminium ...	0	0	
Total iron (all fo...	0	0	
Total suspende...	10.00	965.70	
Volatile suspend...	8.08	780.65	

Options
General
Element : Effluent
Volume :
Area :
Depth :
Temperature 25.00 deg. C.
Location : Output

Parameter	Value	Units
Acetate	0.00	mmol/L
Acetic acid	0.00	mmol/L
Aluminium ion	0	mmol/L
Bicarbonate	3.91	mmol/L
Bisulfate	0	mmol/L
Bisulfide	0	mmol/L
Carbonate	0.00	mmol/L
Divalent act. coeff.	0.63	

Figure 15: Generated Effluent Data

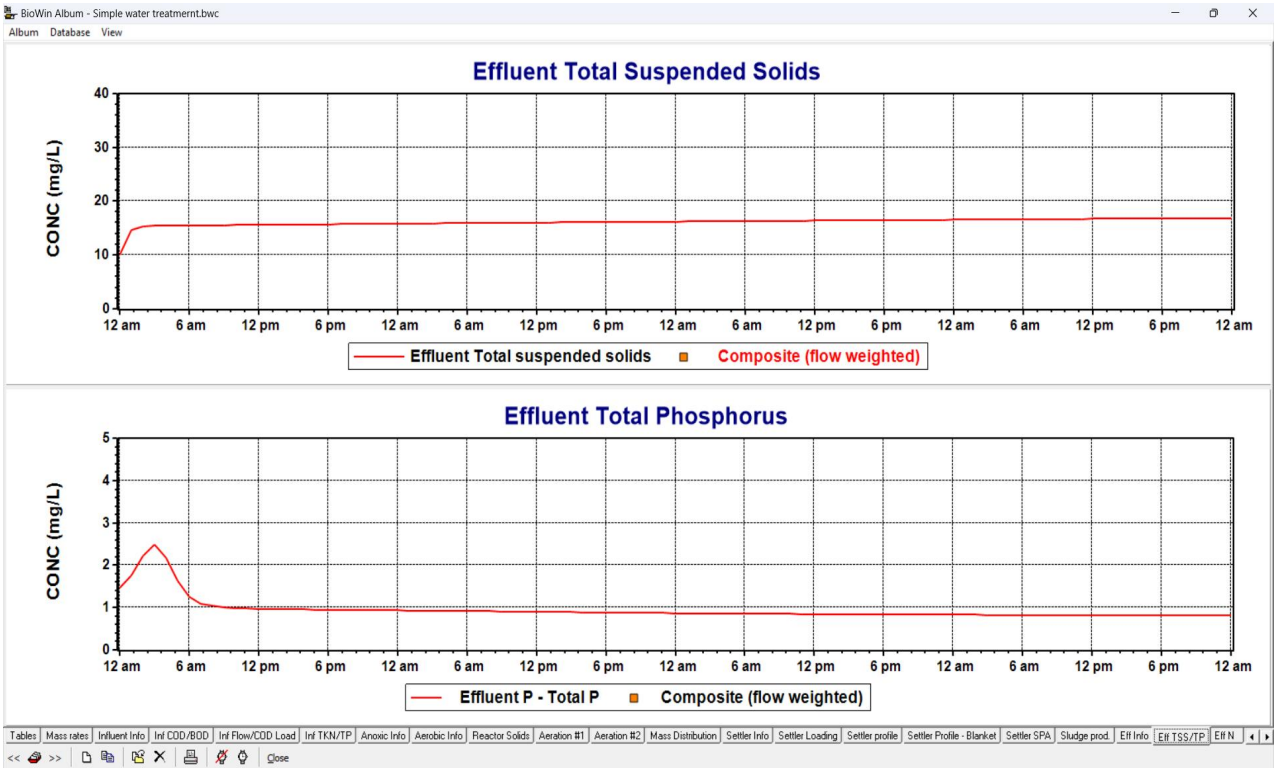

Figure 16: Plots of the Effluent

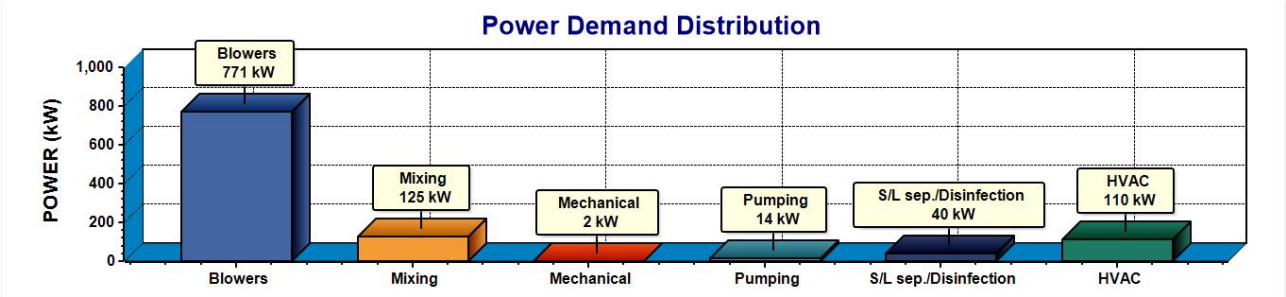

Power Categories	Power Demand [kW]	Cost (Power consumption) [$/hour]
Blowers	770.88	$44.61
Mixing	125.00	$7.23
Mechanical	1.50	$0.09
Pumping	14.33	$0.83
S/L sep./Disinfection	40.24	$2.33
-----	-----	-----
Total of tabulated	951.95	55.09
-----	-----	-----
HVAC	110.00	$6.37
Service Charge	-----	$0.05
Peak Demand Charge	-----	$1.34
-----	-----	-----
System total	1,061.95	$62.85

Figure 17: Power Demand Distribution

The provided results outline the power demands and associated costs across various categories within the system as shown in Figure 17. The categories included the blowers, mixing process**,** mechanical components, pumping operations, and processes related to solid-liquid separation and disinfection. Heating, ventilation, and air conditioning (HVAC) operations also consume 110.00 kW of power, resulting in a cost of $6.37. The peak demand charge of $1.34 could be related to the highest power demand experienced. the comprehensive power demand for the entire system, was 1,061.95 kW, with a total cost of $62.85. These results illustrate the distribution of power demands and associated costs across different operational categories within the system. It offers insights into the energy usage patterns and the financial implications of each component's power consumption. Figure 18 shows the power demand and energy consumption of the different processes.

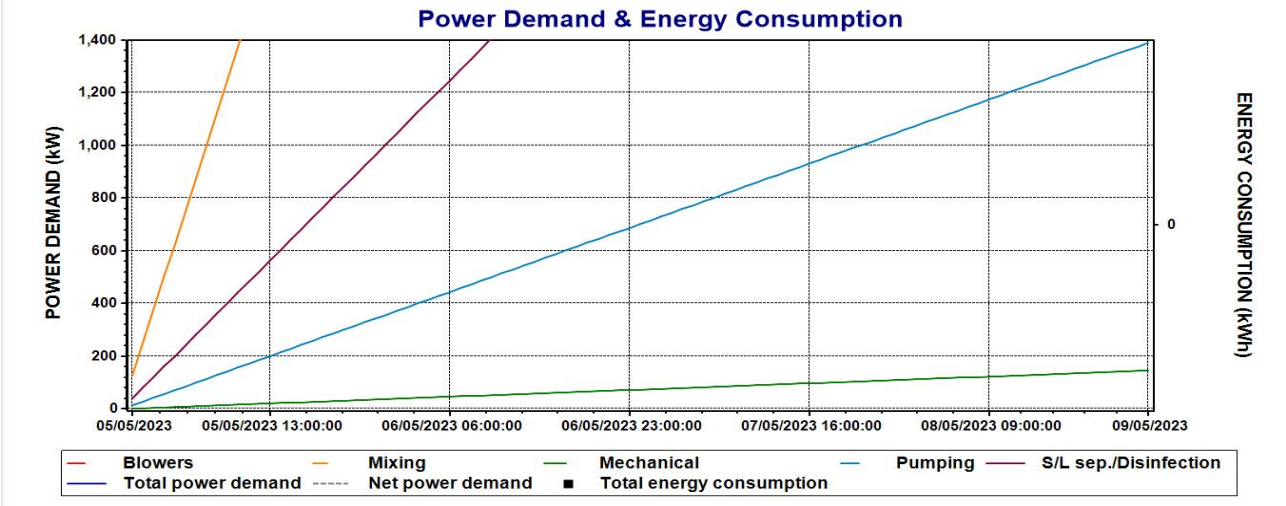

Figure 18: Power Demand and Energy Consumption

4. CONCLUSION

Employing BioWin for the modelling and simulation of a wastewater treatment plant offers numerous advantages and benefits. The utilization of BioWin allows for the simulation of various process configurations and operational parameters to maximize the performance of wastewater treatment plants. The results obtained from the simulation carried out at different runs of the project designed with the aid of BioWin revealed that a valid model that could be used to represent the reactive wastewater treatment process for the treatment of the influent data was developed

successfully with the aid of BioWin. The influent values of COD, BOD, volatile suspended solid and total suspended solid 110,100.00 kg/d, 40,714.98 kg/d, 53,994.69 kg/d, 43,525.34 kg/d, 46,025.34 kg/d were reduced to 7,604.38 kg/d, 6,472.37 kg/d, 1,057.81 kg/d, 780.65 kg/d, 965.70 kg/d respectively. Furthermore, in comparison with the WHO - World Health Organization effluent data, for the COD, BOD, TS, TSS, and DO, using BioWin my effluent data appears better for usage in the paint industry.

ACKNOWLEDGEMENTS

Special thanks go to Aare Afe Babalola, LL.B, FFPA, FNIALS, FCIArb, LL.D, SAN, OFR, CON – The Founder and President, and the Management of Afe Babalola University, Ado-Ekiti, Ekiti State, Nigeria for providing a very conducive environment and the necessary materials that enabled the accomplishment of this work.

REFERENCES

Augustos de Lemos Chernicharo, C. and Von Sperling, M. (2005), "Biological wastewater treatment in warm climate regions, *IWA publishing*, p. 857.

Dadrasnia, A., Usman, M. M., Lim, K. T., Velappan, R. D., Shahsavari, N., Vejan, P., Mahmud, A. F. and Ismail, S. (2017), "Microbial aspects in wastewater treatment–a technical", Environmental Pollution and Protection, 2(2), pp.75-84.

Fazal-ur-Rehman, M. (2019), "Polluted waterborne diseases: Symptoms, causes, treatment and prevention", J Med Chem Sci, 2(1), pp.21-6.

Gerba, C. P. and Pepper, I. L. (2019), "Drinking water treatment", In Environmental and Pollution Science, *Academic Press*, pp. 435-454.

Hoslett, J., Massara, T. M., Malamis, S., Ahmad, D., van den Boogaert, I., Katsou, E., Ahmad, B., Ghazal, H., Simons, S., Wrobel, L. and Jouhara, H. (2018), "Surface water filtration using granular media and membranes: A review", *Science of the Total Environment*, 639, pp.1268-1282.

Pichel, N., Vivar, M. and Fuentes, M. (2019), "The problem of drinking water access: A review of disinfection technologies with an emphasis on solar treatment methods", Chemosphere, 218, pp.1014-1030.

Ray, C. and Jain, R. eds. (2011), "Drinking water treatment: focusing on appropriate technology and sustainability", Springer Science & Business Media.

Solokowski, J. (2009), "Risk Analysis of Water Pollution", *WILEY-VCH Verlag GmbH and Co. KGaA: Weinheim, Germany*, pp. 1–311.

Venugopal, A., Ganesan, H., Raja, S. S. S., Govindasamy, V., Arunachalam, M., Narayanasamy, A., Sivaprakash, P., Rahman, P. K., Gopalakrishnan, A.V., Siama, Z. and Vellingiri, B. (2020), "Novel wastewater surveillance strategy for early detection of coronavirus disease 2019 hotspots", *Current Opinion in Environmental Science and Health*, 17, pp. 8-13.

Xiao, R., Wei, Y., An, D., Li, D., Ta, X., Wu, Y. and Ren, Q. (2019), "A review on the research status and development trend of equipment in water treatment processes of recirculating aquaculture systems", *Reviews in Aquaculture*, 11(3), pp. 863-895.

JOURNAL OF THE NIGERIAN SOCIETY OF CHEMICAL ENGINEERS
INSTRUCTION TO AUTHORS

1. TYPES OF PUBLICATION

The Journal of the Nigerian Society of Chemical Engineers will publish articles on the original research on the science and technology of Chemical Engineering. Preference will be given to articles on new processes or innovative adaptation of existing processes. Critical reviews on current topics of Chemical Engineering are encouraged and may be solicited by the Editorial Board. The following types of articles will be considered for publication:

a. **Full length articles or review papers.**
b. **Communication – a preliminary report on research findings.**
c. **Note – a short paper describing a research finding not sufficiently completed to warrant a full article.**
d. **Letter to the Editor – comments or remarks by readers and/or authors on previously published materials.**

The authors are entirely responsible for the accuracy of data and statements. It is also the responsibility of authors to seek ethical clearance and written permission from persons or agencies concerned, whenever copyrighted material is used.

For now the journal is published twice in a year, March/April and September/October.

2. MANUSCRIPT REQUIREMENTS

a. **The Manuscript should be written in clear and concise English and typed (single column) in Microsoft Word using double spacing on A4-size paper, Times New Romans font and 12 point. A full length article or review should not exceed 20 pages. Margin should be Normal (i.e. 2.54cm for Top, Bottom, Left & Right margins).**
b. **The Manuscript should be prepared in the following format: Abstract, Introduction, Materials and Methods, Results, Discussion, Conclusion, Acknowledgements, and References..**
c. **The Manuscript must contain the full names, address and emails of the authors. In the case of multiple authorship, the person to whom correspondence should be addressed must be indicated with functional email address. As an examples, authors' names should be in this format:**

Momoh, S. O., Adisa, A. A. and Abubakar, A. S.

If the addresses of authors are different, use the following format:

***Momoh, S. O.[1], Adisa, A. A.[2] and Abubakar, A. S.[3]**

Use star * to indicate the corresponding author.

d. **Symbols should conform to America Standard Association. An abridged set of acceptable symbols is available in the fourth edition of Perry's Chemical Engineering Handbook. Greek letters, subscripts and superscripts should be carefully typed. A list of all symbols used in the paper should be included after the main text as Nomenclature.**
e. **All Units must be in the SI units (kg, m, s, N, etc).**
f. **The Abstract should be in English and should not be more than 200 words. The Abstract should state briefly the purpose of the research, methodology, results, major findings and major conclusions. Abstracts are not required for Communications, Notes or Letters.**
g. **Citation must be in the Harvard Format i.e. (Author, Date). Examples are (Smith, 1990) or (Jones et al, 2011). (Kemp, 2000) demonstrated that …..; (Mbuk, 1985; Boma, 1999; Sani, 2000) if more than two authors. (Telma, 2001a), (Telma, 2001b); etc if the citation have the same author and year of publication.**

For more information on Harvard Referencing: Guide visit http://www.citethisforme.com/harvard-referencing

h. **References must also be in the Harvard Format i.e. (Author, Date, Title, Publication Information). References are listed in alphabetical order. Examples are shown below:**

Haghi, A. K. and Ghanadzadeh, H. (2005). A Study of Thermal Drying Process. *Indian Journal of Chemical Technology*, Vol. 12, November 2005, pp. 654-663

Kemp, I.C., Fyhr, C. B., Laurent, S., Roques, M. A., Groenewold, C. E., Tsotsas, E., Sereno, A. A., Bonazzi, C. B., Bimbernet, J. J. and Kind M.(2001). Methods for Processing Experimental Drying Kinetic Data. *Drying Technology,* 19: 15-34.

i. **Tables should contain a minimum of descriptive materials. Tables should be numbered serially throughout the manuscript in Arabic numerals (1, 2, 3, etc), and should be placed at the referenced point with captions (centralised) placed at the top of the table.**
j. **Figures, charts, graphs and all illustrations should be placed at the referenced point, numbered serially throughout the manuscript in**

Arabic numerals (1, 2, 3, etc) and incorporated in the text. Caption for Figures should be placed at the bottom of the Figure (centralised). Lettering set or symbols should be used for all labels on the figures, graphs, charts, photographs even when drawn in colours. (Note that figures drawn in colours may be unreadable if printed in black and white).

k. Equations should be typed using MS Word Equation Editor and should be centred and numbered serially throughout the manuscript (in Arabic numeral) at the right margin.
l. Wherever possible, Fractions should be shown using the oblique slash. E.g. x/y
m. Footnotes should not be incorporated in the text.
n. Acknowledgements should appear at the end of the paper, before the list of references.

3. SUBMISSION OF MANUSCRIPTS

Manuscripts should be submitted by sending a Microsoft Word document (taking into account the Manuscript Requirements described in section 2 above) to the following email address: nschejournal@yahoo.com and copy stevmomoh@yahoo.com.

All correspondences are directed to the Editor-in-Chief using the submission emails addresses: nschejournal@yahoo.com and copy stevmomoh@yahoo.com. Meanwhile the online submission of articles on the journal website will soon be ready.

Authors should note that:

a. All authors listed in the manuscript have significantly contributed to the research.
b. All authors are obliged to provide retractions or corrections of mistakes.
c. All references cited are listed and financial support acknowledged.
d. It is forbidden to publish same research in more than one journal.

The fee charged for paper review and publication will be borne by the authors as follows:

a. Manuscript Review charges = N6,500 payable by both Members and Non-Member. Overseas is $30.00.
b. Publication Charges = N10,000 payable by Non-Members and Members who are not financially up-to-date. Overseas is $40.00.
c. Members would only get one (1) Journal free and buy the other if they so wish.
d. Corresponding Author whose paper is published on a particular edition would get one (1) free copy on behalf of all the co-authors. Other co-authors will buy if they so wish.

All fees are paid after the paper had been accepted for publication. These charges may be reviewed from time to time by the Governing Board of Directors of the Society.

4. ACCEPTED PAPERS

On acceptance, authors will be required to submit a copy of their manuscripts using Microsoft Word by emails to nschejournal@yahoo.com and copy stevmomoh@yahoo.com.

The following additional information should be observed for accepted papers: (i) Typed in Microsoft Word using 1.15 spacing on A4-size paper, Times New Romans font and 10 point; (ii) Margin should be 2.54cm for Top & Bottom; 2.20cm for Left & Right margins; (iii) The abstract should be one column document while the body of the manuscript should be double columns with 0.5cm gutter spacing except some tables and figures that may have to go in for one column document.

5. PUBLICATION

Full NSChE Journal edition in hard copy will be published twice annually – March/April Edition and September/October Edition.

6. REPRINT

Reprints are available on request at a moderate fee per page. Orders must be placed before the paper appears in Print.

7. READER'S INFORMATION

The papers are wholly the view of their author(s) and therefore the publisher and the editors bear no responsibility for such views.

8. SUBSCRIPTION INFORMATION

The subscription price per volume is as follows:

a. Individual Reader - N3,000.00
b. Institutions, Libraries, etc.- N5,000.00
c. Overseas Subscription - $100.00

Request for information or subscription should be sent to the Editor-in-Chief through the following emails addresses: nschejournal@yahoo.com and copy stevmomoh@yahoo.com.

9. COPYRIGHT NOTICE

By submitting your manuscript to the Journal, you have agreed that the copyright of the published material belongs to the journal.

10. PRIVACY STATEMENT

The names and email addresses entered in this journal site will be used exclusively for the stated purposes of this journal and will not be made available for any other purpose or to any other party.